UNIVERSITY OF SOUTHAMPTON

THE SYNTHESIS AND CHARACTERISATION OF OXIDE METAL-INSULATOR MATERIALS

A thesis submitted for the Degree of Doctor of Philosophy

by

Jon Reading

SCHOOL OF CHEMISTRY
FACULTY OF SCIENCE, ENGINEERING AND MATHEMATICS

Aug 2003

UNIVERSITY OF SOUTHAMPTON

ABSTRACT

FACULTY OF SCIENCE, ENGINEERING AND MATHEMATICS
SCHOOL OF CHEMISTRY

Doctor of Philosophy

THE SYNTHESIS AND CHARACTERISATION OF OXIDE METAL-INSULATOR MATERIALS

By Jon Reading

A selection of oxide metal-insulator materials with structures based on pyrochlore and perovskite systems have been synthesised. The structures and electrical properties of these materials have been determined using Rietveld analysis of powder x-ray and powder neutron data and conductivity measurements.

The pyrochlores $Cd_2Os_2O_7$ and $Hg_2Os_2O_7$ have been synthesised by reaction of their respective component oxides sealed in silica ampoules. The materials were found to be isostructural, crystallising in the cubic space group *Fd-3m*. Magnetic measurements were carried out on both materials revealing transitions to antiferromagnetic behaviour at low temperature. In addition, conductivity measurements were performed on $Hg_2Os_2O_7$ from 4 K to room temperature, which showed semi-metallic behaviour across this range with a distinct drop in resistivity centred on the antiferromagnetic transition at 88 K. The crystal structures of the materials were studied using powder neutron diffraction across their respective transition temperatures, which showed weak discontinuities in the structural properties associated with the antiferromagnetic transition.

$Ca_2Os_2O_7$ has been synthesised by the direct reaction of the component oxides in a sealed silica ampoule at ambient pressure. The structure of this system has been determined from analysis of neutron diffraction data at four different temperatures ranging from 100 to 400 K. The material was found to adopt a stoichiometric, orthorhombic weberite structure type rather than the more usual cubic pyrochlore structure. The distortion of the OsO_6 octahedra and eightfold Ca-O co-ordinations decrease with increasing temperature, indicating that this material lies close to the weberite/pyrochlore phase boundary. The electronic behaviour of $Ca_2Os_2O_7$ has been measured by recording variable temperature conductivity measurements showing a metal-insulator transition across room temperature.

The pyrochlores $Pb_2Os_2O_{7-x}$ and $Tl_2Os_2O_{7-x}$ have been synthesised and characterised using powder x-ray and neutron diffraction. Analysis of the data confirmed the presence of oxygen vacancies in the lattice, which was determined as cubic *Fd-3m*. In addition, evidence was found to support that there is a mixing of oxidation states on the 'A' cation site for both materials, inferred from their accurately measured bond lengths. No evidence was found to support the presence of oxygen vacancy ordering, as has been previously found for other post-transition metal pyrochlores.

The only known superconducting pyrochlore, $Cd_2Re_2O_7$, has been prepared at ambient pressure using a ^{114}Cd isotope to enable powder neutron diffraction data collection. The structure for $Cd_2Re_2O_7$ between 320 mK and room temperature has been investigated and a model has been proposed for the superconducting phase. The low temperature (<200 K) structure of $Cd_2Re_2O_7$ was modelled in the space group *F-43m*, where a marked distortion of the ReO_6 octahedra was found to occur. Comparison with the regular ReO_6 octahedra of the high temperature form showed that positional displacements in both the rhenium and oxygen sub-lattices contributed to the distortion, producing a trigonal environment for the rhenium atoms.

A complete solid solution between metallic $LaNiO_3$ and insulating $LaAlO_3$ has been synthesised using a precursor citrate gel technique at ambient pressure. Each composition has been structurally characterised using powder x-ray diffraction and structural trends across the series are discussed. Resistivity measurements were carried out for each composition, which are compared to infra-red spectra recorded for the series to determine the electronic behaviour of the system. The results show a significant increase in resistivity for ≥ 60 % aluminium concentration. An explanation of the electronic behaviour is presented using percolation theory.

TABLE OF CONTENTS

Chapter Two: Experimental Techniques

Chapter Three:The Structure and Physical Properties of Osmium (V) Pyrochlores $A_2Os_2O_7$ (A = Cd and Hg)

Chapter Four: The Synthesis, Structure and Physical Properties of Calcium (V) Osmate

Chapter Five: Synthesis and Structural Characterisation of the Non-Stoichiometric Pyrochlores $A_2Os_2O_{7-x}$ (A = Pb and Tl)

Chapter Six: A Structural Study of Superconducting $Cd_2Re_2O_7$ using Powder Neutron Diffraction

Chapter Seven: Structural Characterisation and Physical Properties of the Perovskite $LaNi_{1-x}Al_xO_3$ System

ACKNOWLEDGEMENTS

Firstly I should like to thank my supervisor Prof. Mark Weller for guidance and support over the past three...ahem...five years. I should also like to thank my sponsor supervisor Dr. Richard Mortimer for his help and patience during my number of experimental visits to DSTL. Special thanks goes to those people who have helped in the collection of powder neutron diffraction data at I.L.L. and R.A.L., including Dr. Andrew Hector, Dr. Paul Henry, Dr. Chris Knee, Doug Booth, Bob Hughes and Paul Vincent. My gratitude also goes to Dr. S. Gordeev who kindly performed VSM experiments for me.

I should also like to thank the following people for helping to make the last five years in Southampton enjoyable. The Weller group past and present, including Beardy, Prof. Fatty, Kenny, Adam Healey, Eric Hughes, Doug Booth, Raekeldoom, Andrew Young, Big Bad Bob, Gypsy, Nichola, Tony, Dr. Ahmed, Vince, Jo, Marianne, Lee, Oliver, Tom, Stuart and Seth.

Finally, and most importantly, I thank SD for her love and support over the past seven years without which this would not have been possible.

In memory of my Mother. You will always be in my thoughts. 

".....and remember this, there is no more important safety rule than to wear these...safety glasses."

- Norm Abram.

Chapter One

Introduction

1.1 Complex Metal Oxides

Complex metal oxides are widely studied because of their interesting chemical and physical properties. This has led to a vast number of these materials being used and developed for important industrial applications[1]. The physical effects exhibited by oxide materials include magnetic and electrical properties. These properties can be utilised in various applications which include rechargeable batteries, solid state devices such as capacitors and heating elements.

Most complex oxides consist of multi-dimensional units constructed from metal-oxygen (M-O) polyhedra. The linked MO_n polyhedra form extended structures, which facilitate co-operative electronic effects, giving rise to materials with applications as conductors[2], semi-conductors[3], superconductors[4], ferroelectrics[5] and piezoelectrics[6]. The discovery of ferroelectricity in $BaTiO_3$ by Von Hippel[7] prompted a large amount of interest in the perovskite structure type. A number of phases exhibiting similar properties adopt the three dimensional (3D) perovskite or a related (2D) layered structure represented by the general formula $(AO)_m(ABO_3)_n$; where 'A' is a lanthanide, alkaline earth or alkali metal and 'B' is a transition metal or post transition metal which may have unusual oxidation states stabilised by the rigid oxide lattice. Studies by Galasso revealed that the 'A' and 'B' sites could each accommodate two or more ions in varying oxidation states[8], which allowed researchers to tune the properties to create new thermistors[9], IR windows[10], semi-conductors[3] and recently high temperature superconductors[11,12].

Since oxide materials have a multitude of applications, research into materials using ambient conditions has been extensive. One possibility for generating new materials with practical applications is to find new preparative methods that allow unusual oxidation states of the elements to be attained. The interest in higher oxidation states has also increased with the recently discovered high temperature superconductors, which contain the rare trivalent copper ion. New methods of producing highly oxidised materials have been developed using both high pressure annealing techniques[13] and electrochemical oxidation[14]. Despite the advantages of synthesising novel phases using high pressure applications, these processes can be costly. Therefore, industrially viable routes to the same product are also sought using low pressure / low temperature routes.

Having synthesised these model phases, structural characterisation is paramount in the understanding of their chemistry and physical properties. Many different experimental techniques exist for the characterisation of oxides, giving information on both the local and long-range structure of the material. These techniques allow the structure/property relationship of a novel material to be investigated and possibly optimised for a specific application.

Following the discovery of high temperature superconductivity within the La-Ba-Cu-O system[15], there has been extensive research carried out synthesising and characterising new complex metal oxides with interesting electronic and magnetic properties. This has produced a wealth of other novel materials, including colossal magneto-resistors and metal-insulators. The development of new techniques to synthesise and characterise these new materials has also led to a greater understanding of the physical properties in terms of structural requirements. This knowledge can be applied to materials containing different, but similar metal ions, to produce new compounds, which may themselves display interesting physical properties.

1.2 Perovskite Materials

The perovskite structure is frequently adopted by materials of the stoichiometry ABO_3 and is potentially the most widespread ternary phase. The name is derived from a specific mineral known as perovskite. The structure of the perovskite mineral, $CaTiO_3$, was first described in the 1830's by Gustav Rose, who named it after the Russian mineralogist Count Lev Aleksevich von Perovski. A range of electronic properties are exhibited by perovskite materials, which can be insulating, semi-conducting and metallic. The majority of perovskites are observed to be insulating, indeed their high electrical resistivities make them ideal for use as dielectric materials. Whilst most perovskites are insulating, some perovskite phases contain the 'B' ions in an oxidation state other than their most stable which can produce fairly good conductors or semi-conductors. Examples of these include $LaNiO_3$, $LaTiO_3$, $CaMoO_3$, $SrMoO_3$ and $LaVO_3$. Other perovskite conductors or semi-conductors are produced by the 'B' ion being present in a mixed valent state e.g. $La_{(1-x)}Sr_{(x)}MnO_3$, $SrTiO_{3-x}$, $SrVO_{3-x}$ and $Ba_{(1-x)}La_{(x)}TiO_3$. The many different examples of

electrical properties exhibited by perovskite oxides include ferroelectric, pyroelectric, piezoelectric, magneto-resistive and high temperature superconducting behaviour.

1.2.1 The Perovskite Structure

For the simple perovskite structure ABO_3, 'A' represents a large electropositive cation *e.g.* Sr^{2+}, Ca^{2+}, Ba^{2+}, Bi^{3+}, Ln^{3+} and 'B' represents a small transition metal/main group ion, *e.g.* Ti^{4+}, Ru^{4+}, Fe^{3+}, Cr^{3+}. The co-ordination geometry is described as follows; the 'A' cation is co-ordinated to 12 oxygens and the 'B' cation to 6 oxygens, hence the structure may be described as a framework of corner-sharing BO_6 octahedra containing 12-co-ordination 'A' cations. Figure 1.1 depicts the perovskite structure, showing both 'A' and 'B' cation centred arrangements. Perovskites form a major structural family of mixed metal oxides, and since the late 1980s, have gained much attention as a key structural motif in high temperature superconductors.

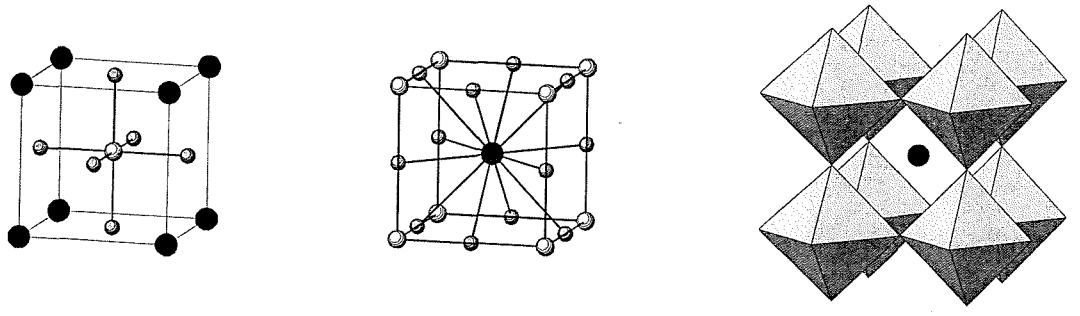

Figure 1.1. The perovskite structure showing (a) 'B' centred cation arrangement, (b) 'A' centred cation arrangement and (c) 3D network of BO_6 octahedra. The 'A' cations are represented by black spheres, 'B' cations by white spheres, oxygens by grey spheres and the BO_6 octahedra by grey polyhedra.

The perovskite mineral, $CaTiO_3$, still retains the name despite later being found to adopt an orthorhombic structure[16]. Further study of perovskite oxides showed that very few materials did actually have this simple cubic structure at ambient temperature. This can be explained by materials adopting the perovskite structure, are often under considerable strain,

which can be attributed to ionic sizes incompatible with the ideal cubic form. This can lead to structural distortions to lower symmetry phases. The most common structure that perovskite materials adopt is an orthorhombic one. This orthorhombic distortion was first determined for $GdFeO_3$[17], so materials with this crystal class are often referred to as the $GdFeO_3$ structure.

1.2.1.1 Tolerance Factors

For any given ternary oxide to adopt a cubic perovskite structure, the size of the ions and the preferential co-ordinations must be simultaneously satisfied. In order to have contact between 'A', 'B' and 'O' ions, $R_A + R_O$ should equal $\sqrt{2}(R_B + R_O)$, where 'R' is the ionic radius. This can be seen in Figure 1.2 below with relevant atoms highlighted.

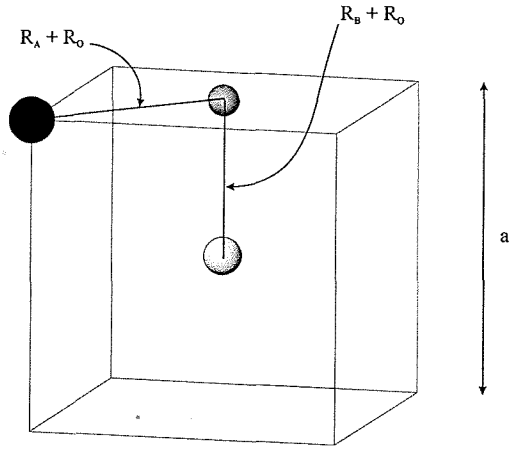

Figure 1.2. Ionic radii relationship between atoms in a perovskite cell. The 'A' cation is represented by the black sphere, the 'B' cation by the white sphere and the oxygen by the grey sphere.

A study by Goldschmidt[18] developed a tolerance factor for perovskite systems, giving a measure of compatibility between any two 'A' and 'B' cations. This is defined as

$$2\,t\,(R_B + R_O) = \sqrt{2}\,(R_A + R_O)$$

where t is the tolerance factor, R_B is the radius of cation 'B', R_O is the radius of the oxygen ion and R_A is the radius of cation 'A'. If the two ions are a perfect fit for the cubic close-packed perovskite structure $t = 1$. An increase of deviation from this value indicates an increase of strain upon the structure. Goldschmidt showed that the perovskite form was stable for $0.85 < t < 1.06$. Stresses associated with a strained structure can often be overcome by a distortion to a lower symmetry system as previously mentioned. If the value of t falls outside these values another structure is normally adopted *e.g.* $LiNbO_3$[19], $LaNiO_3$[20] and $LaAlO_3$[21] reported to have a distorted rhombohedral structure.

1.2.1.2 Perovskite Compositions and Properties

The vast number of perovskite oxides is due both to the range of cation sizes and the number of possible valences, which can be incorporated within the structure. Considering only integral compositions of oxide perovskites, there are three combinations of 'A' and 'B' ions possible to retain charge neutrality and fulfil the co-ordination requirements of the cations. These are i.) $A^{1+}B^{5+}O_3$, ii.) $A^{2+}B^{4+}O_3$ and iii.) $A^{3+}B^{3+}O_3$.

i.) $A^{1+}B^{5+}O_3$ type oxides - This group of oxides is renowned for their ferroelectric properties. Example materials of this type include $KNbO_3$ and $NaNbO_3$ both reported to be orthorhombic[22,23] and $KTaO_3$ which is found to have a cubic structure[24].

ii.) $A^{2+}B^{4+}O_3$ type oxides - This group contains the largest amount of the perovskite compounds, where the 'A' cations are alkaline earth ions, cadmium or lead, and the 'B' cations can be a number of transition metals, post-transition metals or selective lanthanides and actinides. The most widely studied of this class of materials are the titanates, due to the ferroelectric properties exhibited by the lead and barium containing compounds. The majority of true cubic perovskites belong to the $A^{2+}B^{4+}O_3$ group, including compounds $BaZrO_3$, $SrTiO_3$, $SrZrO_3$[25], $CaCeO_3$, $CdCeO_3$[26], $SrRuO_3$[27] and $SrSnO_3$[16].

iii.) $A^{3+}B^{3+}O_3$ type oxides - The majority of this group is found to adopt an orthorhombic crystal class, which for perovskites, is known as the $GdFeO_3$ structure. Taking $GdFeO_3$ as an example, the structure consists of gadolinium ions co-ordinated to 12 oxygens with 8 different bonding distances due to the displacement of the oxygen sites from true face centre positions. The iron ions are co-ordinated to 6 oxygens with 3 different bonding distances,

producing a distorted octahedral environment. Taking a level of iron centred octahedra, they are tilted toward or away from each other in planes joined at the corners, resulting from the distortions. The distorted octahedral environments can be seen clearly in Figures 1.3 and 1.4. The dark spheres represent gadolinium atoms, the grey shaded spheres represent iron atoms and the white spheres, oxygen atoms.

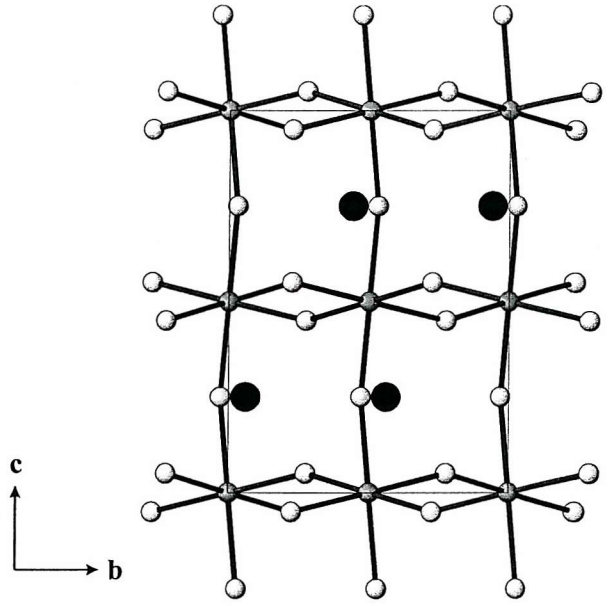

Figure 1.3. Distorted FeO_6 octahedra in the $GdFeO_3$ cell.

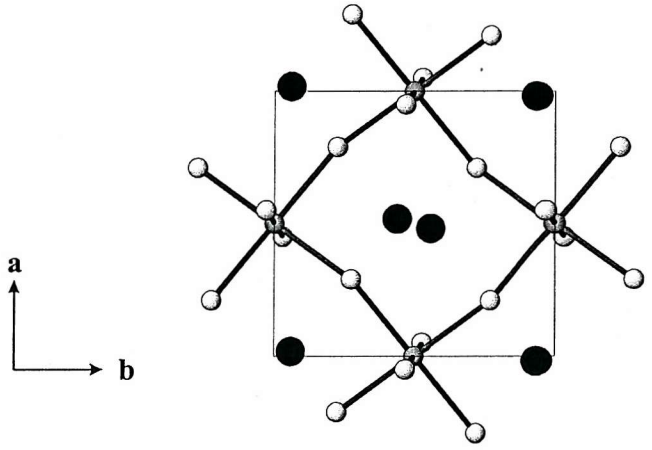

Figure 1.4. Pictorial view of the $GdFeO_3$ structure down the *c*-axis of the unit cell.

Whilst most of the $A^{3+}B^{3+}O_3$ perovskite oxides are found to be orthorhombic, some oxides are closer to satisfying the ideal perovskite structure and thus, less distorted. These compounds can be found to adopt a rhombohedral unit cell, of which examples include $LaNiO_3$[20] and $LaAlO_3$[21].

Gallasso has shown a wide range of non-integral compositions are possible, such as $Ba^{2+}(Sr^{2+}_{0.33}Ta^{5+}_{0.67})O_3$[28], and similarly for the 'A' cation, $Ba_{0.5}Sr_{0.5}SnO_3$[29]. The number of possible stoichiometries is still further increased by the occurrence of both 'A' cation and oxide non-stoichiometries such as the tungsten bronzes Na_xWO_3[30] and the ferrates $SrFeO_{3-x}$[31].

The interesting physical properties exhibited by many perovskites are co-operative effects arising from the 3D network of transition metal ions connected via an oxide lattice. There is a high degree of orbital overlap between the oxide *2p* and *3d* transition metal orbitals which gives rise to these effects. The many industrial applications of perovskites normally utilise the ferro- and piezoelectric properties of the titanates and zirconates such as $BaTiO_3$[32] and the niobates and tantalates such as $KNbO_3$[22]. The properties of the phases can often be accurately controlled by doping at either the 'A' or 'B' cation site. Examples of commercial uses of perovskite materials include high dielectric constant capacitors, blocking-smoothing filters and record player styli[33]. There are many other properties of perovskite phases yet to find commercial applications, such as semiconductors and ferromagnets, and others, which are just being developed for commercial application including cuprate superconductors.

1.2.2 Double Perovskites

Throughout studies on perovskite materials, a central theme has been the systematic change of the size, valence and coordination geometry of the constituent ions in order to investigate the effects of these parameters on magnetic and electrical properties, and crystal chemistry. Much work has centred on double perovskites, which have the formula $AA'BB'O_6$, and the distribution of metals within these systems. Double perovskites show three distinct 'B' cation arrangements, random, rock salt and layered (see Figure 1.5), depending on the charge, size and coordination geometry of the 'B' cations, and the A:B size ratio. As the difference in charge/size of the 'B' cations increases, the systems are more likely to be ordered. The three

'B' cation sublattice types, common cell sizes, crystal systems and space groups are shown in Table 1.1. When assignment of sublattice type is made based on information from powder x-ray diffraction data, ambiguities can arise. In such cases, neutron diffraction or electron microscopy data can be helpful.

Table 1.1. A summary of crystallographic information for common double perovskites; a_p = lattice parameter for cubic ABO_3 perovskite (~ 4 Å).

Sublattice type	Cell size	Crystal system	Space group
Random	$a_p \times a_p \times a_p$	Cubic	*Pm3m*
	$\sqrt{2}a_p \times \sqrt{2}a_p \times 2a_p$	Orthorhombic	*Pbnm*
Rock salt	$2a_p \times 2a_p \times 2a_p$	Cubic	*Fm3m*
	$\sqrt{2}a_p \times \sqrt{2}a_p \times 2a_p$	Monoclinic	$P2_1/n$
Layered	$2a_p \times 2a_p \times 2a_p$	Monoclinic	$P2_1/m$

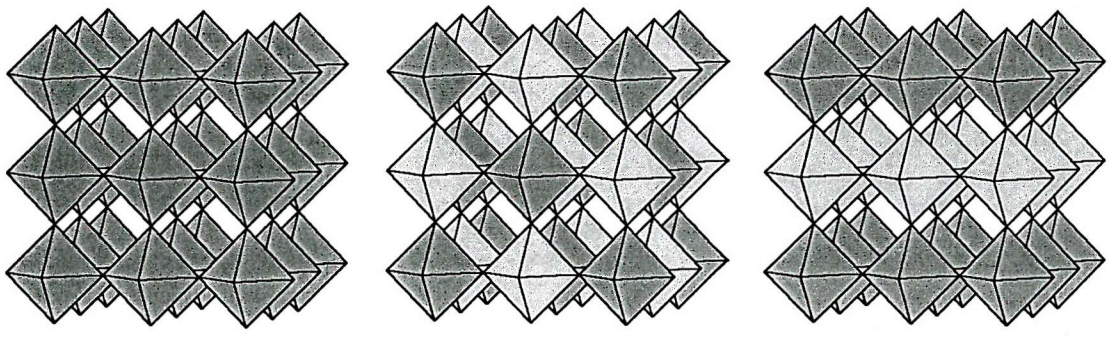

Random Rock salt Layered

Figure 1.5. Possible 'B' cation arrangements in double perovskites.

1.2.2.1 Random Structure Perovskites

Compounds that have a random structure show no evidence of 'B' cation order and generally have a cubic $1a_p$ unit cell such as $BaLaFeMoO_6$[34], or an orthorhombic $\sqrt{2}a_p \times \sqrt{2}a_p \times 2a_p$ unit cell such as that adopted by $SrLaCuRuO_6$[35]. The orthorhombic cell results from rotations of the BO_6 octahedra about the *011* and *100* planes, and results in the absence of *0kl* reflections (where k = 2n+1). The octahedra tilt to reduce internal bond strain within the structure.

1.2.2.2 Rock Salt Structure Perovskites

These systems contrast to the random sublattice in that they have a rock salt sublattice, *i.e.* the 'B' cations B' and B'' resemble the AX arrangement of the anions and cations in the rock salt structure. Generally, they have a cubic $2a_p$ unit cell such as Sr_2CuWO_6[36] or a monoclinic $\sqrt{2}a_p$ x $\sqrt{2}a_p$ x $2a_p$ unit cell such as Sr_2LuRuO_6[37] and Nd_2MgTiO_6[38]. A monoclinic cell usually results from rotation of the BO_6 octahedra about the *011* and *100* planes. Compounds with a rock salt sublattice do show evidence of 'B' cation order. The indication of ordered cations for a cubic cell is lattice parameters doubled with respect to those for a random distribution of cations and the presence of the *111* reflection.

1.2.2.3 Layered Structure Perovskites

One material that exhibits a layered arrangement is La_2CuSnO_6[39]. It has a monoclinic cell derived from a $2a_p \times 2a_p \times 2a_p$ unit cell. The layered arrangement can be distinguished from the random sublattice by the presence of a $2a_p \times 2a_p \times 2a_p$ rather than a $a_p \times a_p \times a_p$ cell. Another well characterised layered perovskite is the oxygen deficient double perovskite $Ba_2InCuO_{4+\delta}$[40] which crystallises with tetragonal symmetry; unit cell $a_p \times a_p \times 2a_p$.

1.3 Pyrochlore Materials

Pyrochlore materials belong to the family of ternary oxides which are isostructural to the mineral pyrochlore, (NaCa)(NbTa)O_6F/(OH), with Greek nomenclature; *pyros* - a fire and *chloros* - green since it turns green on ignition. The compounds have the general formula, $A_2B_2O_7$, where 'A' and 'B' are metals, and are predominately cubic. There are numerous examples of pyrochlore materials (~150), since they lend themselves to a variety of chemical substitutions at the 'A', 'B' and 'O' sites providing the ionic radius and charge neutrality criteria are satisfied. The crystal structure also tolerates vacancies at the 'A' and 'O' sites furthering the possibility for even more examples. Pyrochlore materials are widely studied because they exhibit a wide range of interesting physical properties. This is because the 'B' element can be a transition metal with variable oxidation state or a post transition metal and the 'A' element can be a rare earth {Ln} or an element with inert lone pair of electrons. Therefore the electronic behaviour of pyrochore materials can range from highly insulating through semi-conducting to metallic. Several compounds exhibit a semi-conductor/metal transition which can be induced by a change in temperature or pressure, examples of which include the osmates $Cd_2Os_2O_7$[41], $Hg_2Os_2O_7$[42], $Ca_2Os_2O_7$[43] and the ruthenate $Tl_2Ru_2O_7$[44]. Very recently, superconductivity has been discovered in $Cd_2Re_2O_7$ at ~1 K[45], which is the only pyrochlore to date to exhibit this behaviour and has led to much interest in this compound. Many phases also show interesting dielectric, piezoelectric and ferroelectric behaviour, particularly when the 'A' and 'B' elements are present in their highest oxidation states. The family of pyrochlore materials also has examples of magnetic behaviour ranging from simple paramagnetism to ferro or anti-ferromagnetism.

1.3.1 The Pyrochlore Structure

The general formula of the oxide pyrochlores is $A_2B_2O_7$, which is also expressed as $A_2B_2O_6O'$ to distinguish the four crystallographically non-equivalent types of atom. The ideal form of pyrochlore crystallises in the cubic space group, *Fd-3m*. The structure consists of two different types of cation co-ordination environment. The 'A' cation, usually ~1 Å, is co-ordinated to eight oxygen atoms in a distorted (6+2) arrangement forming scalenohedra (distorted cubes). The 'B' cations are somewhat smaller, ~0.6 Å, and are co-ordinated to six equidistant oxygen atoms to give trigonal anti-prisms. The 'B' cation arrangements are commonly referred to as BO_6 octahedra, even though this is not

technically correct due to the space group symmetry requirements. The cubic pryochlore structure is shown in Figure 1.6 with the conventional 'B' cation origin to the unit cell.

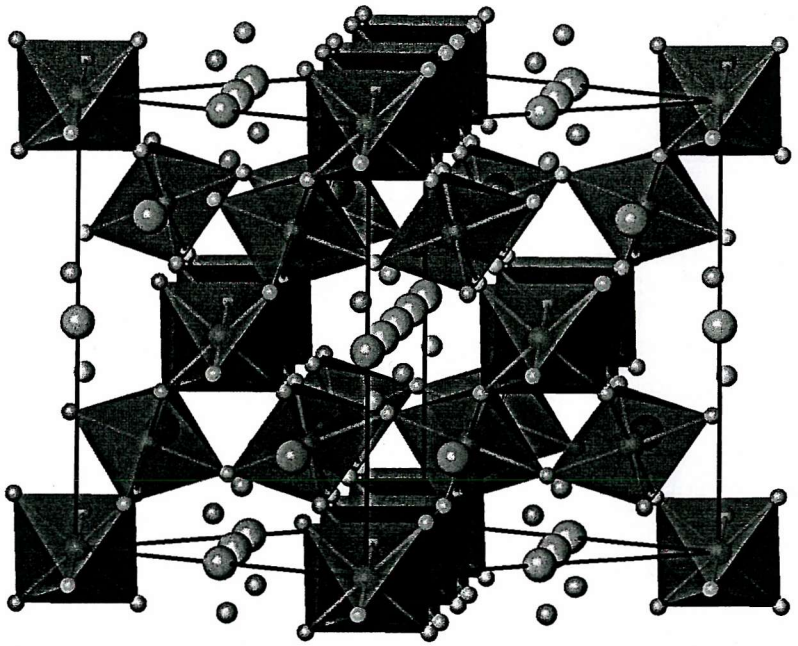

Figure 1.6. The pyrochlore structure, $A_2Os_2O_7$ shown as linked BO_6 octahedra surrounding A cations (large spheres) and O (smaller unlinked spheres).

The structure can be considered as a 3D network of corner linked BO_6 octahedra with the 'A' atoms filling the instices[46]. The eight co-ordinated 'A' cation is in the centre of a puckered hexagonal ring due to the (6+2) surrounding oxygen arrangement. The A-O' bond distance is shorter than the A-O distance. Therefore, by neglecting the A-O interaction the structure can be regarded as interpenetrating networks of B_2O_6 and A_2O' units. The A_2O' linkages form zig-zag chains and two such chains intersect at O'.

1.3.1.1 Pyrochlore Compositions and Properties

The large number of pyrochlore oxides is due both to the large amount of cations that can be incorporated at the 'B' site and the toleration of vacancies at both the 'A' and 'O' sites. Considering only integral compositions of pyrochlore oxides, there are two groups of cation combinations, i.) (3+,4+) pyrochlores and ii.) (2+,5+) pyrochlores.

i.) (3+,4+) pyrochlores – This is the largest group of the known pyrochlore oxides due to the fact that a large number of A^{3+} and B^{4+} cations have suitable ionic radii for the formation of the structure. The A^{3+} cation can be a rare earth, Sc, Y, Bi, Tl or In, whereas the B^{4+} cation can be a 3*d*, 4*d* or 5*d* transition metal or any of the group 14 elements, Si, Ge, Sn and Pb. The recent discovery of colossal magnetoresistance (CMR) in $Tl_2Mn_2O_7$[47,48] has led to considerable interest in this phase. Another group of pyrochlores that have been found to exhibit interesting physical properties are the molybdates. The series $R_2Mo_2O_7$ (R = Nd to Yb including Y) show a variety of electrical and magnetic behaviour. For R = Nd, Sm and Gd, metallic and ferromagnetic behaviour is found, whereas for R = Tb to Yb including Y, semi-conducting behaviour is observed[49,50].

ii.) (2+,5+) pyrochlores – There are considerably fewer (2+,5+) pyrochlore oxides in comparison to (3+,4+) pyrochlore oxides. This is probably due to there being a fewer number of suitable A^{2+} and B^{5+} cations than A^{3+} and B^{4+} cations. In all the (2+,5+) pyrochlores known, A^{2+} is Cd, Hg, Ca, Sr, Pb, Sn, or Mn, and B^{5+} is V, Nb, Ru, Rh, Ta, Re, Os, Ir, Pt, U or Sb. The (2+,5+) pyrochlores are of considerable interest because their covalency, polarisability and electronegativity of the constituent ions give rise to a wide variety of interesting physical properties. In recent decades, $Cd_2Nb_2O_7$ has been the most studied compound of the (2+,5+) pyrochlores. This is because of the interesting electronic behaviour the material possesses. It is a dielectric insulator and exhibits ferroelectricity at low temperatures. The phenomenon of ferroelectricity in $Cd_2Nb_2O_7$ was discovered by Cook and Jaffe in 1952[51,52] and subsequently studied along with the structure by a number of other workers[53 to 59]. Other (2+,5+) pyrochlores of considerable interest are the osmates (A^{2+} = Cd, Ca, Hg) and the ruthenate $Tl_2Ru_2O_7$, which all exhibit metal insulator transitions, and the low temperature superconducting pyrochlore phase, $Cd_2Re_2O_7$, mentioned earlier.

Like perovskite oxide materials, pyrochlores have the potential for numerous practical applications due to their wide spectrum of properties such as electrical, magnetic, dielectric, optical and catalytic behaviour. Examples include solid solutions between $Cd_2Nb_2O_7$ and $Bi_2Ru_2O_7$ for the use in thermistors, $Cd_2Os_2O_7$ as a thermal switch and $Pr_2Zr_2O_7$ for heating elements[1].

1.3.2 Defect Pyrochlore Oxides

The composition of a normal pyrochlore is $A_2B_2O_7$, whereas for a defect pyrochlore there are anion or cation vacancies to give the compositions $A_2B_2O_{7-x}\square_x$ ($0.0<x<1.0$) or ($\square$A)B2{$O_6\square$), where $\square$ represents a vacancy.

The regular pyrochlore structure can be drawn using BO_6 octahedra sharing all vertices with a distorted (6 + 2) cubic co-ordination to the 'A' type cation. Alternatively the structure can be considered as being derived from a fluorite structure with the composition $[A_2B_2]O_8$ by the removal of two oxide anions in a regular fashion producing, $A_2B_2O_7\square$, where $\square$ represents a vacancy. The defect pyrochlore lattice can be explained in a similar way, where the structure is obtained by removing oxygens, O', from their sites in $A_2B_2O_6O'$, to give a generalised composition, $A_2B_2O_6O'_{1-x}\square_x$. There are 8 O' type oxygens in the stoichiometric pyrochlore unit cell, thus the removal of all of these would lead to the composition $A_2B_2O_6$ (ABO_3). The removal of the O' oxygens, however, exposes the 'A' cations to each other through the vacancy, and the resulting electrostatic repulsion would tend to destabilise the structure. The stabilisation of the defect pyrochlore structure has been explained in terms of the bonding of the 'A' cations through the oxygen vacancy[60]. The majority of the $A_2B_2O_{7-x}$ pyrochlore oxides formed with the defect structure are composed of 'A' cations such as Tl^+, Sn^{2+}, Pb^{2+} and Bi^{3+}, which have a polarisable $6s^2$ lone pair of electrons. This so-called 'inert' pair of $6s^2$ electrons is the reasoning behind the proposed stability of the structure. Longo *et al.*[60] explained that the vitual energy levels of the vacancy are comparable in energy to the 6s and 6p levels of the 'A' ions. The latter are hybridised and mixed with the virtual levels of the vacancy, forming band states. This results in a 'trap mediated bond' through the oxygen vacancy between the 'A' ions. The net effect is the polarisation of the 'A' ions by the oxygen vacancy giving stabilisation to the A-A bonds, and ultimately the structure.

1.4 The K_2NiF_4 Structure

The K_2NiF_4 structure[61] is a tetragonal structure closely related to the perovskite structure and adopts a general formula $AO(ABO_3)_n$. When n=1, a 'layered' perovskite structure is formed, see Figure 1.7, which is the structure type of the first member of the Ruddlesden-

Popper series discussed in section 1.5. The K_2NiF_4 structure consists of a single rock salt layer interleaved with a perovskite layer giving a body-centred tetragonal cell. Sheets of NiF_6 octahedra sharing four vertices are separated by K^+ ions in nine-fold coordination to fluorine. Therefore, in the general oxide formula A_2BO_4, the 'A' cation is surrounded by nine oxygens (in contrast to a coordination of twelve in the basic perovskite structure) and the B cation is in six-fold coordination.

The K_2NiF_4 structure is adopted by the superconducting phase $La_{2-x}Ba_xCuO_4$[15] and is observed in many superconducting systems. The lanthanum and barium atoms are similar in size and are randomly distributed over the 'A' cation positions in the structure. The smaller copper atom occupies the 'B' positions. In common with perovskites, this structure is easily distorted from the ideal tetragonal I4/mmm to more complex orthorhombic structures. The structure can also undergo an elongation in the *c* direction with the copper atoms co-ordinated by an elongated octahedron of six oxygens. This elongation is the result of a Jahn-Teller effect and is a reason that Bednorz and Müller[15] chose to investigate these copper oxides for superconductivity.

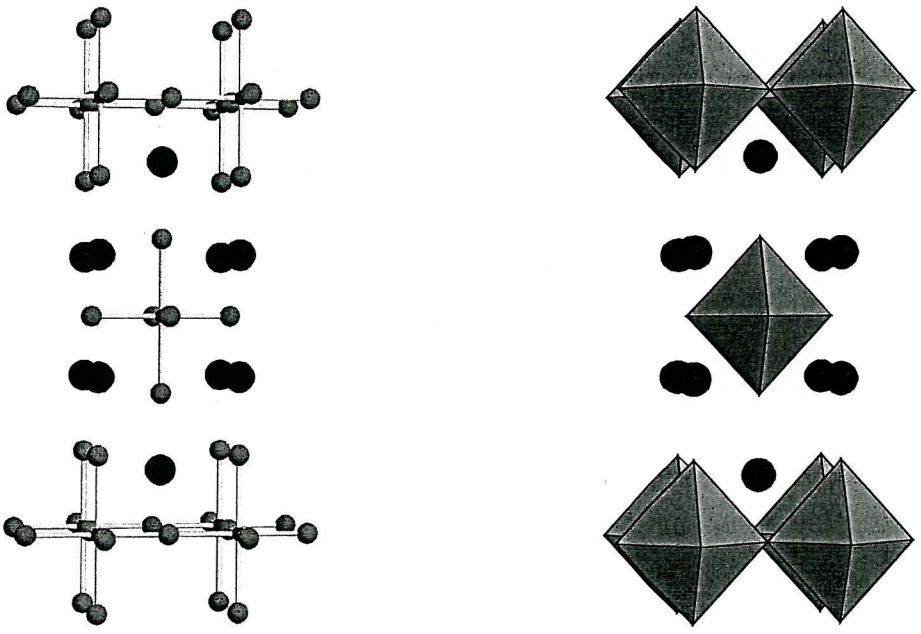

NiF_6 coordination Sheets of NiF_6 octahedra

Figure 1.7. The structure of K_2NiF_4 showing the NiF_6 coordination and the infinite sheets of octahedra.

1.5 The Ruddlesden-Popper Phases

These materials were first characterised in 1957 and named after Ruddlesden and Popper to describe strontium titanate $Sr_3Ti_2O_7$[62]. This series of compounds also adopts a general composition $AO(ABO_3)_n$ where $n \geq 2$ and consist of n ABO_3 perovskite blocks separated by AO rocksalt layers. Ruddlesden-Popper phases are known to exist for the strontium titanate system up to $n = 3$, however, in general, there are no reports of any crystal structures for $n > 4$ due to the increasing probability of stacking faults occurring in the *c* direction. As with the perovskite structure, oxygen non-stoichiometries can be accommodated into these structures which gives rise to phases such as $Sr_3Fe_2O_6$[63] and $La_2SrCu_2O_6$[64].

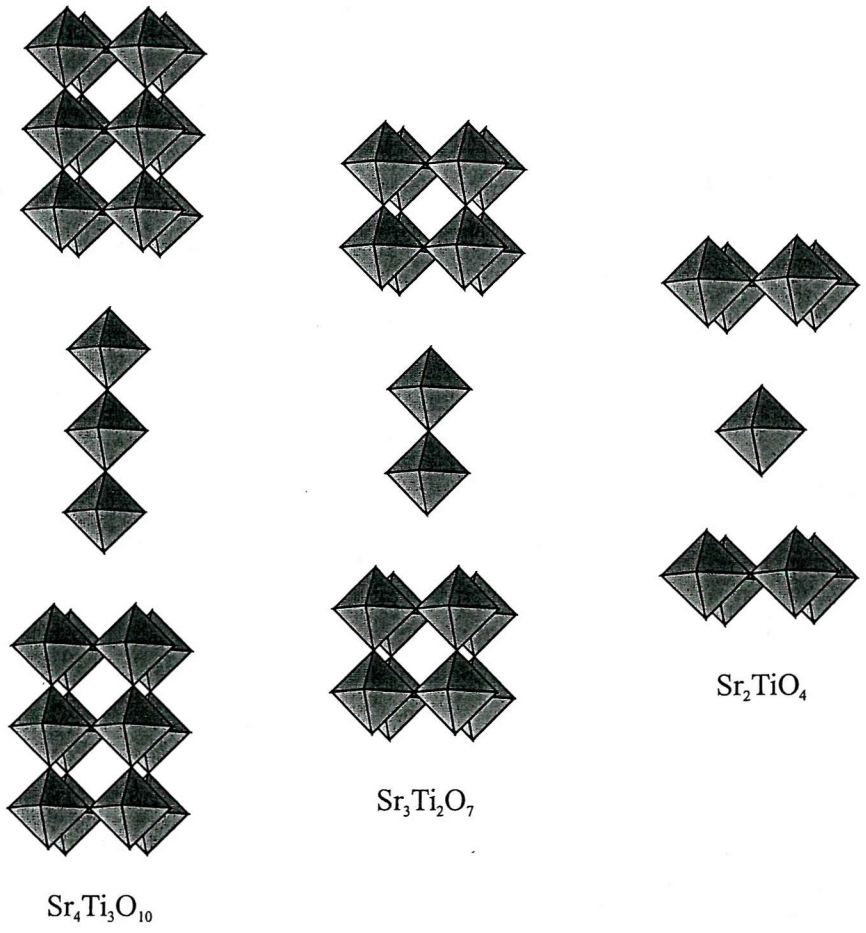

Figure 1.8. The structures of $Sr_4Ti_3O_{10}$, $Sr_3Ti_2O_7$ and Sr_2TiO_4 showing the TiO_6 octahedra only.

1.6 The Electronic Structure of Solids

The methods applied to molecules in terms of chemical bonding can also be used to understand the electronic structure of solids. Applying molecular orbital (MO) theory to a simple diatomic molecule, an atomic orbital on one atom overlaps with an atomic orbital on the other atom. This results in the formation of two molecular orbitals that are delocalised over both atoms. One of the molecular orbitals is bonding and the other is anti-bonding. The bonding molecular orbital (ψ_1) is lower energy than that of the atomic orbitals and the anti-bonding molecular orbital (ψ_2) is higher energy. This can be seen in the energy diagram Figure 1.9.

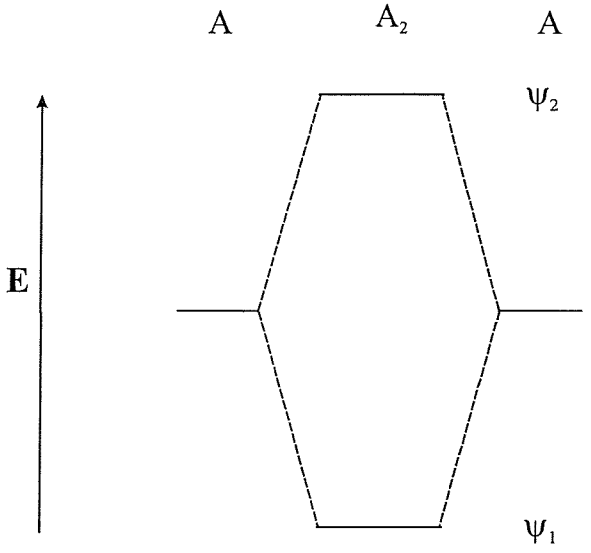

Figure 1.9. MO diagram for a simple diatomic molecule.

The core atomic orbitals of an atom are composed of previously filled electron shells. Generally, core atomic orbitals are of smaller radius than the valence orbitals so their overlap in molecules is small hence they have little bonding influence. Therefore only valence orbitals are considered for the formation of bonds. It follows from MO theory that the total number of molecular orbitals formed (bonding, anti-bonding or non-bonding) is equal to the number of valence atomic orbitals used to make them. An increase in the size of a molecule produces an increase in the number of molecular orbitals it possesses. An increase in size will also reduce the average energy gap between adjacent molecular

orbitals. A solid can be considered as an infinitely large molecule in which there are a huge number of molecular orbitals present. The energy spacings between these orbitals are minuscule to a point where it can be neglected giving continuous bands of energy levels. This is shown schematically in Figure 1.10 below.

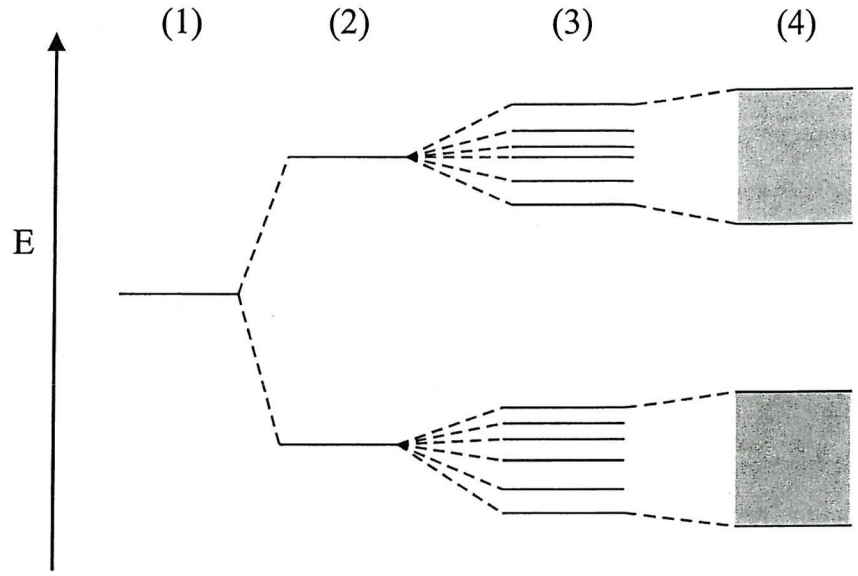

Figure 1.10. Diagram of orbital energies. (1) an atom, (2) a small molecule, (3) a large molecule, (4) a solid.

It should be noted that this is a simplified discussion on band structure in solids, as that is sufficient for the understanding of the work carried out in this thesis. The true band structure can depend upon many different aspects such as structure and symmetry, so for a more detailed account the reader may refer to texts such as the works of Mott[65].

The nature of the bands determines the electronic properties of the solid. This is in terms of their width, separation and the number of electrons they hold. The degree to which orbitals overlap determines the width of the bands, strongly overlapping orbitals produce wide bands and weakly interacting orbitals produce narrow bands. To show the filling of the bands the density of the states (N(E)) is plotted as a function of energy (E). The level to which a band is filled is called the *Fermi level* (E_F), which may fall at the top of a band (drawn as midway between the highest occupied and the lowest unoccupied bands) or in the

middle of a band. The energy spacing between the valence band and the conduction band is denoted as the *Band gap*.

1.6.1 Metals, Insulators and Semiconductors

Metals will conduct electricity down to the lowest attainable temperatures, whilst non-metallic solids may conduct if the temperature is raised. Metals, insulators and semi-conductors may be characterised by the filling of their bands. Each crystal orbital will have electron motion in one direction and an equally opposed electron motion in the other direction. Therefore in a completely filled band the net motion of the electrons will be zero and there will be no conductivity. This is indeed the case for insulators, where their highest occupied band, the valence band, is completely filled and the next band, the conduction band, is completely empty. The *Fermi level* lies midway between the two bands shown in Figure 1.11.

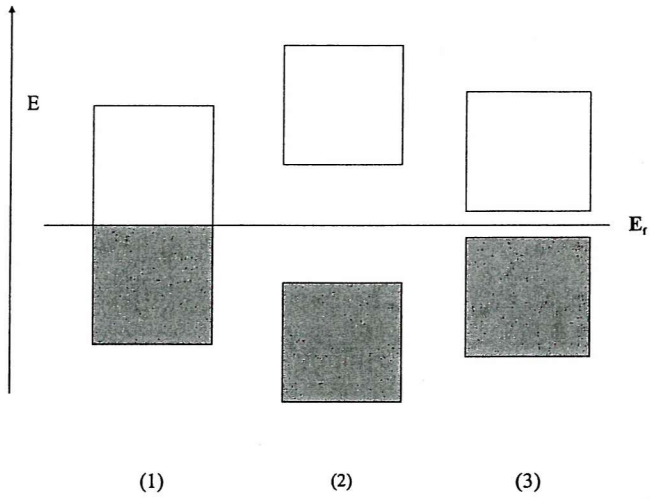

Figure 1.11. Band structures of (1) a conductor, (2) an insulator and (3) a semiconductor. Shading indicates filling of the bands by electrons. The gap between the filled band and the empty band represents the *band gap*.

Band gaps for insulators are typically large, higher than 12 eV for some ionic solids. Metals only have partially filled bands with no band gap above the upper occupied level. If an electric field is applied, electrons close to the top filled level can move into other

orbitals. This gives rise to a net motion of charge within the solid providing a flowing electric current. Semi-conductors have a similar band structure to insulators except the band gap is a lot smaller, around 3 eV down to 0.1 eV. They can conduct electricity through thermal excitation of their electrons across the *band gap*, providing it is small enough. The excited electrons now contained in the otherwise empty conduction band are free to move under the application of an electric field and hence carry current. The smaller the *band gap*, the higher the conductivity and an increase in temperature applied to the solid also results in increased conductivity.

1.7 Metal – Insulator Transitions

As described previously, the energies of the electron states in crystalline materials lie in bands. An insulator has completely full or empty bands and a metal has one or more bands partly full. Any metal-insulator (M-I) transition in a crystalline material at zero temperature must be a transition from where bands overlap to a situation where they do not. Mott described a M-I transition with a picture of a crystalline array of hydrogen like atoms with a lattice constant a that could be varied[66 to 68]. Large values of a would be insulating and small values metallic. This is shown schematically in Figure 1.12 where two atomic levels (W_0 and W_1) broaden into bands as the distance is increased between the two atoms. At the point of overlap where $R = R_0$ (where R is the inter-atomic distance), a M-I transition will take place.

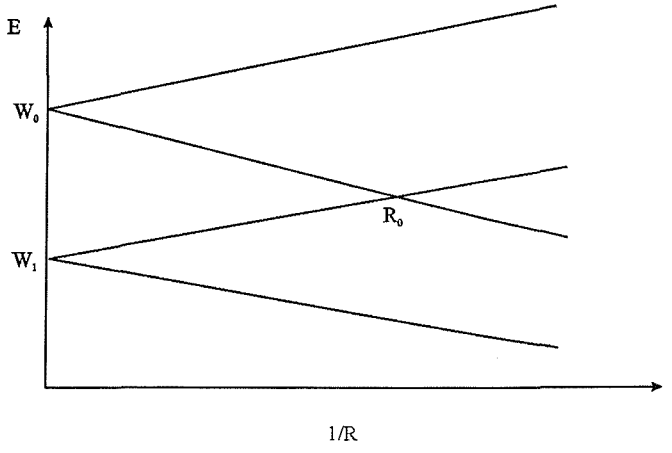

Figure 1.12. Allowed values of the energy of an electron in a crystal as a function of 1/R[65].

A M-I transition of this kind will occur when there is a change in parameters such as volume or alloy composition in such a way that it causes two bands to overlap or cease to overlap. This can be induced, by subjecting the material to a change in pressure or doping with another metal. A change in pressure can bring the metal centres of transition metals closer together producing a continuous band, which is only partially full, hence giving metallic properties. Doping with a different metal can give extra electrons to the system, producing a situation from where there was a completely full and a completely empty band to a completely full and partially full band, again giving metallic properties. A material showing semiconducting behaviour can undergo a transition to a metal with a change in temperature. A rise in temperature can promote a change in the *band gap* distance which can close together, where on completion will be a continuous band that is only partially full, producing metallic behaviour.

1.8 Superconductivty

1.8.1 A Brief History

Normal metals and alloys exhibit a linear decrease in resistivity with decreasing temperature, tending towards zero resistance at 0 K for a pure metal. The electrical resistance results from the interaction between lattice vibrations and the conduction of electrons as they move through the structure. As the temperature of the system decreases, this interaction or scattering of the conduction electrons weakens as the atomic vibrations decrease in amplitude. However, in 1911 Onnes discovered that pure mercury underwent an abrupt transition to a state with an immeasurably small resistance at 4.2 K, and remained at zero below this temperature[69]. This dispelled the theory that electrical resistance of pure metals tended toward zero at T = 0 K. Onnes described the new state as a superconducting state and the temperature at which the transition took place was known as the critical temperature (T_c). In superconducting metals and alloys, the electrons are believed to move through the lattice in a *concerted* way with the lattice vibrations, resulting in no electron scattering and zero resistance.

The discovery of the phenomenon of superconductivity started a search for other superconducting elements, which was later extended to alloys and intermetallic compounds.

The element with the highest transition temperature is niobium, $T_c = 9.2$ K. Accompanying the research on intermetallic compounds, investigations into metal oxides were also undertaken. The first superconducting oxides discovered were TiO and NbO in 1964, with T_c's ~ 1 K. With Nb doping, superconductivity at 0.7 K was reported for the perovskite oxide $SrTiO_{3-x}$[70]. Higher transition temperatures of 13 K were subsequently found on the discovery of the spinel $LiTi_2O_4$[71], and the distorted perovskite $Ba(Pb_{1-x}Bix)O_3$[72]. A dramatic breakthrough was achieved in 1986 when Bednorz and Müller found that $La_{2-x}Ba_xCuO_4$ had a T_c of about 35 K for $x \sim 0.2$[15]. This resulted in a determined search to find superconductivity in other oxide based materials. In 1987 $YBa_2Cu_3O_{7-\delta}$ ($\delta \sim 0.1$) was found to have a T_c of 92 K[73] and one year later $Bi_2Sr_{3-x}Ca_xCu_2O_{8+\delta}$ ($x \leq 1$) raised T_c to 110 K[74]. The highest T_c (at the time of writing) for a material synthesised under ambient pressure is 135 K for the $HgBa_2Ca_2Cu_3O_{8+\delta}$ system[75].

The majority of the known metal oxide superconductors are found for cuprates, but recently superconductivity was found in the layered perovskite Sr_2RuO_4[76]. In this material and the superconducting cuprates, the perovskitelike structures contain RuO_2 or CuO_2 layers are known to play an important role in the occurrence of the superconductivity. Oxide superconductors with non-perovskite based structures are rare. However, very recently superconductivity was found in the pyrochlore oxide $Cd_2Re_2O_7$[45]. This subsequently produced a great deal of interest in the material due to it being the first pyrochlore known to have a superconducting transition. Currently, particular interest is paid to obtaining accurate structural information in the superconducting state and the precise nature of the unconventional superconductivity.

1.8.2 The Superconducting State

The most prominent change in the physical properties of a superconducting material upon cooling below the transition temperature is the abrupt drop in the electrical resistance to effectively zero (see Figure 1.13). The failure to observe the decay of a persistent current within a superconducting loop has allowed an upper limit of $\sim 10^{-26}$ Ω m to be put on the resistivity of superconductors. This compares to a value of the order 10^{-8} Ω m for copper at room temperature[77]. Other properties of the material, such as the thermal conductivity and the specific heat capacity, also undergo sharp changes at the critical temperature.

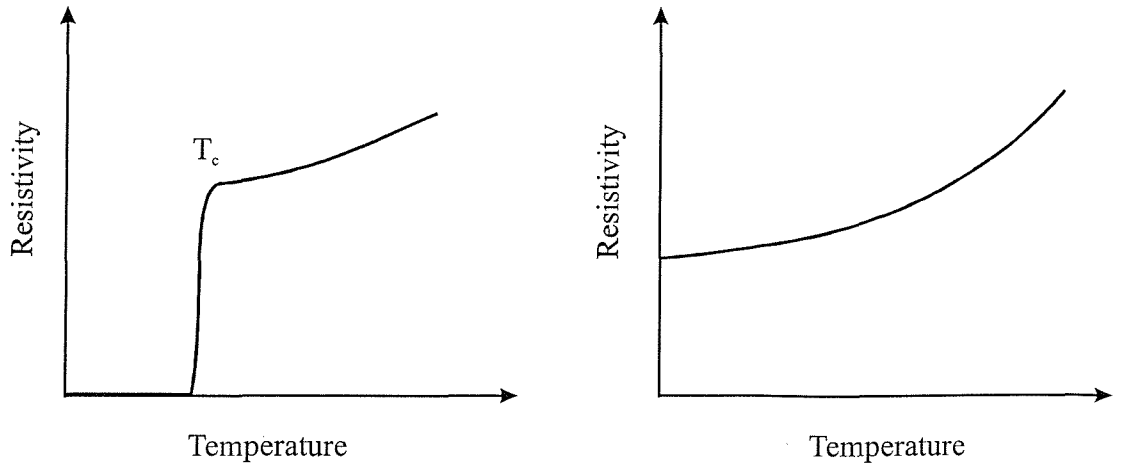

Figure 1.13. The resistive behaviour of a superconductor (left) and a metal (right) upon cooling to 0 K.

1.9 Properties and Applications

The properties and applications of metal oxides are numerous, so only several examples for perovskite and pyrochlore oxides will be discussed in this section, which is relevant to the work, reported in this thesis. The usefulness of perovskite and pyrochlore oxides in various devices is due to their wide spectrum of physical properties such as electrical, magnetic, optical and catalytic behaviour. The properties are usually controlled by physical parameters such as ionic size, polarisability of the ions, electronic configuration and preparative conditions (*i.e.* particle size). Perovskite and Pyrochlore phases provide ideal materials to tune for desired responses for these applications due to their wide scope for chemical tailoring.

1.9.1 Ferroelectrics

Ferroelectric materials have a long range ordering of dipoles below a certain temperature, known as the Curie temperature. On the application of an external electric field the direction of polarisation in the crystal domains line up with the applied field. The most well known perovskite that exhibits ferroelectric behaviour is $BaTiO_3$[32]. In this structure, the titanium ion is occupying a site that is larger than it would prefer. At temperatures above 120°C $BaTiO_3$ adopts the ideal cubic perovskite structure, and on cooling undergoes a

number of phase changes. The phase changes are a result of the structure trying to adopt preferable co-ordination geometry for the titanium ion. The tetragonal phase shows a shift of the titanium ion from its central cubic position towards one of the facial oxide ions. This displacement effects the charge distribution in the cell shifting the negative and positive charges of the constituent ions from coinciding at the cell centre. The overall result gives the cell a high dipole moment. Each unit cell throughout the crystal can have this titanium displacement in the same direction and hence all the dipoles will face the same direction giving $BaTiO_3$ its ferroelectric properties. The high dielectric contstant that $BaTiO_3$ has from the polarisation makes it used in capacitors. The ion displacement observed for the unit cells of $BaTiO_3$ can be different in other perovskite materials. In the case of $PbZrO_3$ the lead ion displacements are in alternately opposite directions for each adjacent unit cell. This polar arrangement deems $PbZrO_3$ an anti-ferroelectric. The different ordering arrangements for dipole moments are in Figure 1.14.

An example of a good ferroelectric pyrochlore oxide is $Cd_2Nb_2O_7$. The material contains elements in their highest oxidation states and the ion polarisability is high giving rise to a high dielectric constant, lending itself for an application in capacitors.

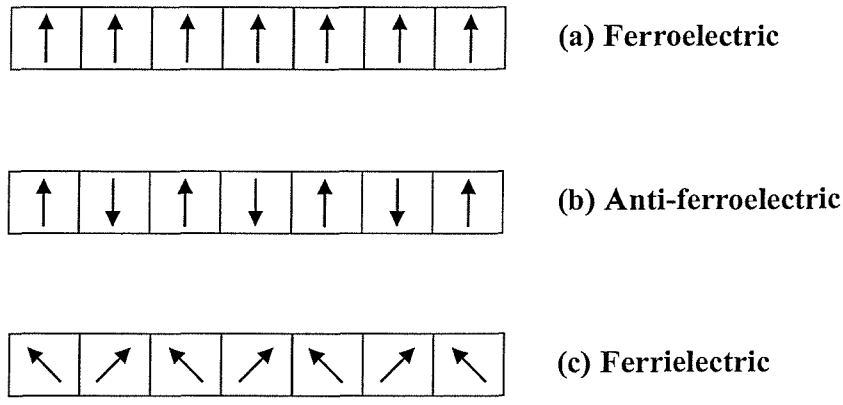

Figure 1.14. Ordering arrangements for dipole moments.

1.9.2 Piezoelectrics

Piezoelectric materials are those that obtain an electric polarisation upon the application of mechanical stress. Crystal compression results in further distortion giving a higher charge polarisation. Ferroelectric materials commonly show piezoelectric behaviour giving a variety of applications that include, the measurement of force or pressure, use in transducers for sound transmission and reception, and ultrasonic cleaning devices. Their main use is for a phonograph pick-up, which transforms mechanical energy to an electrical signal found for record player needles and gas lighters.

1.9.3 Magnetoresistive Materials

Earlier last decade discoveries were made that certain manganese oxides showed a large change in resistance when a magnetic field was applied[78,79]. The manganese oxides that possessed this property were based on the formula $LnMnO_3$ (Ln = lanthanide) and adopt the perovskite structure. Taking $LaMnO_3$ as an example, the phase is insulating. Doping with a divalent alkaline earth element such as calcium or strontium at the lanthanum sites to give $La_{(1-x)}A_{(x)}MnO_3$ (A = alkaline earth), modifies the electrical properties and the material becomes metallic. At a doping level of (x = 0.2 - 0.5) the material is ferromagnetic and applying a magnetic field results in a sudden increase of resistivity. This phenomena was labelled colossal magnetoresistance (CMR). The fundamental interaction in these materials is known as double exchange (DE), where electronic carrier hopping of electrons between heterovalent Mn pairs (Mn^{3+} / Mn^{4+} in the case of $La_{1-x}A_xMnO_3$) is enhanced by the mutual alignment of the Mn magnetic moments[80 to 82]. A widely studied CMR pyrochlore oxide is $Tl_2Mn_2O_7$ after the discovery of the phenomena in the phase[47,48].

1.9.4 Catalysis Materials

Perovskites are widely studied for use in the catalyst industry. Cobaltates, manganates and ruthenates are among the most researched of the perovskite materials. Examples include $SrRuO_3$, $LaRuO_3$ and both $LaMnO_3$ and $LaCoO_3$ doped with ruthenium or rhodium at the 'B' site. These materials are found to be fairly effective at dealing with poisonous gases such as CO and NO converting them to CO_2 and NO_2 respectively. The main advantages of

using perovskites for this application are the conservation of noble metals and most present catalysts can be incorporated into the structure.

1.9.5 Thermistors

Thermistors are materials that show excellent linearity of log ρ as a function of 1/T in a limited temperature range, and are used for accurate measurement of temperature. Other uses of thermistors are for voltage stabilisation and relays. Materials that have been suggested for potential uses as thermistors are a selected few of the pyrochlore oxides[83] which include, $Bi_2Ru_2O_7$ / $Cd_2Nb_2O_7$ solid solution, Bi_2CrNbO_7 and Bi_2CrTaO_7. Other pyrochlore oxides that also possess the required characteristics for themistor employment are $Ln_2Fe_{4/3}W_{2/3}O_7$ and $CdLn(B)WO_7$ (B = Cr, Mn and Fe)[1].

1.9.6 Gas Sensors

Another widely looked at area for perovskite oxides is their use in gas sensors. In the presence of a flammable gas, semi-conducting oxides can show a dramatic change in resistivity. The structure of gas sensors is relatively simple consisting of a layer of semi-conducting oxide covered in a ceramic insulating tube equipped with a heating coil. Uses of sensors are limited by the stability of the perovskite phase in a reducing atmosphere at high temperatures. Perovskites used for this application are $SmCoO_3$ and $LaBO_3$, where B can be V, Cr, Mn, Fe or Co.

1.9.7 Thermal Switches

Thermal switches are materials that exhibit sudden and large changes in electrical conductivity at a given temperature. The change in conductivity can be induced by direct variation of temperature of the material by an external source or by internal heating from a passing current. Well known oxides which display the desired properties for this application are VO_2, V_2O_3 and the doped perovskite $BaTiO_3$, which are currently utilised for temperature sensitive electrical switches, fire extinguishers and temperature controllers[84 to 87]. The pyrochlore oxides that exhibit metal-insulator (M-I) transitions can also be

exploited for thermal switch applications. These include $Cd_2Os_2O_7$, $Hg_2Os_2O_7$, $Ca_2Os_2O_7$, and $Tl_2Ru_2O_7$.

M-I transitions can be monitored using infra-red (IR) spectroscopy. An insulating oxide will absorb at discrete frequencies in the IR frequency associated with the M-O modes. A metallic oxide will generally show a strong absorption across the whole region associated with the collective electronic states. When an oxide material undergoes a transition from an insulator to a metal, it will show this change of absorbance behaviour. This property can be utilised by sensors, which contain thermal switches to detect a change in temperature. When a source of heat is focused on to a sensor of this type, the change in temperature will induce a M-I transition, and the change of absorbance at a particular wavelength can be monitored by a detector.

1.10 Scope of This Work

The importance of metal oxide materials for uses in industrial applications over recent decades has led to numerous studies and new developments. Particular areas of interest lie in the field of superconducting and metal-insulator (M-I) materials. The greater knowledge of the structural requirements of these materials provides a better understanding for the occurrence of these physical phenomena.

The aim of this work was to investigate the structural and physical properties of some key materials at the metal-insulator boundary. The phases studied for this work were pyrochlore and perovskite oxides due to the wide range of electronic properties exhibited by these materials. Emphasis was placed on studying the precise crystal structures of existing and novel M-I pyrochlore and perovskite materials and investigating their electronic behaviour.

The work presented in chapters three to six deals with the attempted syntheses of high oxidation state transition metal pyrochlores. Until recently, they have been lacking in detailed structural characterisation and accurate stoichiometry determination, which is of paramount importance to help understand their physical properties, such as M-I transitions. Accurate structures have been determined for relevant materials at several temperatures leading up to, and through M-I transitions.

In addition, a full solid solution between a metallic and an insulating perovskite has been prepared, which is described in chapter seven. The solid solution has been fully structurally characterised and investigated in terms of its electrical behaviour with composition change.

The primary experimental technique utilised in this work was powder diffraction, with the routine collection of powder x-ray diffraction data for phase identification and structural characterisation and the use of powder neutron diffraction for further structural determination. In addition, the electrical behaviour of the materials was determined with conductivity measurements and further analysed using infra-red analysis.

1.11 References

[1] M. A. Subramanian, G. Aravamudan and G. V. Subba Rao, *J. Solid State Chem.* **31** 329 (1980).

[2] M. E. Straumanias, A. Draveniks, *J. Am. Chem. Soc.* **71** 683 (1949).

[3] F. Galasso and W. Derby, *Inorg. Chem.* **1** 71 (1965).

[4] J. F. Schooley, W. R. Hosler and M. L. Cohen, *Phys. Rev. Letters.* **12** 474 (1964).

[5] V. Ginzburg, *J. Phys. USSR* **10** 107 (1946).

[6] W. L. Cherry and R. Adler, *Phys. Rev.* **72** 981 (1948).

[7] A. Von Hippel *RPTPB* 4660 (1994).

[8] F. Galasso, L. Katz and R. Ward, *J. Am. Chem. Soc.* **81** 820 (1959).

[9] General Ceramics, *Oxide Thermoelectric Materials Final Rpt.* Contract NOBS-78414 (1961).

[10] C. D. Salzberg, *J. Opt. Soc.* **51** 1149 (1961).

[11] R. J. Cava, B. Batlogg, J. J. Kajewski, R. Favrovo, L. W. Rupp, A. E. White, K. Short, W. F. Pecks and T. Komelan, *Nature* **332** 814 (1988).

[12] C. W. Chu, P. H. Hor, R. L. Meng, L. Gao and Z. L. Huang, *Science* **235** 567 (1988).

[13] D. B. Currie and B. Cleaver, *High P. High T.* **22** 263 (1990).

[14] A. Wattiaux, J. C. Park, J. C. Grenier and M. Pouchard, *C. R. Acad. Sci. Serr. 2* **310** 1047 (1990).

[15] J. G. Bednorz and K. A. Müller, *Z. Phys. B.* **64** 189 (1986).

[16] H. D. Megaw, *Proc. Phys. Soc.* **58** 326 (1946).

[17] S. Geller and A.E. Wood, *Acta Crystallogr.* **9** 563 (1956).

[18] V. M. Goldschmidt, *Skrifter Norske Videnskaps-Akad. Oslo* I. Mat.-Naturv. Kl. **8** (1926).

[19] S. C. Abrahams, J. M. Reddy and J. L. Bernstein, *J. Phys. Chem. Solids* **27** 997 (1966).

[20] P. Ganguly and C. N. R. Rao, *Mat. Res. Bull.* **8** 405 (1973).

[21] B. Derighetti, J. E. Drumheller, F. Laves, K. A. Müller and F. Waldner, *Acta Crystallogr.* **18** 557 (1965).

[22] E. A. Wood, *Acta Crystallogr.* **4** 353 (1951).

[23] A. C. Sakowski, K. Lukaszewicz and H. D. Megaw, *Acta Crystallogr. Sect. B* **25** 851 (1969).

[24] E. A. Zhurova, V. E. Zavodnik and V. G. Tsirel'son, *Kristallogr.* **40** 816 (1995).

[25] R. S. Roth, *J. Research NBS* **58** RP 2736 (1957).

[26] I. Náray-Szabó, *Müegyetemi Közle Mények* **1** 30 (1947).

[27] J. J. Randall and R. Ward, *J. Am. Chem. Soc.* **81** 2629 (1959).

[28] F. Gallasso, J. R. Barrante and L Katz, *J. Am. Chem. Soc.* **46** 2830 (1961).

[29] G. Bayer, *J. Am. Chem. Soc.* **83** 604 (1963).

[30] W. F. De Jong, *Z. Krist.* **81** 314 (1932).

[31] C. Brisi, *Ricerca Sci.* **24** 1858 (1954).

[32] H. F. Kay and P. Vousden, *Phil. Mag.* **40** 229 (1948).

[33] F. Gallasso, *Perovskites and High Tc Superconductors* Gordon and Breach Science Publishers (1990).

[34] T. Nakamoto and J. H. Choy, *J. Solid State Chem.* **20** 233 (1977).

[35] M. P. Attfield, P. D. Battle, S. K. Bollen, S. H. Kim, A. V. Powell and M. Workman, *J. Solid State Chem.* **96** 344 (1992).

[36] G. Blassé, *J. Inorg. Nucl. Chem.* **27** 993 (1965).

[37] P. D. Battle and C. W. Jones, *J. Solid State Chem.* **78** 108 (1989).

[38] W. A. Groen, F. P. F. van Berkel and D. J. W. Ijdo, *Acta Crystallogr. Sect. C* **42** 1472 (1986).

[39] M. T. Anderson and K. R. Poeppelmeier, *Chem. Mater.* **3** 476 (1991).

[40] D. H. Gregory and M. T. Weller, *J. Mater. Chem.* **4** 921 (1994).

[41] A. W. Sleight, J. L. Gillson, J. F. Weiher and W. Bindloss, *Solid State Comm.* **14** 357 (1974).

[42] J. Reading, S. Gordeev and M. T. Weller, *J. Mater. Chem.* **12** 646 (2002).

[43] J. Reading, C. S. Knee and M. T. Weller, *J. Mater. Chem.* **12** 2376 (2002).

[44] T. Takeda, M. Nagata, H. Kobayashi, R. Kanno, Y. Kawamoto, M. Takano, T. Kamiyama, F. Izumi and A. W. Sleight, *J. Solid State Chem.* **140** 182 (1998).

[45] M. Hanawa, Y. Muraoka, T. Tayama, T. Sakakibara, J. Yamaura, Z. Hiroi, *Phys. Rev. Lett.* **87** (18) 187001 (2001).

[46] A. Byström, *Ark. Kemi min. Geol.* **18A** 1 (1945).

[47] Y. Shimikawa, Y. Kubo and T. Manako, *Nature (London)* **379** 53 (1996).

[48] M. A. Subramanian, B. H. Toby, A. P. Ramirez, W. J. Marshall, A. W. Sleight and G. H. Kwei, *Science* **273** 81 (1996).

[49] J. E. Greedan, J. N. Reimers, C. V. Stager and S. L. Penny, *Phys. Rev. B* **43** 5682 (1991).

[50] B. D. Gaulin, J. S. Gardner, S. R. Dunsiger, Z. Tun, M. D. Lumsden, R. F. Kiefl, N. P. Raju, J. N. Reimers and J. E. Greedan, *Physica B* **241-243** 511 (1998).

[51] W. R. Cook and H. Jaffe, *Phys. Rev.* **88** 1426 (1952).

[52] W. R. Cook and H. Jaffe, *Phys. Rev.* **89** 1297 (1953).

[53] J. K. Hulm, *Phys. Rev.* **92** 504 (1953).

[54] G. Shirane and P. Pepinsky, *Phys. Rev.* **92** 1507 (1953).

[55] F. Jona, G. Shirane and R. Pepinsky, *Phys. Rev.* **98** 903 (1955).

[56] F. Brisse, D. J. Stewart, V. Seidl and O. Knop, *Can. J. Chem.* **50** 3648 (1972).

[57] V. A. Isupov, G. I. Golovshchikova and I. E. Myl'nkova, *Ferroelectrics* **8** 507 (1974).

[58] G. Jeanne, G. Desgardin and B. Reveau, *Mat. Res. Bull.* **9** 1321 (1974).

[59] G. Jeanne, G. Desgardin, G. Allais and B. Reveau, *J. Solid State Chem.* **15** 193 (1975).

[60] J. M. Longo, P. M. Raccah and J. B. Goodenough, *Mat, Res. Bull.* **4** 191 (1969).

[61] D. Balz and K. Plieth, *Z.Elektrochem.* **59** 545 (1955).

[62] S. N. Ruddlesden and P. Popper, *Acta Crystallogr.* **11** 54 (1958).

[63] S. E. Dann, D. C. Currie and M. T. Weller, *J. Solid State Chem.* **97** 179 (1992).

[64] J. R. Grasmeder and M. T. Weller, *J. Solid State Chem.* **85** 88 (1990).

[65] N. F. Mott, *Metal-Insulator Transitions*, 2nd Edn., Taylor and Francis, London (1990).

[66] N. F. Mott, *Proc. Phys. Soc.* **A62** 416 (1949).

[67] N. F. Mott, *Can. J. Phys.* **34** 1356 (1956).

[68] N. F. Mott, *Phil. Mag.* **6** 287 (1961).

[69] H. K. Onnes, *Leiden. Comm.* **124C** (1911).

[70] J. J. Schooley, W. R. Hosler and M. L. Cohen, *Phys. Rev. Lett.* **12** 474 (1964).

[71] D. C. Johnston, H. Prakash, W. H. Zachariasen and R. Viswanathan, *Mat. Res. Bull.* **8** 777 (1973).

[72] A. W. Sleight, J. L. Gilson and P. E. Bierstedt, *Solid State Commun.* 17 27 (1975).

[73] M. K. Wu, J. R. Ashburn, C. J. Torng, R. L. Meng, L. Gao, Z. J. Huang, Y. Q. Wang, C. W. Chu, *Phys. Rev. Lett.* **58** 909 (1987).

[74] J. M. Tarascon, Y. LePage, P. Barboux, B. G. Bagley, L. H. Greene, W. R. Mckinnon, G. W. Hull, M. Girond and D. H. Hwang, *Phys. Rev. B* **37** 9382 (1988).

[75] A. Schilling, M. Cantoni, J. D. Cuo and H. R. Ott, *Nature* **363** 56 (1993).

[76] Y. Maeno, H. Hashimoto, K. Yoshida, S. Nishizaki, T. Fujita, J. G. Bednorz and F. Lichtenberg, *Nature (London)* **372** 532 (1994).

[77] J. R. Hook and H. E. Hall, *Solid State Physics, 2nd Ed.*, John Wiley and Sons (1991).

[78] R. von Helmholt *et al.*, *Phys. Rev. Lett.* **71** 2331 (1993).

[79] S. Jin *et al.*, *Science* **264** 413 (1994).

[80] C. Zener, *Phys. Rev.* **82** 403 (1951).

[81] P. W. Anderson and H. Hasegawa, *ibid.* **100** 675 (1955).

[82] P. G. de Gennes, *ibid.* **118** 141 (1960).

[83] R. J. Bouchard and D. B. Rogers, *U.S. Patent 2506261* (1975).

[84] H. Futaki, *Japan J. Appl. Phys.* **4** 28 (1965).

[85] R. G. Cope and A. W. Penn, *Brit. J. Appl. Phys.* **1** 161 (1961).

[86] K. Van Steensel, F. Van de Borg and C. Kooy, *Philips Res. Repts.* **22** 170 (1967).

[87] H. Kaiser, *Siemens Rev.* **40** 475 (1973).

Chapter Two

Experimental Techniques

2.1 Introduction

The work carried out in this thesis concerns the synthesis and characterisation of materials in the solid state. A number of synthetic techniques have been utilised to ultimately produce polycrystalline oxides. The primary analytical technique used has been powder x-ray diffraction (PXD). This provided initial phase identification and a method of following reaction progress between steps to reaching the target material and ultimately, detailed structural characterisation. When possible, powder neutron diffraction (PND) has been employed to provide more accurate structural information, especially on oxygen environments, which are readily resolved using this technique. Physical properties of the materials have been routinely investigated using conductivity measurements and infra-red spectrometry. Selected samples have been analysed using a vibrating sample magnetometer (VSM) to give information on magnetic properties. This chapter provides a summary of the synthetic and characterisation techniques that have been employed during the course of this work, and their application to polycrystalline materials.

2.2 Synthetic Methods

Reactions carried out in the solid state have very high activation energies. This requires that both thermodynamics and kinetics are taken into account, necessitating the use of reasonably high temperatures for the synthesis to obtain an appreciable rate of reaction [1]. The rate of the reaction is governed by ion diffusion between the component ionic lattices. The rate of diffusion is increased by elevated temperature but the stability of the target product at the reaction temperature must also be taken into account. A balance between temperature and reaction rate must therefore be maintained. In this work, two main synthetic methods were used to prepare the targeted materials, a standard ceramic technique and a citrate gel precursor technique.

2.2.1 Ceramic Technique

The mixing of individual components, usually oxides or carbonates, is carried out with a mortar and pestle. To aid mixing a volatile organic solvent (acetone or iso-propanol) is often used to form a slurry whilst grinding. After a short period of time the solvent

completely evaporates away. Due to a small level of surface area contact between the reactants, reaction time can be significantly increased. This problem can be partially overcome by pressing small samples into pellets, using a 10 mm die under 10 tonnes of pressure, before they are sintered in a furnace. Frequent regrinding during the course of the reaction also helps increase the interfacial contact of the reactants and achieve a faster rate of reaction.

2.2.2 Citrate gel Precursor Technique

The previously described method for preparing oxide materials is the most traditional but due to the large particle sizes involved, this approach frequently requires the use of high reaction temperatures and repeated milling to generate a homogeneous and single phase material. To overcome the disadvantages of this method, precursors can be generated by sol-gel preparations or co-precipitation of metal ions by precipitating agents such as hydroxide, oxalate, carbonate or citrate ions.

These gel precursors can offer near molecular mixing and provide a reactive environment during subsequent heating and their decomposition. The main advantage of these methods is an improved solid state diffusion resulting from the better mixing which gives a faster reaction rate and allows a considerably lower reaction temperature to be used. Additional advantages are a better control of stoichiometry and purity, wider flexibility in forming thin films and a greater ability to control the particle size important for potential catalysts and fuel cell materials.

A factor that must be taken into account is the solubility of the starting components. The solubility must be high to minimise solvent removal and the components must be compatible with each other to avoid one of them precipitating out as an undesired product.

The precursor method that has been used for this work used a citrate gel to precipitate the ions from relevant nitrate solutions. The starting components used for this method are citric acid, ethylene glycol and a mixed nitrate solution of the desired product cations in appropriate stoichiometry. The citric acid is dissolved in the ethylene glycol and water, which forms a viscous solution with the application of heat and stirring. The solution of nitrates are added and with continuous stirring, boiled down to a viscous gel. The gel is carefully dried to form a resin, ground using a pestle and mortar then decomposed in a furnace at ~500 °C. The resultant product is ground, pelletised and sintered in a furnace at a temperature required for the targeted product.

2.2.3 Controlled Environment Reactions

The majority of the experimental work carried out in this thesis required careful considerations with respect to the reaction environments. The environment can be controlled, by carrying out the reaction in the presence of a gas such as oxygen, argon, nitrogen or hydrogen/nitrogen. These processes can promote desired changes in the metals oxidation states or prevent change. The synthesis of the nickelate materials, see Chapter 7, required the reactions to be carried out in the presence of oxygen gas to promote full oxidation of the Ni^{2+} cation in the reactants to Ni^{3+} in the target phase.

The other method that was used for the control of the reaction environment was to seal the reactants in an evacuated silica tube. This method was essential for the preparation of all the pyrochlore phases reported in this work (Chapters 3 to 6). This was due to the nature of the starting materials, which were highly volatile, very toxic or both. Special considerations had to be given to the choice of reactants and the temperature that was used for the synthesis. It was vital that the starting materials were free from water or carbonate, and that the physical properties of each component were known. This was especially important for the preparation of the mercury containing pyrochlore, see Chapter 3, due to the low decomposition temperature of HgO and low boiling point of Hg (500 °C and 356 °C respectively)[2]. Therefore, if mixtures containing HgO are heated at too high a temperature, it would lead to the disintegration of the tube.

2.3 Powder X-ray Diffraction (PXD)

2.3.1 Theory

Shortly after the discovery of x-rays by Willhelm Röntgen in 1895, Max von Laue recognised that a crystal may act as a three dimensional diffraction grating for x-rays. This was due to the wavelength of x-rays having the same order of magnitude as the interatomic spacings within a crystal (*ca.* 10^{-10} m)[3].

The concept of x-ray diffraction can be shown diagrammatically, by considering a plane wave incident on two parallel planes of atoms separated by a perpendicular distance d (Figure 2.1).

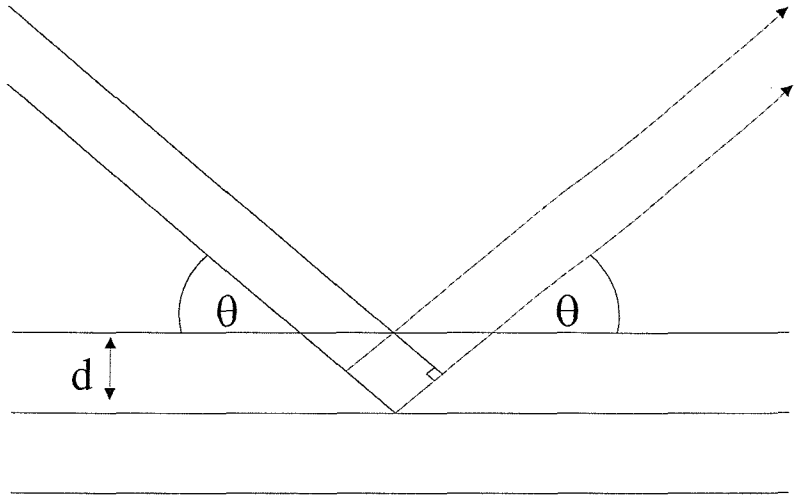

Figure 2.1. Diffraction from parallel planes of point scatterers.

For constructive interference to occur, the path difference between the two diffracted beams must correspond to an integral number of wavelengths. Simple trigonometry yields the Bragg equation[4]:

$$n\lambda = 2d \sin \theta$$

where λ = x-ray wavelength
n = integer (1, 2, 3.....)
d = inter-planar separations
θ = angle of incidence (Bragg angle)

Destructive interference is when the diffracted beams are out of phase, and occurs at any angle other than the Bragg angle. The inter-planar separations in the crystal are calculated by measuring the diffraction maxima, of which only the first order (n = 1) are generally seen. The crystal system can be derived from these d values by identification of the planes involved. Planes are defined by Miller indices, h, k, l, whose reciprocal values are the intersections of the three crystal axes, a, b and c respectively.

In theory, a crystal should display diffraction from each of its lattice planes giving rise to an observed maxima in the diffraction pattern. However, intensity is not always observed from every plane due to the existence of reflection conditions or systematic absences. These result from symmetry elements of the structure and are determined by lattice types such as body centred (I) and face centred (F), as well as space symmetry elements such as glide planes and screw axes[5,6].

2.3.2 The Powder Method

The original use of x-ray diffraction was for single crystal analysis of compounds. Single crystals are difficult to obtain from the direct reaction of most oxides, rendering this technique unusable. An alternative method is powder x-ray diffraction (PXD). This is possible because a powdered sample contains a random orientation of crystallites, many of which satisfy the Bragg equation for each set of their Miller indices. The effect is that each lattice spacing in the crystal will give rise to a cone of diffraction.

2.3.3 Instrumentation

All constant temperature PXD data were recorded on a Siemens D5000 diffractometer using monochromatic radiation, $K_{\alpha 1}$, generated from an x-ray tube. The x-rays were generated from a copper target giving a wavelength of λ = 1.5406 Å. The monochromatic beam is collimated through an aperture diaphragm and directed onto the sample which is mounted flush in a recessed aluminium holder. The diffracted x-rays are detected by a scintillation counter. The sample is rotated for the duration of the experiment at a constant angular velocity, with the detector rotating at precisely double this velocity to obtain a diffraction angle (2θ), twice that of the incident angle (θ). All data were continually recorded on a PC for analysis and storage.

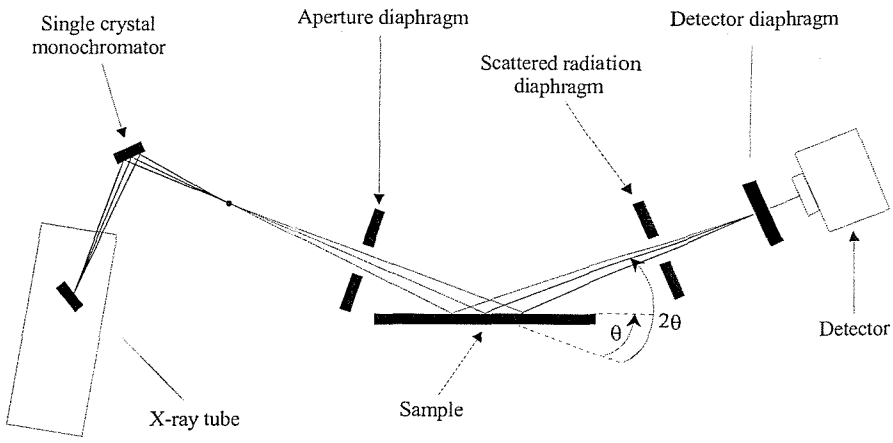

Figure 2.2. Schematic representation of the Siemens D5000 diffractometer.

Variable temperature data were collected on a Bruker D8 Advance diffractometer, which was fitted with a 8 ° position sensitive detector (PSD) enabling rapid data collection. The heating equipment used was an Anton-Paar HTK-1200 high temperature furnace. This allowed data to be collected from room temperature to 1200 °C with a heating rate of 30 °C/min.

2.3.4 Analysis of PXD Data

Data were collected initially for approximately 30 minutes over the 2θ range 10 °- 60 °, to allow phase characterisation and monitoring of a reaction's progress. Longer runs over a wider 2θ range (typically 10 ° - 120 ° for approximately 900 minutes) were performed for accurate structural characterisation. The PXD pattern obtained was checked for phase purity by comparison to a database of known materials stored on the JCPDS Diffraction File[7]. Cell parameters were calculated from the d-spacings using the CELL computer program, which minimises the expression:

$$M = \sum_n W_n (\sin^2 \theta_n^{obs} - \sin^2 \theta_n^{calc})^2$$

This uses an iterative least squares procedure where W_n is a weighting factor proportional to tan θ. This gives greater significance to large 2θ values, improving accuracy. In addition to the CELL program, the LAZY PULVERIX computer program[8] could also be used to aid

cell parameter calculation. The program calculates allowed *hkl* planes and their corresponding 2θ values from a model and simulates a powder diffraction pattern, thus a prediction of possible reflections could be made. The end result provided a suitable starting structural model for further refinement using the Rietveld method of full profile refinement[9,10].

2.4 Powder Neutron Diffraction (PND)

Powder neutron diffraction (PND) is another very useful technique used in solid state chemistry. The technique is advantageous over PXD in a variety of ways. X-rays are diffracted by electrons with a characteristic x-ray form factor that results in the problem of low scattering from light elements, and the inability to distinguish between adjacent elements in the periodic table. This is shown by a proportional relationship of increasing scattering power with atomic number. With neutrons, the atomic nucleii are responsible for the scattering and there is no simple dependence of neutron scattering power over atomic number. It follows that light elements with low electron densities are poorly distinguished using the PXD method of analysis, especially from other light elements, which is not the case with PND. For neutron diffraction experiments the scattering power of a nucleus is dependent on both potential scattering and resonant scattering whose values vary erratically across the periodic table, sometimes giving adjacent elements vastly different scattering factors. Another advantage of using neutrons for analysis is their small size with respect to their wavelength, which eliminates decrease in scattering power at high 2θ values, unlike x-rays. Neutron diffraction may also be used to study the magnetic structure of materials due to neutrons possessing a magnetic dipole moment. The unpaired electrons present in magnetic materials interact with the neutrons, which can give rise to an additional scattering effect producing extra peaks in the observed pattern.

In this work, PND has been used as a complimentary technique to PXD, primarily to accurately locate oxygen atom positions in the presence of heavy elements including lanthanides, cadmium, mercury and thallium. Another advantage of PND utilised was the high penetrating power of neutrons. This enabled the use of refrigeration systems and furnaces to control the sample environment during experiments, permitting the *in-situ* study

of electronic or structural transitions. In addition, the use of low temperature data removes the presence of thermal motion giving a very accurate structural determination.

The two principle sources of neutron radiation suitable for the diffraction technique are time of flight (T.O.F.) and constant wavelength, both of which were used for this work.

2.4.1 Constant Wavelength PND

The instrumentation and theory of the constant wavelength diffractometer are fundamentally similar to those of the PXD experiment, with θ and d variables in the Bragg equation, $n\lambda = 2d \sin \theta$. In this work, data were collected on the D2B high resolution instrument at the high flux reactor Institute Laue Langevin (I.L.L.) in Grenoble, France. The instrument is such that the peaks are near to perfect in a gaussian nature over the 2θ range 3-160 °, permitting refinement of complex structures up to a volume of 2000 $Å^3$.

2.4.2 Instrumentation

The D2B instrument has incident white neutrons monochromated from a 300 mm to a 50 mm beam with a take off angle of 135 ° using a germanium monochromator, giving a resolution of $\Delta d/d \sim 5 \times 10^{-4}$. Samples run on the instrument were mounted in vanadium cans of 7 or 10 mm in diameter, and the scattered neutrons detected. D2B utilises a bank of 128 x (3") collimators and ^{3}He counters at 2.5 ° intervals, which sweep from 0-160 ° in 0.025 ° steps. A range of wavelengths are accessible, but the optimum wavelength of $\lambda = 1.594$ Å was used for this work. A schematic representation of D2B is given in Figure 2.3.

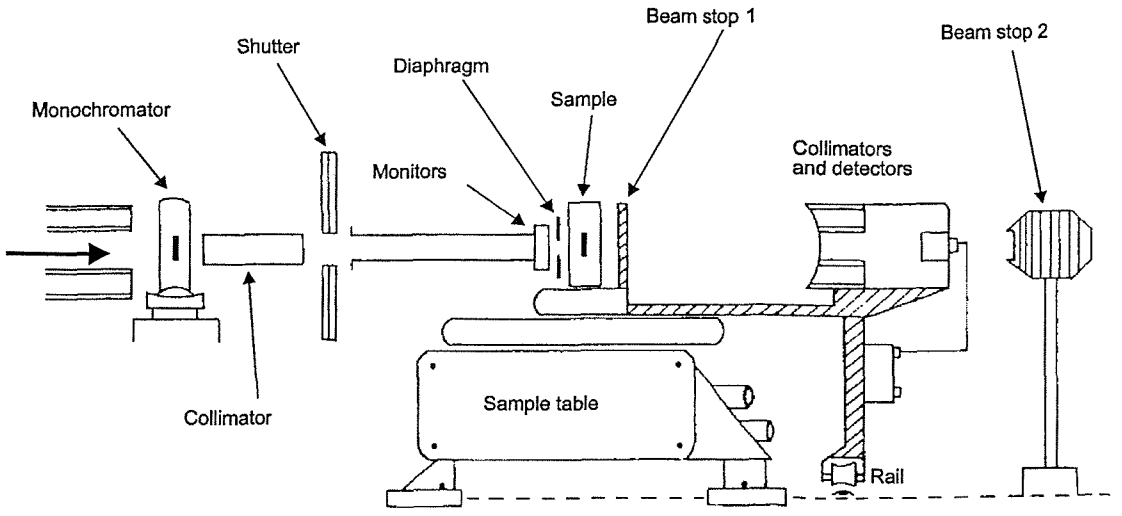

Figure 2.3. The D2B diffractometer.

2.4.3 Time of Flight (T.O.F.) PND

T.O.F. PND data were collected on the high flux medium resolution instrument POLARIS and GEM of the ISIS facility at the Rutherford Appleton Laboratory (R.A.L.), Oxfordshire, U.K. The facility employs a synchrotron spallation source, which provides pulses of a range of neutron wavelengths. Diffracted neutrons are separated according to their time of flight using fixed angle detectors and hence, their wavelength over a fixed distance. In conventional diffraction experiments, the wavelength (λ) is fixed with d and θ as variables (from the Bragg equation). However, for the T.O.F. experiment θ is fixed with λ and d as variables.

A pulsed neutron source diffractometer operates in a fundamentally different way from a conventional constant wavelength diffractometer. POLARIS and GEM measure the Bragg reflections at a fixed scattering angle and monitors the time of arrival of a neutron after the initial burst produced at the target. Conventional diffractometers measure the Bragg reflections by scanning a detector from low to high 2θ. The relationship between T.O.F. and d-spacing is linear and can be derived from the combination of de Broglie's relationship and Bragg's law as shown:

$$\lambda = \frac{h}{p_n} = \frac{h}{m_n v_n} = 2d \sin\theta$$

where h is Planck's constant, m_n, v_n, and p_n are the mass, velocity and momentum of a neutron respectively with d and $\sin\theta$ as derived by Bragg's law. Given a primary flight path (moderator to sample) is a distance L_1, a secondary flight path (sample to detector) is L_2 and the corresponding times of flight are t_1 and t_2, then:

$$\frac{h}{m_n}.\left[\frac{t_1 + t_2}{L_1 + L_2}\right] = 2d \sin\theta$$

Therefore with an overall flight path L and time of flight t such that:

$$L_1 + L_2 = \mathrm{L} \quad \text{and} \quad t_1 + t_2 = t$$

this gives:

$$t = 2dL\left(\frac{m_n}{h}\right)\sin\theta$$

$$\therefore \; t \propto d$$

Thus for a 12 m instrument like POLARIS a 1 Å d-spacing reflection will be detected in the backscattering bank at a T.O.F. of ~ 5000 μs.

2.4.4 Instrumentation

The POLARIS instrument receives short pulses (<90 μs) of neutrons from the proton spallation of a uranium or tantalum target, with neutrons of wavelengths down to 0.2 Å suitable for diffraction. The initial burst of neutrons is slowed in a gadolinium poisoned water monochromator at 295 K to give the required tight neutron pulse over a wide range of wavelengths. A schematic representation of POLARIS is given in Figure 2.4.

The samples were loaded in vanadium cans of 6-12 mm overall diameter, and placed within an evacuated sample chamber. On POLARIS backscattered neutrons are detected by 38 ^{3}He detectors giving a resolution of $\Delta d/d \sim 5 \times 10^{-3}$ and a d-spacing range of 0.2–3.2 Å. Typical data collection periods on POLARIS for samples of 1–2 g were 2-4 hours depending on the sample.

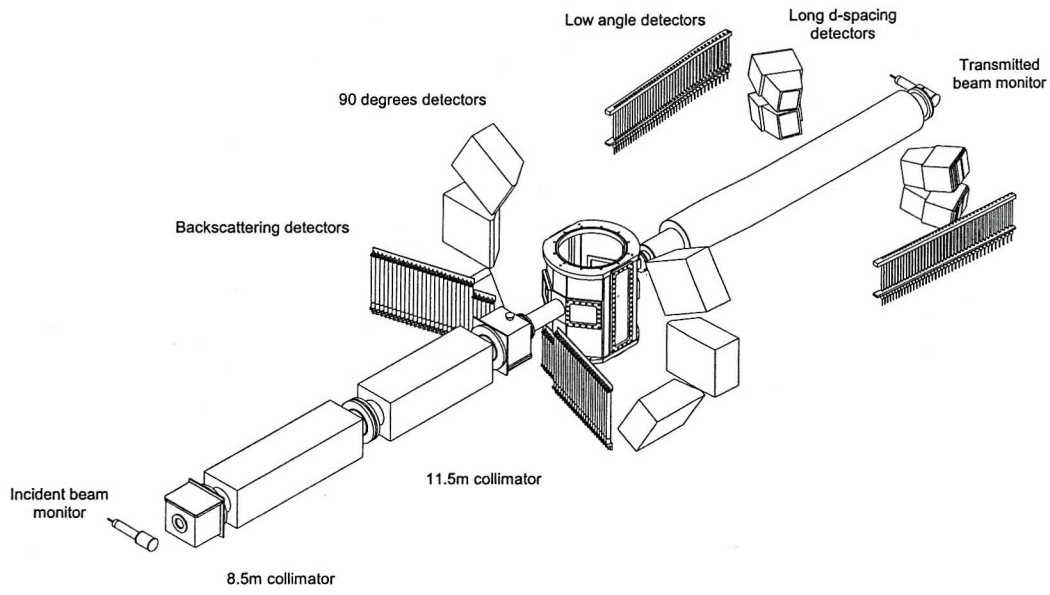

Figure 2.4. The POLARIS diffractometer.

The GEM instrument has only recently been installed at Rutherford. It has been designed to give both high resolution and high flux with a low background count, to facilitate the study of samples under varying conditions such as temperature, pressure and chemical reaction. The combination of a high count rate and good resolution enables data to be collected in very short times and on small samples. The instrument comprises a primary flight path of 17 m and has seven detector banks, which give an overall detector area of *ca.* 10 m^2. The resolution is $\Delta d/d$ = 2-3 x 10^{-3} in backscattering and $\Delta d/d$ = 5 x 10^{-3} at scattering angle of 90 ° at all d-spacings. Typical data collection periods on GEM for samples of 0.5–1 g were 10-20 minutes depending on the sample. A schematic representation of GEM is given in Figure 2.5.

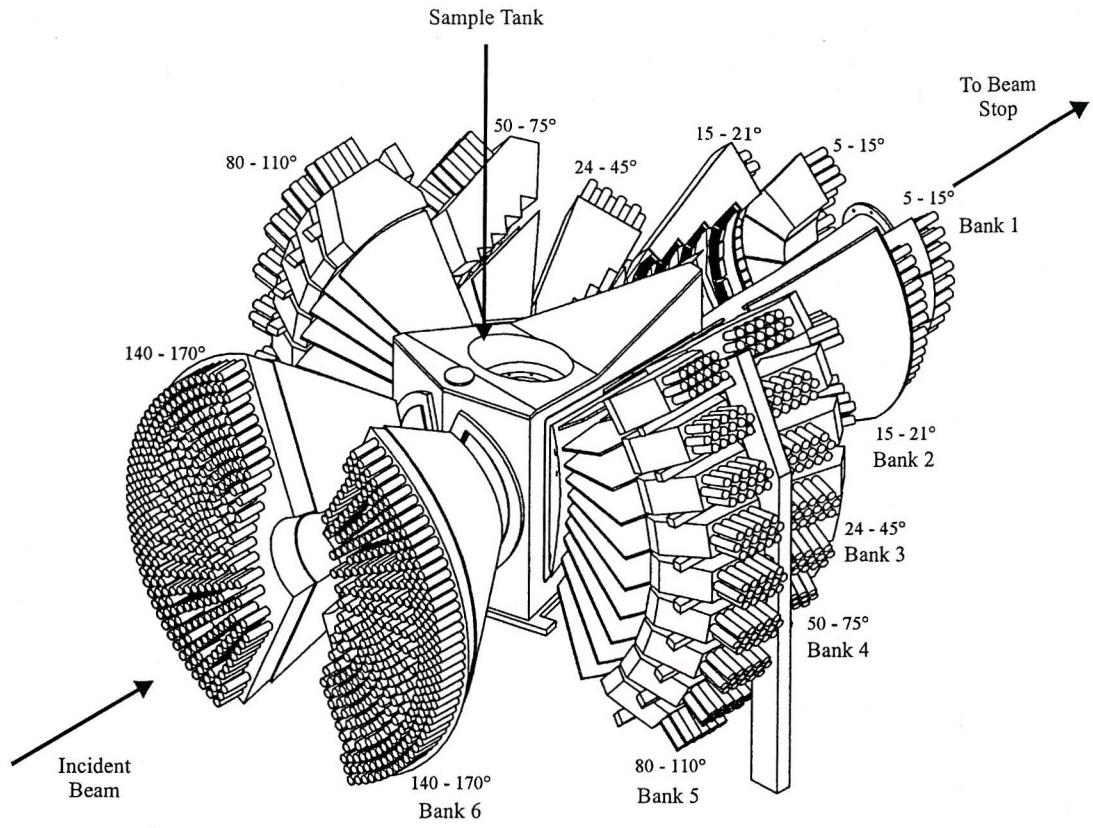

Figure 2.5. The GEM diffractometer.

2.5 Structural Refinement

2.5.1 Theoretical Considerations

It may be shown that for any regular array of stationary atoms, the structure factor, F, is the sum of the contributions of the scattering amplitudes, f, and the phases, ϕ, of each atom[11], giving the expression:

$$F = \sum_{j=1}^{N} f_j \exp[i\phi_j]$$

In a unit cell, the total phase shift of an atom j, at a point (x_j, y_j, z_j) from the origin is the sum of the phases shifts in each direction. When the phase shift is evaluated, the structure factor for one unit cell becomes:

$$F_{hkl} = \sum_{j=1}^{N} f_j \exp\left[2\pi i\left(hx_j + ky_j + lz_j\right)\right]$$

where h, k and l are the Miller indices that define the plane from which the reflection takes place. For very small crystals, it may be shown that the intensity of the scattered beam is proportional to the square of the structure factor.

$$I_{hkl} = kL^2 |F_{hkl}|^2$$

where k is a scaling constant and L is the Lorentz factor, a geometric function of the method of data collection and hence the instrument used[11].

In real crystals, the scattered intensity is modified by imperfections in the lattice structure. Defects and substitutional disorder cause local structural irregularities, particularly in non-stoichiometric materials. In addition, thermal motion causes a reduction in scattered intensity as a result of time dependent vibrations of the atoms about their mean positions: the atoms in a plane *hkl* are displaced randomly from their ideal in-plane positions, disrupting the in-plane behaviour of their combined scattering. The correction to a structure factor reflected by a plane, *hkl*, takes the form[11]:

$$T_{hkl} = \exp\left[-B_{hkl}\frac{\sin^2\theta}{\lambda^2}\right]$$

so that for a unit cell, the structure factor becomes:

$$F_{hkl} = \sum_{j=1}^{N} f_j n_j \exp\left[-B_j\frac{\sin^2\theta}{\lambda^2}\right].\exp\left[2\pi i(hx_j + ky_j + lz_j)\right]$$

where n_j is the occupation factor of the j^{th} atom, equal to unity in a structure free from vacancies. However, this assumes that the displacements due to the thermal motion are equal in all directions (isotropic), which is seldom the case, except in some highly symmetric positions of cubic space groups[12]. A more rigorous analysis[11] describes the anisotropy of thermal motion in the form of an ellipsoid, giving a new definition of T_{hkl}:

$$T_{hkl} = \exp\left[-\tfrac{1}{4}\left(B_{11}h^2a^{*2} + B_{22}k^2b^{*2} + B_{33}l^2c^{*2} + 2B_{12}hka^*b^* + 2B_{23}klb^*c^* + 2B_{13}hla^*c^*\right)\right]$$

There are a number of other expressions for T_{hkl} but the form given here is used to describe the anisotropic temperature factors used in this work. The intensities of the diffracted beams are also governed by the multiplicity of an *hkl* reflection. Therefore, for a particular *hkl* reflection in a given crystal symmetry class, there are a number of equivalent planes diffracting at the same angle to give an increased intensity.

The theory summarised above allows the calculation of a simulated diffraction pattern from an initial structural model using cell parameters, atomic positions and symmetry elements. Section 2.5.2 gives details on diffraction data analysis using the Rietveld method[9,10].

2.5.2 The Rietveld Method

Early methods of analysis of diffraction data were carried out following the principles developed for single crystal diffraction patterns. This utilised a least squares refinement using | F | values based on structure factors extracted from the pattern. Since powder diffraction data often contains many overlapping peaks, structure factor extraction was difficult and sometimes impossible. A technique was devised by H. M. Rietveld[9,10] to utilise the full information content at each step of the powder pattern, which allowed structure determination using a method of profile refinement.

The typical process adopted for refinement is as follows:

i. Start with an approximate model of the structure.
ii. Refine the scale factor and background parameters.
iii. Determine lattice parameters, zero-point correction and sample displacement to allow accurate location of Bragg reflections. Preliminary refinement of the peak profile coefficients may also be carried out at this stage.
iv. Locate and refine atom positions in the structure thus altering the peak intensities.
v. Refine the isotropic temperature factors accounting for atomic vibrations.
vi. Establish peak shape parameters to account for sample broadening effects.

vii. If possible vary the anisotropic temperature factors.

In this work, the Rietveld method was used for refinement of data collected on both x-ray and neutron instruments. The difference between the data sources influences the preparation that is required and the instrumental parameters that are refined, however, the general method carried out is in principle the same. In all cases, the 'best fit' sought is the minimum difference at all the intensities at each step.

The observed background corrected counts, y_i^{obs}, are compared with the calculated counts, y_I^{calc}, for a trial structure at each point 2θi on the profile. The quantity minimised in the least squares refinement is the function M and is the sum over all the data points.

$$M = \sum_i w_i (y_i^{obs} - y_i^{calc})^2$$

Where w_i is a weighting factor given by $1/y_i^{obs}$. A polynomial background is fitted to the background intensity of the recorded pattern.

For PXD, the calculated intensities, y_I^{calc}, are determines from the structural model by summing the calculated contributions from neighbouring Bragg reflections, *k*, plus the background, *bi*:

$$y_i^{calc} = s\sum_k L_k |F_k|^2 \phi(2\theta_i - 2\theta_k) P_k A + y_{bi}$$

Where:

s is the scale factor

Lk contains Lorentz polarisation and multiplicity factors

Φ is the reflection profile function

Fk is the structure factor for the *k*th Bragg reflection

Pk is the preferred orientation function

A is an absorption factor

ybi is the background intensity at the *i*th step

Since a comparison of intensities is performed at each point, it is essential for the construction of the calculated profile to accurately describe the shape of the Bragg reflections (peak shape). The peak shape used in this work is the pseudo-Voigt function, which is a linear approximation to the convolution of the Gaussian and Lorentzian components of the peaks, given as:

$$\eta L + (1-\eta)G$$

Where L and G are the Lorentzian and Gaussian contributions to the peak shape and η is the mixing parameter which can be refined as a linear function of 2θ.

$$\eta = N_A + N_B(2\theta)$$

Where N_A and N_B are refinable parameters.

The Gaussian and Lorentzian contributions to the peak shape are defined by the equations:

$$G = \frac{(4\ln 2)^{1/2}}{H_k\sqrt{\pi}} \exp\left(-4\ln 2(2\theta_i - 2\theta_k)^2 / H_k^2\right)$$

and

$$L = \frac{2}{\pi H_k} 1 \Big/ \left[1 + 4\frac{(2\theta_i - 2\theta_k)^2}{H_k^2}\right]$$

Where $2\theta_k$ is the calculated position for the kth Bragg peak corrected for the counter zero point and H_k is the full width at half maximum of the kth Bragg reflection.

The full width at half maximum, H_k of a Gaussian peak varies with the scattering angle $2\theta_k$ and is modelled as:

$$H_k^2 = U\tan^2\theta + V\tan\theta + W$$

where *U, V* and *W* are refinable parameters and are both instrument and sample dependent. This formula can take into account peak broadening resulting from particle size.

At low scattering angles the peaks become asymmetric owing to the detector and sample heights. This results in the peak maxima shifting to lower angles while the integrated intensity remains unchanged. This can be corrected by the following semi-empirical correction factor:

$$1-\frac{sP(2\theta_i-2\theta_k)^2}{\tan\theta_k}$$

where P is the symmetry parameter and s = +1, 0, -1 when $(2\theta_i - 2\theta_k)$ is positive, zero or negative.

The least squares parameters fall into two distinct groups. The first group defines the position and shape of the peaks and consists of the unit cell parameters, the counter zero offset and the asymmetry factor. The second group, comprising the structural and thermal parameters, defines the contents of the unit cell. These consist of the profile scale factor as well as the coordinates, occupation and temperature factor of each atom.

In order to make a quantitative assessment of the agreement between observed and calculated profiles a number of reliability indices are defined as follows:

$$R_{profile} = R_p = 100\left[\frac{\sum_i \left|y_i^{obs} - y_i^{calc}\right|}{\sum_i y_i^{obs}}\right]$$

This may be compared with the reliability index $R_{expected}$ derived purely from statistical considerations:

$$R_{expected} = R_{exp} = 100\left[\frac{(N-P+C)}{\sum_i \omega_i (y_i^{obs})^2}\right]^{1/2}$$

where N is the number of observations, P is the number of refinable parameters and C is the number of constraints. In addition, R_{wp} may be defined as:

$$R_{wp} = 100\left[\frac{\sum_i \omega_i \left[y_i^{obs} - y_i^{calc}\right]^2}{\sum_i \omega_i \left[y_i^{obs}\right]^2}\right]^{1/2}$$

The final measure of the whole fit that is minimised during the refinement is the chi-squared parameter, and is defined as:

$$\chi^2 = \left[\frac{R_{weightedprofile}}{R_{exp}}\right]^2$$

Therefore, a better fit is obtained as the weighted profile R-factor approaches the statistical expected R-factor value *i.e.* χ^2 should approach unity. The goodness of fit can also be estimated visually by examining a plot of the profile fit. A good fit is seen when the difference line between calculated and observed data is as flat as possible, with fluctuations consistent with noise.

In this work, PXD and PND data were analysed using the GSAS package of Larsen and Von Dreele[13] on a PC. The R_p, R_{wp} and χ^2 values obtained for a refinement have been quoted to give an indication of the goodness of fit achieved to the data. The R-factor values obtained for PXD refinements are generally larger than would be expected. This has been attributed to the low background obtained when they were run on the Siemens D5000 and D8 diffractometers. The inability to accurately model the low background leads to the term:

$$\left|Y_{bi}^{obs} - Y_{bi}^{calc}\right|$$

(where Y_{bi} is the background intensity at the i^{th} step) becoming large and consequently the R-factors are artificially high.

2.6 Vibrating Sample Magnetometry (VSM)

The magnetic properties of several materials were characterised using the technique of vibrating sample magnetometry. The material is loaded into a small, magnetically neutral plastic container, which is subjected to a magnetic field between two search coils. The sample is then vibrated rapidly and the temperature dependence of the magnetic susceptibility is measured. In this work, an applied field of 0.5 and 5 T were used on a sample size of ~ 100 mg. A schematic diagram of the VSM instrument is shown in Figure 2.6.

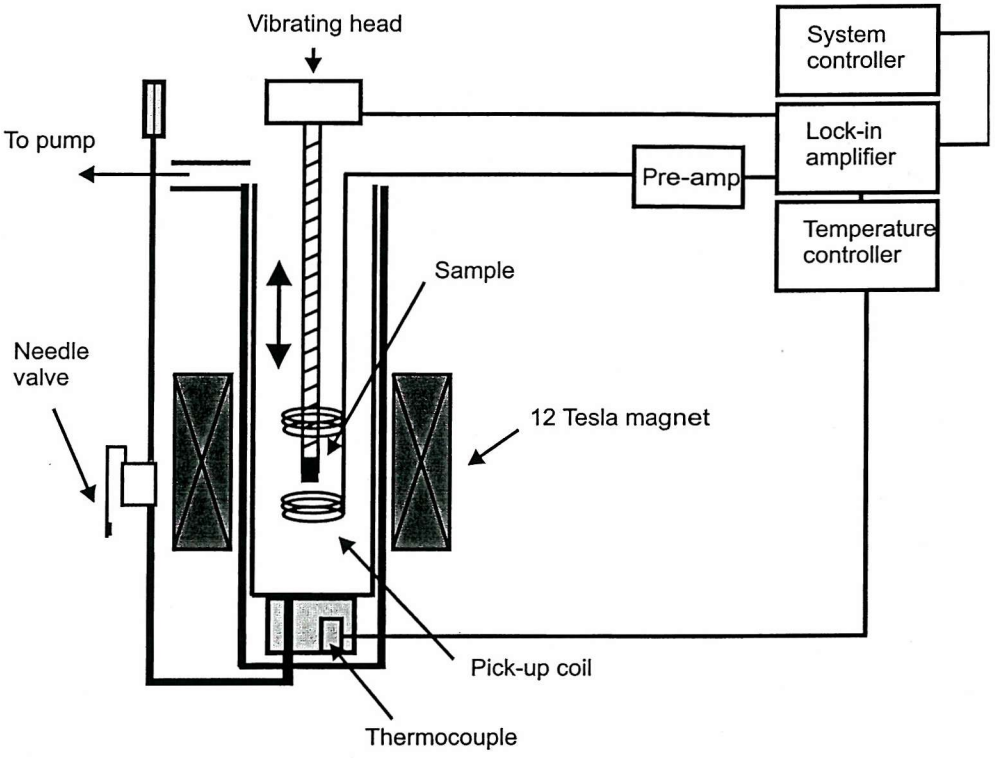

Figure 2.6. Schematic diagram of the VSM instrument.

Examination of the data reveals what type of magnetic behaviour the material exhibits *i.e.* paramagnetism, ferromagnetism or antiferromagnetism. For paramagnetic materials, the molar magnetic susceptibility, χ, which is related to the number of unpaired electrons present in the material, may be determined using the Curie-Weiss expression,

$$\chi = \frac{C}{(T - \theta)}$$

Where C is the Curie constant, θ is the Weiss constant, and T is the temperature. This states that magnetic susceptibility is inversely proportional to temperature.

2.7 Resistivity Measurements

Resistivity measurements were made on many of the materials obtained in this work. They were carried out using the four-probe technique, depicted in Figure 2.7. The sample is pressed into a pellet under ~10 tonnes/cm^2 and carefully cut to form a bar of approximate dimensions 8 x 4 x 2 mm and uniform in size. The dimensions of the pellet were accurately recorded using a set of digital callipers. Four wires were attached to the pellet using silver conductive paint. When extreme variable temperature work was carried out the pellets were coated in gold, instead of silver, at the contacts to ensure accurate data was obtained. The potential difference and the four terminal resistance was measured using a Fluke 8840A multimeter with a d.c. current source. Variable temperature experiments were carried out using a modified Oxford Instruments cryostat enabling continuous measurements to be made in the temperature range 14-750 K. Sub-ambient cooling was made by an Edwards continuous cycle cooler. The sample temperature was measured by a calibrated iron-rhodium resistance thermometer embedded in the sample holder in close proximity to the sample.

Applying a current , I, through a bar of cross sectional area (A = w x d) and measuring the potential difference, V, across a length, L, of the sample enables the determination of the resistivity, ρ, by combining the equation:

$$\rho = RA / L$$

with Ohms law:

$$V = IR$$

to give

$$\rho = VA / LI$$

The large internal resistance of the voltmeter ensured minimal current being drawn into the measuring loop, which is in parallel with R_S and so the contact resistances, R_{CV}^+ and R_{CV}^- were assured to have no effect on the measurement of R_S. The use of the four-probe method eliminates the problems of the contact resistances, R_{CI}^+ and R_{CI}^-, as the potential difference is not measured across them.

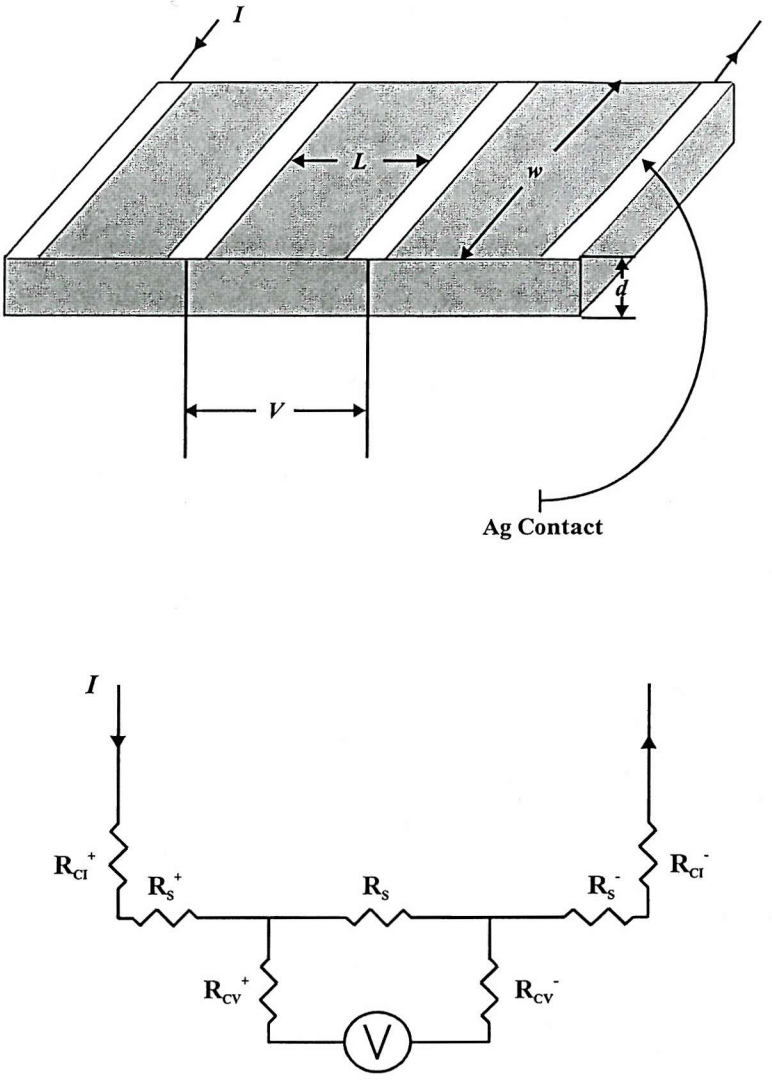

Figure 2.7. Diagramatic representation of the 4-probe resistivity experiment.

2.8 Infra-red Spectroscopy (IR)

Typically, atoms in solids vibrate at frequencies ~10^{12} to 10^{13} Hz. The absorption of infra-red radiation at the appropriate frequency can excite vibrational modes, involving pairs or groups of bonded atoms to higher energy states. Infra-red spectra are plots of absorption intensity as a function of frequency. The frequency of the incident radiation is varied and the quantity of the radiation absorbed or transmitted by the sample is obtained. Infra-red spectra can be complex with numerous peaks, each corresponding to a particular molecular vibration mode, although it is usually possible to assign each vibration.

Infra-red spectroscopy was also used in this work to investigate the electronic nature of the materials. A metallic oxide will generally show a strong absorption across the whole region associated with the collective electronic states. An insulating oxide will absorb at discrete frequencies in the infra-red region associated with the M-O modes. In general, perovskite related oxides show two prominent bands in the region 1000-250 cm^{-1}, which are assigned to the internal modes of the BO_6 octahedra. The higher $\nu_{B\text{-}O}$ frequency band is usually assigned to a metal-oxygen stretching frequency and the lower $\delta_{B\text{-}O}$ frequency band to a deformation mode of BO_6 octahedra. The integrated area under the two bands is observed to increase in the order of increasing electrical resistivity, and in the event of a material passing through an insulator-metal phase transition, the two bands will no longer be observed. This observed phenomena, makes it possible to map each different material's electronic behaviour using this technique.

The room temperature data were collected on a Perkin-Elmer Spectrum One Fourier-Transform Infra-red Spectrometer (FT-IR) with CsI optics. Variable temperature data were collected simultaneously with resistivity measurements sharing the same cryogenic equipment and were recorded on a Nicolet Magna 760 Infra-red spectrometer. The materials were intimately ground with spectroscopic KBr in a quantitative manner to allow an accurate comparison of spectra. Spectra were recorded over a range of 4000-250 cm^{-1}, with a resolution of 2 cm^{-1}.

2.9 Thermogravimetric Analysis (TGA)

Thermal stability and accurate oxygen determination of materials were studied using a Polymer Laboratories PL-STA 1500 simultaneous thermal analysis machine, see Figure 2.8. This allows thermogravimetric analysis (TGA) and differential thermal analysis (DTA) to be carried out simultaneously, however, only TGA was used in this work.

TGA is a technique where the analysis of a solid material is performed by measuring its weight as a function of temperature or time. The sample can be heated at a rate of 1-50 °C/min in a controlled atmosphere and the weight loss measured. This can produce valuable information such as water content, oxygen content of oxides or decomposition temperature.

In a typical experiment ~15mg of sample was heated to 1000 °C at a rate of 20 °C/min under 5 % H_2/N_2 gas with a flow rate of ~ 90 ml/min. The target temperature was maintained for 30 minutes to ensure that the total weight loss had occurred and the sample was then cooled to room temperature at 40 °C/min. Data points were collected every 4 seconds and displayed in real time.

TGA experiments were only performed on the perovskite materials reported in this work. The pyrochlore materials were excluded from investigation in this way due to the volatility and toxicity of the elements contained in them.

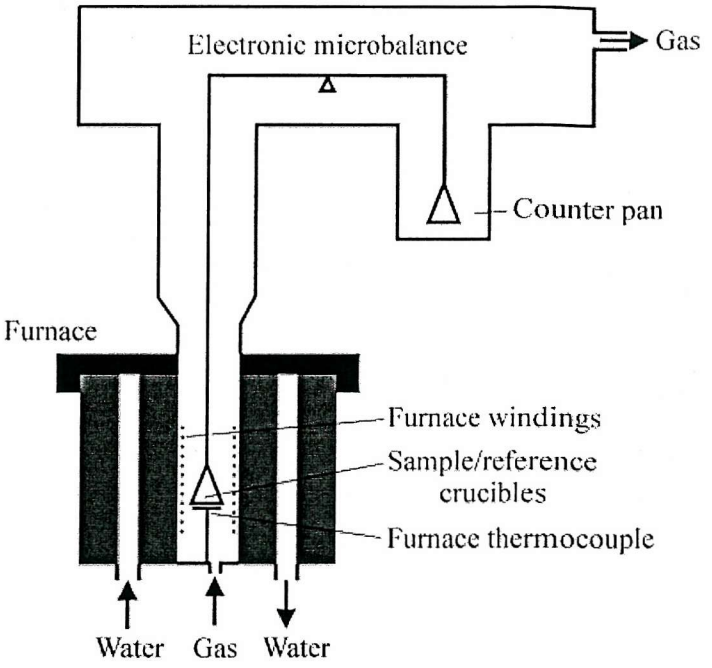

Figure 2.8. Schematic diagram of the PL-STA 1500.

2.10 Bond Valence Calculations

Bond valence theory is an empirical approach, which aims to give an indication of the strength of the bonding within crystalline solids. Bond valence calculations have been used in this work to provide an indication of the chemical validity of the structural models derived from refinements of diffraction data and to estimate the valence of an ion situated in a particular co-ordination environment.

The assignment of single, double or triple bonds, applicable to organic and co-ordination chemistry cannot be applied to crystalline non-molecular inorganic solids. Purely geometric descriptions do not give any indication of the bond strengths, and hence an empirical approach, bond valence theory, was developed by Zachariasen[14] and Brown[15]. Bond valence theory assigns strengths, or valences, to individual bonds, thus allowing the valence of a site to be summed; bond strength is directly related to bond length with longer bonds implying a weaker interaction with the cation. Bond valence theory ultimately derives a valence for the atom in question from the observed bond lengths about that site. The valence sum rule is simply given by:

$$V_i = \sum_j S_{ij}$$

where S_{ij} is the valence of a bond between atoms i and j and V_i is the valence of atom i. In an inorganic system bond strength can therefore be accurately determined from experimentally measured bond lengths. By consideration of a vast range of inorganic crystalline systems a correlation between bond lengths and valence has been established. This is an inverse relation and can be described by the expression:

$$S_{ij} = \exp\left[\frac{R_o - R_{ij}}{B}\right]$$

where R_{ij} is the length of a bond around the ion and R_0 and B are empirically determined parameters, many of which have been tabulated. In most cases the effective valence calculated lies within 0.2 of the actual valence. Actual values of R_o used are those derived by Altermatt and Brown[16].

A disadvantage of these calculations is that they assume that the system under study is relaxed. However, this is not always the case in rigid oxide lattices where there can often be a large amount of structural strain present. Systems under compression give shorter bond lengths and correspondingly larger, 'over bonded', valences. Conversely, those which are over stretched give longer bond lengths and 'under bonded' sites.

2.11 References

[1] A. R. West, *Solid State Chemistry and its Applications*, John Wiley & Sons, (1984).

[2] R. C. Weast *(Editor), Handbook of Chemistry and Physics,* 56th Ed., CRC Press, (1975).

[3] M. M. Woolfson, *An Introduction to X-ray Crystallography,* Cambridge University Press (1970).

[4] W. L. Bragg, *Proc. Camb. Phil. Soc.,* **17** 43 (1913).

[5] A. K. Cheetham and P. Day, *Solid State Chemistry: Techniques,* Oxford Science Publications, Clarenden Press, Oxford, 54 (1988).

[6] T. Hahn, *International Tables for Crystallography,* D. Reidel, Dordrecht **A** 26 (1983).

[7] *International Centre for Diffraction Data,* 12 Campus Boulevard, Newton Square, Pennsylvania 19073-3273, U.S.A., (1995).

[8] K. Yvon, W. Jeitschko and E. Parthe, *J. Appl. Crystallogr.,* **10** 73 (1977).

[9] H. M. Rietveld, *Acta Cryst.* **22** 151 (1967).

[10] H. M. Rietveld, *J. Appl. Cryst.* **2** 65 (1969).

[11] M. J. Buerger, *Contempory Crystallography,* McGraw-Hill (1970).

[12] B. T. M. Willis and A. W. Pryor, *Thermal Vibrations in Crystollography,* Cambridge University Press (1975).

[13] A. C. Larson and R. B. Von Dreele, *Generalsied Structure and Analysis System,* MS-H805, Los Almos, NM 87545 (1990).

[14] W. H. Zachariasen, *Acta Cryst.,* **16** 385 (1963).

[15] I. D. Brown, *Acta. Cryst.* **33** 1305 (1977).

[16] D. Aldermatt and I. D. Brown, *Acta Cryst.* **41** 240 (1985).

Chapter Three

The Structure and Physical Properties of Osmium(V) Pyrochlores $A_2Os_2O_7$ (A = Cd and Hg)

3.1 Introduction

The pyrochlore structure is commonly adopted by materials of the composition $A_2B_2O_{7-x}$ where 'A' is a larger mono-, di- or tri-valent cation and 'B' is smaller tetra-, penta- or hexa-valent cation. Examples include $Mn_2Sb_2O_7$, $Sn_2Ta_2O_7$ and $Pb_2U_2O_7$. The structure can be drawn using BO_6 octahedra sharing all vertices with a distorted (6 + 2) cubic co-ordination to the 'A' type cation. Alternatively the structure can be considered as being derived from a fluorite structure with the composition $[A_2B_2]O_8$ by the removal of two oxide anions in a regular fashion producing, $A_2B_2O_7\square$, where $\square$ represents a vacancy. A detailed review of the pyrochlore system describing the wealth of materials adopting this structure type and their properties has been published by Subramanian and co-workers[1]. Recently much work on pyrochlore chemistry has been directed at the magnetic and electronic properties of materials in this system that contain late second row transition elements as the 'B' type cation. For example, the ruthenium (IV) pyrochlores such as $Ln_2Ru_2O_7$ and $Y_2Ru_2O_7$ have been investigated in terms of their magnetic structures and magnetic frustration by a number of groups[2 to 4]. Further attention has been focussed on $Tl_2Ru_2O_7$ which exhibits strong magnetoresistive effects[5,6].

One of the pyrochlores originally reported by Sleight[7] as part of a systematic study of materials with this structure type in the early 1970s was the more unusual (2+,5+) material $Cd_2Os_2O_7$. This compound, studied as single crystals, was found to exhibit an electronic second order metal–semiconductor/insulator transition T_{MI} at 225 K, with associated antiferromagnetic ordering. The low temperature resistive behaviour was interpreted in terms of a slow collapse of a semiconductor band gap to zero, while the high temperature resistive behaviour was unusual in exhibiting a very small increase with temperature. It is of note that while two different crystals demonstrated similar low temperature resistivity behaviour between 225 and 150K, below 150K marked variations occurred. Magnetic susceptibility measurements show clear antiferromagnetic ordering at 225 K; the high temperature behaviour in the metallic state is atypical and not fitted by a Curie–Weiss expression.

The observation of osmium (V) in complex oxides is extremely rare and previous to the work on $Cd_2Os_2O_7$ only one other Os(V) complex oxide has had its structure reported,

namely $NdOsO_4$[8], which also has a structure based on linked OsO_6 octahedra. In their review article Subramiam et al[1] summarised the known (2+,5+) pyrochlores oxides for late transition metals in terms of their ionic radii. From these considerations based on cation sizes it is clear that many Hg(II) based pyrochlores should exist with this ion in combination with a variety of pentavalent species. Of these compositions only $Hg_2B_2O_7$ with B = Nb, Ta, Sb and V have been synthesised and characterised. Following this theory, it should be possible to synthesise $Hg_2Os_2O_7$ due to Hg^{2+} and Cd^{2+} possessing similar ionic radii (Hg^{2+} $^{VIII}r = 1.14$ Å, Cd^{2+} $^{VIII}r = 1.10$ Å)[9].

This chapter reports the synthesis and characterisation of two Os(V) pyrochlores $A_2Os_2O_7$, where A = Cd and Hg. The materials are preliminary characterised by PXD and Rietveld analysis of the data is performed to determine structural information. The materials are magnetically characterised, along with variable temperature resistivity data recorded for $Hg_2Os_2O_7$. In addition, both materials are fully characterised using PND over a temperature range of 12 K to room temperature, defining any structural changes that occur. Furthermore, comparisons of the two materials are made in terms of their structural and physical properties.

3.2 Preparation of $A_2Os_2O_7$ Pyrochlores (A = Cd and Hg)

3.2.1 Synthesis of $Cd_2Os_2O_7$

Samples of $Cd_2Os_2O_7$ were prepared by grinding together high purity stoichiometric mixtures of CdO, Os and OsO_4. The basis of the method used was following the original report by Sleight. The mixture was loaded into a silica ampoule and sealed under vacuum with the sample end immersed in liquid nitrogen to avoid osmium loss due to the volatility of OsO_4. Numerous attempts were carried out using different synthesis temperatures and reaction times, and the combination that gave the most crystalline material was used. The mixture was heated at 800 °C for 1 day then cooled and the silica ampoule opened. The product at this stage was reground, resealed and heated to 800 °C for a further 3 days. Powder x-ray diffraction data were recorded on the black product using a Siemens D5000

diffractometer operating with Cu $K_{\alpha 1}$ radiation. The pattern was consistent with phase pure pyrochlore product material, with the exception of a small trace of OsO_2 (I/I_0 <2%).

3.2.2 Synthesis of $Hg_2Os_2O_7$

Samples of $Hg_2Os_2O_7$ were prepared by grinding together high purity stoichiometric mixtures of HgO, Os and OsO_4. The mixture was loaded into a silica ampoule and sealed under vacuum with the sample end immersed in liquid nitrogen to avoid osmium loss due to the volatility of OsO_4. The temperature used for this preparation had to be considerably lower than for the cadmium example due to HgO decomposing to Hg in excess of 500 °C, which could lead to the disintegration of the silica ampoule. Sleight reported the preparation of some mercury pyrochlores, $Hg_2Nb_2O_7$ and $Hg_2Ta_2O_7$, where reaction conditions of 500 °C for 2 days were used[10]. Since osmium oxides are considerably more reactive than niobium and tantalum oxides, the same temperature was used for this preparation with a reaction time of just 1 day. Powder x-ray diffraction data were recorded on the black product using a Siemens D5000 diffractometer operating with Cu $K_{\alpha 1}$ radiation. The pattern was consistent with phase pure pyrochlore product material.

3.3 PXD Structure Refinements

PXD data were collected over a 2θ range of 20°–120° for a period of 15 hours using a 0.02° step size, for both samples. Cell parameters were calculated from the d-spacings using the CELL computer program. Using the Rietveld technique, refinement of the data commenced using the computer program GSAS[11]. The refinement was started based on the cubic pyrochlore model, *Fd-3m*. A uniform approach to the structure refinement was undertaken for both data sets obtained to ensure consistent results. Cell parameters, peak shape parameters, atomic positions and isotropic temperature factors were sequentially added to the refinement. The refinements converged smoothly to yield acceptable *R*-factors and accurate cell parameters were determined for both materials along with atom positions, derived bond lengths and bond angles, which are summerised in Tables 3.1 and 3.2. Profile fits for achieved for $Cd_2Os_2O_7$ and $Hg_2Os_2O_7$ are shown in Figures 3.1 and 3.2.

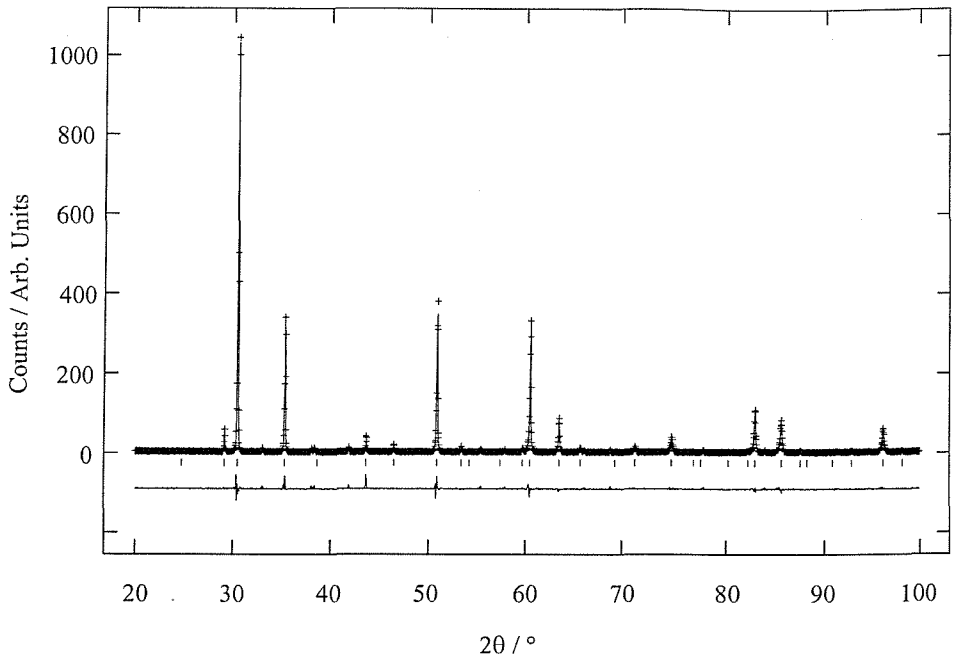

Figure 3.1. Profile fit to PXD data for $Cd_2Os_2O_7$. Experimental data points are shown as crosses, upper continuous line the calculated profile, lower continuous line the difference. Allowed reflection positions for $Cd_2Os_2O_7$ are shown with tick marks.

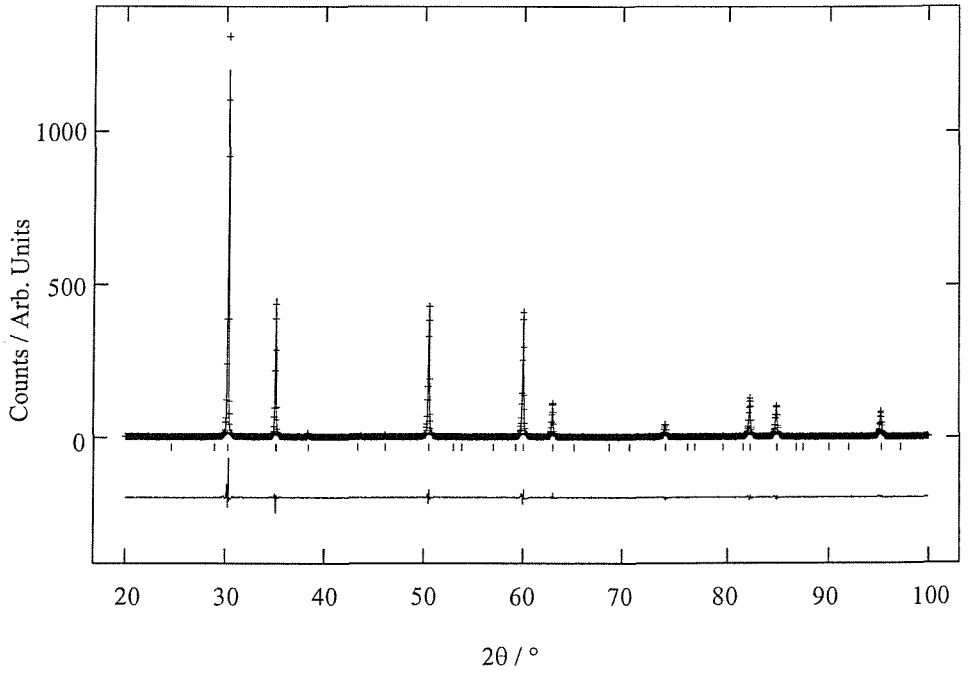

Figure 3.2. Profile fit to PXD data for $Hg_2Os_2O_7$. Experimental data points are shown as crosses, upper continuous line the calculated profile, lower continuous line the difference. Allowed reflection positions for $Hg_2Os_2O_7$ are shown with tick marks.

Table 3.1. Summary of derived atomic, thermal and profile fit parameters for $Cd_2Os_2O_7$ and $Hg_2Os_2O_7$; *esds* are given in the parentheses. Space group *Fd-3m*. Cd/Hg on (½,½,½), Os on (0,0,0), O1 on (x,⅛,⅛) and O2 on (⅜,⅜,⅜).

	$Cd_2Os_2O_7$	$Hg_2Os_2O_7$
a / Å	10.1437(2)	10.2213(1)
O1 x	0.3218(13)	0.3177(19)
Cd/Hg U_{eq} × 100 Å^2	1.41(8)	1.39(12)
Os U_{eq} × 100 Å^2	1.16(9)	0.90(12)
O1 U_{eq} × 100 Å^2	0.3(5)	1.7(6)
O2 U_{eq} × 100 Å^2	6.8(18)	0.8(18)
R_{wp} (%)	18.22	14.69
R_p (%)	11.94	10.84
χ^2	0.2764	0.2148

Table 3.2. Selected bond lengths and bond angles for $Cd_2Os_2O_7$ and $Hg_2Os_2O_7$.

	$Cd_2Os_2O_7$	$Hg_2Os_2O_7$
Cd/Hg-O1 (×6) / Å	2.546(10)	2.595(14)
Cd/Hg-O2 (×2) / Å	2.19618(2)	2.21297(1)
Os-O1 (×6) / Å	1.936(5)	1.935(7)
O1-Os-O1 / °	93.7(5)	92.1(8)
Os-O1-Os / °	135.8(7)	138.1(7)

3.4 Discussion

Both $Cd_2Os_2O_7$ and $Hg_2Os_2O_7$ are found to crystallise in a cubic pyrochlore unit cell, space group Fd $\bar{3}$m. The structure, illustrated below in Figure 3.3, is comprised of OsO_6 octahedra sharing all vertices with a distorted (6 + 2) cubic co-ordination to the Cd or Hg cations. The cell parameters in Table 3.1 show $Hg_2Os_2O_7$ to be the largest of the two structures, which is expected due to the larger ionic size of Hg^{2+} (^{VIII}r = 1.14 Å) compared to Cd^{2+} (^{VIII}r = 1.10 Å)[9]. From Table 3.2, it is apparent that the main changes in bond lengths occur at the Cd/Hg-O environment, particularly the metal to O1 bonds showing an increase of ~ 0.05 Å for the Hg pyrochlore. An increase following the same pattern is also observed for the apical Cd/Hg-O2 bonds but at a third of the intensity of ~ 0.017 Å. These Cd/Hg-O bond distances have relatively large *esds* associated with them, reflecting the limitations of PXD data, so exact values are not important, only the general trend.

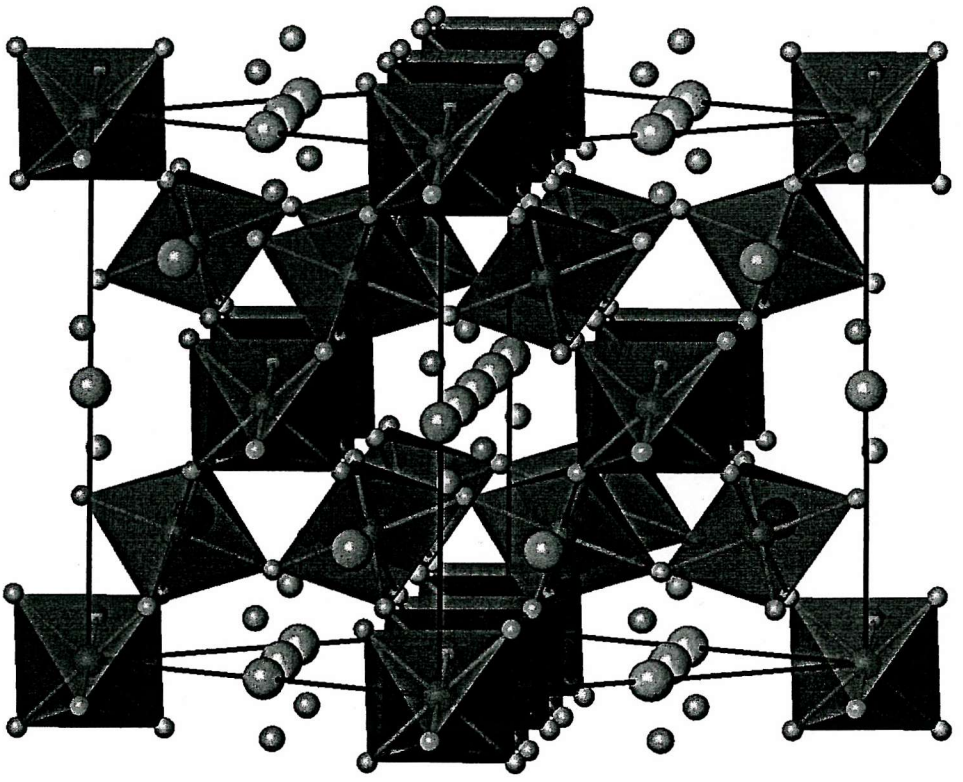

Figure 3.3. The pyrochlore structure, $A_2Os_2O_7$ shown as linked OsO_6 octahedra surrounding A cations (large spheres) and O (smaller unlinked spheres).

3.5 Magnetic Characterisation

The magnetic susceptibility of $Cd_2Os_2O_7$ and $Hg_2Os_2O_7$ was measured between 4 K and 298 K using VSM described in Chapter 2. Both materials showed broad cusps centred on 225 K for $Cd_2Os_2O_7$ (Figure 3.4) and 88 K for $Hg_2Os_2O_7$ (Figure 3.5). This behaviour reflects weak antiferromagnetic ordering at these temperatures. The data collected for $Cd_2Os_2O_7$ is consistent with previous observations[7,12].

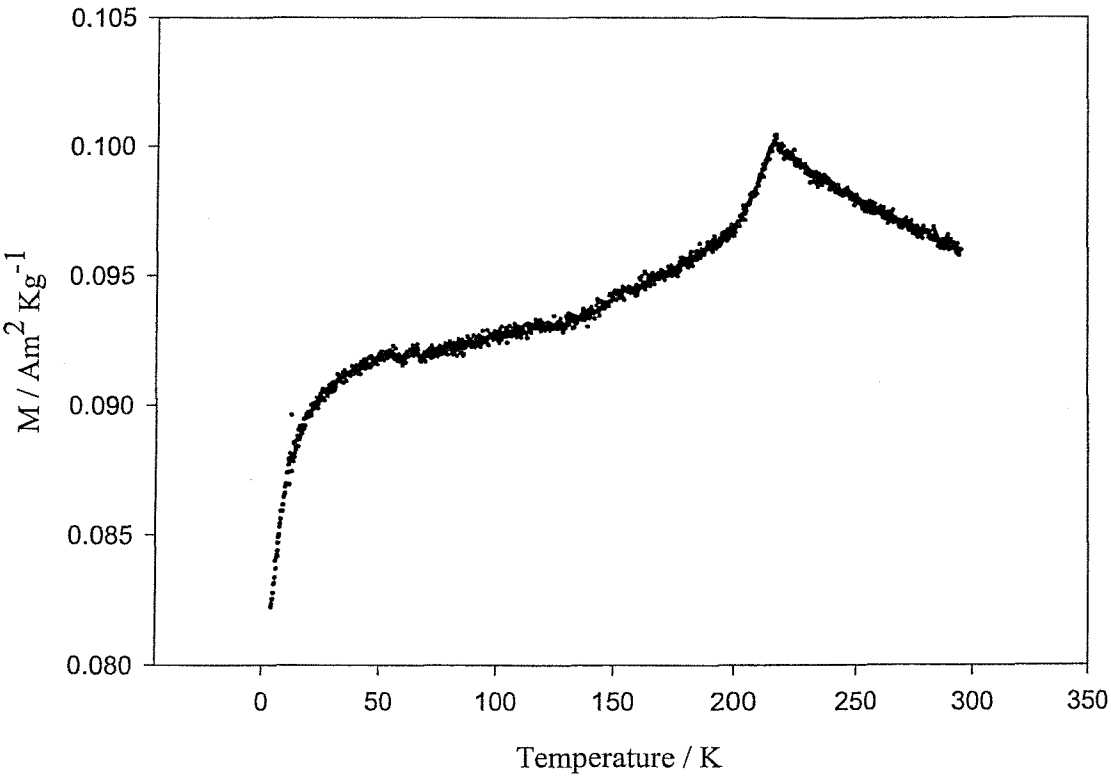

Figure 3.4. The temperature dependence of the magnetic susceptibility for $Cd_2Os_2O_7$.

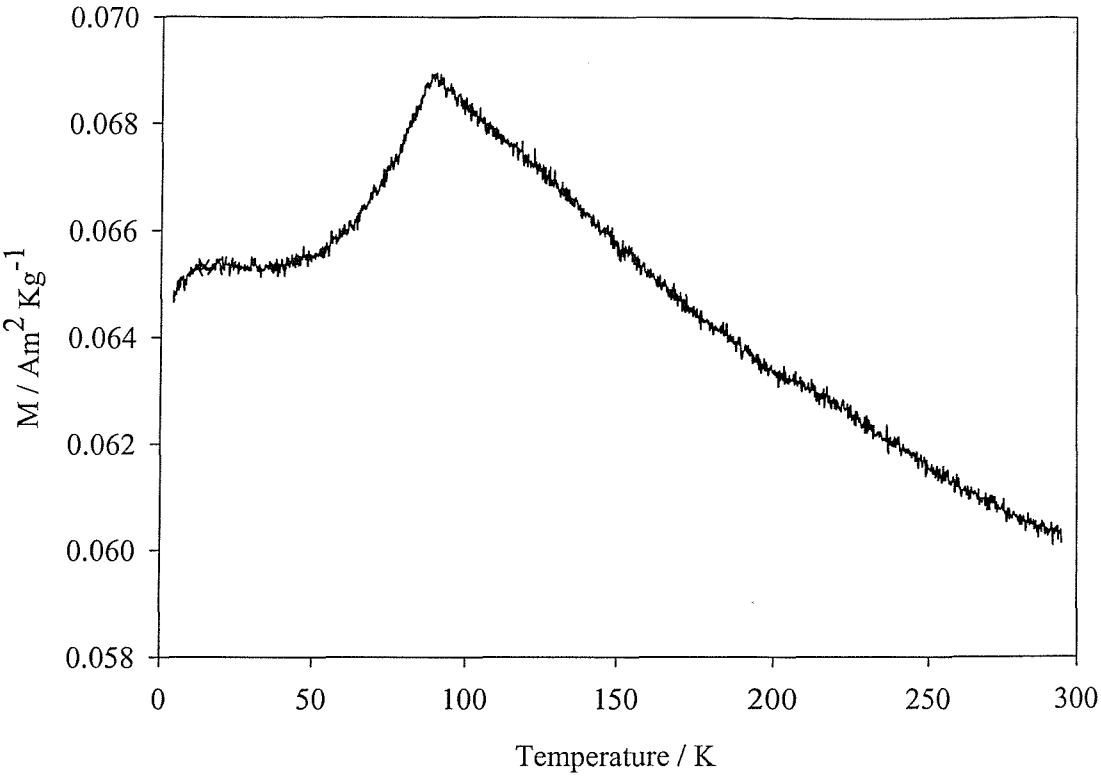

Figure 3.5. The temperature dependence of the magnetic susceptibility for $Hg_2Os_2O_7$.

The behaviour observed would tend to suggest that both materials are local-moment antiferromagnets, as long range order is not expected because the pyrochlore lattice is known to be geometrically frustrated[4,13,14]. Further evidence for the lack of long range magnetic ordering will be explored later in this chapter using powder neutron diffraction.

3.6 Resistivity Measurements

Resistivity data were collected for $Hg_2Os_2O_7$ from 4 K to 298 K, and are shown in Figure 3.6. The upper data set was obtained from the sample cooled in zero magnetic field while the lower trace, obtained on heating, was in a magnetic field of 5 T. Data were not collected for $Cd_2Os_2O_7$ due to previous well documented results already available for this material by several authors[7,12].

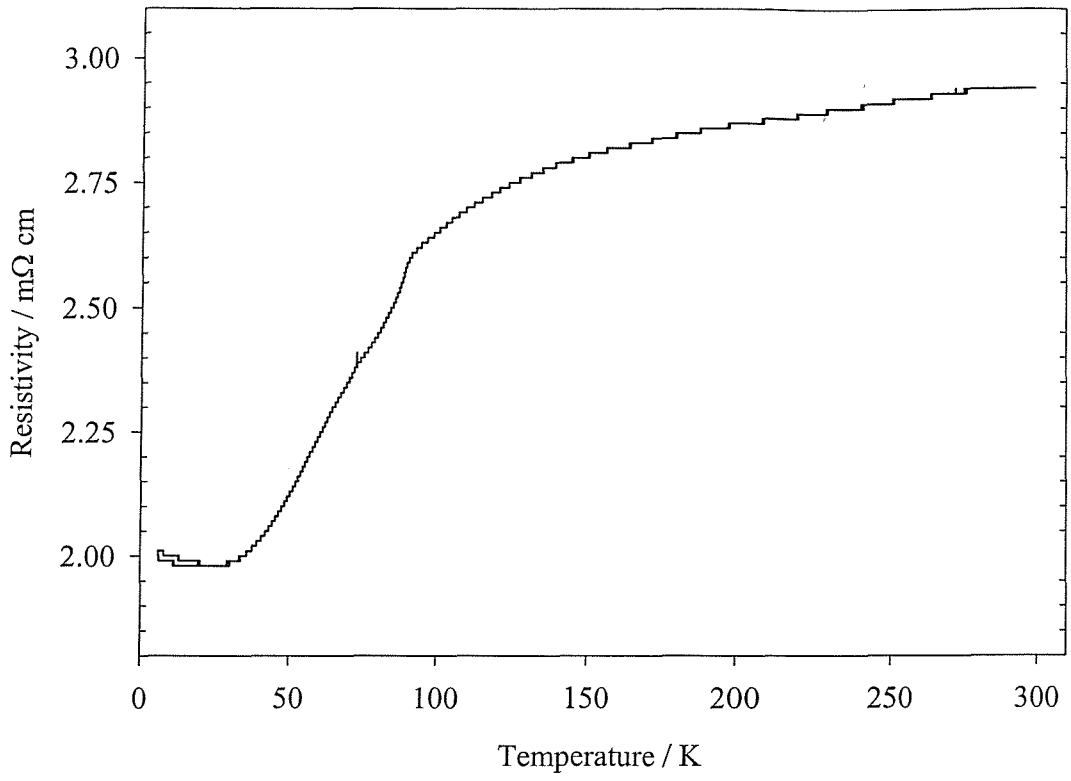

Figure 3.6. The temperature dependence of the resistivity for $Hg_2Os_2O_7$.

The results show an absolute value near 0.0025 Ωcm, which is typical of a poor metal and only changes very weakly with temperature. A small, but marked decrease, centred on 88 K, is apparent but this change is much weaker than the orders of magnitude change observed at 225 K for $Cd_2Os_2O_7$[7,12]. Interestingly, the change at 88 K for $Hg_2Os_2O_7$ is in the opposite direction of the 225 K transition of $Cd_2Os_2O_7$. The transition of $Cd_2Os_2O_7$ is described as an semiconductor to metal transition on increasing temperature, whereas the results for $Hg_2Os_2O_7$ show a metal/semiconductor to semiconductor transition. The absolute values are similar to those found for $Cd_2Re_2O_7$[15] which was recently found to be superconducting below 1 K, but there was no sign of superconductivity for $Hg_2Os_2O_7$ above 4 K, and it was impossible to cool the sample below this temperature with the equipment used. Similar electronic behaviour has also been observed for $Cd_2Ru_2O_7$[16] and interpreted in terms of the stabilisation of a spin-density wave at 100 K for this material.

3.7 Variable Temperature PND Study

Investigations of the $Cd_2Os_2O_7$ structure at room temperature and 77 K using single crystal x-ray methods showed no difference, in terms of lower symmetry, or peak broadening effects[7,12]. However, single crystal x-ray methods are not ideal for the investigation of such structure variations in this material for a number of reasons. Firstly single crystal methods are poor at resolving small changes in lattice parameters, due to the limited angular range of the diffraction data, and secondly, x-ray methods are insensitive to oxygen positions in such heavy metal oxides. The method of choice in investigating the structure of $Cd_2Os_2O_7$ is neutron diffraction; this technique can also supply information on any long range magnetic ordering occurring in the structure. However, natural cadmium (containing 12% ^{113}Cd) is an extremely strong absorber of neutrons (absorption cross-section = 2.06×10^{-20} cm^2)[17] making investigation of the structures of materials containing moderate levels of cadmium using neutron methods impossible. Nevertheless some isotopes of cadmium have negligible neutron absorption characteristics, e.g. ^{114}Cd (absorption cross-section = 3.40×10^{-25} cm^2)[17], making material containing one of these isotopes alone suitable for neutron diffraction work. Therefore, a ^{114}Cd enriched sample of CdO was used (99% ^{114}CdO, Trace Sciences International) for the preparation of the $Cd_2Os_2O_7$ material. The $Hg_2Os_2O_7$ material did not need any special treatment due to all the elements having negligible absorptions.

3.7.1 $Cd_2Os_2O_7$

Time of flight (TOF) powder neutron diffraction data were collected on the POLARIS diffractometer at the Rutherford Appleton Laboratory, Oxfordshire, U.K. The experiment was carried out using a closed cycle refrigeration (CCR) system at a series of temperatures, ranging from 12 K to room temperature. Data were collected for 75 minutes at each temperature with the exception of those around the transition (200 – 230 K), room temperature and 12 K, which were run for 135 minutes, 210 minutes and 190 minutes respectively. The room temperature data set was collected initially followed by cooling to 12 K and staged heating back to 250 K.

Rietveld refinement of the structure was undertaken using GSAS[11] and used the cubic pyrochlore model in the space group *Fd-3m*. For these refinements only the back-scattering bank data was used with time-of-flights ranging from 3000 to 19500 μs corresponding to the d-spacing range 0.5 - 3.1 Å. A uniform approach to the structure refinement was undertaken for each of the data sets obtained at different temperatures to ensure consistent results. Cell parameters, peak shape parameters, atomic positions and isotropic temperature factors were sequentially added to the refinement. The scattering length for the ^{114}Cd isotope was taken as 7.5 fm [17]. The fractional occupancies of the oxygen positions were investigated for site deficiency but all values refined to full occupancy within *esds*. Refinement of the osmium site occupancy showed no deviation from unity. For cadmium a small deficiency could be refined but this was associated with a strongly correlated reduction in isotropic displacement parameter and statistically insignificant improvement in profile fit factors; the cadmium occupancy was therefore fixed at unity. The small level of OsO_2 impurity (~2%) was modelled to improve the overall final profile fit. Final stages of the refinement included anisotropic temperature factors for all atoms. For each data set the refinement converged smoothly. Figure 3.7 shows the (typical) fit obtained to the room temperature data. Derived lattice parameters, atomic co-ordinates, displacement factors (100 U_{eq}) and profile fit parameters at each temperature are summarised in Table 3.3 together with the crystallographic description of the structure. Fit parameters and χ^2 values show behaviour in line with the data collection times.

Table 3.3. Summary of derived atomic, thermal and profile fit parameters for $Cd_2Os_2O_7$ as a function of temperature; *esds* are given in the parentheses. Space group Fd $\bar{3}$m. Cd on (½,½,½), Os on (0,0,0), O1 on (x,⅛,⅛) and O2 on (⅜,⅜,⅜).

T / K	a /Å	O1 x	Cd U_{eq} × 100 / Å^2	Os U_{eq} × 100 / Å^2	O1 U_{eq} × 100 / Å^2	O2 U_{eq} × 100 / Å^2	R_{wp} / %	R_P / %	χ^2
12	10.16043(5)	0.32078(7)	0.89(3)	0.02(1)	0.31(2)	0.33(2)	2.73	5.41	2.31
50	10.16078(7)	0.32072(8)	0.94(3)	0.04(1)	0.32(2)	0.33(2)	3.26	6.88	1.37
75	10.16139(7)	0.32064(9)	1.01(3)	0.06(1)	0.34(2)	0.35(2)	3.30	7.03	1.30
100	10.16227(7)	0.32069(9)	1.08(3)	0.08(1)	0.38(2)	0.44(2)	3.28	6.92	1.29
125	10.16324(7)	0.32058(9)	1.15(3)	0.08(1)	0.40(2)	0.41(2)	3.35	7.11	1.31
150	10.16414(7)	0.32055(9)	1.21(3)	0.11(1)	0.45(2)	0.46(2)	3.22	7.12	1.21
175	10.16511(7)	0.32035(9)	1.33(3)	0.12(1)	0.51(2)	0.51(2)	3.21	7.09	1.22
200	10.16613(7)	0.32026(9)	1.36(4)	0.16(1)	0.54(2)	0.57(2)	3.23	7.12	1.22
212	10.16669(6)	0.32034(9)	1.40(4)	0.14(1)	0.55(3)	0.57(3)	2.84	6.07	1.49
225	10.16679(6)	0.32028(9)	1.44(4)	0.15(1)	0.59(3)	0.59(3)	2.82	5.98	1.44
230	10.16702(7)	0.32023(9)	1.44(4)	0.15(1)	0.58(3)	0.57(3)	2.91	6.15	1.42
250	10.16811(7)	0.32026(9)	1.54(4)	0.17(1)	0.65(3)	0.68(3)	3.21	7.04	1.07
300	10.17063(7)	0.32017(9)	1.46(4)	0.20(1)	0.71(3)	0.72(3)	2.83	6.32	1.41

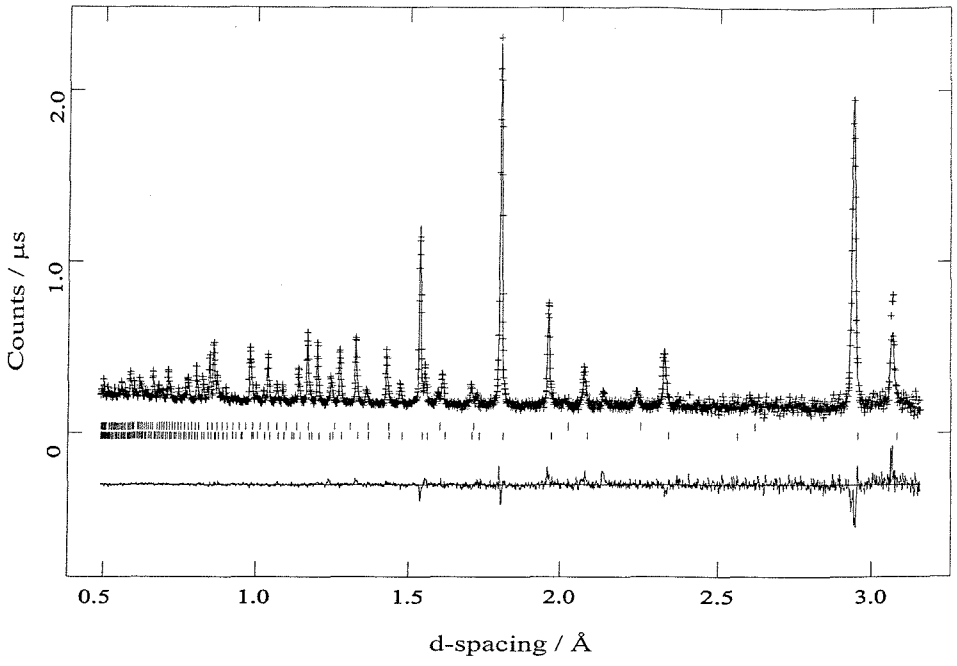

Figure 3.7. Example of the fit achieved to powder neutron diffraction data at T = 300 K. Crosses are experimental points, the upper continuous line the calculated profile and the lower continuous line the difference. Tick marks show reflection positions: $Cd_2Os_2O_7$ (lower) and OsO_2 (upper).

Figure 3.8 shows the variation in the lattice parameter as a function of temperature. A smooth increase, attenuated at the lowest temperatures, is seen between 12 K and 220 K consistent with characteristic thermal expansion. Over the range 100-200 K the thermal expansion co-efficient is 3.8×10^{-5} Å K^{-1} typical of a framework oxide; a similar rate of thermal expansion is seen above 230 K. A clear inflection is seen in the lattice parameter at the semiconductor – metal transition temperature (T_{MI}) that is presumably associated with the delocalisation of the electrons and abrupt change in resistive behaviour (3 to 4 orders of magnitude drop in resistivity)[7,12]. This decrease in lattice constants on approaching T_{MI} is similar to those observed in some other metal-insulator transition materials such as $SmNiO_3$[18 to 20]. In this compound the electron delocalisation leads to a clear decrease of all the Ni-O distances. In $Tl_2Ru_2O_7$[5], which has also been investigated by powder neutron diffraction through a T_{MI} transition temperature (142 K, though this material is metallic at low temperatures and semiconducting above T_{MI}), only a smooth variation in lattice parameter as a function of temperature is seen. Changes in oxygen positional parameter

result in an overall increase in the Ru-O distance and the Ru-O-Ru bond angle at higher temperatures. However, the lack of data points either side of the transition temperature make any difference trends either side of this point difficult to discern.

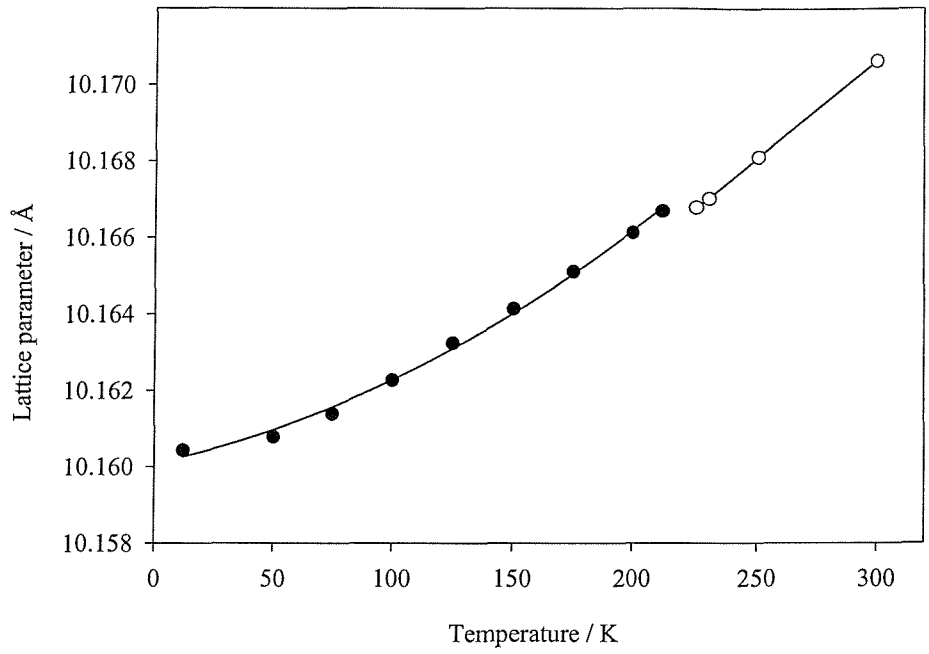

Figure 3.8. Variation of the cubic lattice parameter of $Cd_2Os_2O_7$ between 12 and 298 K. Error bars on the lattice parameter values are within the marker dimensions.

In terms of the structural parameters only one position is refineable in the pyrochlore structural model, the O1 *x* co-ordinate; for a value of 0.3125 this produces perfect MO_6 octahedra. The refined value in $Cd_2Os_2O_7$ is around 0.320-0.321 which represents a small trigonal distortion of this unit producing bond angles around osmium of approximately 93° (× 3) and 87° (× 3). The variation of this oxygen co-ordinate as a function of temperature is plotted in Figure 3.9 and shows a general decrease with increasing temperature.

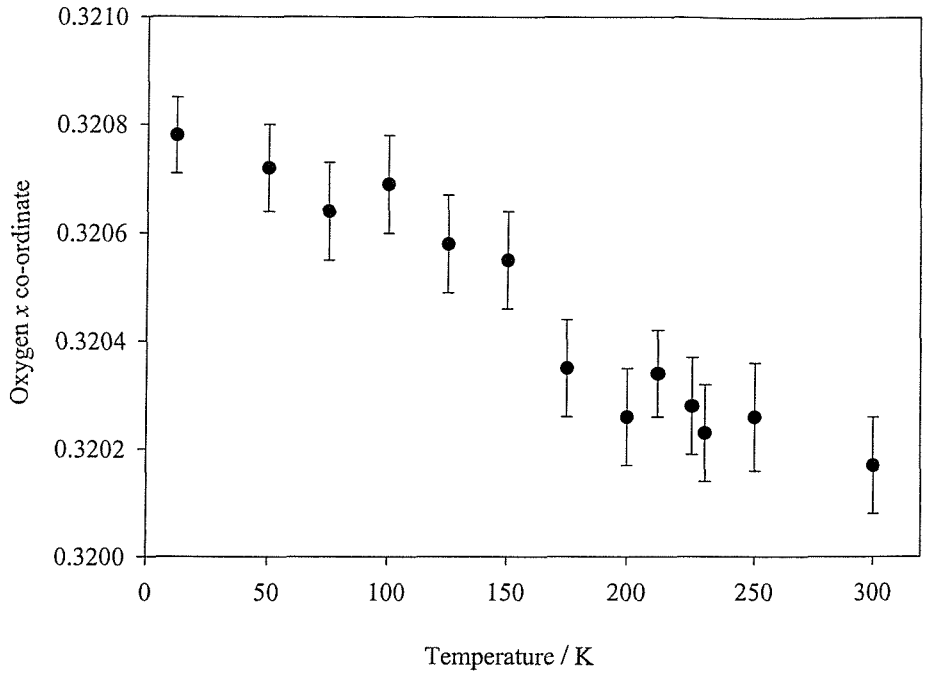

Figure 3.9. Variation of the O1 *x* co-ordinate for $Cd_2Os_2O_7$ between 12 and 298 K.

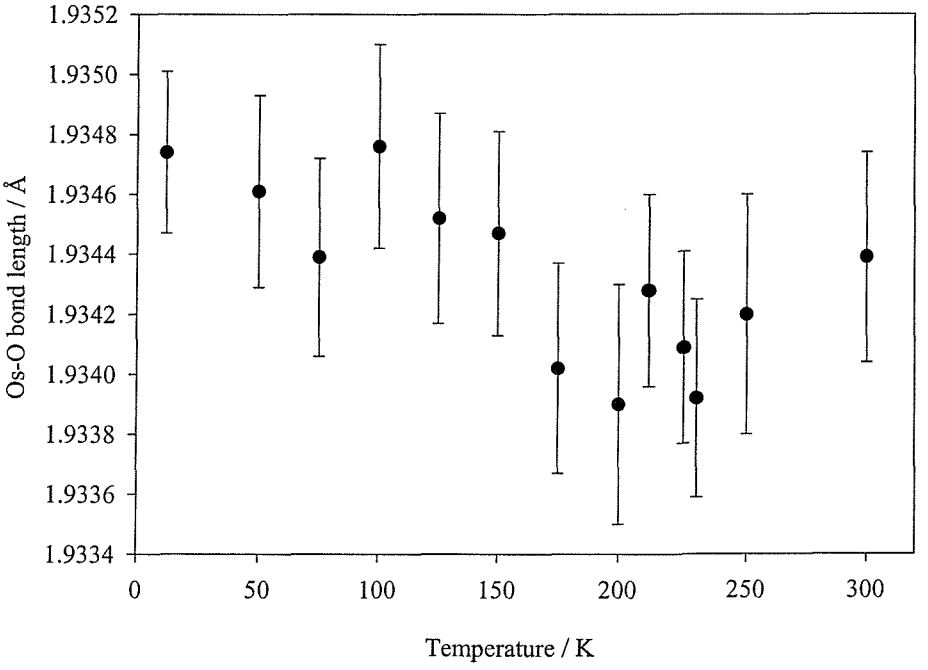

Figure 3.10. Variation of the derived Os-O distance for $Cd_2Os_2O_7$ as a function of temperature between 12 and 298 K.

Coupling the change in this oxygen position with the increasing lattice parameter produces the variations in Os-O bond length in the OsO_6 octahedron seen in Figure 3.10 and the inter-OsO_6 octahedral angle in Figure 3.11. At the same time the OsO_6 octahedra become more regular as shown in Figure 3.12 and the Cd-O distances increase, Figure 3.13. The overall effect is an unusual, but marked, decrease in the Os-O bond length with increasing temperature (up to the semiconductor to metal transition) associated with an increasing angle between the linked polyhedra. This decrease in bond length is most marked between 125 K and 220 K, *i.e.* prior to but not at the semiconductor to metal transition temperature; the plateauing of the lattice parameter at 225 K (Figure 3.8) has little direct effect on the Os-O bond length (effectively leading to a reduction of less than 0.0002 Å) compared with the overall contraction of over 0.001 Å seen between 12 and 200 K. Above 225 K the Os-O distance starts to increase as would be expected from thermal expansion considerations.

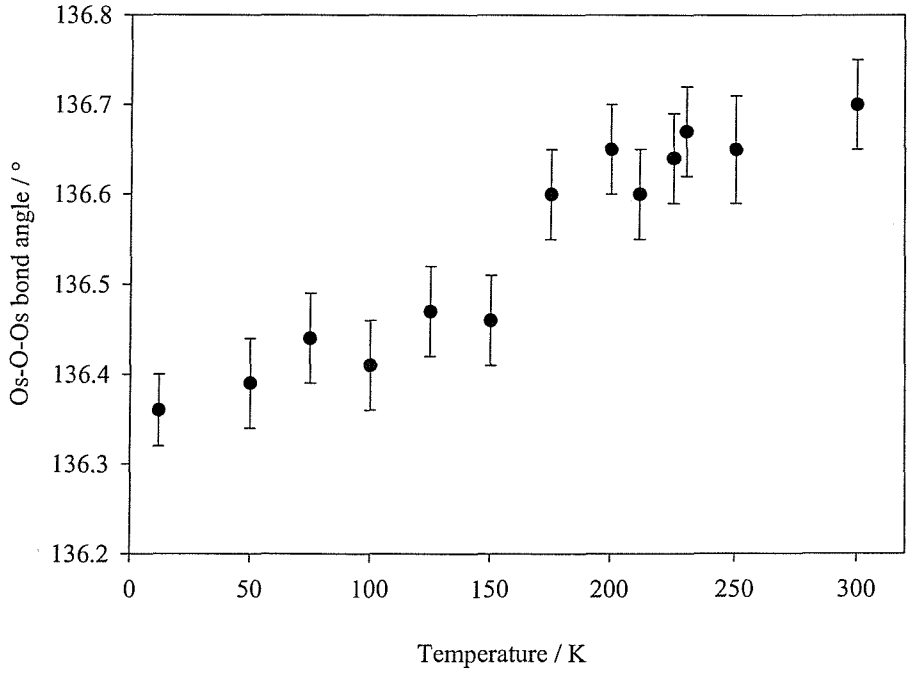

Figure 3.11. Variation of the derived Os-O-Os angle for $Cd_2Os_2O_7$ as a function of temperature between 12 and 298 K.

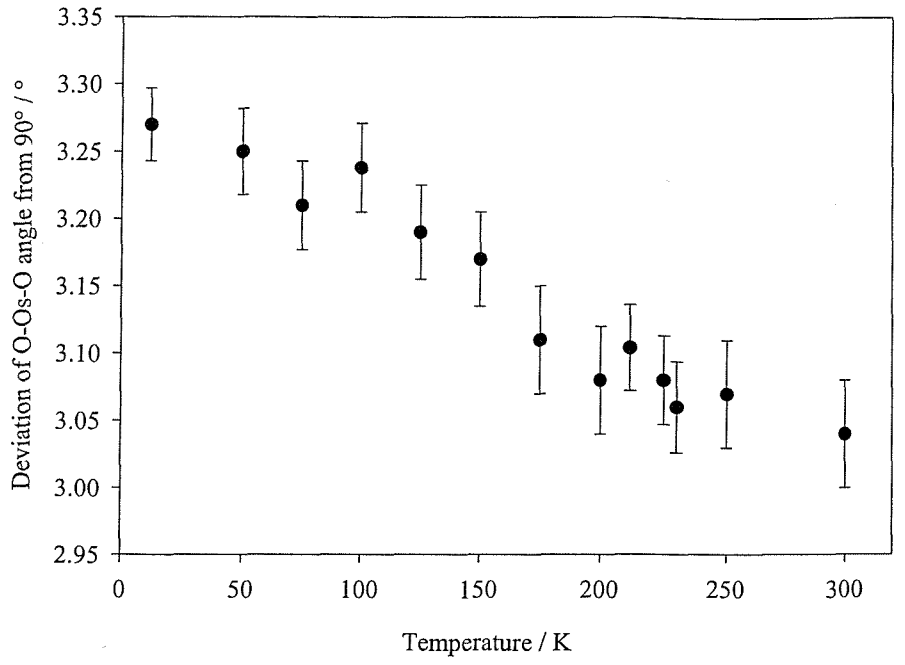

Figure 3.12. Variation of the deviation of the O-Os-O angle from 90° for $Cd_2Os_2O_7$ as a function of temperature between 12 and 298 K.

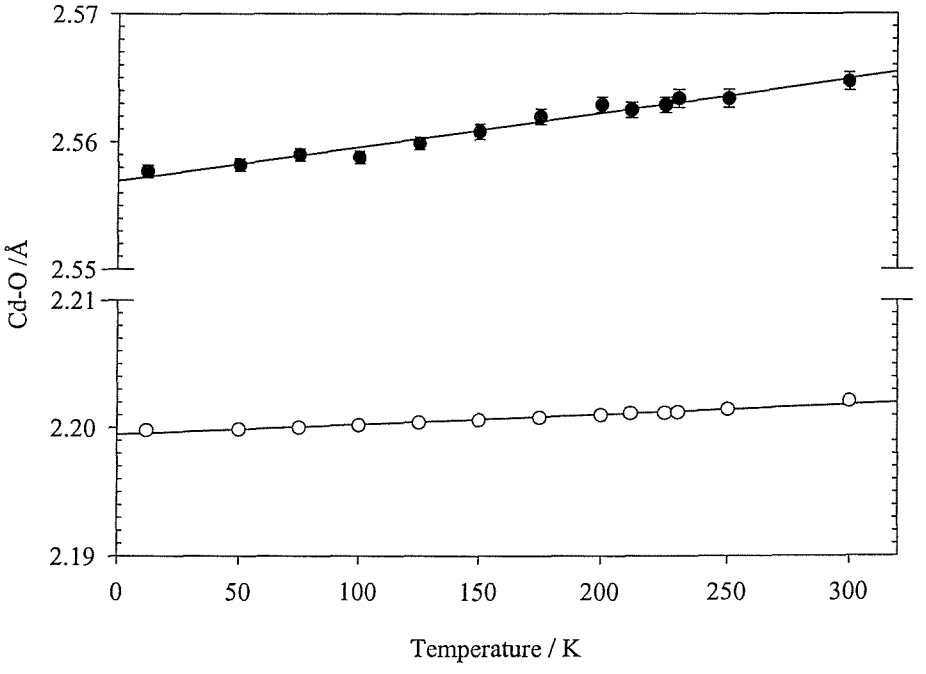

Figure 3.13. Variation of the Cd-O1 (upper) and Cd-O2 (lower) distances of $Cd_2Os_2O_7$ as a function of temperature between 12 and 298 K.

The evolution of displacement parameters with temperature for the four sites is shown in Figure 3.14. The behaviours observed are typical for the pyrochlore structure with notably larger thermal parameters for the "channel" cation, Cd, which may reflect some slight positional disorder. For all sites a smooth increase is seen throughout the temperature range and any variations near T_{MI} are less than the esds. A slightly anomalous value was obtained for the cadmium site at room temperature, which may be derived from the fact that this point was obtained prior to the sample cooling and heating cycle.

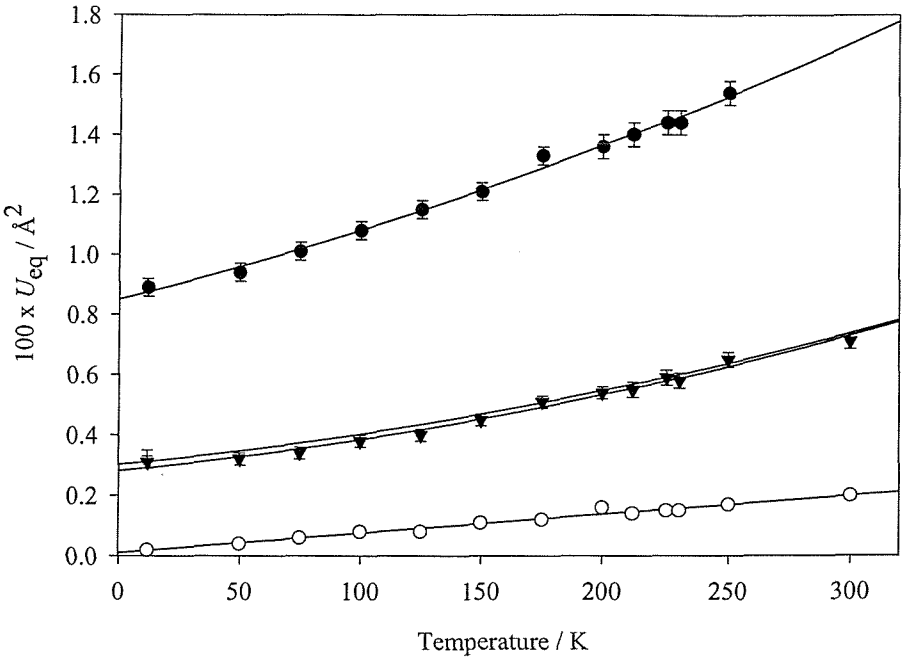

Figure 3.14. Evolution of the thermal parameters of $Cd_2Os_2O_7$ for the individual atom sites between 12 and 298 K.

Careful inspection of the data from the large d-spacing collected in the A Bank on POLARIS, Figure 3.15, showed that no additional peaks appeared on cooling below 225 K, the antiferromagnetic ordering temperature observed in the magnetic measurements. This demonstrates that the magnetic ordering is not long range in nature but must occur locally in the pyrochlore structure. In view of results on other pyrochlores, for example the $R_2Mo_2O_7$ systems[3,4], this is not surprising as frustrated magnetic behaviour and the formation of spin glass structures for these materials is common. In $Y_2Mo_2O_7$ no magnetic scattering is observed below the spin glass transition temperature, a feature that the authors attribute to the small magnetic moment on Mo^{4+}. Even where larger magnetic moments are present, e.g. $Tb_2Mo_2O_7$, the magnetic scattering is extremely broad and diffuse and associated with short range antiferromagnetic interactions. The absence of magnetic reflections in the powder pattern of $Cd_2Os_2O_7$, which demands the presence of long range three dimensional magnetic order, is thus not unexpected.

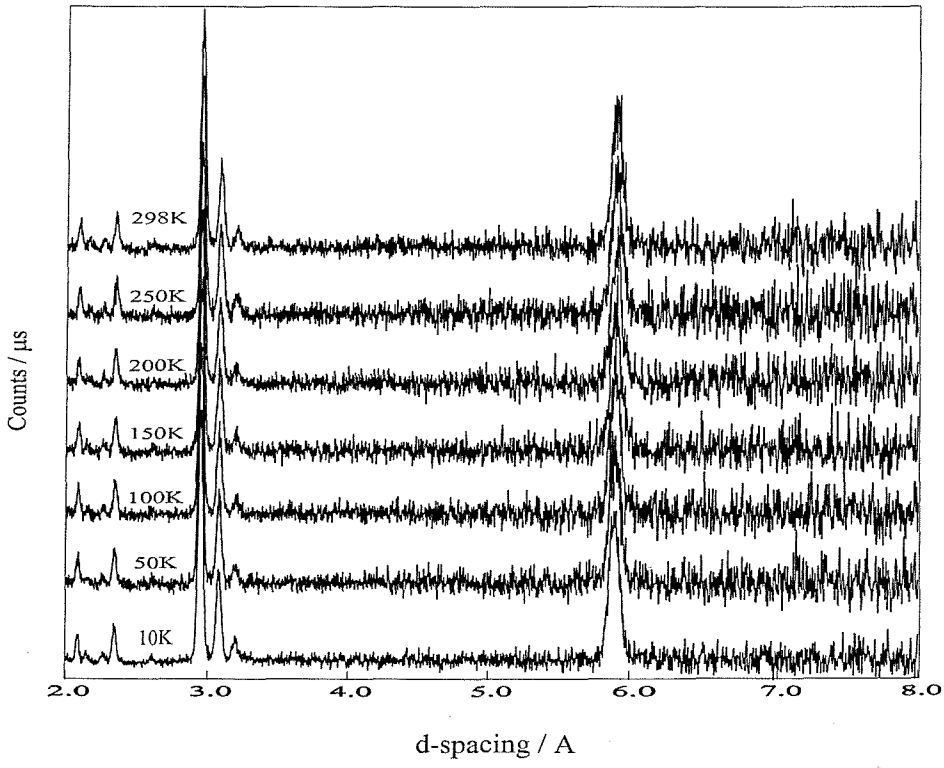

Figure 3.15. Large *d*-spacing data, 2.0 Å ≤ *d* ≤ 8 Å, from $Cd_2Os_2O_7$ plotted at approximately 50 K intervals between 12 and 298 K, showing no evidence of magnetic reflections.

3.7.2 $Hg_2Os_2O_7$

Time of flight (TOF) powder neutron diffraction data were collected on the GEM and POLARIS diffractometers at the Rutherford Appleton Laboratory, Oxfordshire, U.K. The experiment was carried out using a closed cycle refrigeration (CCR) system at a series of temperatures, ranging from 12 K to room temperature. Data were collected for periods between 60 and 135 minutes at each temperature; the shorter times being used for the higher flux GEM instrument. The room temperature data set was collected initially followed by cooling to 12 K and staged heating back to 50 K (POLARIS) or cooling to 70 K and staged heating back to room temperature (GEM). The lower temperature data were collected on POLARIS due to problems in reaching and maintaining temperature stability using existing cryoloop equipment on GEM. No additional reflection was observed in the data collected at the lowest temperatures indicating that no long range magnetic ordering occurs in this material.

Rietveld refinement of structure was undertaken using GSAS[11] and used the cubic pyrochlore model in the space group *Fd-3m* together with the accepted neutron scattering lengths[17]. For the structure refinements using the POLARIS data only the back-scattering bank was used, for the GEM data all four banks were used. A uniform approach to the structure refinement was undertaken for each of the data sets obtained at different temperatures to ensure consistent results. Cell parameters, peak shape parameters, atomic positions and isotropic temperature factors were sequentially added to the refinement. No evidence of fractional site occupancies was observed. For each data set the refinement converged smoothly; Figures 3.16 and 3.17 show the (typical) fit obtained to the room temperature data from GEM. Derived lattice parameters, atomic co-ordinates, displacement factors ($100U_{eq}$/ Å^2) and profile fit parameters at each temperature are summarised in Table 3.4 together with the crystallographic description of the structure. Fit parameters and χ^2 values show behaviour in line with the data collection times.

Table 3.4. Summary of derived atomic, thermal and profile fit parameters for $Hg_2Os_2O_7$ as a function of temperature; *esds* are given in the parentheses. Space group Fd $\bar{3}$m. Hg on (½,½,½), Os on (0,0,0), O1 on (x,⅛,⅛) and O2 on (⅜,⅜,⅜).

T / K	a / Å	O1 x	Hg U_{eq} × 100 / Å^2	Os U_{eq} × 100 / Å^2	O1 U_{eq} × 100 / Å^2	O2 U_{eq} × 100 / Å^2	Rwp (%)	Rp(%)	χ^2
12$^{\phi}$	10.23469(3)	0.31736(6)	0.111(5)	0.112(6)	0.382(6)	0.38(2)	1.98	5.18	2.56
25$^{\phi}$	10.23486(3)	0.31729(6)	0.118(6)	0.139(7)	0.387(6)	0.43(2)	2.50	7.44	1.44
50$^{\phi}$	10.23519(3)	0.31731(6)	0.157(6)	0.129(7)	0.394(6)	0.43(2)	2.38	7.49	1.32
70	10.23563(3)	0.31736(6)	0.078(6)	0.003(6)	0.264(6)	0.35(2)	4.39	3.63	4.54
75	10.23580(3)	0.31731(6)	0.095(6)	0.008(6)	0.271(6)	0.38(2)	4.31	3.58	4.37
80	10.23592(3)	0.31727(6)	0.107(6)	0.008(6)	0.282(6)	0.38(2)	4.32	3.66	4.41
85	10.23608(3)	0.31735(6)	0.109(6)	0.014(6)	0.277(6)	0.39(2)	4.24	3.59	4.23
90	10.23615(3)	0.31736(6)	0.115(6)	0.016(6)	0.281(6)	0.39(2)	4.28	3.57	4.31
95	10.23629(3)	0.31725(6)	0.115(6)	0.013(6)	0.279(6)	0.39(2)	4.25	3.56	4.24
100	10.23640(3)	0.31727(6)	0.124(6)	0.016(7)	0.286(6)	0.40(2)	4.29	3.62	4.35
110	10.23658(3)	0.31727(6)	0.125(6)	0.025(6)	0.297(6)	0.40(2)	4.21	3.59	4.16
130	10.23701(3)	0.31731(6)	0.141(6)	0.026(6)	0.298(6)	0.42(2)	4.20	3.55	4.14
160	10.23790(3)	0.31710(6)	0.176(7)	0.037(7)	0.318(6)	0.46(2)	4.16	3.50	4.10
200	10.23961(3)	0.31710(5)	0.232(7)	0.063(7)	0.367(6)	0.55(2)	4.06	3.46	3.91
250	10.24258(3)	0.31701(7)	0.320(8)	0.102(7)	0.434(6)	0.68(2)	3.86	3.31	3.54
300	10.24681(3)	0.31686(7)	0.429(9)	0.142(8)	0.524(6)	0.81(2)	3.83	3.36	3.53

$^{\phi}$POLARIS data

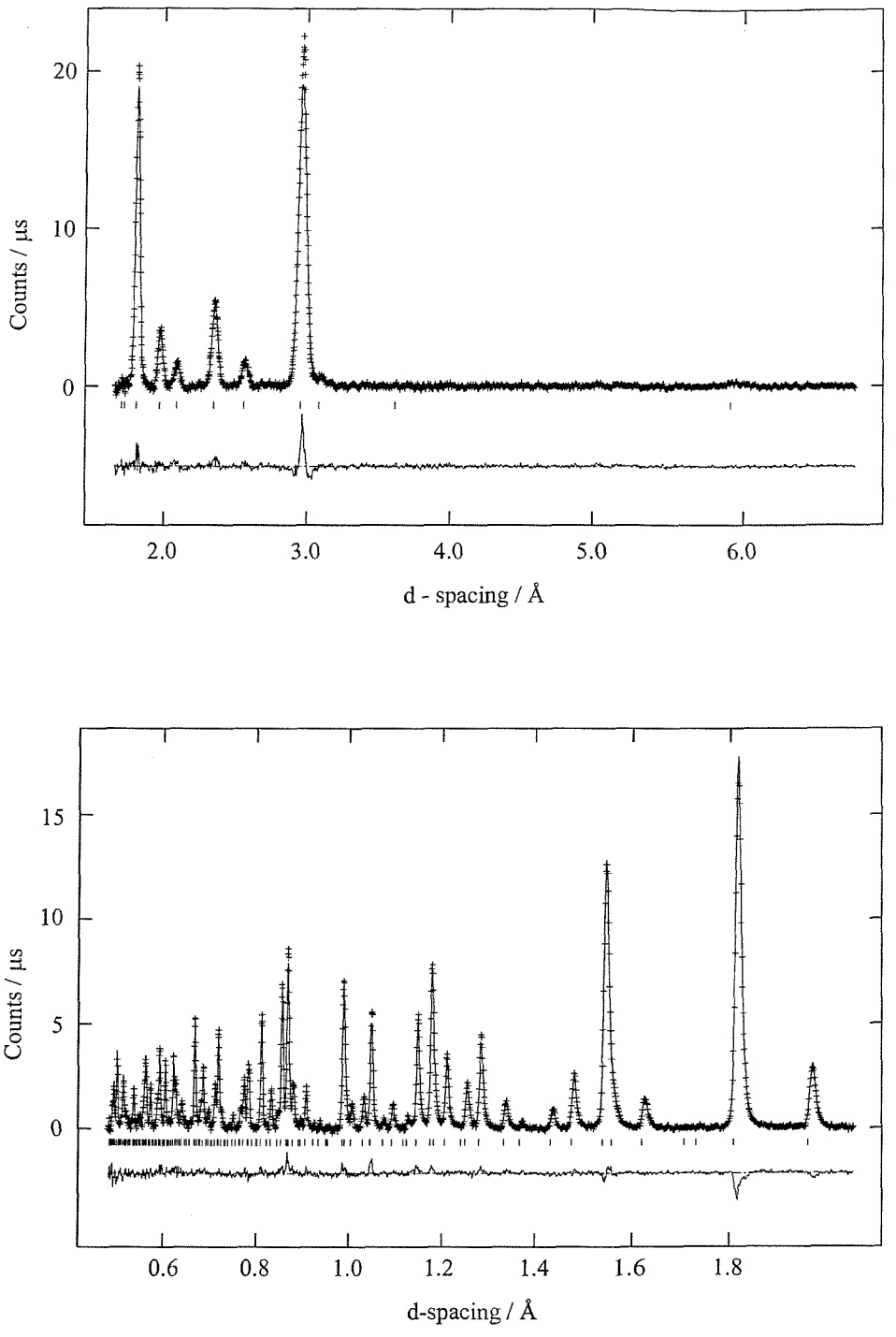

Figure 3.16. Fits obtained to the powder neutron diffraction data at room temperature for $Hg_2Os_2O_7$. Data from the 18 and 64° banks are shown in terms of *d*-spacing, from top to bottom.

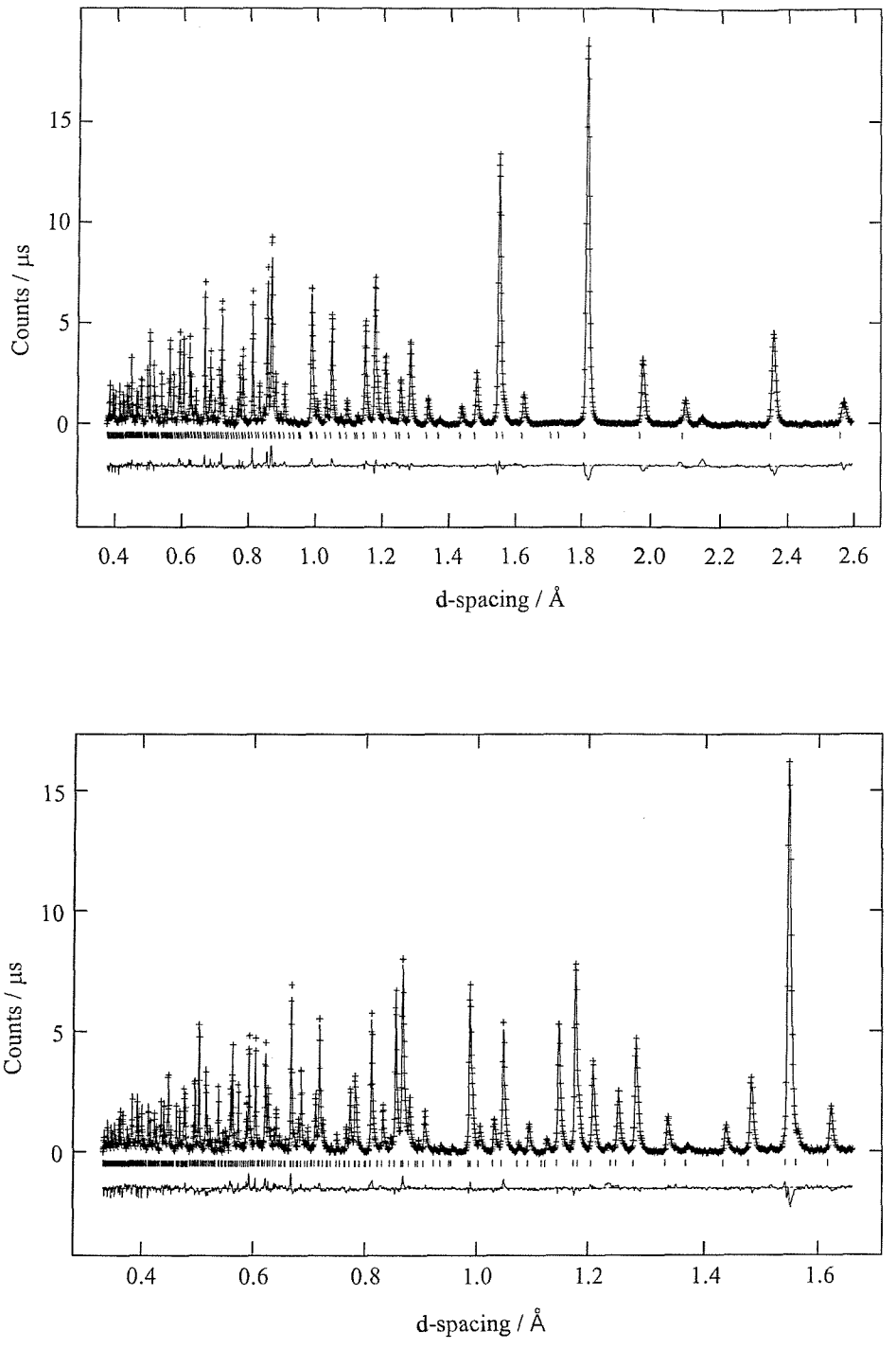

Figure 3.17. Fits obtained to the powder neutron diffraction data at room temperature for $Hg_2Os_2O_7$. Data from the 91 and 154° banks are shown in terms of *d*-spacing, from top to bottom.

The variation of the lattice parameter of $Hg_2Os_2O_7$ between 12 K and room temperature is shown in Figure 3.18. Normal expansion of a complex oxide would generally result in a close to linear increase in cell parameter as a function of temperature, with a less rapid decrease as the sample temperature approaches 0 K. The data show somewhat anomalous behaviour at around 85 – 90 K, Figure 3.18 inset, which shows almost no increase in lattice parameter between these temperatures. Below 80 K and between 90 and 200 K the lattice parameter increases approximately linearly at around 1.5×10^{-5} $ÅK^{-1}$. The very small inflection seen between 85 and 90 K might be associated with the weak antiferromagnetic transition observed at 88 K.

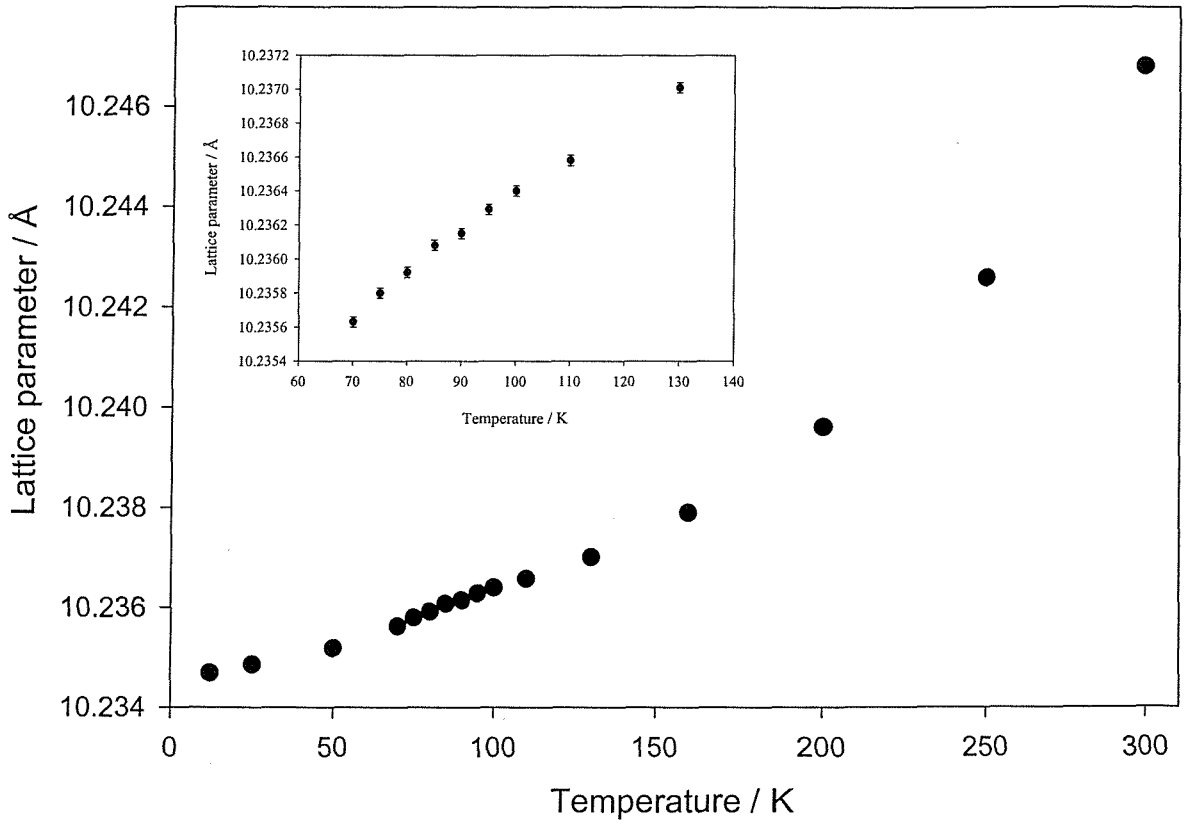

Figure 3.18. The variation of the lattice parameter of $Hg_2Os_2O_7$ as a function of temperature between 12 and 298 K. The inset expands the region between 70 and 130 K. Error bars are shown but in the main graph are within the plotted symbol dimensions.

With respect to structural parameters, like $Cd_2Os_2O_7$, only one atomic position is refinable in the pyrochlore model, the O1 x co-ordinate. A value of 0.3125 would produce perfect MO_6 octahedra. The refined value in $Hg_2Os_2O_7$ is around 0.317 which represents a small trigonal distortion of this unit producing bond angles around osmium of approximately 91.9° (×3) and 88.1° (×3). The variation of this oxygen co-ordinate as a function of temperature is plotted in Figure 3.19 and shows a steady value up to around 130 K before a significant decrease with increasing temperature. Coupling the change in this oxygen position with the increasing lattice parameter produces the variations in Os-O bond length in the OsO_6 octahedron seen in Figure 3.20 and the internal O-Os-O octahedral angle shown in Figure 3.21.

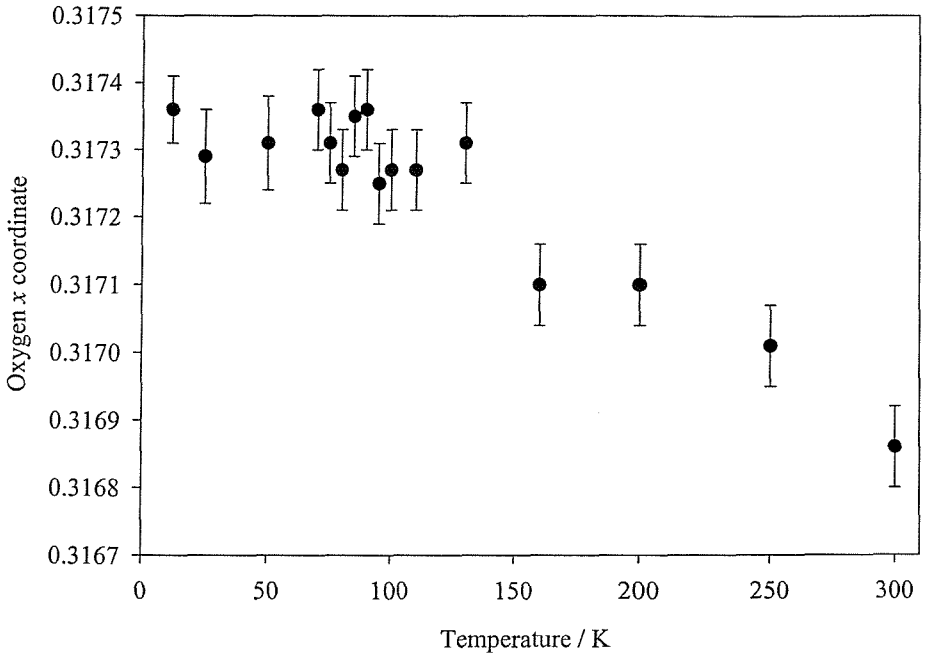

Figure 3.19. Variation of the O1 x co-ordinate for $Hg_2Os_2O_7$ between 12 and 298 K.

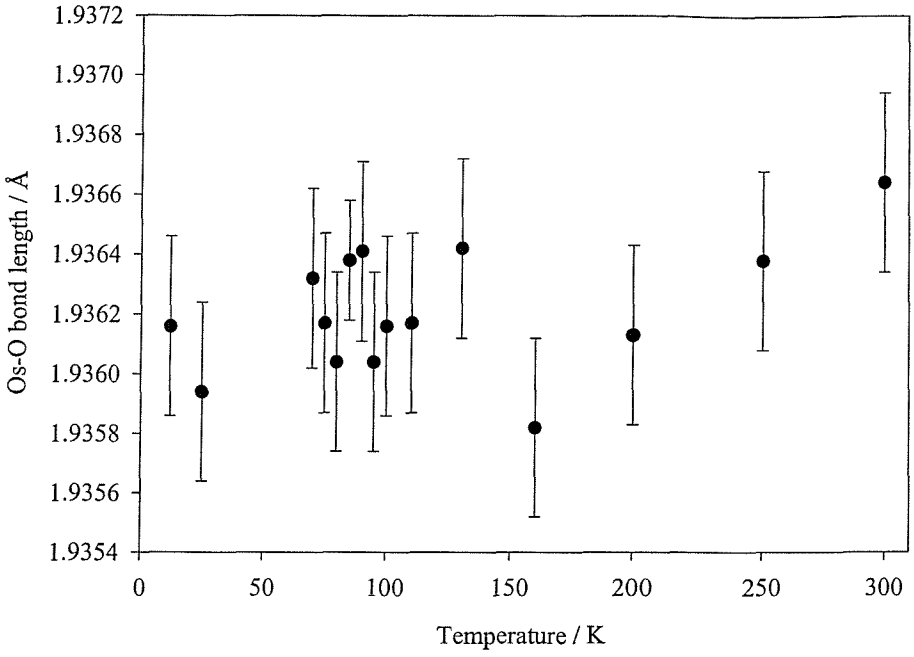

Figure 3.20. Variation of the derived Os-O distance for $Hg_2Os_2O_7$ as a function of temperature between 12 and 298 K.

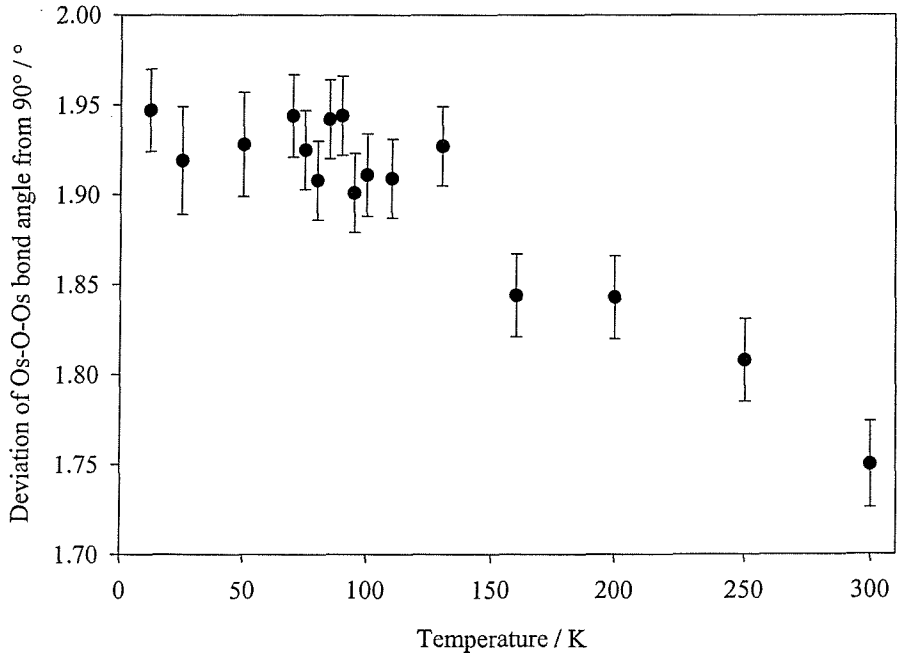

Figure 3.21. Variation of the deviation of the O-Os-O angle from 90° for $Hg_2Os_2O_7$ as a function of temperature between 12 and 298 K.

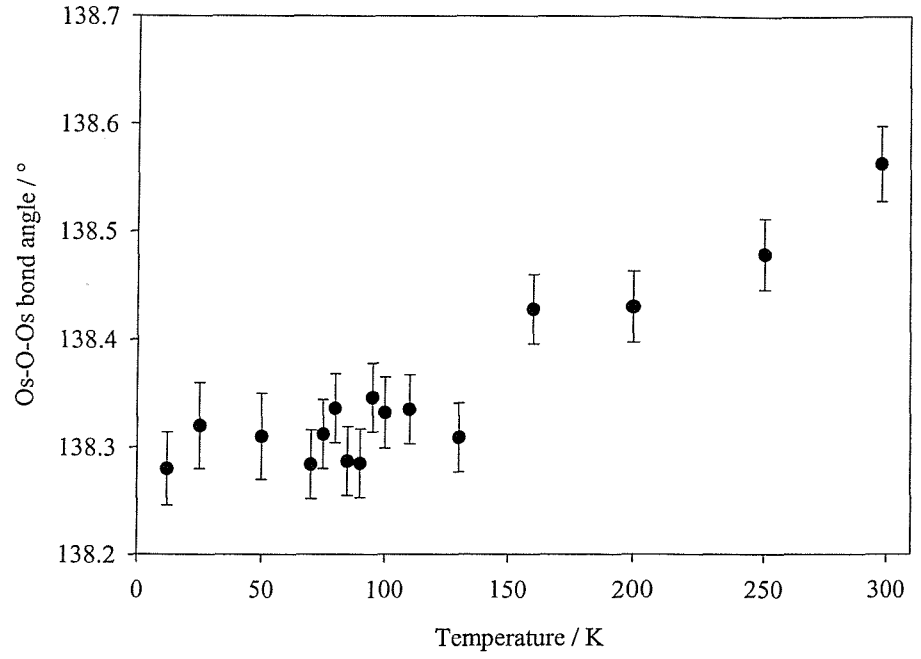

Figure 3.22. Variation of the derived Os-O-Os angle for $Hg_2Os_2O_7$ as a function of temperature between 12 and 298 K.

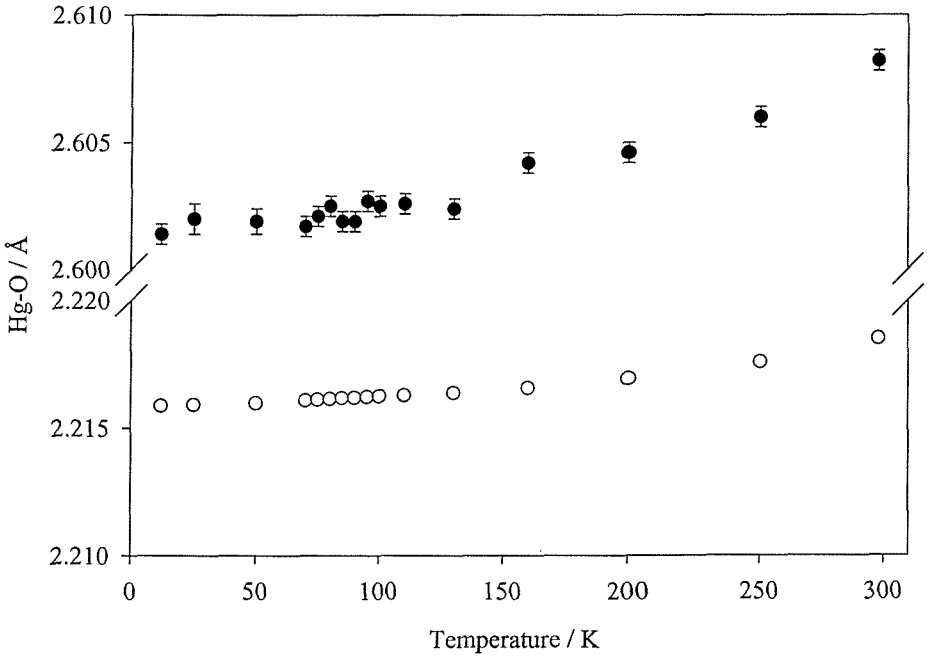

Figure 3.23. Variation of the Hg-O1 (upper) and Hg-O2 (lower) distances of $Hg_2Os_2O_7$ as a function of temperature between 12 and 298 K.

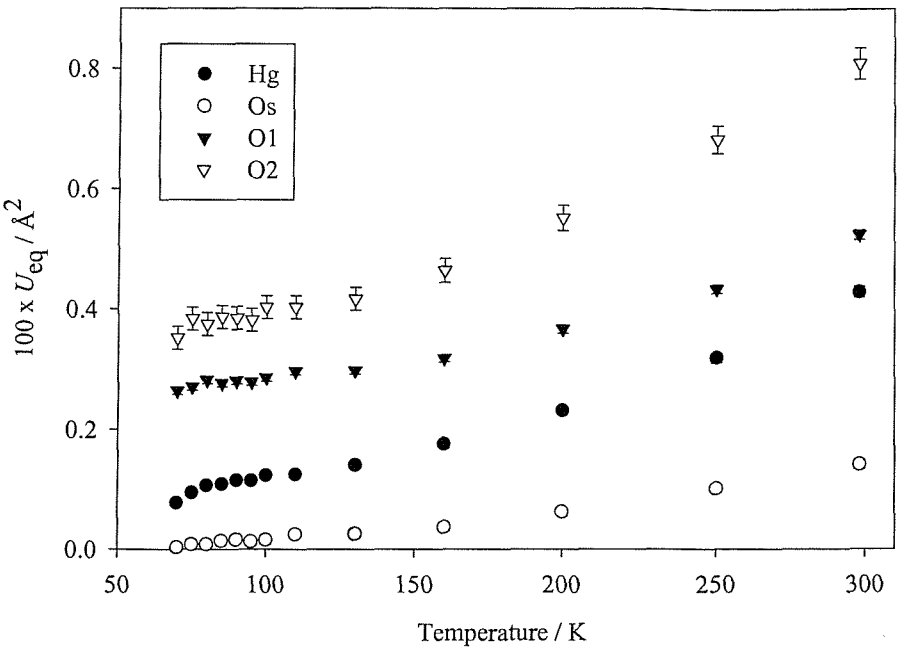

Figure 3.24. Evolution of the thermal parameters of $Hg_2Os_2O_7$ for the individual atom sites between 12 and 298 K.

The normal behaviour of structures built from MO_6 octahedra would be a smooth increase in metal oxygen bond lengths as the structure expands, associated with the formation of more regular octahedra. The data here is abnormal in terms of totally static behaviour below 130 K before the structural parameters show the normal manifestations of expansion. At the same time the inter OsO_6 octahedra angle become more regular as shown in Figure 3.22 and the Hg-O distances increase, Figure 3.23. The Os-O bond length is similar to that found in $Cd_2Os_2O_7$ consistent with the description of this material as containing Os (V).

The variations of the individual thermal parameters are shown in Figure 3.24. As the data from the lowest three temperatures, 12, 25 and 50 K, were collected on POLARIS they are not shown on these graphs; due to the different instrument parameters, sample size and mounting, small differences are expected from different instruments. The data from POLARIS show similar trends to that from GEM, as shown in Table 3.4, but displaced to higher U_{eq} values by typically 0.0012 Å^2. For each atom the variation of thermal displacement parameters shows similar behaviour with the expected increase with

temperature. Some evidence is apparent of a levelling off in each case between 80 and 100 K but the significance of this, in terms of the sizes of the *esds* on thermal displacement parameters, may not be high.

Careful inspection of the data from the large d-spacing collected in the 18° Bank on GEM, Figure 3.16 (upper), showed that no additional peaks appeared on cooling below 88 K, the antiferromagnetic ordering temperature observed in the magnetic measurements. This demonstrates that the magnetic ordering is not long range in nature but must occur locally in the pyrochlore structure. This is certainly due to magnetic frustration also present for the $Cd_2Os_2O_7$ material.

3.8 Conclusions

The transition from semiconducting to metallic behaviour in $Cd_2Os_2O_7$ at 225 K is marked by a small but distinct inflection in the cell parameter, which is reduced with respect to that expected from linear thermal expansion. In terms of structural parameters the second order nature of the transition is represented by a slow decrease in the Os-O distance up to 225 K with thermal expansion thereafter. Presumably the increasing stresses in the system as the osmium to oxygen distances contract and the band gap decreases are relieved suddenly at 225 K with a large drop in resistivity and break in the lattice parameter expansion. Kennedy[2] has investigated structural trends in some Ru and Ir pyrochlores and discussed the results in terms of their electronic structures. The ruthenate pyrochlores can be divided into two classes in respect of their electronic properties in that the Ru-O distances in the metallic ruthenates are lower than those expected on the basis of their lattice parameters and 'A' cation size in comparison with the semiconducting materials. This behaviour has been explained in terms of electron transfer from the 4d bands of ruthenium to the 6s bands of the 'A' type cation in the metallic regime. Such explanations accord with the behaviour observed in this work on $Cd_2Os_2O_7$. The narrowing and disappearance of the band gap between the Os 5d and Cd 5s on approaching T_{MI}, involves transfer of electrons from osmium or, in simple chemical terms, oxidation of Os and reduction of Cd. This leads to the unusual observed decrease in the Os-O distances and increase in the Cd-O distances as T_{MI} is approached (Figures 3.10 and 3.13). The antiferromagnetic ordering below 225 K is

localised in nature and does not lead to any magnetic reflections in the diffraction profile above 12 K.

This structural, electronic and magnetic behaviour of $Hg_2Os_2O_7$ shows some similarities with that of $Cd_2Os_2O_7$ but in each case the magnitude of any variations are far less marked. In terms of anti-ferromagnetic ordering this occurs at a much lower temperature, 88 K, than in the cadmium compound. As in the cadmium system anomalous behaviour in the Os-O distances for $Hg_2Os_2O_7$ is seen on approaching the transition temperature from below though, possibly because of the lower ordering temperature this variation is only weakly discernible. Neutron diffraction methods are required to observe these changes with any accuracy but the normal increase in metal oxygen bond lengths on heating a material is not observed. This may be coupled with subtle changes in the electron distributions, which seem to occur below about 100 K in $Hg_2Os_2O_7$. The non-appearance of magnetic reflections in the low temperature neutron diffraction data, supports the view that the antiferromagnetic ordering is frustrated and has no long range order.

Clearly however there are marked differences in the electronic properties of these two osmate pyrochlore materials with $Hg_2Os_2O_7$ remaining semi-metallic down to 4K in behaviour similar to that of $Cd_2Re_2O_7$. The origin of these differences will require more detailed calculations on the band structure of $Hg_2Os_2O_7$. However Mandrus *et al*[8] note that the Cd states have a presence at the Fermi level of $Cd_2Os_2O_7$ so that hybridisation between the osmium-oxygen and cadmium oxygen levels is probably important in defining the electronic properties of this material. Hence replacement of cadmium by mercury can clearly be expected to modify the electronic behaviour quite markedly. An alternative explanation might lie in material non-stoichiometry as has been proposed for the difference between $Cd_2Re_2O_7$ and $Cd_2Os_2O_7$ with the former possibly being off-stoichiometry. However any such deviation must be small and no significant discrepancy in Hg site occupancy could be refined for $Hg_2Os_2O_7$ in this work.

3.9 References

[1] M. A. Subramanian, G. Aravamudan, G. V. Subba Rao, *Prog. Solid State Chem.* **15**(2) 55 (1983).

[2] B. J. Kennedy, *Physica B* **241-243** 303 (1998).

[3] J. E. Greedan, J.N.Reimers, C.V.Stager and S.L.Penny, *Phys. Rev. B* **43** 5682 (1991).

[4] B. D. Gaulin, J. S. Gardner, S. R. Dunsiger, Z. Tun, M. D. Lumsden, R. F. Kiefl, N. P. Raju, J. N. Reimers and J. E. Greedan. *Physica B* **241-243** 511 (1998).

[5] Y.Shimakawa, Y.Kubo, T.Mnako, Y.V.Sushko, D.N.Argyriou and J.D.Jorgensen, *Phys. Rev. B* **55** 6399 (1997).

[6] M.A.Subramanian, B.H.Toby, A.P.Ramirez, W.J.Marshall, A.W.Sleight and G.H.Kewi, *Science* **273** 81 (1996).

[7] A. W. Sleight, J. L. Gillson, J. F. Weiher and W. Bindloss, *Solid State Comm.* **14** 357 (1974).

[8] F.Abraham, J. Trehoux and D. Thomas, *Journal of Inorganic and Nuclear Chemistry* **42** 1627 (1980).

[9] R. D. Shannon, *Acta Cryst.* **A32** 751 (1976).

[10] A. W. Sleight, *Inorganic Chemistry* **7**(9) 1704 (1968).

[11] A. C. Larson and R. B. Von Dreele, *Generalsied Structure and Analysis System,* MS-H805, Los Almos, NM 87545 (1990).

[12] D. Mandrus, J. R. Thompson, R. Gaal, L. Forro, J. C. Bryan, B. C. Chakoumakos, L. M. Woods, B. C. Sales, R. S. Fishman and V. Keppens, *Phys. Rev. B* **63** 195104 (2001).

[13] J. E. Greedan, J. N. Reimers, C. V. Stager and S. L. Penny, *Phys. Rev. B* **43** 5682 (1991).

[14] J. E. Greedan, *J. Mater. Chem.* **11** 37 (2001).

[15] H. Sakai, K Yoshimura, H. Ohno, H. Kato, S. Kambe, R.E. Walstedt, D.T. Matsuda,Y. Haga, Y. Onuki, *J. Phys.: Condens. Matter* **13** L785 (2001).

[16] R. Wang and A. Sleight, *Mater. Res. Bull.* **33** 1005 (1998).

[17] *Neutron News* **3** 29 (1992).

[18] J. Rodríguez-Carvajal, S. Rosenkranz, M. Medarde, P. Lacorre, M. T. Fernandez-Díaz, F. Fauth and V. Trounov, *Phys. Rev. B* **57** 456 (1998).

[19] P. F. Henry and M. T. Weller, *MRS Symposium Proceedings* **658** GG 3.31 (2001).

[20] P. F. Henry and M. T. Weller, *Chem. Mater.* **14**(10) 4104 (2002).

Chapter Four

The Synthesis, Structure and Physical Properties of Calcium (V) Osmate

4.1 Introduction

Pyrochlores containing the 2nd and 3rd row transition metals have recently become of considerable interest due to the unusual electronic, ionic and magnetic properties they exhibit[1]. Examples include the molybdate (IV) pyrochlores of the type $Ln_2Mo_2O_7$ which have been shown to be excellent mixed ionic/electronic conductors[2,3] and the thallium ruthenates $Tl_{2-x}Ru_{2-y}O_{7-z}$, studied in detail by Takeda *et al*[4]. The ruthenates exhibit complex electronic and structural behaviour, in this case dependent on composition, including metal-insulator transitions and magnetoresistive properties. The unusual oxidation state (in the solid state) Re(V) may be obtained in the oxide pyrochlore structure within $Cd_2Re_2O_7$; this compound shows a number of complex electronic and structural behaviours culminating with a transition to superconducting behaviour below 1.4 K[5].

The weberite structure, also adopted by some materials of the stoichiometry $A_2B_2O_7$, e.g. $Sr_2Sb_2O_7$[6] is closely related to the pyrochlore structure in that the 'B' type cations adopt octahedral co-ordination to oxygen but in this structure, only half the octahedra have all vertices linked to neighbouring BO_6 units, the remainder are linked through four vertices only (Figure 4.1). The two different 'A' cation environments still involve co-ordination to eight oxide ions which are best described in both cases as strongly distorted cubic; in one case, by contraction along a C_4 axis producing 4+4 co-ordination and in the other, by contraction along a C_3 axis producing hexagonal bipyramidal co-ordination.

The behaviour of $A_2Sb_2O_7$ phases as a function of 'A' and adoption of pyrochlore or weberite structure has been studied in detail by Knop[7]. For this system $Ca_2Sb_2O_7$ lies at the borderline of phase stability occurring as pyrochlore or weberite depending on the pressure used during phase formation, with high pressures favouring pyrochlore formation. For 'A' = Cd the pyrochlore structure readily forms, indicating that increased covalency in the A-O bond promotes the pyrochlore arrangement.

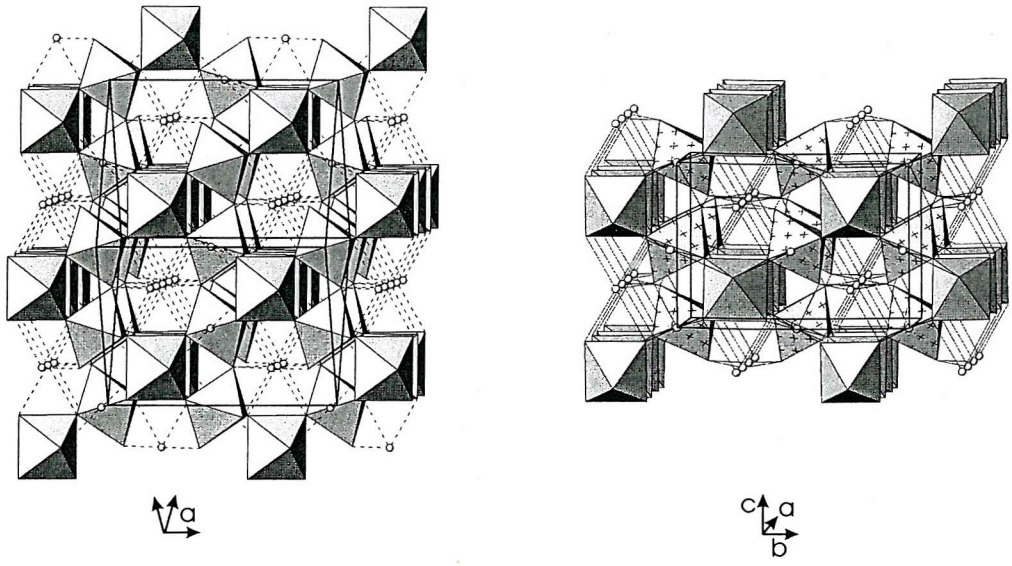

Figure 4.1. The two related structures adopted by materials of the stoichiometry $A_2B_2O_7$. The pyrochlore (left) and the weberite (right) shown as linked OsO_6 octahedra with the 'A' cation co-ordination shown as lines.

While $(A_2^{2+}B_2^{5+})O_7$ systems have been studied in detail for 'B' = Sb, Nb, Ta, osmium (V) systems have been less well studied with the exception of $A_2Os_2O_7$, 'A' = Cd, Hg[8 to 11]. $Cd_2Os_2O_7$ undergoes a Slater-like transition at 225 K with minor changes in structure which also lead to a ferromagnetic state. Recently reported, $Hg_2Os_2O_7$, shows weaker electronic and magnetic transitions near 88 K[11]. Calcium osmate pyrochlores have also been reported in the literature though there is a great deal of confusion over the stoichiometry, structure and properties of these compounds. Both Chamberland[12,13] and Shaplygin[14,15] have reported formation of a stoichiometric phase of the composition $Ca_2Os_2O_7$ though differing routes. Decomposition of $CaOs(OH)_6$ leads to a cubic phase while direct reaction of CaO and OsO_2 at 1000 °C results to a tetragonal phase with lattice parameters 10.12 Å and 10.69 Å. An orthorhombic phase, of undetermined stoichiometry and purity, can also be obtained by thermal decomposition of $CaOsO_3$[14]. A non-stoichiometric example is also reported with the reaction of CaO and OsO_2 under high pressure which leads to a cubic calcium deficient phase $Ca_{1.7}Os_2O_7$[16].

This chapter reports the synthesis and characterisation of the Os(V) pyrochlore $Ca_2Os_2O_7$ at ambient pressure. The material is preliminary characterised by PXD and Rietveld analysis

of the data is performed to determine structural information. The physical properties of the material are examined by recording variable temperature resistivity and variable temperature infra-red measurements. In addition, the material is fully characterised using PND over a range of four temperatures, from 100 to 400 K, defining any structural changes that occur. Furthermore, comparisons are made to related materials in terms of structural and physical properties.

4.2 Preparation of $Ca_2Os_2O_7$ at Ambient Pressure

A sample of $Ca_2Os_2O_7$ was prepared by grinding together the appropriate stoichiometric mixture of high purity CaO (99+%), Os (99.8%) and OsO_4 (99.95%). CaO was prepared by heating $CaCO_3$ at 1000 °C for 1 week. The stoichiometric mixture was loaded into a silica ampoule and sealed under vacuum; with the end of the ampoule immersed in liquid nitrogen to avoid osmium loss due to the volatility of OsO_4. The sample was fired at 800 °C for 2 days, then furnace cooled to room temperature. Powder x-ray diffraction (PXD) data were recorded and showed traces of unreacted component oxides. The process of resealing the material in a silica ampoule was repeated, which was then placed in a furnace and fired at 1000 °C for 1 day.

PXD data were recorded from the black product using a Siemens D5000 diffractometer operating with Cu $K_{\alpha 1}$ radiation. The result showed a more complex pattern than a cubic pyrochlore, indicative of an orthorhombically distorted cubic unit cell of dimensions similar to a pyrochlore. Comparison of this unit cell to those in the literature for distorted pyrochlores and related phases showed that the data could be indexed on a cell of approximate dimensions 7.3 × 7.5 × 10.2 Å (corresponding roughly to $a_p/\sqrt{2} \times a_p/\sqrt{2} \times a_p$ where a_p is the cubic pyrochlore lattice parameter), which are similar to the values found for $Ca_2Sb_2O_7$, with the weberite structure[7]. Heating the material to 600 °C *in situ* on a Bruker D8 diffractometer using the HTK stage showed that the structure remains orthorhombic to this temperature and does not undergo transformation to the pyrochlore prior to its decomposition that occurs above 700 °C in air.

4.3 PXD Structure Refinements

PXD data were collected over a 2θ range of 20°–120° for a period of 15 hours using a 0.02° step size. Cell parameters were calculated from the d-spacings using the CELL computer program. Using the Rietveld technique, refinement of the data commenced using the computer program GSAS[17]. The refinement was started based on the weberite structure and the co-ordinate description for $Sr_2Sb_2O_7$, given by Groen and Ijdo, with a space group of Imma[6]. Cell parameters, peak shape parameters, atomic positions and isotropic temperature factors were sequentially added to the refinement. The refinement converged smoothly to yield acceptable *R*-factors and accurate cell parameters were determined for the material along with atom positions and derived bond lengths, which are summarised in Tables 4.1 and 4.2. The profile fit achieved for $Ca_2Os_2O_7$ is shown in Figure 4.2.

Table 4.1. Refined atomic co-ordinates for $Ca_2Os_2O_7$. *Esds* are given in the parentheses. Space group Imma: a = 7.1934(5), b = 10.1027(8), c = 7.3512(5) Å. R_{wp} = 2.00 %, R_p = 1.53 %, χ^2 = 0.30.

Atom	x	y	z	$U_{eq} \times 100$ / Å^2
Ca1	0	0	0	1.12(25)
Ca2	0.25	0.25	0.75	1.12(25)
Os1	0.25	0.25	0.25	0.86(13)
Os2	0	0	0.5	0.84(14)
O1	0	0.25	0.170(7)	1.3(17)
O2	0	0.399(3)	0.714(4)	3.1(8)
O3	0.206(3)	0.373(2)	0.417(3)	1.1(7)

Table 4.2. Refined inter-atomic distances for $Ca_2Os_2O_7$. *Esds* are given in the parentheses.

Bond	Length / Å
Ca1-O1 (×2)	2.82(3)
Ca1-O2 (×2)	2.34(3)
Ca1-O3 (×4)	2.55(3)
Ca2-O2 (×4)	2.36(2)
Ca2-O3 (×4)	2.77(3)
Os1-O1 (×2)	1.89(2)
Os1-O3 (×4)	1.77(3)
Os2-O2 (×2)	1.88(3)
Os2-O3 (×4)	2.06(3)

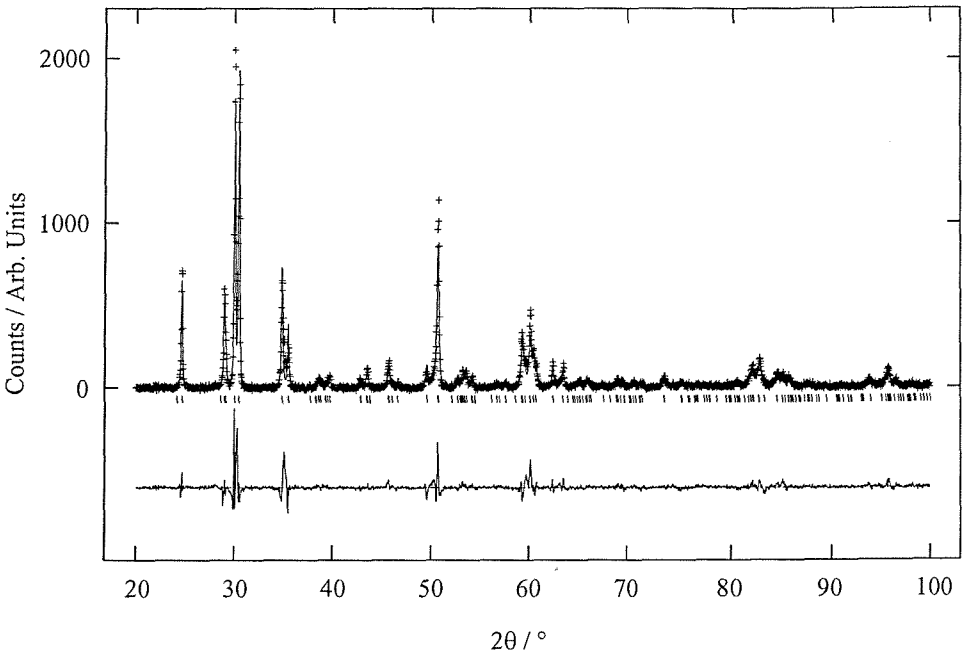

Figure 4.2. Profile fit to PXD data for $Ca_2Os_2O_7$. Experimental data points are shown as crosses, upper continuous line the calculated profile, lower continuous line the difference. Allowed reflection positions for $Ca_2Os_2O_7$ are shown with tick marks.

$Ca_2Os_2O_7$ is found to crystallise in an orthorhombic weberite unit cell, space group Imma, when synthesised under ambient pressure conditions rather than the distorted pyrochlore structures reported previously for this material. The adoption of this structure type presumably results from the electropositivity and co-ordination preferences of calcium as the osmate octahedra are similar in the two structure types, which will be discussed in more detail later in this chapter. The Ca-O and Os-O bond distances have relatively large *esds* associated with them, reflecting the limitations of PXD data and necessitating the use of powder neutron diffraction to enable an accurate structural investigation of this material.

4.4 Variable Temperature Powder Neutron Diffraction

Time of flight (TOF) powder neutron diffraction data were collected on the POLARIS diffractometer at the Rutherford Appleton Laboratory, Oxfordshire, U.K. The experiment was carried out using a closed cycle refrigeration (CCR) system at four temperatures, ranging from 100 to 400 K of which data were collected for 75 minutes at each temperature.

The data collected for $Ca_2Os_2O_7$ at all temperatures were consistent with the adoption of the weberite structure and the previous PXD data collected at room temperature, so this was used as a starting model. Rietveld refinement of structure was undertaken using GSAS[16] using the orthorhombic weberite model in the space group Imma. For these refinements only the back-scattering bank data was used with time-of-flights ranging from 3000 to 19500 μs corresponding to the d-spacing range 0.5 - 3.1 Å. A uniform approach to the structure refinement was undertaken for each of the data sets obtained at different temperatures to ensure consistent results. Cell parameters, peak shape parameters, atomic positions and isotropic temperature factors were sequentially added to the refinement. The fractional occupancies of the oxygen positions were investigated for site deficiency but all values refined to full occupancy within *esds*. Refinement of the osmium site occupancy showed no deviation from unity. For each data set the refinement converged smoothly. Figure 4.3 shows the (typical) fit obtained to the room temperature data. Derived lattice parameters, atomic co-ordinates, displacement factors (100 U_{eq}) and profile fit parameters at each temperature are summarised in Table 4.3 together with the crystallographic description

of the structure. Fit parameters and χ^2 values show behaviour in line with the data collection times.

Table 4.3. Refined structural data for $Ca_2Os_2O_7$ as a function of temperature. Orthorhombic, space group Imma. Ca1 on (0,0,0), Ca2 on (¼, ¼,¾), Os1 on (¼,¼,¼), Os2 on (0,0,½), O1 on (0, ¼, z), O2 on (0,y,z) and O3 on (x,y,z). *Esds* are given in the parentheses.

	Temperature / K			
	100	200	298	400
a / Å	7.2062(2)	7.2076(2)	7.2104(2)	7.2131(2)
b / Å	10.1089(2)	10.1135(2)	10.1211(3)	10.1279(3)
c / Å	7.3746(2)	7.3775(2)	7.3813(2)	7.3853(2)
O1*z*	0.1625(4)	0.1615(4)	0.1597(5)	0.1578(4)
O2*y*	0.4038(2)	0.4037(2)	0.4036(2)	0.4036(2)
O2*z*	0.7279(2)	0.7280(2)	0.7282(3)	0.7283(3)
O3*x*	0.2059(2)	0.2057(2)	0.2051(2)	0.2041(2)
O3*y*	0.3834(1)	0.3833(1)	0.3830(2)	0.3830(2)
O3*z*	0.4356(2)	0.4354(2)	0.4350(2)	0.4348(2)
Ca1 $U_{eq} \times 100$ / Å^2	0.25(5)	0.50(6)	0.80(8)	1.02(8)
Ca2 $U_{eq} \times 100$ / Å^2	0.21(6)	0.47(7)	0.74(8)	1.06(9)
Os1 $U_{eq} \times 100$ / Å^2	0.04(2)	0.08(3)	0.15(3)	0.19(3)
Os2 $U_{eq} \times 100$ / Å^2	0.00(2)	0.09(2)	0.15(3)	0.20(3)
O1 $U_{eq} \times 100$ / Å^2	0.55(4)	0.75(4)	0.94(5)	1.04(5)
O2 $U_{eq} \times 100$ / Å^2	0.26(3)	0.39(3)	0.54(4)	0.74(4)
O3 $U_{eq} \times 100$ / Å^2	0.21(2)	0.33(2)	0.48(2)	0.62(2)
R_{wp} / %	2.70	3.47	3.81	4.11
R_P / %	3.27	3.22	3.44	3.16
χ^2	6.27	5.27	2.84	5.02

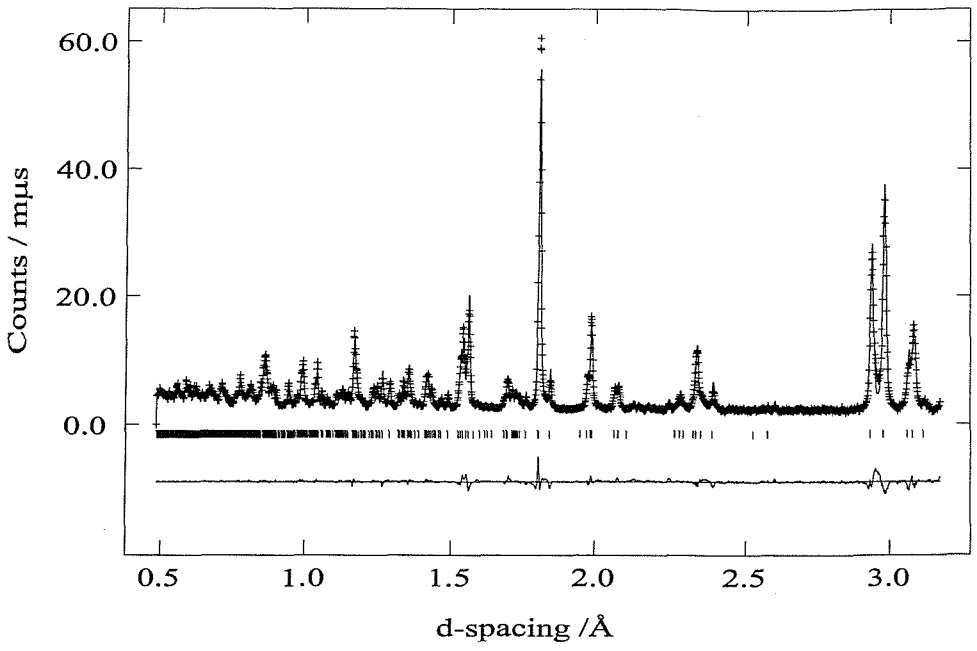

Figure 4.3. Example of the fit achieved to powder neutron diffraction data at T = 298 K. Crosses are experimental points, the upper continuous line the calculated profile and the lower continuous line the difference. Tick marks show allowed reflection positions for $Ca_2Os_2O_7$.

4.5 Discussion

Consistent with the PXD data, the neutron experiments showed the adoption of the weberite structure for $Ca_2Os_2O_7$ at all the temperatures investigated.

The main structural features, of $Ca_2Os_2O_7$ shows that it contains two types of 'A' cation co-ordination and two types of 'B' cation co-ordination. There are two types of OsO_6 octahedra which both show small distortions from perfect symmetry; bond lengths are shown in Figure 4.4. $Os(1)O_6$ is linked through six vertices to adjacent octahedral units with internal bond angles between 85 and 90° and inter-octahedral angles of 139.4(2) and 135.9(1)°. $Os(2)O_6$ is linked to four adjacent octahedral OsO_6 units with bond angles of 135.9(1)° and is also moderately distorted with internal angles between 81.7(1) and 98.3(1)°. Overall the level of distortion in the octahedra are only slightly larger than those found in other osmates confirming that the main driving force for the formation of the

weberite structure is probably the co-ordination preferences of the 'A' type cations rather than those of the 'B' type cations.

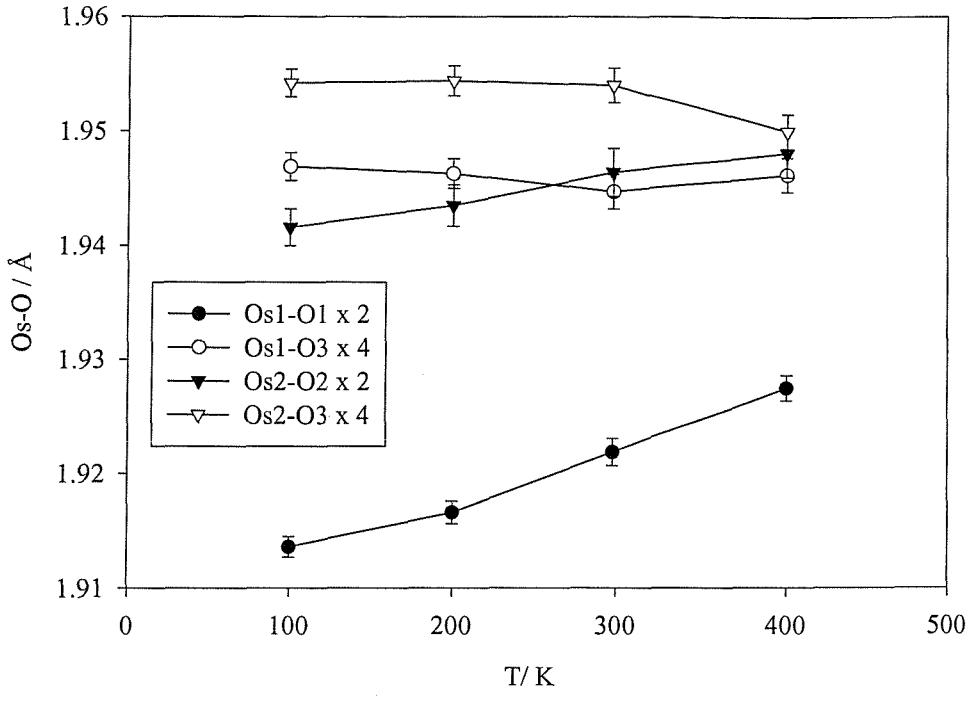

Figure 4.4. Variation of the Os-O bond distances in $Ca_2Os_2O_7$ as a function of temperature.

Variations in the bond lengths between 2 K and 400 K derived from the neutron diffraction data are summarised in Figures 4.4 and 4.5. These data show mainly the expected increases in the various bond lengths as a function of temperature though these are not identical. Indications are that the structure becomes more regular at the highest temperatures for example the shortest Os1-O1 bond expands most rapidly approaching the values of the other Os-O bond lengths in this material. Similarly the Ca1 to O1 and O3 distances start to converge the former shortening significantly between 2 K and 400 K while the latter lengthens. The environment of this cation therefore becomes more like the 2+6 co-ordination found in pyrochlores. However extrapolation of these changes to higher temperatures indicates that the more regular co-ordinations of the pyrochlore structure would not be approached until well above the decomposition temperature of $Ca_2Os_2O_7$, near 700°C in air.

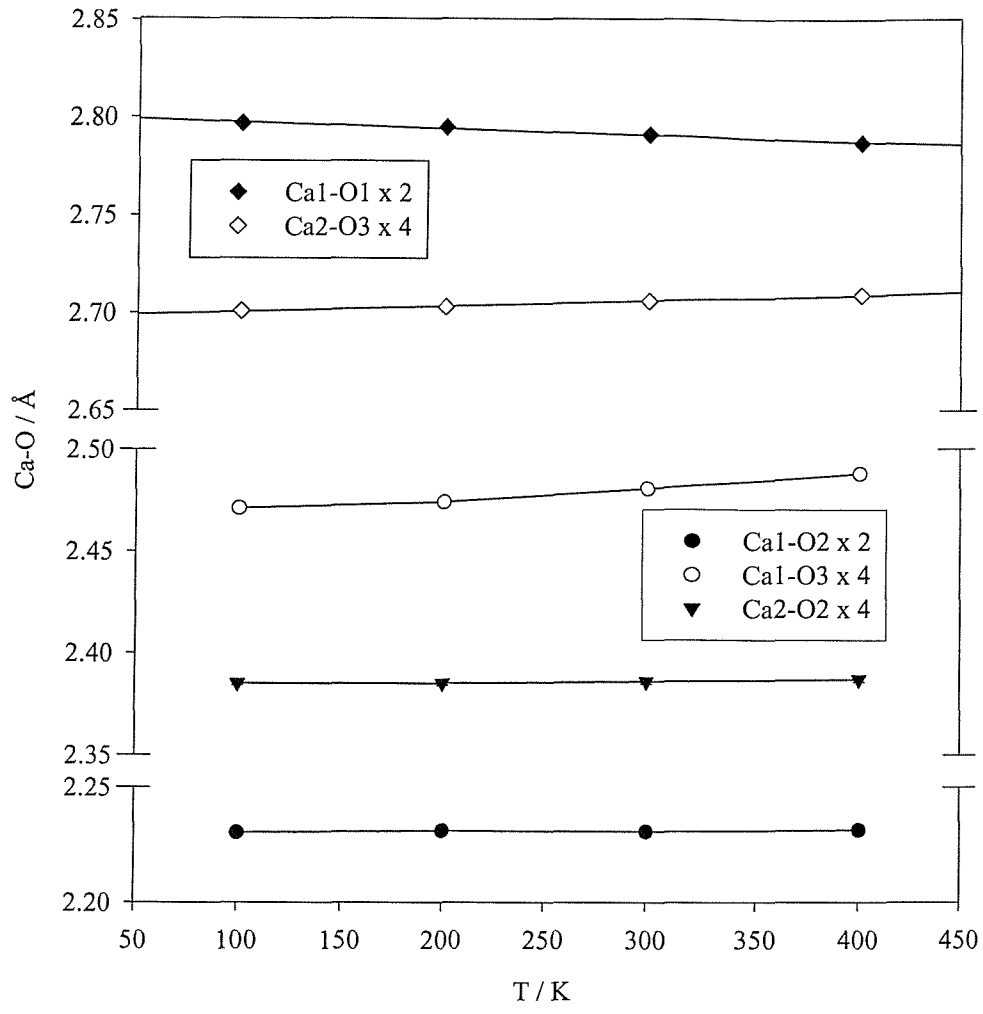

Figure 4.5. Variation of the Ca-O distances in $Ca_2Os_2O_7$ as a function of temperature.

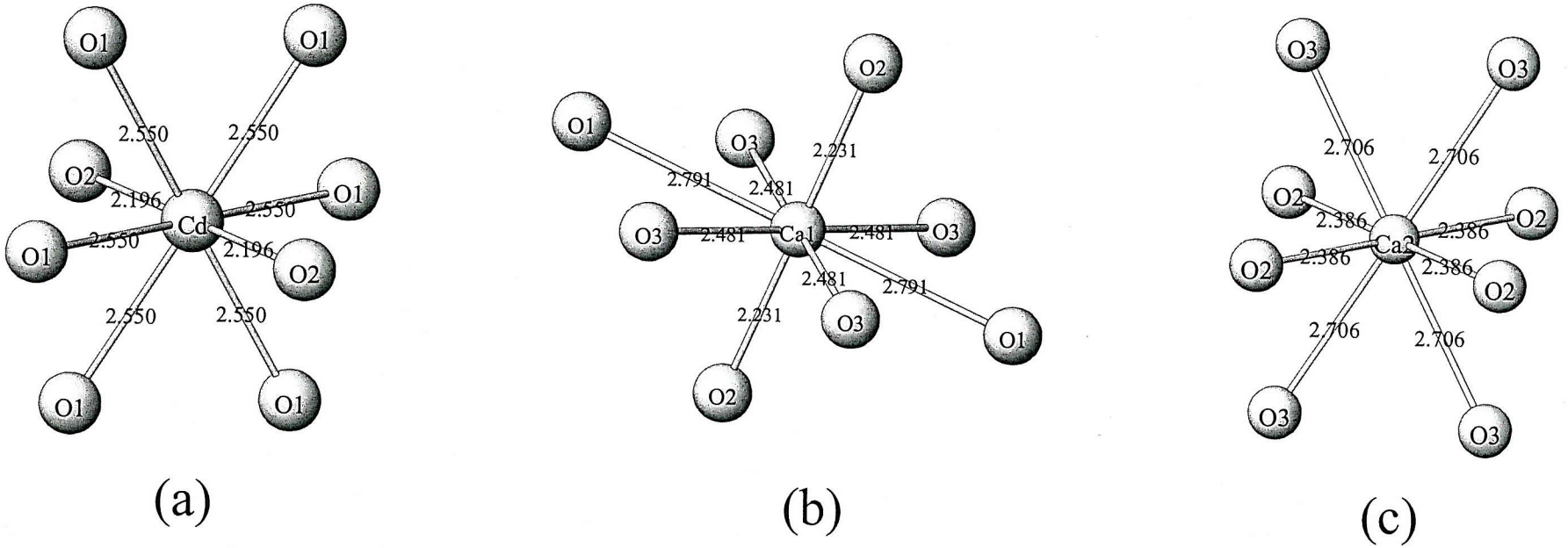

Figure 4.6. 'A' type cation co-ordination environments in (a) pyrochlore and (b) and (c) weberite structures.

A comparison of the co-ordination environment of calcium in $Ca_2Os_2O_7$ (weberite) and cadmium in $Cd_2Os_2O_7$ (pyrochlore)[10] is shown in Figure 4.6. Accepted ionic radii for these cations in 8-fold co-ordination are r (Ca^{2+}) = 1.12 Å and r (Cd^{2+}) = 1.10 Å so similar bond lengths would be expected for these two ions. In both materials the cations are 8-co-ordinate to oxygen as would be expected for structures based on the fluorite sub-lattice, however, these co-ordination geometries are strongly distorted from cubic in each case. The most noticeable feature of the 'A' cation co-ordination in the pyrochlore structure is the very short A-O2 distance, which is 2.196 Å for Cd-O in $Cd_2Os_2O_7$ compared with the sum of the ionic radii, 2.36 Å. Clearly for d^{10} species such as Cd^{2+}, Hg^{2+} and Ag^{2+} which prefer linear co-ordinations, this structural motif helps stabilise the pyrochlore structure. In the weberite structure, one of the 'A' cation sites has a similar geometry though the Ca-O distance is less obviously shortened, Ca-O is 2.231 Å, and the other site has a much more regular 4+4 geometry with the shortest Ca-O interaction at 2.386 Å. This tendency to avoid very short A(Ca)-O distances is reflected in the other reported $Ca_2B_2O_7$ phases. Only $Ca_2Sb_2O_7$ formed under 60 kbar pressure is well characterised as a pyrochlore, where pressure presumably favours short Ca-O distances[7].

The phase behaviour of materials of the stoichiometry $A^{2+}{}_2B^{5+}{}_2O_7$ has been studied by several authors. Very few oxides are known to adopt the weberite structure, the extent being limited, prior to this work, to $Ba_2U_2O_7$, $Sr_2Sb_2O_7$ and $(Cd,Ca)Sb_2O_7$ under certain synthesis conditions. Phase formation behaviour from many complex oxide systems can be reasoned in terms of the ionic radii of the various component cations. So for example, materials of the composition ABO_3, the perovskite structure and various distorted forms may be predicted for certain values of the ionic radii of 'A' and 'B'. Similar considerations have been made for the pyrochlore structure and data for the 2+/5+ systems is summarised in Figure 4.7. Although the range of data is limited to around 20 compounds it is clear that there is little correlation between ion sizes and choice of the weberite or the pyrochlore structure, suggesting that some other factor must influence the energetics.

Bonding in these structures has a significant covalent character particularly for the 'A' site and its interaction with the O2 site in the pyrochlore structure. Similarly, for the weberite arrangement short directional covalent interactions between the 'A' cation and oxygen sites are significant as shown in Figure 4.6.

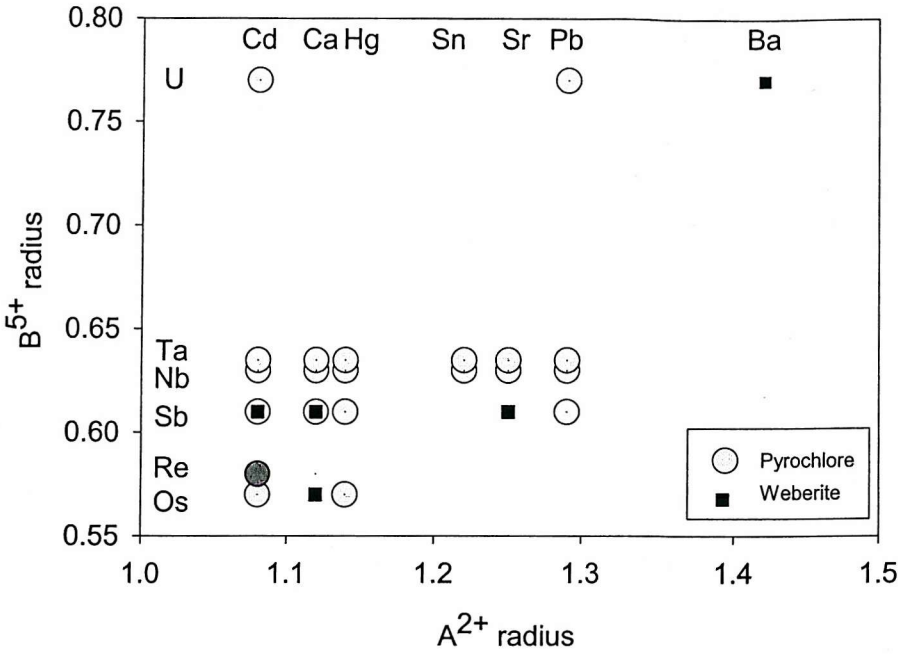

Figure 4.7. Phase formation for $A_2B_2O_7$ phases as a function of the 'A' and 'B' cationic radii.

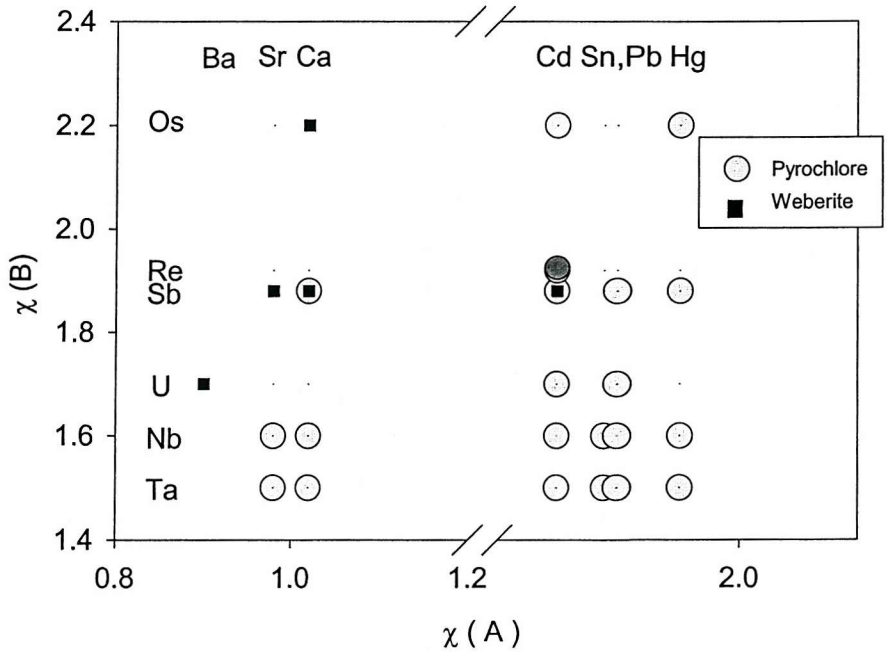

Figure 4.8. Phase formation for $A_2B_2O_7$ phases as a function of the 'A' and 'B' electronegativities.

Therefore, an additional driving force for the choice of structure would be the level of covalency in the bonding, which may be quantified in terms of the electronegativity of the species present relative to the oxide. Figure 4.8 plots the phase behaviour as a function of the electronegativity of the 'A' and 'B' cations. Domains of adoption of the weberite and pyrochlore structures are now clear, with the weberite structure being adopted when the 'A' cation is most electropositive and the 'B' cation most electronegative i.e. the upper left hand portion of the diagram. Probably most crucial is the covalency in the bonding of the 'A' cation with its very irregular 2+6 co-ordination in the pyrochlore structure.

Bond valence calculations for the calcium and osmium sites are given in Table 4.4 and are dependent on the assumed oxidation states. The results provide further evidence in accordance with the neutron data that the material is stoichiometric $Ca^{2+}_2Os^{5+}_2O_7$[18].

Table 4.4. Calculated Bond Valence Sums for the cations in $Ca_2Os_2O_7$ at 298 K. An extrapolated r_o value of 1.868 was used for Os(V) based on literature data[18].

Atom	Bond Valence Sum
Ca1	2.19
Ca2	1.83
Os1	4.98
Os2	4.79

4.6 Physical Measurements

The physical properties of $Ca_2Os_2O_7$ were investigated using variable temperature resistivity measurements. This would enable the determination of the electronic state of the material below and above room temperature. In addition, variable temperature infra-red data were also recorded for the material to provide further evidence of the electronic nature across the experimental temperature range. The resistivity and infra-red data were collected simultaneously sharing the same cryogenic equipment across a temperature range of 200 K to 450 K. A preliminary experimental run was carried out on a sample of $Ca_2Os_2O_7$ at several temperatures across the range to establish any significant electronic changes. This enabled a sufficient temperature step size at which data points were to be recorded across these regions, providing greater accuracy. The step size used was ~ 5 K from 200 to 340 K, ~ 10 K from 340-370 K, and ~ 15 K from 370-450 K.

4.6.1 Resistivity Measurements

Resistivity data were collected for $Ca_2Os_2O_7$ from 200 K to 450 K, and are shown in Figure 4.9. The four-probe technique was used on a small pellet pressed under ~ 10 tonnes/cm^2 (as described previously).

The behaviour of $Ca_2Os_2O_7$ over this temperature range shows a significant drop in resistivity, about two orders of magnitude, similar to that observed for polycrystalline $Cd_2Os_2O_7$ between 175 and 230 K. Unlike $Cd_2Os_2O_7$, there is no rapid change in resistivity, but more of a gradual transition from semiconducting behaviour to a metallic state. This is clarified by plotting log resistivity as a function of temperature, Figure 4.10. Here it can be seen that the most significant change in resistivity occurs between just below room temperature and just above room temperature. Even after this main transition occurs, there is still a further drop in resistivity indicating that the change may not be complete to a full metallic state, rather that the transition is semiconducting / semiconducting. Further data at higher temperatures are needed to accurately conclude the electronic behaviour of this material, this however, was outside the limitations of the experimental equipment used.

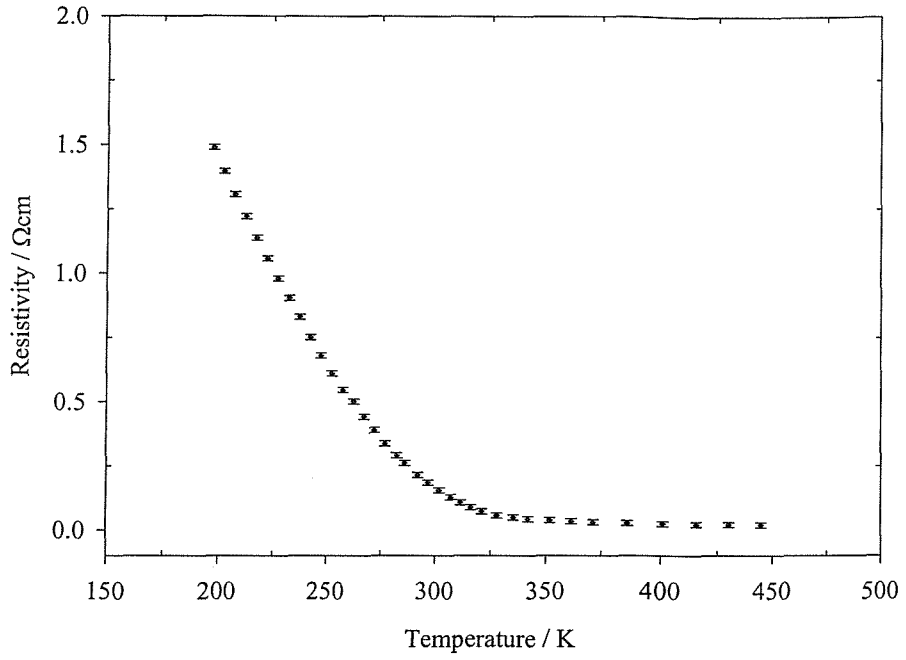

Figure 4.9. The resistivity of $Ca_2Os_2O_7$ over the temperature range 200-450 K.

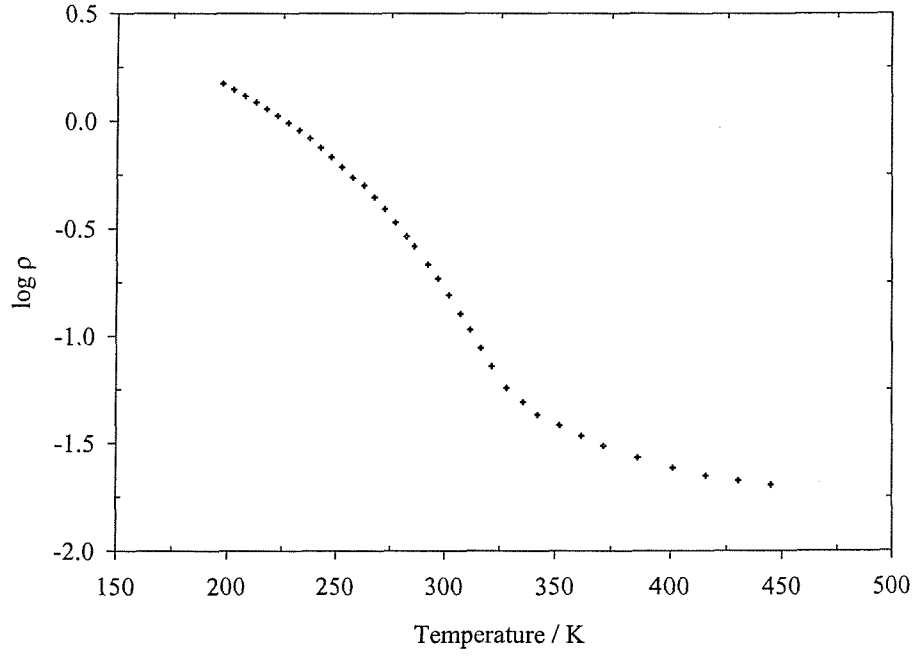

Figure 4.10. The log resistivity of $Ca_2Os_2O_7$ over the temperature range 200-450 K.

4.6.2 Infra-red Measurements

Infra-red data were collected for $Ca_2Os_2O_7$ across a temperature range of 200 K to 450 K, and were recorded on a Nicolet Magna 760 Infra-red spectrometer. The material was intimately ground with spectroscopic KBr in a quantitative manner to allow an accurate comparison of spectra. Spectra were recorded over a range of 4000-250 cm^{-1}, with a resolution of 2 cm^{-1}.

In the infra-red spectrum, a metallic oxide will generally show a strong absorption across the whole region associated with the collective electronic states, drowning out any lattice modes. An insulating oxide will absorb at discrete frequencies in the infra-red region associated with the M-O modes. Similar to perovskite oxides, pyrochlores ($A_2B_2O_7$), show two prominent bands in the region 1000-250 cm^{-1}, which can be assigned to the internal modes of the BO_6 octahedra. The integrated area under the two bands is observed to decrease with increasing electrical conductivity, and in the event of a material passing through an insulator-metal phase transition, the two bands will no longer be observed.

The spectra collected for the $Ca_2Os_2O_7$ sample were found to contain two distinct bands at ~ 640 and 570 cm^{-1} whose intensity decreased on heating, indicative of a change of electronic behaviour. An example of the spectra collected is shown in Figure 4.11 for the low and high temperature data. The combined area under the two bands was calculated for each spectrum and plotted as a function of temperature, Figure 4.12. The results show a significant reduction in band intensity across the experimental temperature range. The start of the change is seen to occur at ~ 230 K, preceding a linear decrease to 316 K. Above 320 K a slower decrease of band intensity is seen. An inflection in the data series is seen at 316 K, which could be associated with a second order electronic transition from a semi-conductive state to a metallic state. However, it is impossible to conclude that the change in electronic behaviour is complete due to the absence of further data at higher temperatures.

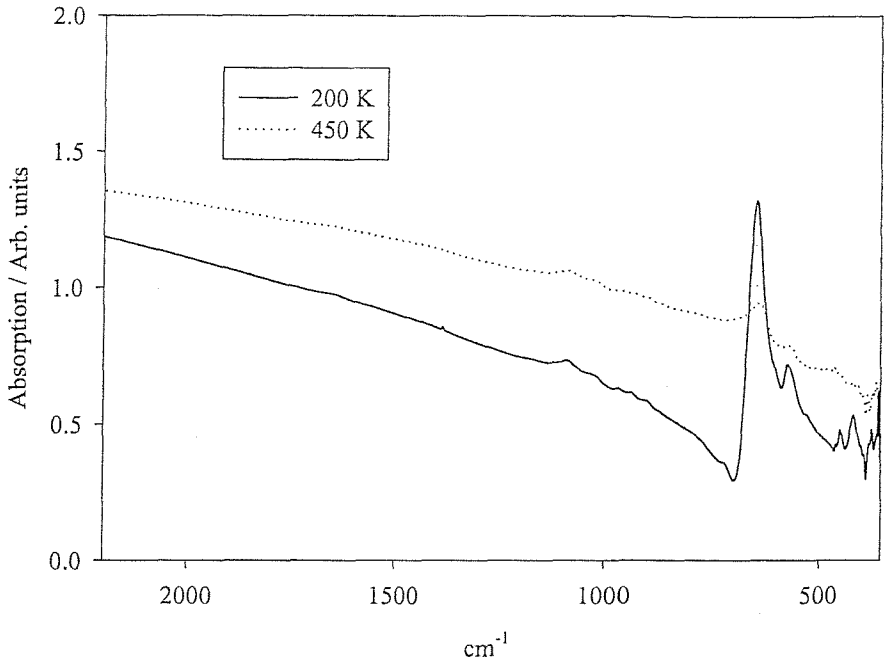

Figure 4.11. Examples of the infra-red spectra collected for $Ca_2Os_2O_7$ at 200 and 450 K

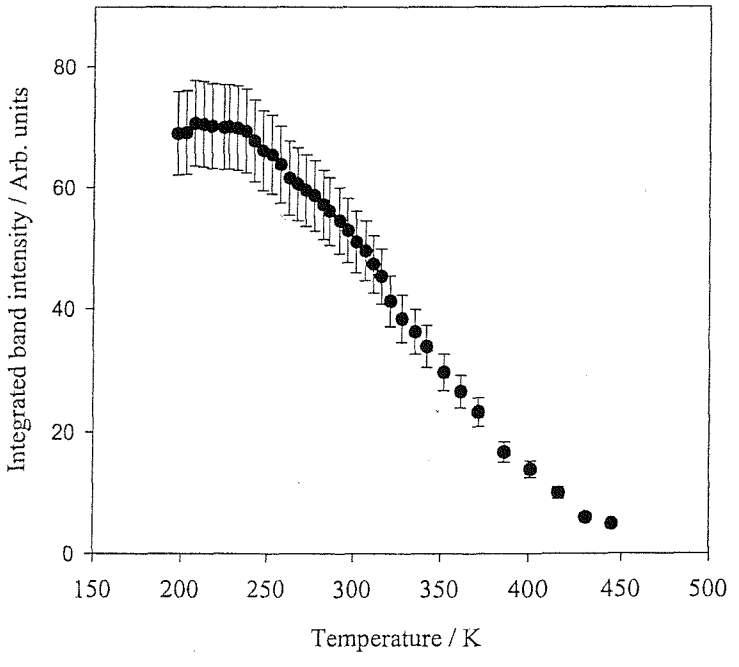

Figure 4.12. Temperature dependent variation of the integrated band intensity of ν_{Os-O} for $Ca_2Os_2O_7$.

4.6.3 Discussion

From the sets of infra-red spectra and resistivity measurements similar trends are immediately apparent. The integrated band intensity of the material decreases as the temperature increases, which is also what is observed for the resistivity. The band intensities start to change in line with the resistivity and decrease at the same rate. A direct comparison to the two sets of data is easily made, by overlapping their respective plots on the same graph, Figure 4.13.

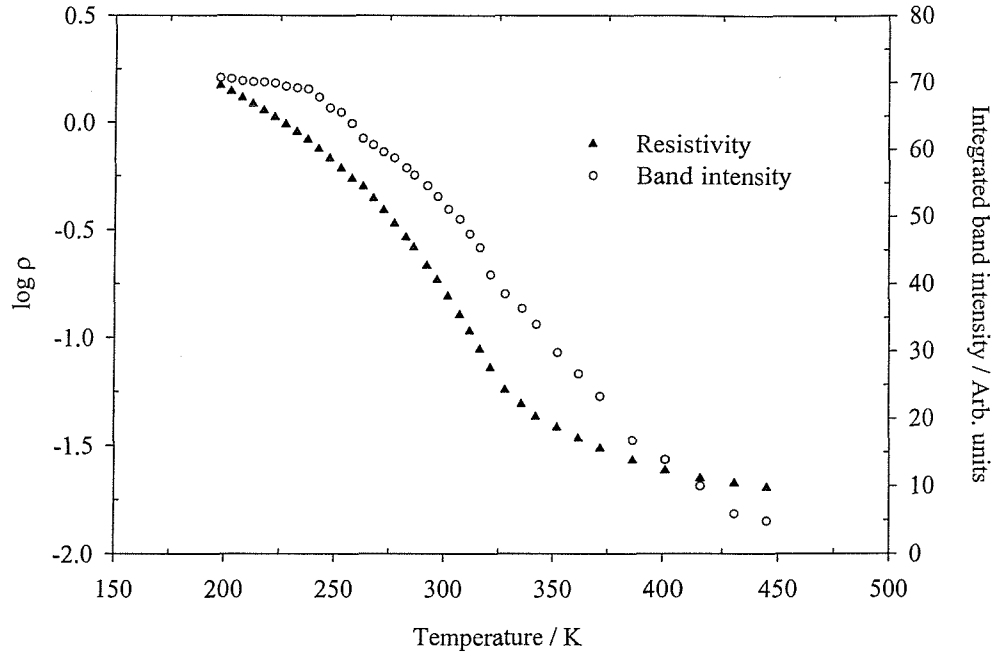

Figure 4.13. Resistivity and integrated band intensity of $Ca_2Os_2O_7$ as a function of temperature.

In conclusion, the results from both infra-red and resistivity measurements support a distinct electronic change in $Ca_2Os_2O_7$ with temperature. The material is seen to undergo some kind of semiconductor/metal transition through room temperature which is second order in nature, with a change of resistivity of about two orders of magnitude.

4.7 Comparison of Previous Calcium Osmate Studies

Previous studies of reported pyrochlore calcium osmates have yielded a variety of different results. Chamberland reported a cubic phase obtained from the decomposition of $CaOs(OH)_6$, and a tetragonal phase obtained by the direct reaction of CaO and OsO_2 at 1000 °C[14,15]. However, Shaplygin and Lazarev found that $CaOsO_3$ decomposes on heating to form $Ca_2Os_2O_7$ with an orthorhombic structure, and on heating above 855 °C, the material loses oxygen to give $Ca_2Os_2O_{7-\delta}$ with a cubic pyrochlore structure[14]. The only other report on the formation of a calcium osmate is by Sleight, who reacted OsO_2 and CaO under high pressure (700 °C, 3 kbar, $KClO_3$), and obtained a non-stoichiometric pyrochlore, $Ca_{1.7}Os_2O_7$[15]. The electronic behaviour of the calcium osmate materials from these previous findings differs significantly, and a summary can be found in Table 4.5.

The electronic behaviour observed in this work shows some similarities with the findings of Chamberland[12] with his cubic pyrochlore type material. A semiconductor/metal transition at 315 K was reported, but no actual physical data or graphical representation of the results was shown, making it impossible to comment in further detail of any other similarities. Also the extent of the impurities present was not mentioned, which would question the validity of the electrical measurements. Although the previous findings of the calcium osmate materials are in contrast with each other, they all show poor metallic behaviour of ~ 2 - 5×10^{-2} Ωcm at a given temperature, indicating that the materials are not vastly different from each other, and that similar transport mechanisms may be at work.

Table 4.5. A summary of the crystallograpghic and electronic observations of calcium osmates reported to date.

Compound	Impurity	Crystal Type	Crystal Symmetry	Electronic Behaviour	Ref.
$Ca_2Os_2O_7$	CaO + Os metal	PY	cubic	semiconductor/metal transition (315 K)	12
$Ca_2Os_2O_7$	Os metal + $CaOsO_3$	PY	tetragonal	unknown	13
$Ca_2Os_2O_7$	unknown	*	orthorhombic	metallic $\rho_{(300\ K)} \sim 4.6\times10^{-2}$ Ωcm	14
$Ca_2Os_2O_{7-\delta}$ $\delta = 0.5$	unknown	PY	cubic	metallic $\rho_{(300\ K)} \sim 2\text{-}5.6\times10^{-2}$ Ωcm	15
$Ca_{1.7}Os_2O_7$	none	PY	cubic	temperature independent $\rho_{(80\text{-}470\ K)} \sim 1$ Ωcm	16
$Ca_2Os_2O_7$	none	WEB	orthorhombic	semiconductor/metal transition (~ 300 K)	this work

PY = pyrochlore type structure * = $Ca_2Nb_2O_7$ type structure WEB = weberite type structure

4.8 Conclusions

$Ca_2Os_2O_7$ prepared under ambient pressure conditions is the first osmate found to adopt the weberite structure. Consideration of the relative stabilities of the weberite and pyrochlore structures for $A_2B_2O_7$ systems reported previously indicate that synthesis under higher pressures should lead to formation of the pyrochlore structure for $Ca_2Os_2O_7$, as has indeed been observed by Chamberland[12]. Adoption of the weberite structure with slightly different connectivities in the osmium-oxygen sub-lattice has no significant influence on the electronic properties of this material, i.e. both $Cd_2Os_2O_7$ and $Ca_2Os_2O_7$ exhibit poor metallic properties near room temperature. The differences in the connectivities of the BO_6 octahedra are shown in detail in Figure 4.13. In both structures chains of vertex sharing octahedra can be considered as being cross-linked by additional octahedra; in pyrochlore these linking units share all vertices and additional oxide ions reside in the channels thus formed while in weberite only four vertices are shared and terminal oxide ions exist. The extensive Os 5d orbitals allow, in the presence of three dimensionally linked OsO_6 octahedra, direct interaction of the osmium centres. While for the pyrochlore systems it seems that the interaction of the Cd and Hg 4 and 5d levels with the Os 5d levels is believed to occur at the Slater transition and, be necessary for the metallic regime, this is not so critical for the weberite structure. The origin of this behaviour may lie in the lower symmetry of weberite and would need detailed band structure calculations on this different structure type. Physical measurements carried out at higher temperatures would also provide further proof as to the nature of the room temperature electronic transition.

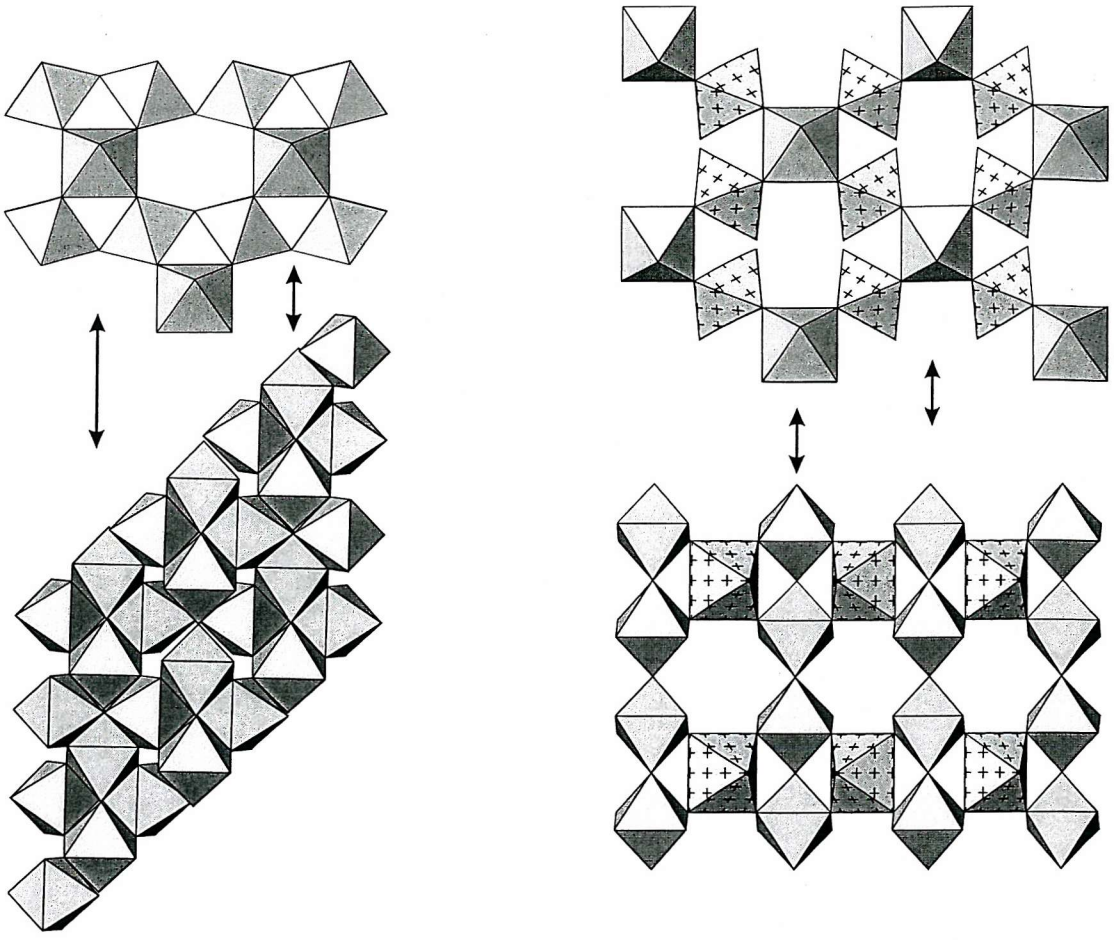

Figure 4.14. Polyhedra representations of the pyrochlore (left) and weberite (right) structures. The upper diagrams view the structures along the main channels containing the 'A' cations. The lower diagrams view the structures perpendicular to this direction showing the different connectivity of the BO_6 octahedra, linking the main chains formed from BO_6 octahedra linked through opposite vertices (marked).

4.9 References

[1] M. A. Subramanian, G. Aravamudan, G. V. Subba Rao, *Prog. Solid State Chem.* **15**(2) 55 (1983).

[2] J. E. Greedan, J.N.Reimers, C.V.Stager and S.L.Penny, *Phys. Rev. B* **43** 5682 (1991).

[3] B. D. Gaulin, J. S. Gardner, S. R. Dunsiger, Z. Tun, M. D. Lumsden, R. F. Kiefl, N. P. Raju, J. N. Reimers and J. E. Greedan, *Physica B* **241-243** 511 (1998).

[4] T. Takeda, M. Nagata, H. Kobayashi, R. Kanno, Y. Kawamoto, M. Takano, T. Kamiyama, F. Izumi and A. W. Sleight, *J. Solid State Chem.* **140** 182 (1998).

[5] H. Sakai, K. Yoshimura, H. Ohno, T. D. Matsuda, H. Kato, S. Kambe, R. Walstedt, Y. Haga and Y. Onuki, *J. Phys. : Condens. Matter* **13** L785 (2001).

[6] W. A. Groen and D. J. W. Ijdo, *Acta Crystallogr. Sec. C* **44** 782 (1988).

[7] O. Knop, G. Demazeau and P. Hagenmuller, *Can. J. Chem.* **58** 2221 (1980).

[8] A. W. Sleight, J. L. Gillson, J. F. Weiher and W. Bindloss, *Solid State Commun.* **14** 357 (1974).

[9] D. Mandrus, J. R. Thompson, R. Gaal, L. Forro, J. C. Bryan, B. C. Chakoumakos, L. M. Woods, B. C. Sales, R. S. Fishman and V. Keppens, *Phys Rev. B* **63** 195104 (2001).

[10] J. Reading and M. T. Weller, *J. Mater. Chem.* **11** 2373(2001).

[11] J. Reading, S. Gordeev and M. T. Weller, *J. Mater. Chem.* **12** 646 (2002).

[12] R. F. Sarkozy and B. L. Chamberland, *Mat. Res. Bull.* **8** 1351 (1973).

[13] B. L. Chamberland, *Mat. Res. Bull.* **13** 1273 (1978).

[14] I. S. Shaplygin and V. B. Lazarev, *Thermochim. Acta* **20** 381 (1977).

[15] I. S. Shaplygin and V. B. Lazarev, *Thermochim. Acta* **33** 53 (1979).

[16] A. W. Sleight, *Mat. Res. Bull.* **9** 1177 (1974).

[17] A. C. Larson and R. B. Von Dreele, *Generalsied Structure and Analysis System,* MS-H805, Los Almos, NM 87545 (1990).

[18] D. Altermatt and I. D. Brown, *Acta Crystallogr. Sect. B* **53** 135 (1997).

Chapter Five

Synthesis and Structural Characterisation of the Non-Stoichiometric Pyrochlores $A_2Os_2O_{7-x}$ (A = Pb and Tl)

5.1 Introduction

This pyrochlore family of compounds exhibit a wide range of physical properties with most research attention paid to the electrical nature of the materials, which can be insulating, semi-conducting, metallic and very recently superconducting[1].

Table 5.1. The pyrochlore atomic co-ordinates, space group *Fd-3m*.

Atom	*x*	*y*	*z*	Multiplicity
A	½	½	½	16
B	0	0	0	16
O1	*x*	⅛	⅛	48
O2	⅜	⅜	⅜	8

The majority of pyrochlores are cubic and fall into the space group *Fd-3m* with eight molecules per unit cell (Z = 8). The location of the atoms, atomic co-ordinates and multiplicity are given in Table 5.1. There is only one positional parameter, the O1 oxygen *x* parameter, which is found to range from 0.309 to 0.355 (with 'B' as the origin).

This group of compounds have a common composition of $A_2B_2O_7$ and can lend themselves to a variety of chemical substitutions at the 'A', 'B' and 'O' sites, providing the ion size and charge neutrality criteria are satisfied, similar to perovskite materials. The crystal structure also tolerates vacancies at the 'A' and 'O' sites giving an even wider scope of materials. These defect pyrochlores have cation or anion vacancies existing in the lattice shifting the normal pyrochlore composition, $A_2B_2O_7$, to give the compositions $A_2B_2O_{7-x}\square_x$ ($0.0<x<1.0$) or ($\square$A)B2($O_6\square$), where $\square$ represents a vacancy. Further structural details of defect pyrochlores can be found in Chapter 1.

A number of Pb^{2+} containing pyrochlores have been sucessfully synthesised over the years, examples including $Pb_2B_2O_{7-x}$ (B = Nb, Ta, Sb). These materials are found to crystallise with the cubic pyrochlore lattice but are non-stoichiometric and may contain the presence of

Pb^{4+} ions. The Pb^{4+} ions are thought to mix with the 'B' site ions to give a general formula, $Pb_2^{2+}(Pb_x^{4+} B_{2-x}^{5+}) O_{7-0.5x}$. Exact stoichiometric phases have also been reported for $Pb_2Nb_2O_7$ and $Pb_2Sb_2O_7$, with the structures undergoing a rhombohedral distortion[2 to 4]. Precious metal containing Pb^{2+} pyrochlores (B = Tc, Ru, Re, Os, Ir, Pt) are thought to be mostly non-stoichiometric, to which the extent of the ion deficiencies depend on the synthesis conditions used. Although all the reported examples are found to be cubic, there is some confusion over the existance of $Pb^{2+/4+}$ ion mixing and the exact stoichiometry of the compounds.

$Pb_2Os_2O_{7-x}$ has been prepared and characterised by several workers at ambient pressure, with contrasting results. Badauld *et al.* prepared a sample by heating PbO and OsO_2 in an ampoule at 580 °C to give a composition of $Pb_2Os_2O_{6.0 \pm 0.1}$[5] whilst Sarkozy *et al.* decomposed $PbOs(OH)_6$ at 400 °C in air to give $Pb_2Os_2O_{7-x}$[6]. Shaplygin and Lazarev investigated several different synthesis methods at 600 °C and produced varying composition materials of $Pb_2Os_2O_{7-x}$, where $x = 0.2 - 1.0$[7]. The only other report is by Sleight, who prepared a stoichiometric sample ($x = 0$) by a high pressure route, reacting PbO with OsO_2 at 700 °C and under 3 kbar[8]. In all cases the samples showed metallic behaviour, $\rho_{(298\ K)}$ 3 - 4×10^{-4} Ωcm. All the structural reports on the lead osmate materials are based solely on x-ray diffraction data, which will not accurately define oxygen positions in a structure, especially in a heavy metal oxide. Therefore, there is a great deal of confusion as to the exact stoichiometry of the samples, and the nature of the cation distributions over the 'A' and 'B' sites *i.e.* $Pb^{2+}Os^{5+}$ or $(Pb^{2+}, Pb^{4+})Os^{4+}$.

Thallium pyrochlores were less well documented in the literature until the recent discovery of colossal-magnetoresistance in $Tl_2Mn_2O_7$, which has been investigated in terms of structure and physical properties by several workers[9 to 12]. Another thallium pyrochlore that displays interesting structural and physical behaviour is $Tl_2Ru_2O_{7-x}$. The synthesis of thallium ruthenate was first reported by Sleight and Gillson, where they reacted Tl_2O_3 and RuO_2 at 700 °C under 0.3 GPa of applied pressure[13]. The results showed that the material was a cubic pyrochlore at room temperature and at 4.2 K, and showed electronic behaviour consistent with a semi-conductor. A few years later, Jarrett *et al.*[14] reported the high pressure synthesis of $Tl_2Ru_2O_{7-x}$, which showed a metal / semi-conductor transition around 120 K. They showed that the transition behaviour in the system was complex, and the

results were unclear in their relationship to the structure and composition of the material. Recently, the $Tl_2Ru_2O_{7-x}$ system has been investigated in detail by Takeda *et al.*[15], where numerous different syntheses were carried out at both ambient and high pressure to produce thallium ruthenate pyrochlore materials with varying oxygen composition. The results showed that the materials exhibited complex electronic and structural behaviour, in this case dependent on composition, including metal/insulator transitions and magnetoresistive properties.

The only report for the synthesis of thallium osmate, $Tl_2Os_2O_7$, was by Sleight and Gillson[13], who systematically studied the precious metal pyrochlores of $Tl_2M_2O_7$ (M = Ru, Rh, Os, Ir and Pt). They prepared a sample of $Tl_2Os_2O_7$ from the reaction of Tl_2O_3 and OsO_2 at 700 °C under an applied pressure of 0.3 GPa. A variable temperature study confirmed the material to be metallic. The structure was determined as cubic, *Fd-3m*, with powder x-ray diffraction. No further structural work or other investigations have been carried out on the $Tl_2Os_2O_7$ phase, which, on the evidence of the further work carried out on $Tl_2Ru_2O_{7-x}$, has the potential to display equally interesting physical and structural behaviour.

This chapter reports the synthesis and characterisation of the oxygen deficient pyrochlores $Pb_2Os_2O_{7-x}$ and $Tl_2Os_2O_{7-x}$ at ambient pressure. Each material is preliminary characterised by powder x-ray diffraction (PXD) and Rietveld analysis of the data is performed to determine structural information. In addition, the material is fully characterised using powder neutron diffraction at room temperature for $Pb_2Os_2O_{7-x}$, and at room temperature and low temperature (1.8 K) for $Tl_2Os_2O_{7-x}$ to determine accurate structures in terms of composition and ion distribution. Furthermore, comparisons are made to related materials in terms of structural and physical properties.

5.2 Preparation of $Pb_2Os_2O_{7-x}$ and $Tl_2Os_2O_{7-x}$ at Ambient Pressure

Samples of $Pb_2Os_2O_{7-x}$ and $Tl_2Os_2O_{7-x}$ were prepared by grinding together the appropriate stoichiometric mixtures of high purity PbO (99.9+ %), Tl_2O_3 (99.9 %), OsO_2 (99.99 %), Os (99.8%) and OsO_4 (99.95%). Tl_2O_3 and PbO were pre-dried at 300 °C for 1 day before use. $Tl_2Os_2O_{7-x}$ was synthesised using Tl_2O_3 and OsO_2 targeting an Os(IV) compound. For $Pb_2Os_2O_{7-x}$, appropriate mixtures of PbO, OsO_4 and Os were used. The stoichiometric

mixtures were loaded into silica ampoules and sealed under vacuum; in the case of $Pb_2Os_2O_{7-x}$ the end of the ampoule was immersed in liquid nitrogen to avoid osmium loss due to the volatility of OsO_4. The synthesis temperatures for $Pb_2Os_2O_{7-x}$ and $Tl_2Os_2O_{7-x}$ were 800 and 500 °C respectively, with a reaction period of 1 day in each case. PXD data were recorded from the products using a Siemens D5000 diffractometer operating with Cu $K_{\alpha 1}$ radiation. The patterns were consistent with cubic pyrochlore phase materials, with the exception of a small amount of Tl_2O_3 impurity (<3 %) in $Tl_2Os_2O_{7-x}$.

5.3 PXD Structure Refinements

PXD data were collected over a 2θ range of 20°–120° for a period of 15 hours using a 0.02° step size, for both samples. Cell parameters were calculated from the d-spacings using the CELL computer program. Using the Rietveld technique, refinement of the data commenced using the computer program GSAS[16]. The refinement was started based on the cubic pyrochlore model, *Fd-3m*. A uniform approach to the structure refinement was undertaken for both data sets obtained to ensure consistent results. Cell parameters, peak shape parameters atomic positions and isotropic temperature factors were sequentially added to the refinement. The site occupancies were refined showing no evidence of fractional occupancy for both Pb and Tl atoms within *esds*, and unrealistic values for the oxygen sites so they were left at unity. The refinements converged smoothly to yield acceptable *R*-factors and accurate cell parameters were determined for both materials along with atom positions, derived bond lengths and bond angles, which are summerised in Tables 5.2 and 5.3. Profile fits for achieved for $Pb_2Os_2O_{7-x}$ and $Tl_2Os_2O_{7-x}$ are shown in Figures 5.1 and 5.2.

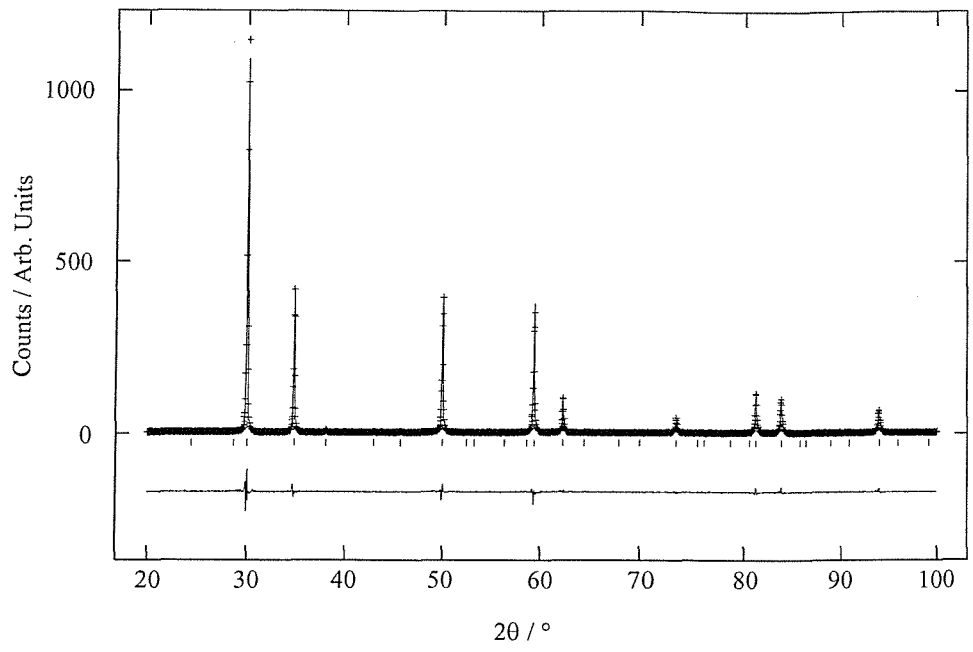

Figure 5.1. Profile fit to PXD data for $Pb_2Os_2O_{7-x}$. Experimental data points are shown as crosses, upper continuous line the calculated profile, lower continuous line the difference. Allowed reflection positions for $Pb_2Os_2O_{7-x}$ are shown with tick marks.

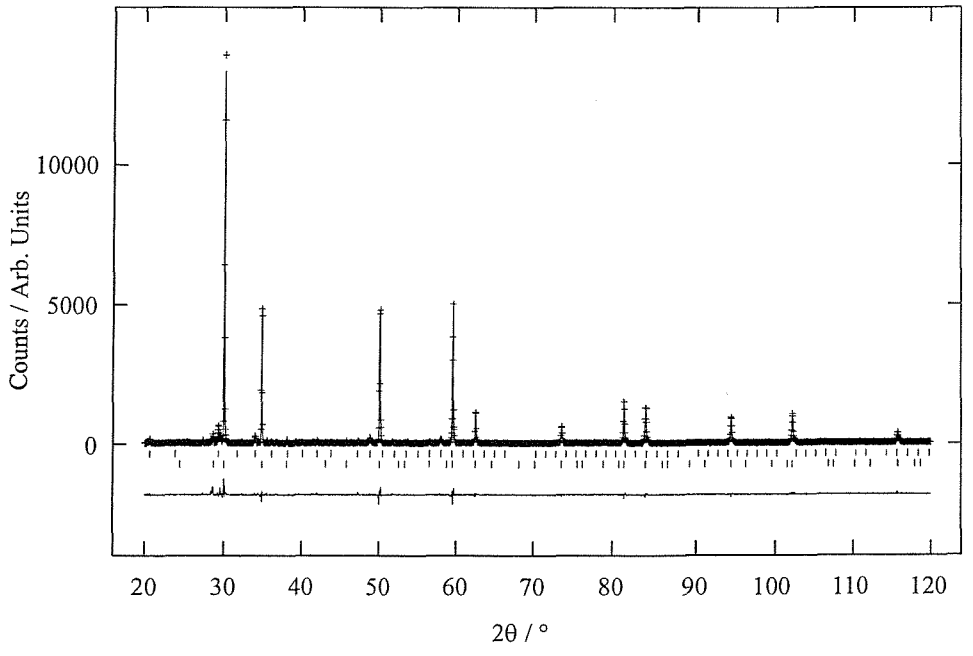

Figure 5.2. Profile fit to PXD data for $Tl_2Os_2O_{7-x}$. Experimental data points are shown as crosses, upper continuous line the calculated profile, lower continuous line the difference. Allowed reflection positions for $Tl_2Os_2O_{7-x}$ (lower) and Tl_2O_3 (upper) are shown with tick marks.

Table 5.2. Summary of derived atomic, thermal and profile fit parameters for $Pb_2Os_2O_{7-x}$ and $Tl_2Os_2O_{7-x}$; *esds* are given in the parentheses. Space group *Fd-3m*. Pb/Tl on (½,½,½), Os on (0,0,0), O1 on (x,⅛,⅛) and O2 on (⅜,⅜,⅜).

	$Pb_2Os_2O_{7-x}$	$Tl_2Os_2O_{7-x}$
a / Å	10.3239(2)	10.28975(4)
O1 x	0.3359(30)	0.3175(19)
Pb/Tl U_{eq} × 100 Å^2	1.69(12)	2.11(11)
Os U_{eq} × 100 Å^2	1.72(13)	0.98(9)
O1 U_{eq} × 100 Å^2	6.7(11)	3.55(8)
O2 U_{eq} × 100 Å^2	26.2(73)	0.01(12)
R_{wp} (%)	14.16	17.49
R_p (%)	10.45	11.71
χ^2	0.2076	3.077

Table 5.3. Selected bond lengths and bond angles for $Pb_2Os_2O_{7-x}$ and $Tl_2Os_2O_{7-x}$.

	$Pb_2Os_2O_{7-x}$	$Tl_2Os_2O_{7-x}$
Pb/Tl-O1 (×6) / Å	2.490(21)	2.615(14)
Pb/Tl-O2 (×2) / Å	2.23518(2)	2.22780(1)
Os-O1 (×6) / Å	2.029(14)	1.947(7)
O1-Os-O1 / °	98.7(10)	92.0(7)
Os-O1-Os / °	128.2(16)	138.2(11)

Both $Pb_2Os_2O_{7-x}$ and $Tl_2Os_2O_{7-x}$ are found to crystallise in a cubic pyrochlore unit cell, space group *Fd-3m*. The structure is comprised of OsO_6 octahedra sharing all vertices with a distorted (6 + 2) cubic co-ordination to the Pb or Tl cations. The cell parameters in Table 5.2 show the lead pyrochlore to be the largest of the two structures, which is expected from ionic considerations; assumed oxidation states Pb^{2+} ^{VIII}r = 1.29 Å, Tl^{3+} ^{VIII}r = 0.98 Å[17].

Other than accurate cell parameters, little more reliable structural information can be gained form the PXD refinements at this stage, due to the large *esds* associated with the data. To enable an accurate structural study of both materials necessitates the use of powder neutron diffraction (PND). This will also provide valuable information with regard to exact composition, cation valencies and ion distribution.

5.4 Structural Study using PND

Time of flight (TOF) powder neutron diffraction data were collected on the POLARIS diffractometer at the Rutherford Appleton Laboratory, Oxfordshire, U.K. Data were collected for ~ 2 hours; at 2 K and room temperature for $Tl_2Os_2O_{7-x}$ and at room temperature only for $Pb_2Os_2O_{7-x}$. Only data from the back-scattering bank were used in the structure refinement, whereas large *d*-spacing data obtained in the low angle bank were inspected only for the presence of magnetic reflections but none was seen for each of the samples at any temperature. Rietveld refinement of structures were undertaken using GSAS[16].

The data collected for both $Tl_2Os_2O_{7-x}$ and $Pb_2Os_2O_{7-x}$ at all temperatures could be fully indexed using a cubic unit cell except for a few weak reflections from the vanadium can, and for the thallium-containing sample, a small level of Tl_2O_3 impurity. Refinement of the structures for these data sets was carried out using the normal pyrochlore crystallographic description in the space group *Fd-3m*, using the room temperature PXD results as starting models. Refinements initially converged rapidly in each case with the use of isotropic thermal displacement parameters (TDP) for all the atoms. However, inspection of the refined values showed unreasonably large TDP values for the O2 site; for example with $Tl_2Os_2O_{7-x}$ U_{iso} was 0.07 $Å^2$ for O2 compared with 0.002-0.006 $Å^2$ for the other three atom sites. Thus in the later stages of the refinement the occupancy factors for the oxygen, and for completeness, the thallium/lead sub-lattices were probed. The O2 site occupancy refined to a value significantly below unity, in the range 0.6-0.8 in both cases, but the thallium and lead site occupancies refined to values of 1.02(3) and 1.00(2), respectively, demonstrating that this site was fully occupied. The final stages of the refinements maintained the site occupancies of all atoms at unity except for O2 and included anisotropic thermal displacement parameters for all atoms. The additional impurity phase of Tl_2O_3 was

included where necessary. Final refined cell and atomic parameters are summarised in Table 5.4, and derived bond lengths and angles of significance are given in Table 5.5. The profile fits for each data set can be found in Figures 5.3 and 5.4. The use of isotropic or anisotropic TDPs in the models had little effect upon the key positional parameters showing acceptably low correlations in these parameters for the cubic structure with low parameter numbers and well resolved reflections.

Table 5.4. Summary of derived atomic, thermal and profile fit parameters for $Pb_2Os_2O_{7-x}$ and $Tl_2Os_2O_{7-x}$; *esds* are given in the parentheses. Space group *Fd-3m*. Pb/Tl on (½,½,½), Os on (0,0,0), O1 on (x,⅛,⅛) and O2 on (⅜,⅜,⅜).

	$Tl_2Os_2O_{7-x}$ (2 K)	$Tl_2Os_2O_{7-x}$ (298 K)	$Pb_2Os_2O_{7-x}$ (298 K)
a / Å	10.27315(5)	10.29218(3)	10.35128(3)
O1 x	0.32077(11)	0.31978(7)	0.31961(5)
Tl/Pb U_{eq} × 100 Å^2	0.38(20)	1.02(2)	1.23(1)
Os U_{eq} × 100 Å^2	0.15(2)	0.25(1)	0.18(1)
O1 U_{eq} × 100 Å^2	0.76(3)	0.97(2)	0.65(1)
O2 U_{eq} × 100 Å^2	0.59(7)	1.35(7)	3.5(1)
O2 occupancy	0.69(2)	0.77(1)	0.63(1)
R_{wp} (%)	1.00	3.03	2.40
R_p (%)	1.74	6.17	5.10
χ^2	1.75	1.10	1.18

Table 5.5. Selected bond lengths and bond angles for $Tl_2Os_2O_{7-x}$ and $Pb_2Os_2O_{7-x}$.

	$Tl_2Os_2O_{7-x}$ (2 K)	$Tl_2Os_2O_{7-x}$ (298 K)	$Pb_2Os_2O_{7-x}$ (298 K)
Pb/Tl-O1 (×6) / Å	2.5862(8)	2.5982(5)	2.6144(3)
Pb/Tl-O2 (×2) / Å	2.22420(1)	2.22832(1)	2.24112(1)
Os-O1 (×6) / Å	1.9562(4)	1.9560(3)	1.9666(2)
O1-Os-O1 / °	93.27(4)	92.88(3)	92.82(2)
Os-O1-Os / °	136.36(1)	136.92(4)	137.01(3)

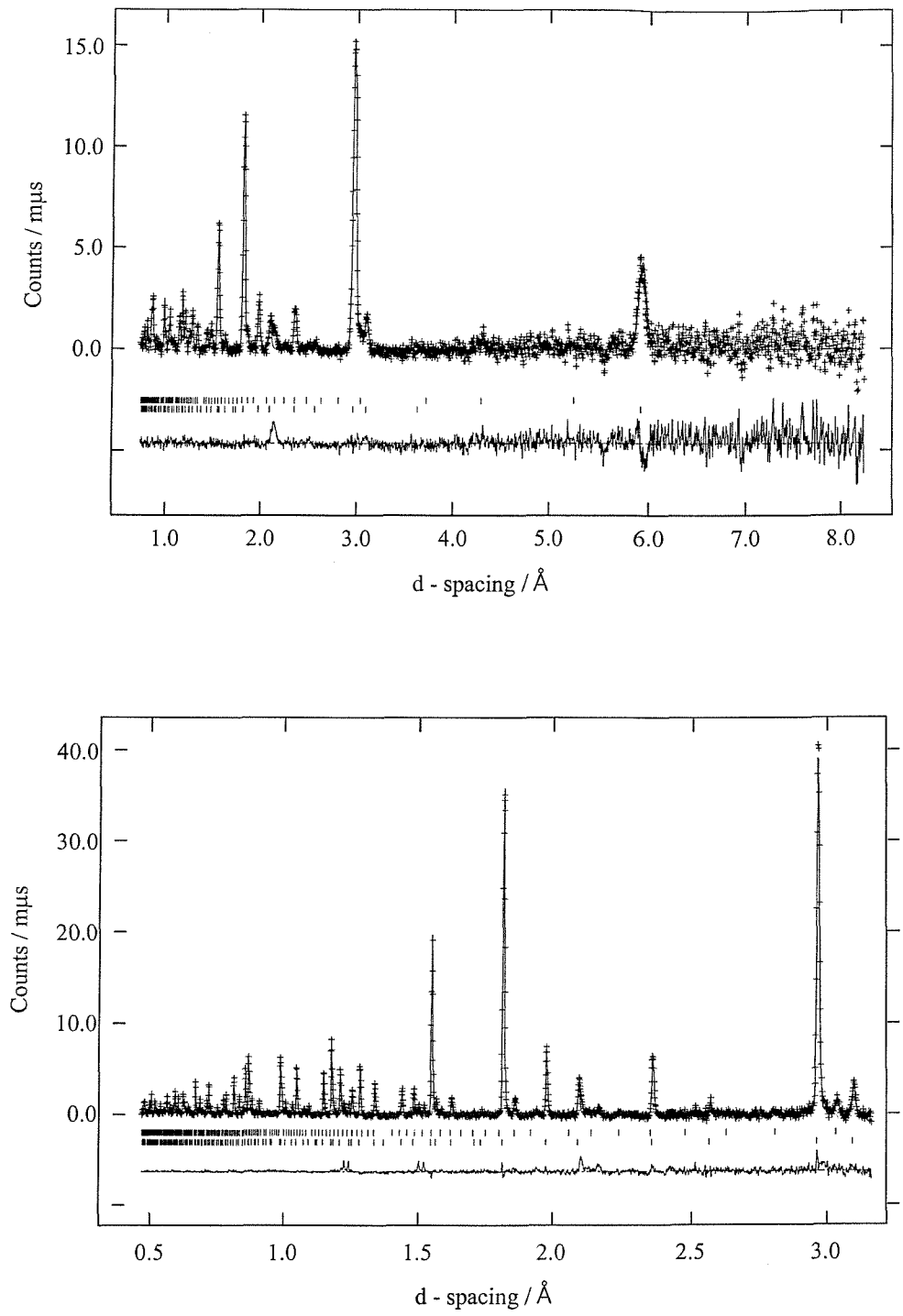

Figure 5.3. The profile fits achieved for $Tl_2Os_2O_{7-x}$ at 2 K. Crosses are experimental points, the upper continuous line the calculated profile and the lower continuous line the difference. Allowed reflection positions for $Tl_2Os_2O_{7-x}$ (lower) and Tl_2O_3 (upper) are shown with tick marks. The upper diagram displays the large *d*-spacing data showing the absence of magnetic peaks.

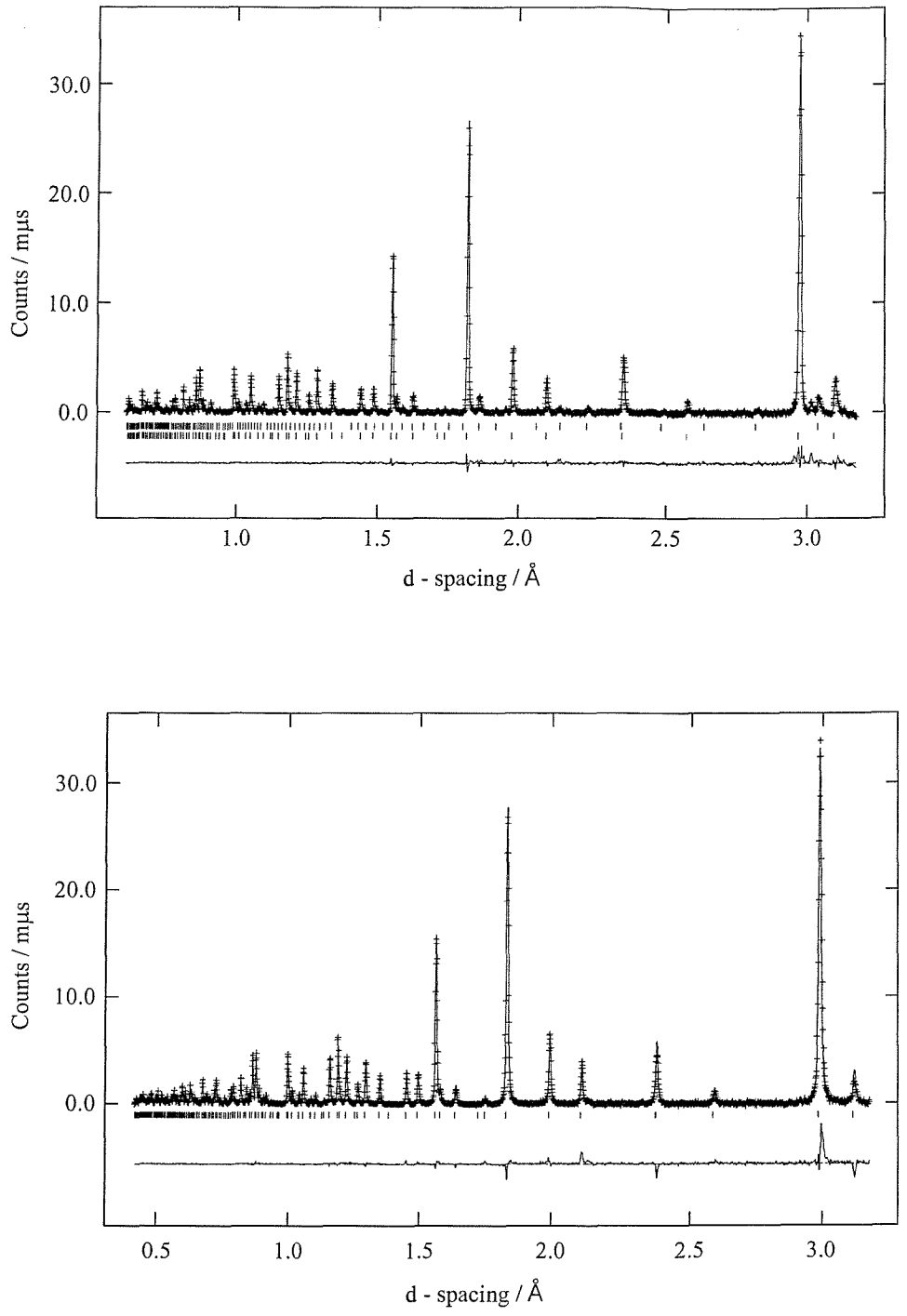

Figure 5.4. The profile fits achieved for $Tl_2Os_2O_{7-x}$ (upper diagram) and $Pb_2Os_2O_{7-x}$ (lower diagram) at 298 K. Experimental data points are shown as crosses, upper continuous line the calculated profile, lower continuous line the difference. Allowed reflection positions for $Tl_2Os_2O_{7-x}$ (lower), Tl_2O_3 (upper) and $Pb_2Os_2O_{7-x}$ are shown with tick marks on the relevant diagrams.

5.5 Discussion

5.5.1 Structure of $Tl_2Os_2O_{7-x}$

$Tl_2Os_2O_{7-x}$ adopts a cubic pyrochlore structure, though the material made by direct reaction of Tl_2O_3 and OsO_2, targeting the osmate (IV) $Tl^{3+}{}_2Os^{4+}{}_2O_7$, is oxygen deficient with the stoichiometry $Tl_2Os_2O_{6.69(2)}$ (composition obtained from the 2 K PND data). The refined composition at room temperature, $Tl_2Os_2O_{6.77(1)}$, was slightly higher presumably due to parameter correlation problems inherent in the Rietveld analysis in simultaneously refining the occupancy, thermal displacement parameters and background. These compositions are similar to the ones obtained by Takeda *et al*[15] for the corresponding thallium ruthenates synthesised under ambient pressure, $Tl_2Ru_2O_{6.71}$, at 1173 K.

Bond valence calculations for the thallium and osmium sites are given in Table 5.6 and are dependent on the assumed oxidation states. The value for osmium corresponds most closely to Os(IV) while neither Tl^+ nor Tl^{3+} produces a good fit for the thallium site producing intermediate values, though Tl^{3+} is somewhat better. This material is, therefore, probably correctly represented as $Tl^+{}_{0.23}Tl^{3+}{}_{1.77}Os^{4+}{}_2O_{6.77}$. Reaction under oxygen, especially at high pressure, would be expected to yield stoichiometric $Tl_2{}^{3+}Os_2{}^{4+}O_7$ as found by Sleight and Gillson[13].

5.5.2 Structure of $Pb_2Os_2O_{7-x}$

$Pb_2Os_2O_{7-x}$ is formed under the conditions described in section 5.2 and adopts an oxygen deficient cubic pyrochlore, with the composition of $Pb_2Os_2O_{6.63}$. The material is similar to $Tl_2Os_2O_{7-x}$ but with an enlarged lattice parameter of 10.35128(3) compared with 10.29218(3). This is reflected in longer Os-O and A-O bond lengths in the lead derivative. Initially these differences seem inconsistent with the formal osmium oxidation state which based on the use of PbO and the Os:OsO_4 starting ratio in the reaction mixture, is Os(V). However this calculation assumes that the lead remains as Pb^{2+} during the reaction.

In previous work, the observed small lattice parameter of 10.112 Å for $Pb_2Rh_2O_7$ in comparison with other $Pb_2B_2O_7$ phases has been shown to indicate that this material is correctly written as $Pb^{4+}{}_2Rh^{3+}{}_2O_7$ rather than $Pb^{2+}{}_2Rh^{5+}{}_2O_7$ or $Pb^{2+}Pb^{4+}Rh^{4+}{}_2O_7$[8].

The observed lattice parameters, bond lengths and bond valence sums found in this work, Tables 5.5 and 5.6, also support the idea that $Pb_2Os_2O_{7-x}$ is not a Pb(II)/Os(V) pyrochlore but is better described as $Pb^{2+}_{0.63}\ Pb^{4+}_{1.37}Os^{4+}_2O_{6.63}$ with mixed lead oxidation states and osmium (IV).

Table 5.5. Calculated Bond Valence Sums for the cations in $Tl_2Os_2O_{7-x}$ and $Pb_2Os_2O_{7-x}$ at 298 K. An extrapolated r_o value of 1.868 was used for Os(V) based on literature data[18].

	Bond Valence Sum	
	Full O2 site occupancy	Refined O2 site occupancy
$Tl_2Os_2O_{7-x}$		
Tl (Tl^{+1} r_0)	3.61	3.21
Tl (Tl^{+3} r_0)	2.28	2.04
Os (Os^{+4} r_0)	4.06	-
Os (Os^{+5} r_0)	4.73	-
$Pb_2Os_2O_{7-x}$		
Pb (Pb^{+2} r_0)	2.95	2.43
Pb (Pb^{+4} r_0)	2.45	2.01
Os (Os^{+4} r_0)	3.94	-
Os (Os^{+5} r_0)	4.60	-

5.5.3 Structure of Defect Pyrochlore Oxides

Previous work on other lead based precious metal pyrochlores such as $Pb_2Ru_2O_{7-x}$ and $Pb_2Ir_2O_{7-x}$ has described both oxygen deficient and stoichiometric forms[8]. Studies by Longo *et al.* were also conducted on lead pyrochlores, $Pb_2M_2O_{7-x}$ (M = Ru, Ir, and Re). They reported that their materials were highly oxygen deficient on the evidence of data collected from thermogravimetric analysis. The structures were analysed by PXD and were found to be consistent with the formal cubic pyrochlore model, space group *Fd-3m*.

The stability of defect pyrochlores with oxygen vacancies has been rationalised by Longo *et al.*[19]. The majority of the $A_2B_2O_{7-x}$ pyrochlore oxides formed with the defect structure are composed of 'A' cations such as Tl^+, Pb^{2+} and Bi^{3+}, which have a polarisable $6s^2$ lone pair of electrons. This so-called 'inert' pair of $6s^2$ electrons is the reasoning behind the proposed stability of the structure. Longo *et al.* explained that the virtual energy levels of the vacancy are comaprable in energy to the 6s and 6p levels of the 'A' ions. The latter are hybridised and mixed with the virtual levels of the vacancy, forming band states. This results in a 'trap mediated bond' through the oxygen vacancy between the 'A' ions. The net effect is the polarisation of the 'A' ions by the oxygen vacancy giving stabilisation to the A-A bonds, and ultimately the structure.

More recent investigations into defect lead pyrochlores have yielded further interesting results in terms of their structure[20 to 22]. Beyerlein *et al.* studied the structures of the defect pyrochlores $Pb_2Ru_2O_{6.5}$ and $PbTlNb_2O_{6.5}$ using powder neutron diffraction (PND)[20]. Initially, they refined $Pb_2Ru_2O_{6.5}$ in the conventional space group, *Fd-3m*, which seemed to fit the data fine and determined the oxygen stoichiometry. However on closer examination they discovered the presence of several extra weak lines forbidden in the chosen space group. The weak (420) reflection was the most visible in their neutron data, which was consistent with the loss of inversion symmetry at the cation sites, which would occur if the oxygen vacancies were ordered. Their second refinement was successfully carried out using the space group *F-4 3m,* a sub-group of *Fd-3m*, which proved the presence of oxygen vacancy ordering and a slight displacement of the lead ions in the direction of the vacancy. Oxygen vacancy ordering was also found for the $PbTlNb_2O_{6.5}$ material in their study, but a different space group was used to accommodate the ordering of the lead and thallium on the 'A' site. On the evidence of their observations, the authors predicted that oxygen vacancy ordering could be a frequently encountered phenomenon amongst oxygen deficient pyrochlores containing the post transition metal cations such as Tl^+, Pb^{2+} or Bi^{3+} on the 'A' site. This claim is supported by the recent discoveries of Kobayashi *et al.* who synthesised and structurally characterised some lead-lanthanide pyrochlores, $Pb_{2-x}Ln_xRu_2O_{7-y}$ (*Ln* = Nd, Gd)[21]. They found two monophasic regions in both the neodymium and gadolinium systems; an oxygen vacancy ordered phase with *F-4 3m* symmetry for the lead rich region, $0.0 \leq x \leq 0.2$, and a vacancy disordered phase with *Fd-3m* symmetry for the lanthanide rich region, $1.0 \leq x \leq 2.0$. Further evidence of oxygen vacancy ordering among lead pyrochlores

has been found for $Pb_2Re_2O_{7-x}$[22]. Several oxygen deficient compositions were synthesised under high pressure and structurally characterised using a number of techniques including PXD. Evidence was found from the data collected that a couple of the compositions of $Pb_2Re_2O_{7-x}$ adopted structures with the possibility of oxygen vacancy ordering, although this was not without ambiguity.

From these previous observations of related post-transition metal pyrochlore oxides, the chosen models used in this study were analysed. The PXD and PND data were carefully examined for additional lines such as the previous reports of a (420) reflection. The data collected for $Pb_2Os_2O_{6.63}$ showed no evidence of any such reflections for both PXD and PND. Likewise for $Tl_2Os_2O_{6.77}$, the data collected from PXD and PND low temperature and room temperature showed no presence of any extra lines in the patterns. However, this does not exclude beyond doubt the possibility of these materials adopting a different structure with lower symmetry, because any extra peaks that would be observed would be of very low intensity. To investigate these materials with an increased certainty of the chosen space group would require the use of a higher resolution PND, such as HRPD.

5.5.4 Physical Properties

The physical properties of $Pb_2Os_2O_{6.63}$ and $Tl_2Os_2O_{6.77}$ were investigated only at room temperature by using infra-red spectroscopy and resistivity measurements. The resistivity measurements were carried out using the four-probe technique on a small pellet pressed under ~ 10 tonnes/cm^2 (described in Chpt. 2).

The resistivity measured for both materials showed metallic conductivity, $\rho \sim 10^{-4}$ Ωcm. Further evidence of room temperature metallic conductivity for both materials was found with infra-red spectra, which showed no absorption bands for both phases, which is characteristic for metallic compounds.

Previous work carried out on lead osmate pyrochlores has shown the materials to display metallic behaviour[5 to 8], in agreement with these findings. In the case of the thallium material, the observed behaviour is similar to the result found for $Tl_2Ru_2O_{6.71}$ by Takeda *et*

al.[15], which also showed metallic type conductivity. Takeda *et al.* showed that the stoichiometry of the $Tl_2Ru_2O_7$ phase greatly influenced the electronic properties. While $Tl_2Ru_2O_{6.5}$ shows metallic behaviour at room temperature, the incorporation of thallium vacancies, as $Tl_{1.8}Ru_2O_7$, or full oxidation, as in $Tl_2Ru_2O_7$, generates materials with metal/insulator transitions at ~ 100 K. Therefore, further definition of the relationship between stoichiometry and electronic properties in this system would be of interest to see if similar behaviour is exhibited.

5.6 Conclusions

Lead and thallium osmium(IV) pyrochlores have been readily obtained using sealed tube reactions at ambient pressure, rather than the high pressure techniques previously employed by previous workers to obtain the phases. Materials formed under these conditions, however, are deficient in oxygen. In addition, evidence supports that there is a mixing of oxidation states on the 'A' cation site for both materials, inferred from accurately measured bond lengths.

The thallium and lead osmate pyrochlores produced in this study were both found to crystallise in the conventional cubic pyrochlore lattice with space group *Fd-3m.* No evidence was found to support the presence of oxygen vacancy ordering, described by other workers for related post-transition metal pyrochlore oxides.

The results for the lead pyrochlore in this work are in agreement with the findings of Shaplygin and Lazarev[7] who produced a number of defect lead osmate pyrochlores with oxygen deficiencies, using different synthesis methods. The metallic conductivity measured at room temperature for $Pb_2Os_2O_{6.63}$ is also similar to their findings, however, the structure in their work was not accurately determined with respect to composition and ion distributions.

5.7 References

[1] M. Hanawa, Y. Muraoka, T. Tayama, T. Sakakibara, J. Yamaura, Z. Hiroi, *Phys. Rev. Lett.* **87** (18) 187001 (2001).

[2] F. Jona, G. Shirane and R. Perpinsky, *Phys. Rev.* **98** 903 (1955).

[3] E. C. Subbarao, *J. Am. Ceram. Soc.* **44** 92 (1961).

[4] G. Burchard and W. Rüdorff, *Z. anorg. allg. Chem.* **447** 149 (1978).

[5] J. P. Badaud and J. Omaley, *Compt. Rend.Acad. Sci.* **C274** 178 (1972).

[6] R. F. Sarkozy and B. L. Chamberland, *Mat. Res. Bull.* **8** 1351 (1973).

[7] I. S. Shaplygin and V. B. Lazarev, *Russ. J. Inorg. Chem.* **23**(3) 403 (1978).

[8] A. W. Sleight, *Mat. Res. Bull.* **6** 775 (1971).

[9] Y. Shimikawa, Y. Kubo and T. Manako, *Nature (London)* **379** 53 (1996).

[10] M. A. Subramanian, B. H. Toby, A. P. Ramirez, W. J. Marshall, A. W. Sleight and G. H. Kwei, *Science* **273** 81 (1996).

[11] G. H. Kwei, C. H. Booth, F. Bridges and M. A. Subramanian, *Phys. Rev. B* **55**(2) R688 (1997).

[12] Y. Shimikawa, Y. Kubo, T. Manako, Y. V. Sushko, D. N. Krgyriou and J. D. Jorgensen, *Phys. Rev. B* **55**(10) 6399 (1997).

[13] A. W. Sleight and J. L. Gillson, *Mat. Res. Bull.* **6** 781 (1971).

[14] H. S. Jarrett, A. W. Sleight, J. F. Weiher, J. L. Gillson, C. G. Frederick, G. A. Jones, R. S. Swingle, D. Swartzfager, J. E. Gulley and P. C. Hoell, *"Valence Instabilities and Related Narrow-Band Phenomena"* (R. D. Parks, Ed.), p.545, Plenum, New York (1977).

[15] T. Takeda, M. Nagata, H. Kobayashi, R. Kanno, Y. Kawamoto, M. Takano, T. Kamiyama, F. Izumi and A. W. Sleight, *J. Solid State Chem.* **140** 182 (1998).

[16] A. C. Larson and R. B. Von Dreele, *Generalsied Structure and Analysis System,* MS-H805, Los Almos, NM 87545 (1990).

[17] R. D. Shannon, *Acta Cryst.* **A32** 751 (1976).

[18] D. Altermatt and I. D. Brown, *Acta Crystallogr. Sect. B* **53** 135 (1997).

[19] J. M. Longo, P. M. Raccah and J. B. Goodenough, *Mat, Res. Bull.* **4** 191 (1969).

[20] R. A. Beyerlein, H. S. Horowitz, J. M. Longo and M. E. Leonowicz, *J. Solid State Chem.* **51** 253 (1984).

[21] H. Kobayashi, R. Kanno, Y. Kawamoto, T. Kamiyama, F. Izumi and A. W. Sleight, *J. Solid State Chem.* **114** 15 (1995).

[22] A. M. Abakumov, R. V. Shpanchenko, E. V. Antipov, E. M. Kopnin, J. J. Capponi, M. Marezio, O. I. Lebedev, G. Van Tendeloo and S. Amelinckx, *J. Solid State Chem.* **138** 220 (1998).

Chapter Six

A Structural Study of Superconducting $Cd_2Re_2O_7$ using Powder Neutron Diffraction

6.1 Introduction

The synthesis and properties of $Cd_2Re_2O_7$ were first reported by Donohue *et al*[1] in 1965. The material was found to be metallic with low resistivity of $\rho_{(300\ K)} \sim 2.0\times10^{-3}$ Ωcm. Recently, there has been the discovery of superconductivity in $Cd_2Re_2O_7$, which adopts a pyrochlore structure type and has $T_c \sim 1$ K. This has promoted major efforts investigating the properties of this material[2 to 4]. Such work has included detailed studies of the electronic and magnetic properties in the superconducting and normal states and these results show that the Cooper pairs are probably composed of heavy quasi-particles[5 to 7]. Reported structural work on this material has been limited to x-ray diffraction measurements. The lattice parameter variation below room temperature shows a contraction down to 200 K followed by expansion before further contraction at the very lowest temperatures[8]. These changes in lattice parameter were initially ascribed to a single, second order phase transition in this material starting below 200 K but not complete until below 150 K. Hiroi *et al.* have shown that the appearance of additional reflections in single crystal data and synchrotron x-ray powder data are not consistent with the normal *Fd-3m* space group of pyrochlores that is adopted by $Cd_2Re_2O_7$ at room temperature[9,10]. They have suggested that the low temperature phase probably crystallises in the space group *F-43m*, or possibly $F4_132$, based on the sub-groups of *Fd-3m* and the Miller indices of the additional reflections observed in the sub-200 K diffraction data. Castellan *et al.* have indicated that the material may undergo a transition of a tetragonally distorted form based on the presence of shoulders on some reflections in their single crystal data[11]. However, this splitting is extremely small with lattice parameters given as 10.221 Å and 10.228 Å in the low temperature phase. A second phase transition, near to 120 K, has also been reported by Hiroi *et al.* on the basis of physical property measurements though structurally this seems to be an extremely weak transition with little evidence in the form of changes in reflection intensities[9].

Further local structural information has been derived from nuclear quadrupole resonance (NQR) measurements on ^{185,187}Re and nuclear magnetic resonance (NMR) measurements using the ^{111}Cd nucleus[12]. These results imply that the rhenium site symmetry at 5 K is lower than 3-fold with a small measured asymmetry co-efficient. However, it should be noted that this small, measured asymmetry is in the local environment of rhenium rather

than the average bulk structure determined through diffraction methods. While a narrow peak width implies a lack of non-uniform charge density, domains of locally shifted but environmentally equivalent rhenium ions could be averaged in the bulk material. No NQR information was reported for $Cd_2Re_2O_7$ between 100 and 200 K to support the choice of space group in this temperature region.

Overall, it is clear that no model has yet been presented for the structure of $Cd_2Re_2O_7$ below room temperature in any of the regions of interest, *i.e.* between 100 K and 200 K, where the material undergoes its initial transition from *Fd-3m*, between 2 K and 100 K below the second proposed transition or in the superconducting region below 1 K. The reasons for this are derived from complexity and subtlety of the phase transitions and the limitations of the techniques used to investigate this material. For example, extreme care must also be taken when cooling single crystals through phase transitions in terms of the formation of mosaics of sub-crystallites and x-ray methods are relatively insensitive to small structural distortions of oxides. Therefore powder neutron diffraction is the method of choice for investigating $Cd_2Re_2O_7$ due to (i) the need to study the structure through one or more phase transition and (ii) the requirement to accurately determine the oxygen sub-lattice in the presence of the two heavy transition metals.

However, powder neutron diffraction studies of $Cd_2Re_2O_7$ formally have two significant problems. Firstly natural cadmium is a strong neutron absorber leading to experimental difficulties. Secondly the intensity and resolution of many neutron diffractometers is significantly lower than that of x-ray sources, potentially making subtle structural distortions difficult to observe. The initial problem may be overcome by using a sample isotopically enriched with a non-absorbing isotope; the second requires application of the highest resolution powder neutron diffractometers.

This chapter reports the synthesis of $Cd_2Re_2O_7$ at ambient pressure using a ^{114}Cd isotope to enable powder neutron diffraction data collection. The structure for $Cd_2Re_2O_7$ between 320 mK and room temperature is investigated, and the structure in the superconducting phase is defined for the first time. Comparisons to previous observations by other workers are made.

6.2 Preparation of $^{114}Cd_2Re_2O_7$

Samples of $Cd_2Re_2O_7$ were prepared by grinding together high purity stoichiometric mixtures of CdO (99.8%), Re (99.995%) and Re_2O_7 (99.9+%) under an argon atmosphere. The CdO was pre-dried in a furnace at 400 °C for 24 hours. As ^{113}Cd is a highly absorbing isotope (absorption cross-section = 2.06×10^{-20} cm^2), natural abundance CdO (containing *ca.* 12 % ^{113}Cd) could not be used for neutron diffraction work. A ^{114}Cd (absorption cross-section = 3.40×10^{-25} cm^2) enriched sample of CdO was used (99% ^{114}Cd, Trace Sciences International). The mixture was loaded into a silica ampoule and sealed under vacuum, and then heated at 800 °C for 1 day then furnace cooled to room temperature. The silica ampoule was opened and the product was reground, resealed and heated to 800 °C for a further 3 days. Powder x-ray diffraction data were recorded on the black product using a Siemens D5000 diffractometer operating with Cu $K_{\alpha1}$ radiation. The pattern was consistent with phase pure pyrochlore product material, with a cubic unit cell of dimension a = 10.217(4) Å.

6.3 Variable Temperature Powder Neutron Diffraction

Powder neutron diffraction data were collected on the high resolution constant wavelength diffractometer D2B at the Institut Laue-Langevin, Grenoble, operating at the optimum wavelength $\lambda \sim 1.59$ Å. The sample, ~1 g, was placed into a 7 mm diameter vanadium can and cooled using a ^3He dilution refrigerator insert housed inside a standard orange cryostat. A full $5 \leq 2\theta/° \leq 160$ pattern was obtained by stepping the 64 detectors through 2.5 ° in increments of 0.05 °. The scan was repeated four times and data summed to enhance the statistics. Data were collected for 8 hours at 320 mK, 5 K and 220 K, and for 4 hours at 290 K. Further powder neutron diffraction data were collected at 150 K and 250 K using the high intensity, medium resolution time-of-flight POLARIS diffractometer at the Rutherford Appleton Laboratory, Oxfordshire, U.K. and a scan time of 6 hours per temperature.

Reduction of the D2B data involved summing the four data blocks obtained at each temperature and simultaneously calibrating the data to correct for detector efficiency discrepancies. An instrument calibration run had been carried out immediately prior to the

experiment and an instrument parameter file using the refined wavelength from this data was 1.5966 Å. Data beyond 146° was discarded due to the presence of reflections from the cryostat body.

6.3.1 Structure Analysis

Data were analysed using the GSAS suite of programmes[13]. In the initial stages of the refinement only the higher resolution data from D2B were analysed. The presence of several (nine) aluminium peaks from the cryostat necessitated placing these in excluded regions. Data were corrected for a small amount of residual sample absorption caused by the presence of approximately 0.2% of ^{113}Cd in the sample.

In the initial stages of the data analysis the standard, high symmetry pyrochlore model in *Fd-3m* was used for all four, high and low temperature, data sets. Refined parameters included, in order of incorporation into the refinement, the scale factor, background parameters (cosine Fourier series - 12 parameters in total), peak shape parameters (U, V, W and asymmetry parameter), the O(1) positional parameter, *x*, and isotropic thermal displacement parameters for all atoms. Attempts to incorporate anisotropic thermal displacement parameters (TDPs) for all atoms did not improve the profile fit significantly and lead to one or two unphysical values presumably a result of the low number of observed reflections and weak modulations in the background, caused by the cryostat. Therefore anisotropic displacement parameters were only included for the O(1) site, which, because of its low symmetry environment, might be expected to show the largest anisotropy in its thermal displacement behaviour. The results of these refinements are summarised in Table 6.1 in terms of the final crystallographic parameters, derived bond lengths of interest and profile fit parameters. The final profile fit achieved to the 220 K data is shown in Figure 6.1.

In order to determine how well the data were being fitted in the *Fd-3m* space group Le Bail extractions were undertaken on each data set. This allows a fit to the data to be undertaken based on peak shape and positions alone. Peak fitting at each allowed reflection position occurs without calculation of the peak intensity from the atomic positions and indicates how good a profile fit could be achieved to the data within the restraint of that particular space group. Calculations were also carried out for the space group *F-43m* which allows any

additional intensity for the reflections such as (*00l*) l=2n and (*0kl*) *k+l* = 4n+2 to be fitted. Overall there is little difference between the two fits achieved in the different space groups though there are some small improvements for the low temperature (5 K and 320 mK) data sets which would be derived from fitting additional profile intensity in regions where peaks are forbidden in *Fd-3m*. *Chi* squared values obtained from this analysis are also summarised in Table 6.1.

Table 6.1. Final crystallographic parameters for structure refinement in *Fd-3m*. With Cd on (½,½,½), Re on (0,0,0) O(1) on (*x*,1/8,1/8) and O(2) on (3/8,3/8,3/8). *Esds* are given in parentheses.

Temperature / K	290.0	220.0	5.0	0.32
a / Å	10.2352(5)	10.2344(3)	10.2376(4)	10.2374(4)
Cd U_{iso} ×100/Å^2	2.51(17)	2.53(11)	2.44(11)	2.63(12)
Re U_{iso} ×100/Å^2	0.38(10)	0.18(6)	-0.01(6)	0.10(6)
O(1) *x*	0.3172(5)	0.3169(3)	0.3175(3)	0.3173(4)
O(1) U_{11} ×100/Å^2	1.50(23)	1.35(15)	1.49(15)	1.65(16)
O(1) U_{33} ×100/Å^2	1.18(16)	1.15(10)	0.71(9)	0.69(10)
O(1) U_{23} ×100/Å^2	0.39(20)	0.06(13)	-0.06(12)	0.45(13)
O(2) U_{iso} ×100/Å^2	0.80(23)	0.75(14)	0.78(14)	0.99(17)
U	78(9)	82(6)	79(6)	90(6)
V	-209(26)	-216(16)	-204(17)	-235(18)
W	275(15)	270(10)	276(10)	289(11)
Cd-O(1) /Å	2.602(4)	2.604(2)	2.601(2)	2.602(3)
Cd-O(2) /Å	2.2160(1)	2.21581(5)	2.21649(6)	2.21646(6)
Re-O(1) /Å	1.936(2)	1.935(1)	1.938(1)	1.937(1)
O(1)-Re-O(1) /°	88.1(2)	88.2(1)	88.0(1)	88.1(1)
Chi sq.	1.01	1.29	1.47	1.77
R_{wp} %	8.94	5.77	6.33	7.01
R_p %	6.81	4.48	4.88	5.42
Chi sq. Le Bail *Fd-3m*	0.95	1.18	1.31	1.64
Chi sq. Le Bail *F-43m*	0.96	1.19	1.29	1.63

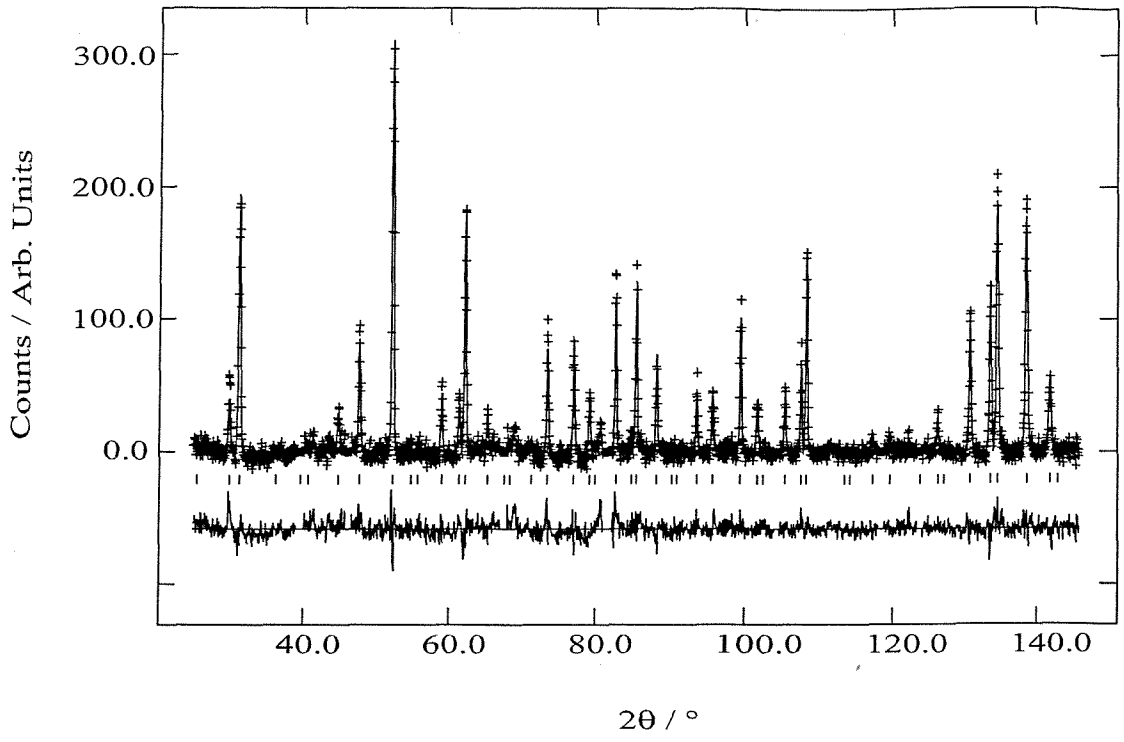

Figure 6.1. Final profile fit achieved to the 220 K data in *Fd-3m*. Cross marks are observed intensities, upper continuous line the calculated profile and lower continuous line the difference. Tick marks give reflection positions in *Fd-3m*. Nine small (<1 °) regions have been excluded in the range 10-146 ° due to aluminium peaks from the cryostat.

Further inspection of the profile fit figures-of-merit obtained for *Fd-3m* in Table 6.1 also indicates that more significant deficiencies exist for the low temperature models. This may, in part, arise from the lower quality of these data sets but the major contribution would be in poor fitting of reflection intensity at reflection positions common to the *Fd-3m* and *F-43m* models. This can be seen in some areas of the profiles as shown in Figure 6.2 which shows the Le Bail fits between 2θ = 100 and 120 ° in the space group *F-43m*. The reflection near 114° is reasonably strong in the 5 K data set but not present with any significant intensity in the 220 K data set. This reflection may be indexed as just the {8,6,4} in the *Fd-3m* space group but the {*8,6,4*} and {*10,4,0*} together in *F-43m* where reflections with (*hk0*) and *h+k* = 2n become allowed. Of particular note is the fact that the {*8,6,4*} reflection has zero intensity for the regular pyrochlore structure where only the 48f, 16d, 16c and 8a sites are filled. This is also true for the {*4,4,2*}, {*4,4,6*} and {*2,4,8*} reflections which do not have {*h+k+l*} = 4n with {*h, k, l*} =2n. It has also been reported that the {*10,4,0*} is one reflection

which gains significant intensity in the single crystal x-ray diffraction data below 220 K[9]. Hence the presence of intensity at 114 ° is definitive evidence of a lower symmetry space group that *Fd-3m* or displacement of atoms within *Fd-3m* onto lower symmetry sites, which then gives intensity to the {*2,4,8*} reflection. Given the evidence from x-ray diffraction methods that this intensity is at least in part due to the {*10,4,0*} further refinement was undertaken in the *F-43m* space group.

A structure model for pyrochlore in the *F-43m* space group was adapted from that used by Kennedy[14] for the oxide ion deficient structure of $Pb_2Ir_2O_{6.5}$. Analysis was originally undertaken using the 5 K data set and then extended to the data collected at the other temperatures. The refinement proceeded well and converged rapidly using the same systematic parameter introduction method given above for the *Fd-3m* space group. Isotropic thermal displacement parameters were used for all atoms. For the two structurally similar oxygen sites at (0,0,0) and (¾,¾,¾) the TDPs were highly correlated and tended to diverge to one large positive and one negative value so the TDPs for these two sites were constrained to be equal. The possibility of oxygen deficiency on these sites, as has been found previously in $Pb_2(Ru,Ir_2)O_{7-x}$ was probed but refinement of either led to values slightly in excess of unity and therefore these were returned to, and maintained at, full occupancy. Final cycles of refinement produced a marked improvement in *chi* squared values dropping from 1.47 for *Fd-3m* to 1.40 for *F-43m* significantly closer to the idealised Le Bail extraction value of 1.3. The final crystallographic model is summarised in Table 6.2, the profile fit achieved shown in Figure 6.3 and derived bond lengths and angles of interest given in Table 6.3. Analysis of the 320 mK data set using this model also markedly improved the fit to the profile with an appreciable reduction in *chi* squared; results are again summarised in Tables 6.2 and 6.3. For the 220 K and 290 K data sets refinement in *F-43m* proved problematical; while this could be achieved there was no improvement in the profile fit parameters and large damping factors had to be imposed on all atomic positions and TDPs. This provides further support for the conclusion that the structure of $Cd_2Re_2O_7$ at T > 200 K is best modelled in the higher symmetry space group.

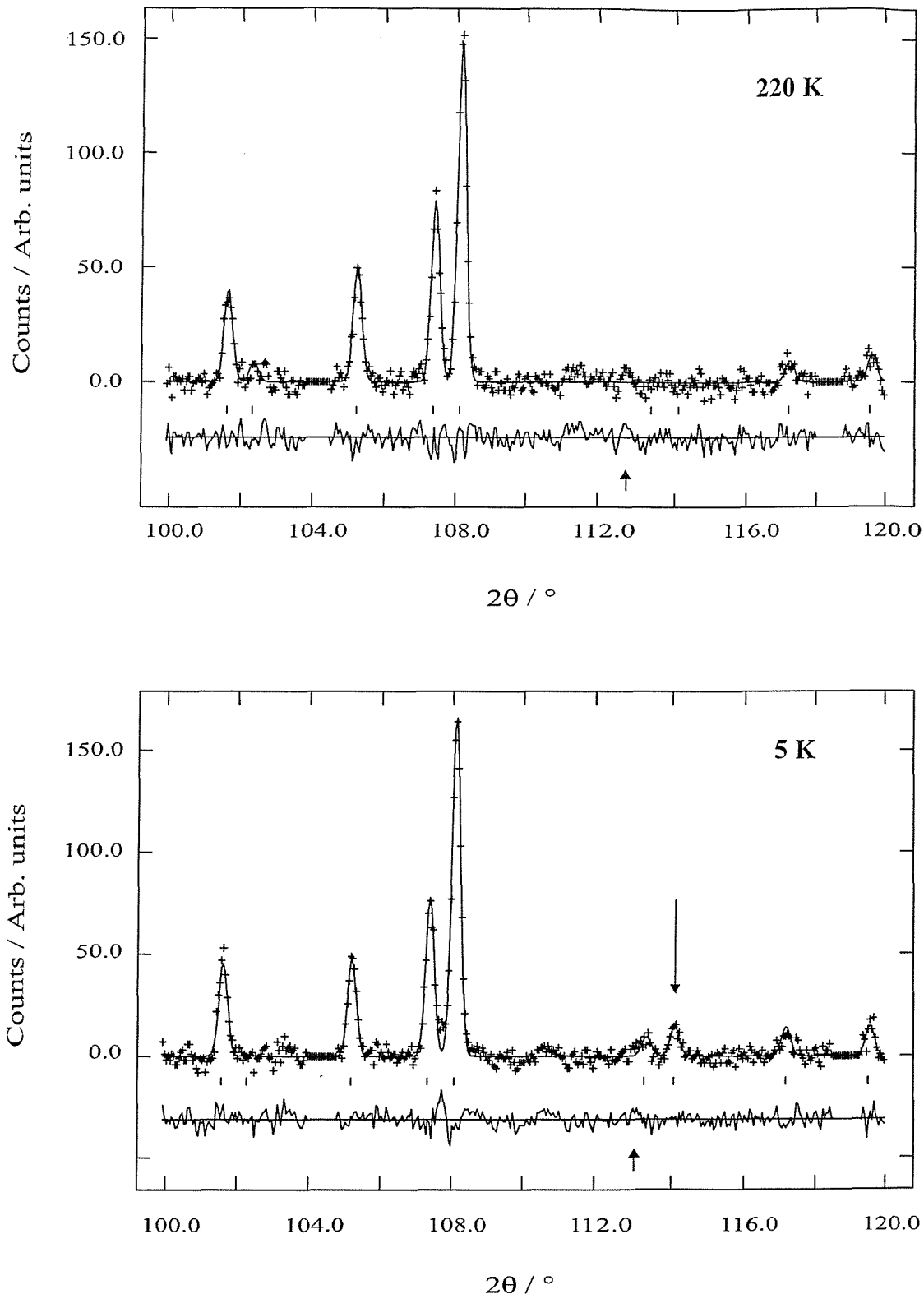

Figure 6.2. Sections of the diffraction data between 100 and 120° at 220 and 5 K. The presence of the {10,4,0} reflection in only the low temperature data sets is clear. The very weak peak at 112.5° (small lower arrow) is from the vanadium can.

Table 6.2. Final crystallographic parameters for structure refinement in *F-43m* at 5 K and 320 mK. With Cd on (*x*,*y*,*z*), Re on (*x*,*y*,*z*), O(1) on (*x*,0,0), O(2) on (*x*,¼,¼), O(3) on (0,0,0) and O(4) on (¾,¾,¾). Upper row is 5 K data and lower row 320 mk data. *Esds* are given in parentheses. Refined lattice parameters 10.2383(3) Å (5 K) and 10.2383(3) Å (320 mK).

Atom	*x*	*y*	*z*	$U_{iso}\times100/Å^2$
Cd	0.8703(7) 0.8716(7)	0.8703(7)	0.8703(7)	2.06(12) 2.26(12)
Re	0.3741(4) 0.3735(5)	0.3741(4)	0.3741(4)	0.00(5) 0.06(6)
O(1)	0.2994(8) 0.2990(8)	0.00	0.00	0.33(14) 0.28(5)
O(2)	0.4329(7) 0.4324(8)	0.25	0.25	1.14(22) 1.10(23)
O(3)	0.0	0.0	0.0	0.58(15) 0.88(17)
O(4)	0.75	0.75	0.75	0.58

Table 6.3. Derived bond lengths and angles of interest at 5 K and 320 mK for the refined *F-43m* model.

Bond length / Å	5K	320mK	Bond angle /°	5K	320mK
Re-O(1) × 3 Re-O(2) × 3	1.977(6) 1.894(5)	1.984(6) 1.888(6)	O(1)-Re-O(1) O(1)-Re-O(2) O(2)-Re-O(2)	94.5(3) 88.4(2) 88.5(4)	94.4(3) 88.4(2) 88.8(4)
Cd-O(1) × 3 Cd-O(2) × 3 Cd-O(3) × 1 Cd-O(4) × 1	2.558(7) 2.666(6) 2.299(12) 2.134(12)	2.551(7) 2.670(6) 2.277(13) 2.157(13)	Re-O(2)-Re Re-O(1)-Re	143.1(6) 134.5(6)	142.8(6) 134.8(6)

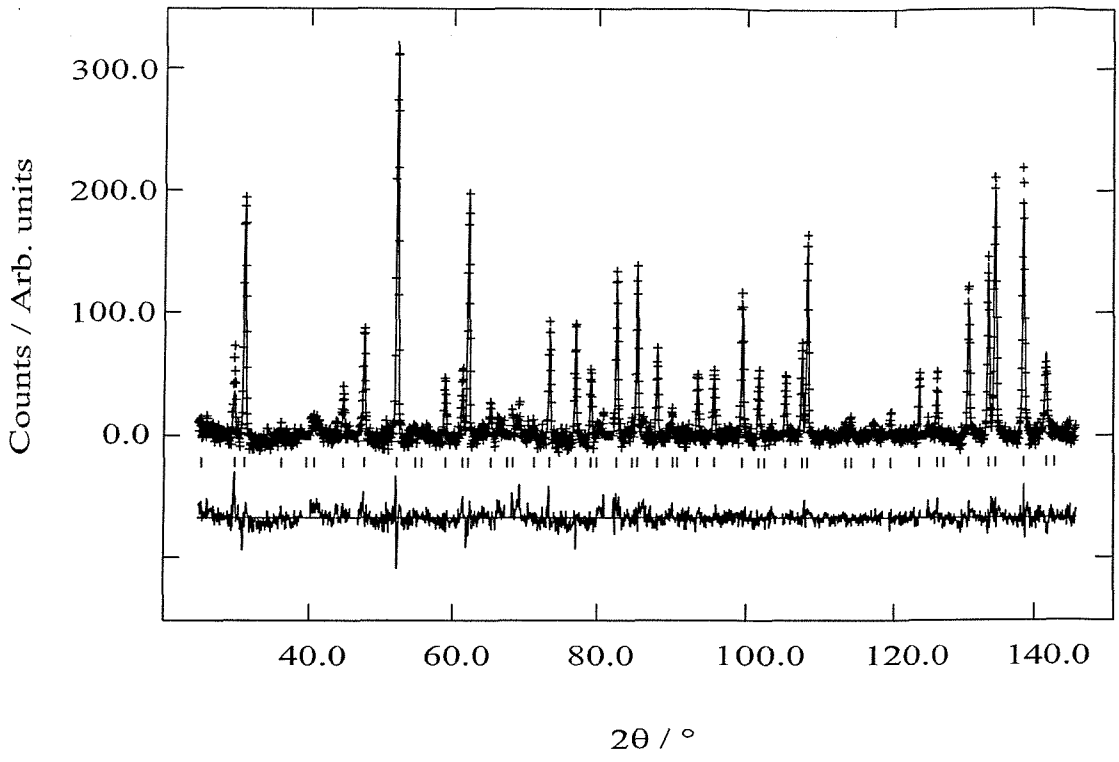

Figure 6.3. Final profile fit achieved to the 5 K data in *F-43m*. Cross marks are observed intensities, upper continuous line the calculated profile and lower continuous line the difference. Tick marks give reflection positions in *F-43m*. Nine small regions (<1°) have been excluded in the range 10-146° due to aluminium peaks from the cryostat.

Finally the possibility of a transition to a lower symmetry crystal system, as reported by Castellan *et al.*[11] was investigated. D2B is a high resolution powder diffractometer (at best $\Delta d/d = 6\times10^{-4}$) and formation of a tetragonal unit cell with dimensions 10.221 and 10.228 Å should be visible in the peaks. Figure 6.4 shows a dummy histogram calculated for the *{12,0,0}/{0,0,12}/{8,8,4}/{4,8,8}* reflection set calculated using these lattice parameters compared with the experimental peak observed in this region at 5 K. It is clear that a significant peak broadening should be observed. Similar calculations in the high resolution sections of the data below 100° also indicate that peak broadening or shoulders should be visible. Furthermore inspection of the half-width parameters refined for the 5 K and 220 K data sets, Table 6.1, show these to be identical implying that a simple, single peak can be fitted to each of the reflections. There is therefore, no evidence from this data for a reduction of cell symmetry from cubic to tetragonal. We cannot rule out a very small distortion but it would have to be substantially less that the *c/a* value 1.0007 reported

previously probably of the order of 1.0004. It is noteworthy that Hiroi *et al.* did not report a tetragonal unit cell in their synchrotron powder x-ray diffraction study of $Cd_2Re_2O_7$, where any peak splitting should have been observable with high intensity, high resolution diffraction data[10].

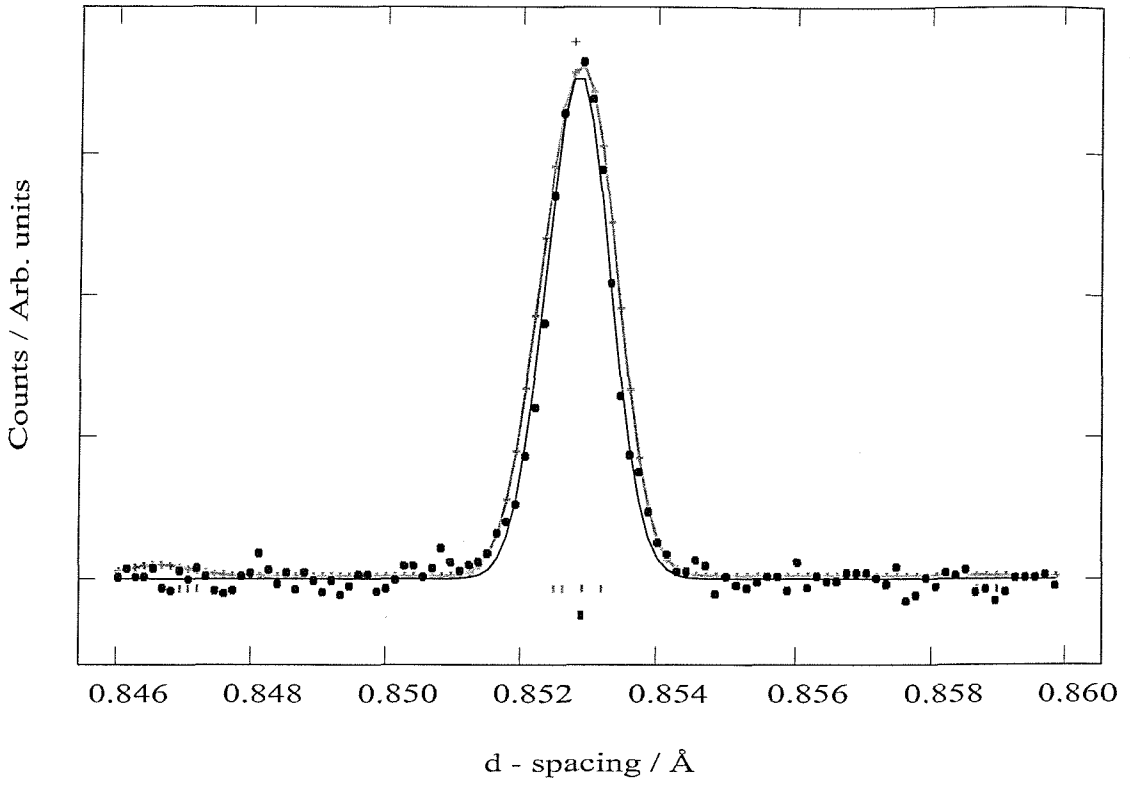

Figure 6.4. Observed (thin black line) and calculated (thicker gray line) peak shapes for the {12,0,0}/{8,8,4} sets of reflections using a tetragonal crystal system with a = 10.221 Å and c=10.228 Å and standard D2B peak width parameters. Tick marks show calculated peak positions.

Analysis of the POLARIS data collected, at 150 K and 250 K, was subsequently undertaken again using the two cubic, crystal system models. Inspection of the 150 K data showed a weak {*10,4,0*} reflection consistent with the *F-43m* space group though this reflection was slightly weaker than in the 5 K and 320 mK data sets collected on D2B, Figure 6.5. No peak intensity corresponding to the {*10, 4, 0*} / (*8, 6, 4*} reflections was observed in the 250 K data. Refinements were therefore completed in the *Fd-3m* (250 K) and *F-43m* (150 K) space groups respectively. Convergence was rapid for the higher temperature data set but

less robust for the 150 K data. The origin of this slow convergence was found to be in the positional parameters, which only diverged slightly from the special positions equivalent to those of the *Fd-3m* description and presumably the lower resolution of the POLARIS data. Small damping factors applied to the positional parameter shifts overcame the tendency for these atoms to oscillate close to the special positions and the final *chi* squared value obtained in the *F-43m* description were markedly lower than that in *Fd-3m*. Final atomic positions are summarised in Table 6.4i and 6.4ii.

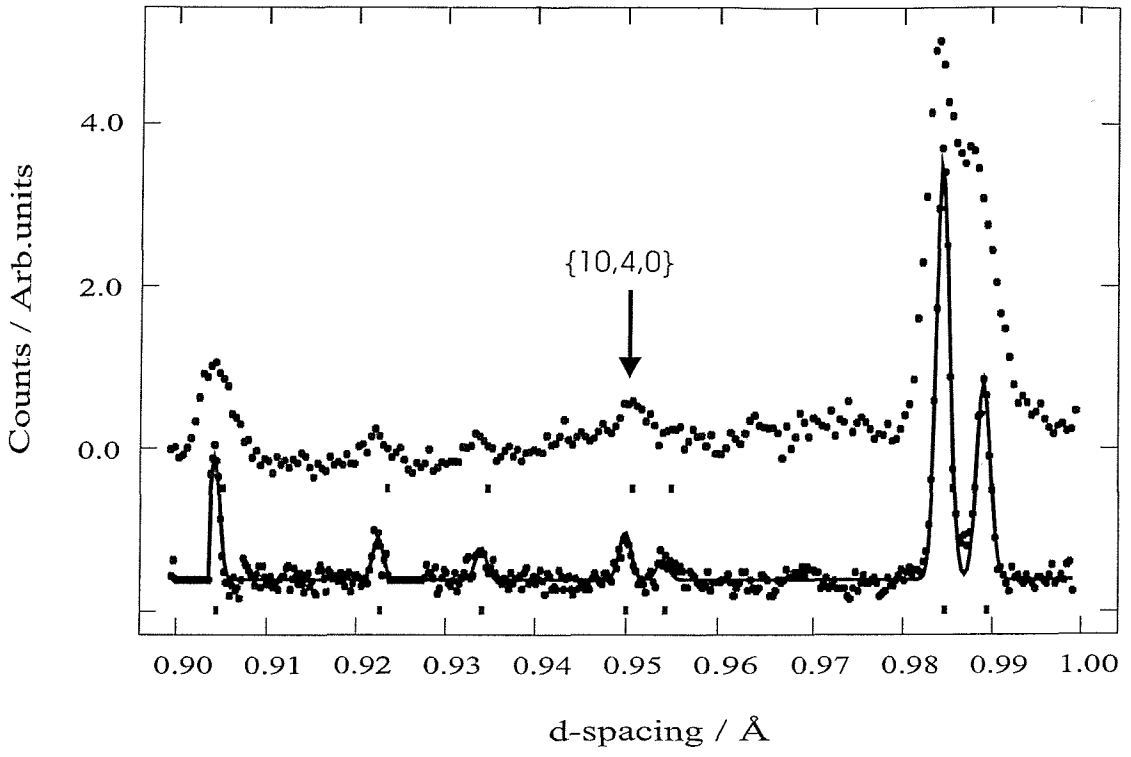

Figure 6.5. Sections of the POLARIS data at 150 K (upper) and D2B at 5 K (lower) in the d-spacing range 0.9 - 1.0 Å showing the presence of a weak {10,4,0} reflection at 150 K.

Lattice parameters derived for $Cd_2Re_2O_7$ and their variations as a function of temperature are in good agreement with literature values[8]. The contraction between 290 K and 220 K of 0.0008 Å is followed by a marked expansion of 0.0032 Å between 220 K and 5 K. The small relative discrepancies between instruments for the same sample are typical of differences between x-ray and neutron diffraction methods and constant wavelength and TOF data without the use of an internal standard.

Table 6.4. Structural parameters for $Cd_2Re_2O_7$ obtained from the POLARIS data; *Esds* are given in parentheses.

i) 250 K *Fd-3m* a = 10.2131(1) Å, Re-O(1) = 1.9315(7) Å.

Atom / parameter	
Cd 100 × U_{iso}	0.31(4)Å^2
Re 100 × U_{iso}	0.02(2)Å^2,
O(1) x	0.3161(2),
O(1) 100 × U_{11}	1.26(7) Å^2
O(1) 100 × U_{33}	0.51(4) Å^2
O(1) 100 × U_{23}	0.24(5) Å^2
O(2) 100 × U_{iso}	0.40(5) Å^2

ii) 150 K *F-43m* a = 10.2152(1) Å, Re-O(1) = 1.965(3) Å (×3), Re-O(2) = 1.893(3) Å (×3).

Atom	x	y	z	100×U_{iso}/Å^2
Cd	0.8767(5)	0.8767(5)	0.8767(5)	1.06(5)
Re	0.3743(2)	0.3743(4)	0.3743(4)	0.07(2)
O(1)	0.3010(3)	0.00	0.00	0.35(4)
O(2)	0.4330(3	0.25	0.25	0.59(6)
O(3)	0.0	0.0	0.0	0.42(4)
O(4)	0.75	0.75	0.75	0.42(4)

6.4 Discussion and Conclusions

The low temperature (<200 K) structure of polycrystalline $Cd_2Re_2O_7$ can be best modelled in the space group *F-43m*. In this structural description a marked distortion of the ReO_6 octahedra occurs as shown in Figure 6.6. Comparison with the regular ReO_6 octahedra of the high temperature form show that positional displacements in both the rhenium and oxygen sub-lattices contribute to this distortion, which produces a trigonal environment for rhenium with three oxygens at 1.977(6) Å and three at 1.894(5) Å at 5 K. These values should be compared with the six equivalent Re-O distances of 1.936(2) Å at 290 K. The bond angles within the ReO_6 octahedra at 5 K show small deviations from 90° but these are

similar to those found in the room temperature structure. The cadmium environment also undergoes a reduction in symmetry in the O(5)-Cd-O(6) unit, which is derived from the symmetrical O(2)-Cd-O(2) moiety in the *Fd-3m* pyrochlore structure, producing alternating long and short interactions at 2.299 Å and 2.134 Å, instead of 2.216 Å (×2).

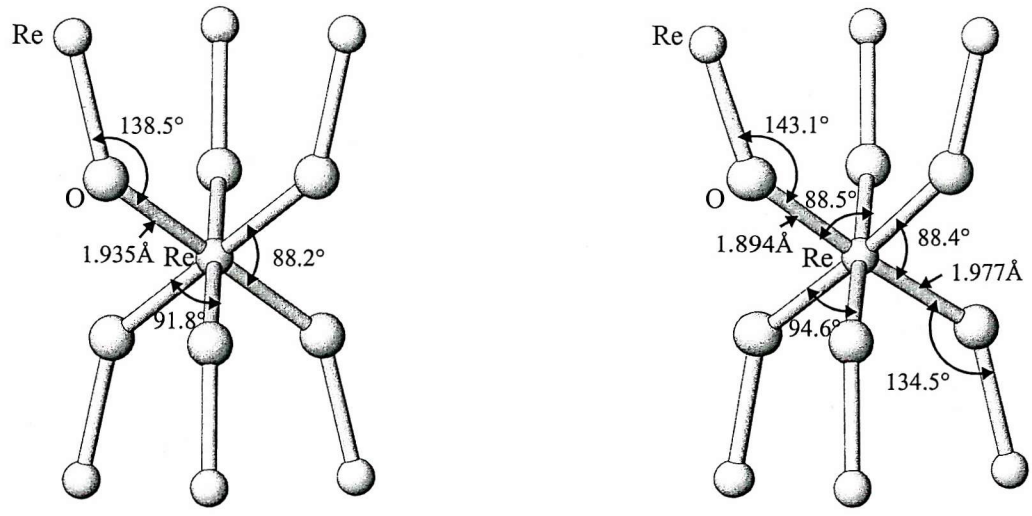

Figure 6.6. Comparison of the rhenium atom environments in the high temperature (220 K) and low temperature (5 K) phases.

Inspection of the model obtained from 150 K data using POLARIS shows that this process, distorting the ReO_6 units, is not complete at this temperature with a rhenium environment that is slightly less distorted than found at 5 K. This is in agreement with the transition being second order in nature as observed in resistivity and other physical data[10].

The structure above and below the superconducting critical temperature of 1.3 K, Table 6.1, is, within the determined errors identical, *i.e.* refined parameters are identical within two standard deviations. Transition to the superconducting state has thus been found to have little manifestation in terms of the structure; such behaviour has been found in other superconducting systems. For example in $YBa_2Cu_3O_7$ the only structural change that has been observed on travelling through T_c is in one of the oxygen atom anisotropic TDPs and even this change is barely significant with respect to the error on these values[15]. It is clear from this work that $Cd_2Re_2O_7$ does not undergo a structural phase transition on becoming

superconducting and even higher quality data would be required to observe small changes in the lattice modes, manifested in TDP values, that might be associated with this transition.

No evidence was found for the formation of a tetragonal pyrochlore structure and any tetragonal distortion must be extremely small. It was estimated that c/a >1.0004 would have been observable in our data sets and determination of such a small distortion would require the application of a very high resolution powder method.

The effect of the transition to the *F-43m* description on the rhenium atom sub-lattice is shown in Figure 6.7. As noted by Hiroi *et al.*, this produces a three dimensional network of alternating large and small Re_4 units[9]. How this affects the electronic properties of this material and its band structure would require detailed calculations based on the crystallographic models presented in this work. Furthermore the refined bulk structure in the temperature range 320 mK to 5 K maintains a three-fold symmetry at the rhenium site which is formally in disagreement with the NQR results[12]. However the asymmetry in the rhenium site is extremely small and may result from the presence of local domains that average to give the *F-43m* symmetry. It is also quite possible that this distortion is so small as to be unresolvable even with the highest resolution diffractometers. In terms of resolution HRPD on ISIS offers the highest available resolution at delta-d/d=4×10^{-4} at small *d*-spacings which may enable a slightly smaller structural distortion than the one reported here to be resolved. Once again neutron diffraction methods will be of choice in investigating such structures. It is noteworthy that the intensity of the {*10,4,0*} reflection in the *F-43m* description is about 6% that of the main reflection. Calculations using the *F-43m* structural model determined here but for x-ray radiation show that the most intense additional reflections are only 1% of the main peak and peaks such as the {*2,0,0*} observed in synchrotron work only 0.1%. Therefore, this would lead to considerable difficulties in determining the true structure from x-ray diffraction techniques.

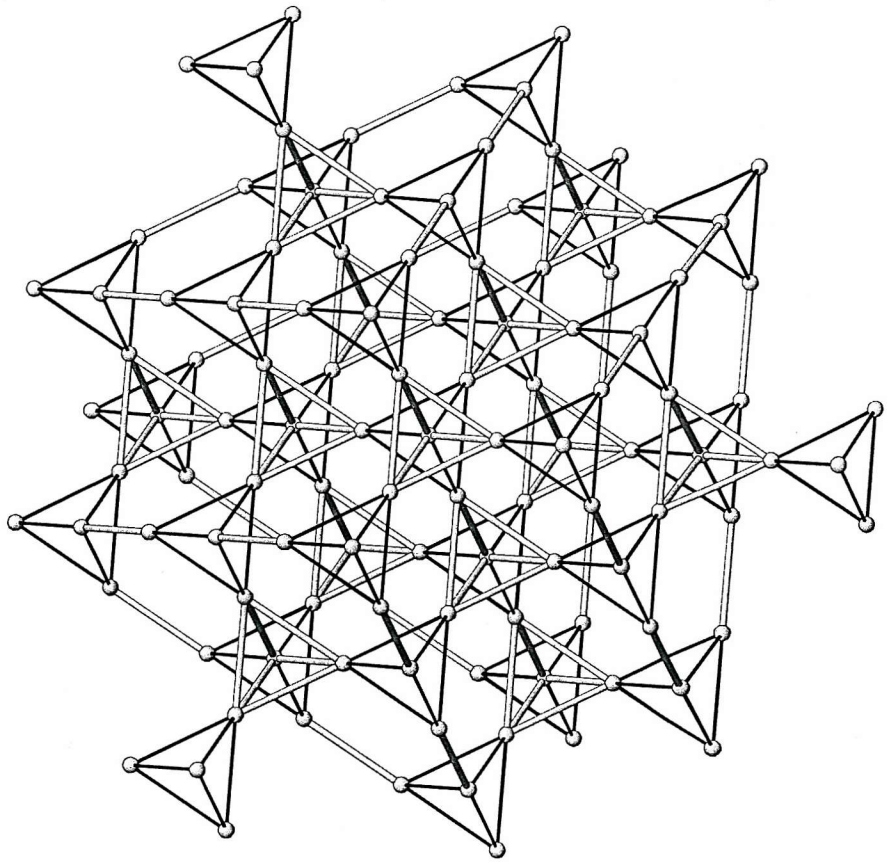

Figure 6.7. Network of Re centres viewed down [111] showing alternating tetrahedral blocks with long (gray) and short (black) interactions.

6.5 References

[1] P. C. Donohue, J. M. Longo, R. D. Rosenstein and L. Katz, *Inorg. Chem.***4** 1152 (1965).

[2] R. Jin, J. He, S. McCall, C.S. Alexander, F. Drymiotis and D. Mandrus, *Phys. Rev. B* **64**(18) 180503 (2001).

[3] M. Hanawa, Y. Muraoka, T. Tayama, T. Sakakibara, J. Yamaura, Z. Hiroi, *Phys. Rev. Lett.* **87** (18) 187001 (2001).

[4] H. Sakai, K Yoshimura, H. Ohno, H. Kato, S. Kambe, R. E. Walstedt, D. T. Matsuda, Y. Haga, Y. Onuki, *J. Phys.: Condens. Matter*, **13** L785 (2001).

[5] R. Jin, J. He, J. R. Thompson, M. F. Chisholm, B. C. Sales, E. W. Plummer, D. Mandrus, *J. Phys.: Condens. Matter* **14**(5) L117 (2002).

[6] Z. Hiroi, M. Manawa, cond-mat / 0111126.

[7] M. D. Lumsden, S. R. Dunsiger, J. E. Sonier, R. I. Miller, R. F. Kiefl, R. Jin, J. He, D. Mandrus, S. T. Bramwell, J. S. Gardner, cond-mat / 0111187.

[8] M. Hanawa, J. Yamaura, Y. Muraoka, F. Sakai, Z. Hiroi, *J. Phys. Chem. Solids* **63** 1027 (2002).

[9] Z. Hiroi, T. Yamauchi, T. Yamada, M. Hanawa, Y. Ohishi, O. Shimomura, M. Abliz, M. Hedo, Y. Uwatoko, cond-mat / 0111388.

[10] Z. Hiroi, J. Yamaura, Y. Muraoka, M. Hanawa, *J. Phys. Soc. Jpn.* **71** 1634 (2002).

[11] J. P. Castellan, B. D. Gaulin, J. van Duijn, J. Lewis, M. D. Lumsden, R. Jin, J. He, S. E. Nagler, D. Mandrus, cond-mat / 0201513.

[12] O. Vyaselev, K. Arai, K. Kobayashi, J. Yamazaki, K. Kodama, M. Takigawa, M. Hanawa, Z. Hiroi, *Phys. Rev. Lett.* **89** 017001 (2002).

[13] A. C. Larson and R. B. Von Dreele, *Generalsied Structure and Analysis System,* MS-H805, Los Almos, NM 87545 (1990).

[14] B. J. Kennedy, *J. Solid State Chem.* **123** 14 (1996).

[15] M. Francois, A. Junod, K. Yvon, A. W. Hewat, J. J. Capponi, P. Strobel, M. Marezio and P. Fisher, *Solid State Comm.* **66** 1117 (1988).

Chapter Seven

Structural Characterisation and Physical Properties of the Perovskite $LaNi_{1-x}Al_xO_3$ System

7.1 Introduction

Studies of the perovskite oxide family have shown the majority of the materials to be electronically insulating at ambient temperature. However, examples of metallic perovskites are often found to contain the 'B' cation with an oxidation state other than their most stable, which has produced materials with good conducting properties. Examples of such oxides include $LaNiO_3$, $LaTiO_3$, and $LaVO_3$. Following this observation, the discovery of metal-insulator (M-I) transitions which occur as a function of temperature in the $RNiO_3$ series (R = rare earth metal) has prompted much research into these compounds chemical and physical properties[1 to 7]. $RNiO_3$ (R = Eu, Sm, Nd and Pr) perovskites crystallise in the orthorhombic structure whilst $LaNiO_3$ has a less distorted rhombohedral structure. The temperatures at which the M-I transition takes place (T_{M-I}) decreases as the rare earth ionic size becomes smaller and the distortion from the ideal parent cubic perovskite structure decreases. $LaNiO_3$ possessing the less distorted structure has metallic properties right down to a temperature of 1.5 K[8,9]. The band gap in this class of materials is determined by the overlap of the transition metal 3d and oxygen 2p orbitals. The magnitude that which this occurs is strongly affected by the geometrical arrangement of the transition metal and oxygen ions. This means that only a small lattice distortion may provoke a M-I transition in the materials. Indeed this is observed with the $RNiO_3$ series (R = Eu, Sm, Nd and Pr) where the T_{M-I} decreases, occuring at 460, 400, 200 and 135 K respectively, with a decrease of the Ni-O-Ni bond angle which governs the transfer integral for the Ni 3d and O 2p orbitals[1].

Doping $LaNiO_3$ with trivalent cations at the 'B' site can also lead to contractions or expansions of the metal-oxygen bond lengths in the structure, and thus provoke changes in the physical properties of the material. To successfully achieve substitutions the size and preferred co-ordination geometry of the cations has to be taken into account. Trivalent aluminium has a similar ionic radius to low-spin nickel(III) ($Al^{3+}\ ^{VI}r$ = 0.535 Å, $Ni^{3+}\ ^{VI}r$ = 0.56 Å)[10] and is most stable in this oxidation state making it a good candidate for substituting into $LaNiO_3$ at the expense of nickel. Structural and physical property studies of $LaAlO_3$ have been reported by a number of workers in past years[11 to 14]. The phase is found to crystalise in a rhombohedral structure, the same as $LaNiO_3$, but with only a very small distortion from the ideal perovskite cubic form. Recently, Martínez-Lope *et al.* reported a structural study by neutrons of the series $R(Ni_{1-x}Al_x)O_3$ (R = La, Nd; $0.0 \leq x \leq$

0.5). In this work the compounds were prepared at 1000 °C under an oxygen pressure of 200 bar[15]. This method was unsuitable due to the use of the high pressure needed. It is possible to synthesise $LaNiO_3$ without the use of extreme reaction conditions using a citrate gel precursor technique and a furnace with a flowing oxygen atmosphere. $LaAlO_3$ should also be readily obtained using this method, enabling the possibility of preparing the complete solid-solution between the two phases at ambient pressure and a reasonably low temperature.

The work reported in the following section is the synthesis of the system $LaNi_{1-x}Al_xO_3$ at ambient pressure. Each composition is structurally characterised using PXD and trends across the series are discussed. Resistivity measurements are carried out for each composition, which are compared to infra-red spectra recorded for the series. Finally, the results are compared to other nickelate systems in terms of structural and physical properties and conclusions are made as to whether the study series undergoes a M-I transition as a function of composition.

7.2 Experimental

The synthesis of the system $LaNi_{1-x}Al_xO_3$ ($0.0 \leq x \leq 1.0$) was carried out for various compositions. Several attempts at different temperatures were made and the method that produced materials with the greatest crystallinity was chosen.

The starting materials used were ethylene glycol, citric acid, $Al(NO_3)_3.9H_2O$, $Ni(NO_3)_2.6H_2O$, and La_2O_3. Solutions were prepared with the appropriate stoichiometries by dissolving La_2O_3 and the relevant nitrate in excess dilute nitric acid. Citric acid (10.0g) was dissolved in ethylene glycol (4ml) and water (20ml), which was added to the nitrate solution. The solution was heated at ~60 °C and stirred constantly. After ~30 minutes a viscous gel formed. The gel was transferred to a crucible, placed in a furnace and heated to 250 °C gradually over a 2 hour period. The resinous product was ground to a fine powder and sintered in a furnace at 500 °C for 4 hours to remove the organics present. The resultant powder was milled, pressed as a pellet and fired under flowing O_2 gas at 650 °C

for 6 days with intermittent grindings during the course. A seventh day of firing under O_2 was carried out with an increase of temperature to 750 °C.

The colour of the materials was black for the majority of the compositions with $LaNi_{0.2}Al_{0.8}O_3$ dark brown, $LaNi_{0.1}Al_{0.9}O_3$ a lighter brown and $LaAlO_3$ white. The products were examined by PXD and were found to be target phase pure with the exception of a small amount of NiO present in the end member $LaNiO_3$. The oxygen content for the $LaNi_{1-x}Al_xO_{3-\delta}$ samples was determined from TGA. Each composition was heated to 1000 °C at a rate of 20 °C/min under 5 % H_2/N_2 gas with a flow rate of ~ 90 ml/min. The target temperature was maintained for 30 minutes to ensure that the total weight loss had occurred and the sample was then cooled to room temperature at 40 °C/min. Data points were collected every 4 seconds and displayed in real time. A small oxygen deficiency was detected for $LaNiO_{3-\delta}$ ($\delta = 0.03$) whilst all the remaining materials showed a near perfect stoichiometric composition ($\delta = 0.00 \pm 0.01$).

7.3 PXD Structure Refinements

PXD data were collected collected over a 2θ range of 20°–120° for a period of 15 hours using a 0.02° step size, for all the samples. Cell parameters were calculated from the d-spacings using the CELL computer program. Using the Rietveld technique, refinement of the data commenced using the computer program GSAS[16]. The refinement was started based on the existing model determined for $LaNiO_3$ using the rhombohedral space group R-3c in the hexagonal setting. A uniform approach to the structure refinement was undertaken for each of the data sets obtained for the different compositions to ensure consistent results. Cell parameters, peak shape parameters atomic positions and isotropic temperature factors were sequentially added to the refinement. Thermal parameters of the B site were constrained to be equal for the whole series, and the oxygen sites were set at $U_{iso} = 0.025$ Å^2 due to their poor scattering of x-rays. The refinements converged smoothly to yield acceptable *R*-factors. Accurate cell parameters were determined for each composition from the refinement along with atom positions, derived bond lengths and bond angles, which can be found in Tables 7.1 and 7.2. An example of a final fit of data can be seen for $LaAl_{0.8}Ni_{0.2}O_3$ in Figure 7.1 and the structure in Figure 7.2.

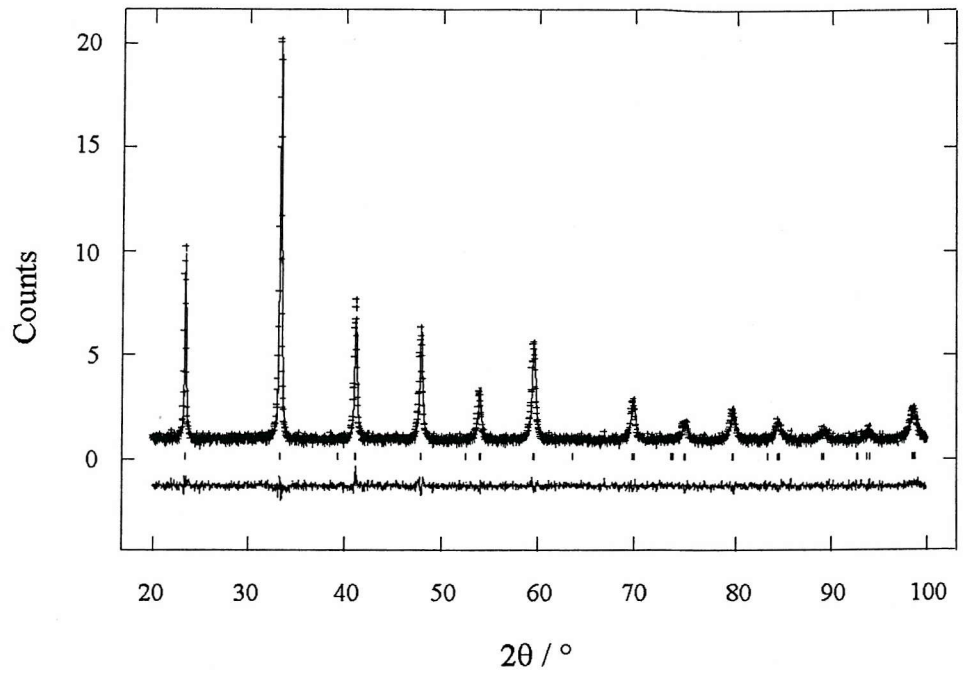

Figure 7.1. Profile fit to PXD data for $LaAl_{0.8}Ni_{0.2}O_3$. Experimental data points are shown as crosses, upper continuous line the calculated profile, lower continuous line the difference. Allowed reflection positions for $LaAl_{0.8}Ni_{0.2}O_3$ are shown with tick marks.

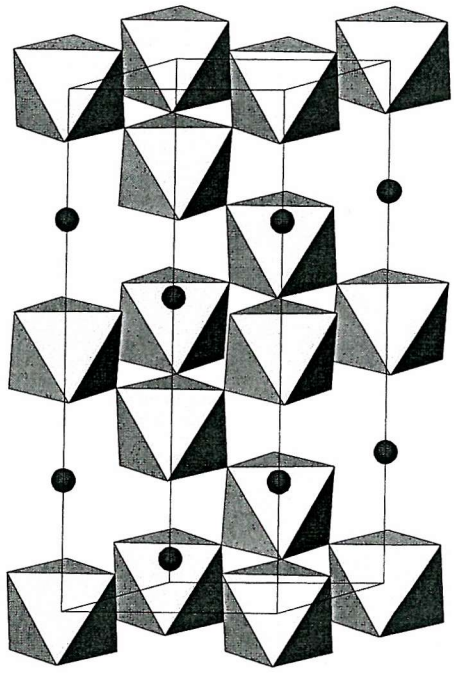

Figure 7.2. The crystal structure of $LaNi_{1-x}Al_xO_3$. The dark spheres are lanthanum atoms and the shaded polyhedra represent NiO_6 and AlO_6 octahedra distributed at random across the stucture.

Table 7.1. Summary of derived atomic, thermal and profile fit parameters for $LaNi_{1-x}Al_xO_3$ as a function of composition; *esds are given in parentheses.* Space group *R*-3*c*. La on (0,0,¼), Ni/Al on (0,0,0) and O on (*x*, 0, ¼).

x	*a* / Å	*c* / Å	Volume / Å^3	O *x*	La U_{iso} × 100 Å^2	Ni/Al U_{iso} × 100 Å^2	O U_{iso} × 100 Å^2	R_{wp} (%)	R_p (%)
0.00	5.4520(2)	13.161(1)	338.78(2)	0.535(4)	1.69(9)	1.25(9)	2.5	8.68	6.96
0.10	5.4321(3)	13.146(2)	335.94(4)	0.537(4)	1.92(9)	1.06(14)	2.5	10.63	8.29
0.20	5.4159(2)	13.126(1)	334.20(2)	0.543(3)	1.68(6)	1.89(11)	2.5	9.18	7.22
0.25	5.4140(3)	13.145(1)	333.69(4)	0.535(4)	1.62(7)	1.48(13)	2.5	10.03	7.96
0.30	5.4115(4)	13.157(2)	333.66(6)	0.525(5)	1.58(9)	0.93(15)	2.5	10.82	8.54
0.35	5.4042(4)	13.149(2)	332.56(6)	0.530(4)	1.49(7)	1.36(13)	2.5	10.12	8.02
0.40	5.3999(2)	13.123(1)	331.37(2)	0.527(4)	1.51(6)	2.06(13)	2.5	10.26	8.02
0.45	5.3878(4)	13.131(2)	330.11(5)	0.526(4)	1.69(7)	2.24(15)	2.5	9.74	7.77
0.50	5.3678(3)	13.213(2)	329.70(4)	0.504(9)	1.28(6)	2.25(13)	2.5	8.96	7.03
0.55	5.3678(3)	13.190(2)	329.14(4)	0.525(4)	1.37(5)	2.43(11)	2.5	8.12	6.35
0.60	5.3637(3)	13.176(2)	328.28(4)	0.515(6)	1.42(5)	2.32(12)	2.5	9.05	7.11
0.65	5.3662(4)	13.134(1)	327.53(2)	0.524(4)	1.20(5)	2.26(13)	2.5	8.65	6.69
0.70	5.3668(4)	13.109(3)	326.98(6)	0.513(6)	1.69(6)	2.14(14)	2.5	9.20	7.24
0.80	5.3519(3)	13.148(2)	326.14(4)	0.515(5)	1.28(5)	2.06(13)	2.5	8.72	6.81
0.90	5.3456(3)	13.116(2)	324.56(4)	0.534(3)	1.18(5)	1.81(15)	2.5	9.32	7.35
1.00	5.3430(4)	13.115(2)	324.70(3)	0.482(2)	1.57(12)	0.86(35)	2.5	15.16	11.97

Table 7.2. Summary of derived bond lengths and bond angles for $LaNi_{1-x}Al_xO_3$ as a function of composition; *esds are given in parentheses.* Distortion coefficient, Δ_d, is defined in the text.

	Bond distance / Å				Bond angle variance		Bond angle / °		
x	Ni/Al-O	La-O (×3)	La-O (×3)	La-O (×6)	<La-O>	Δ_d	O-Ni/Al-O	O-Ni/Al-O	Ni/Al-O-Ni/Al
0.00	1.928(2)	2.54(2)	2.92(2)	2.707(2)	2.719(9)	0.073	90.83(5)	89.17(5)	168.7(11)
0.10	1.924(2)	2.51(2)	2.92(2)	2.702(2)	2.709(9)	0.084	90.77(6)	89.23(6)	167.9(11)
0.20	1.922(2)	2.48(2)	2.94(2)	2.699(1)	2.705(9)	0.106	90.82(4)	89.18(4)	166.1(7)
0.25	1.918(2)	2.52(2)	2.89(2)	2.698(2)	2.702(9)	0.068	90.61(5)	89.39(5)	168.8(10)
0.30	1.914(3)	2.57(3)	2.84(3)	2.696(2)	2.701(9)	0.037	90.43(6)	89.57(6)	171.7(17)
0.35	1.913(2)	2.54(2)	2.86(2)	2.695(2)	2.698(9)	0.051	90.46(5)	89.54(5)	170.4(12)
0.40	1.910(2)	2.55(2)	2.85(2)	2.690(1)	2.695(9)	0.045	90.47(4)	89.53(4)	171.2(11)
0.45	1.907(2)	2.55(3)	2.84(3)	2.689(2)	2.692(9)	0.042	90.35(5)	89.65(5)	171.5(13)
0.50	1.901(2)	2.73(6)	2.64(6)	2.693(1)	2.689(9)	0.004	90.17(4)	89.83(4)	178.0(10)
0.55	1.905(2)	2.55(2)	2.82(2)	2.693(9)	2.689(9)	0.036	90.02(4)	89.98(4)	172.0(11)
0.60	1.900(2)	2.60(3)	2.76(3)	2.688(9)	2.684(9)	0.013	90.06(4)	89.94(4)	175.1(12)
0.65	1.901(2)	2.56(2)	2.81(2)	2.685(2)	2.685(9)	0.031	90.16(4)	89.84(4)	172.4(12)
0.70	1.897(2)	2.62(4)	2.75(4)	2.679(9)	2.682(9)	0.008	90.15(4)	89.85(4)	175.8(20)
0.80	1.896(2)	2.59(3)	2.76(3)	2.683(9)	2.679(9)	0.014	90.06(4)	89.94(4)	175.0(17)
0.90	1.900(2)	2.49(2)	2.85(2)	2.682(1)	2.676(9)	0.065	90.19(4)	89.81(4)	169.1(19)
1.00	1.898(3)	2.78(6)	2.58(6)	2.681(3)	2.681(9)	0.020	90.16(9)	89.84(9)	174.0(20)

7.3.1 Discussion

The incorporation of Al onto the Ni sub-lattice leads to a unit cell contraction. This is explained by simple steric considerations in view of the smaller ionic size of Al^{3+} (0.535 Å) compared to low-spin Ni^{3+} (0.56 Å)[10]. This can be observed by viewing plots of volume and *a* lattice parameter as a function of composition (see Figures 7.3 and 7.4). In this crystal structure model used, the Ni and Al ions are arranged on a single site at random and in terms of structural parameters there is only one refineable position, namely the O *x* co-ordinate. The gradual shift in this position reflects the reduction in the average Ni/Al-O bond length on increasing aluminium concentration, which can be seen in Figures 7.5 and 7.6. Calculating tolerance factors (*t*) for selected samples of the series gives a clearer picture of the evolution of the structure. Taking the equation given by Goldschmidt[17] showing the relationship of ionic radii between atoms in a perovskite cell,

$$t = d_{A\text{-}O}/\sqrt{2}d_{B\text{-}O}$$

tolerance factors were calculated, using the refined bond distances, for the compositions x = 0.0, 0.6 and 1.0, giving values of 0.996, 0.998 and 0.999 respectively. A value of one would represent the ideal cubic perovskite cubic form and any deviation above or below from this value would show evidence of structural strain. The progressively higher tolerance factors obtained for the increasing concentration of aluminium in the system indicates a lower degree of distortion of the rhombohedral structure from the ideal cubic form. Further evidence of a less distorted structure on increasing aluminium content, is shown by looking at the evolution of the Ni/Al-O-Ni/Al bond angle. This is the angle between adjacent octahedra which is seen to increase as aluminium content increases which is shown in Figure 7.7. The angle in the cubic undistorted ABO_3 perovskite is 180 °, which is approached in the aluminium rich compositions. It is difficult to see the linked octahedra in the conventional representation of the rhombohedral perovskite (Figure 7.2) so another view is shown for greater clarity (Figure 7.8).

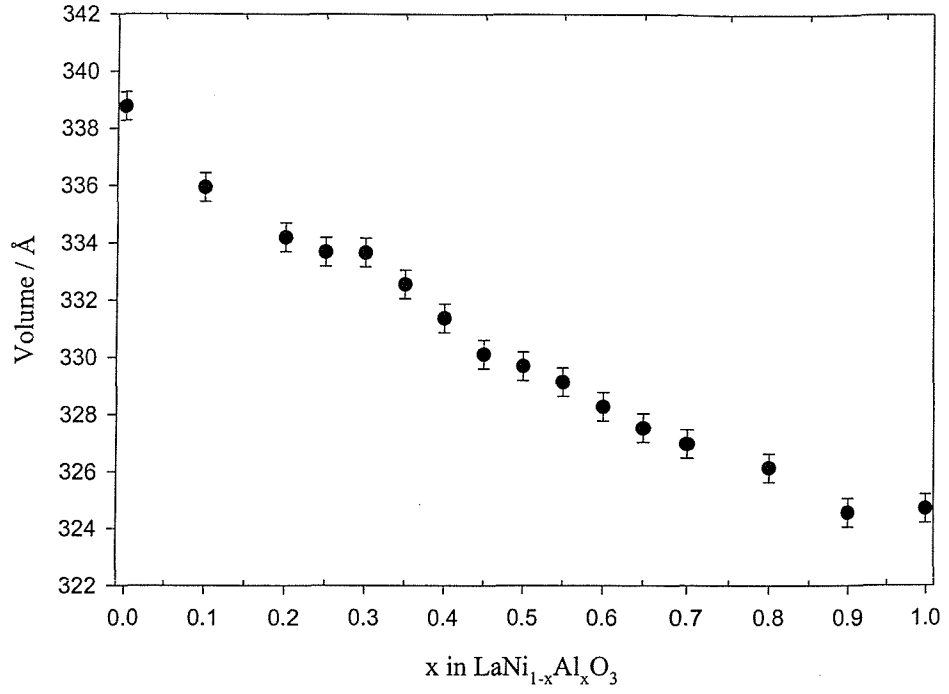

Figure 7.3. Variation of the cell volume of $LaNi_{1-x}Al_xO_3$ with composition.

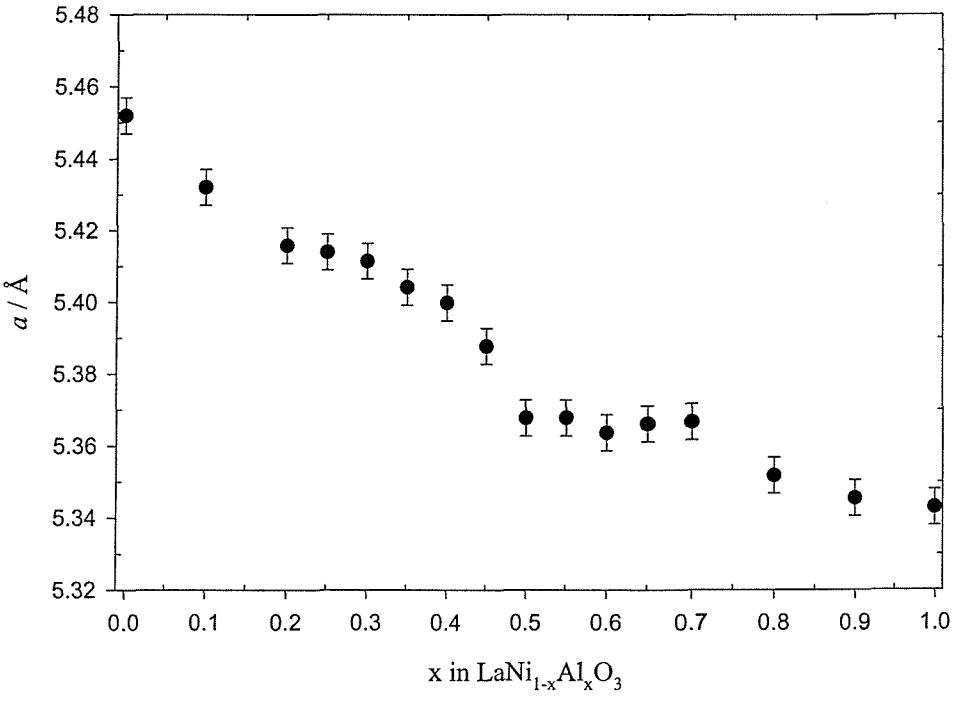

Figure 7.4. Variation of the *a* lattice parameter of $LaNi_{1-x}Al_xO_3$ with composition.

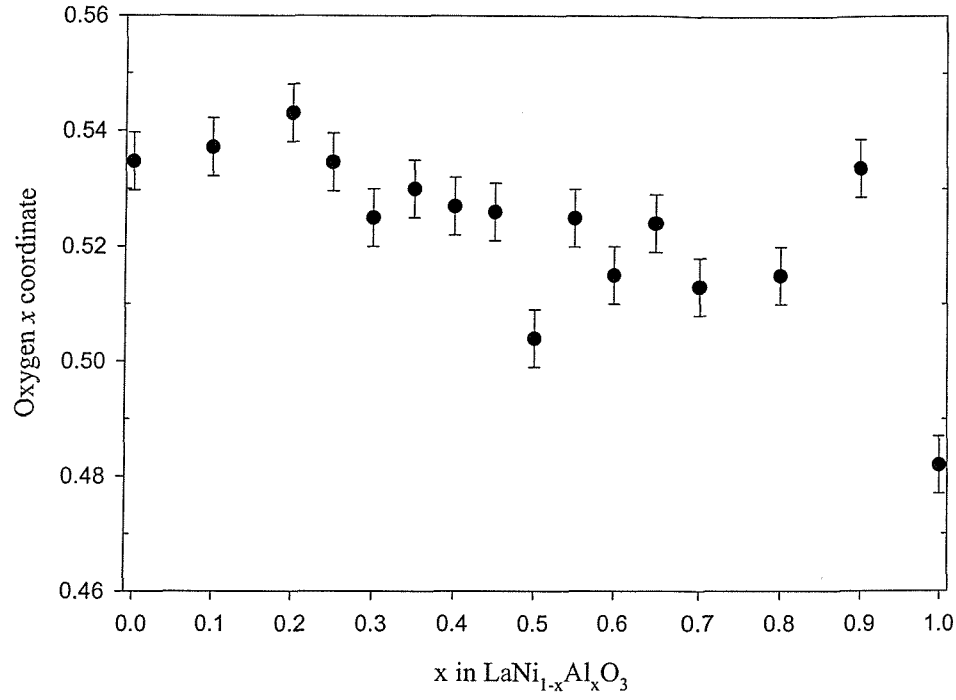

Figure 7.5. Variation of the O *x* co-ordinate of $LaNi_{1-x}Al_xO_3$ with composition.

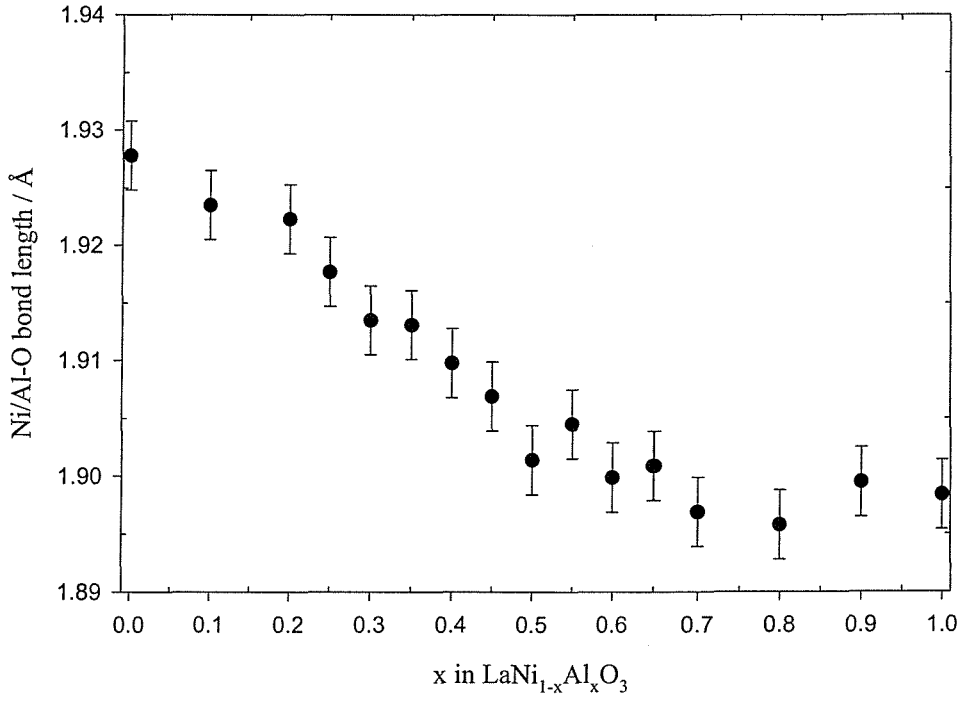

Figure 7.6. Variation of the derived B-O bond length of $LaNi_{1-x}Al_xO_3$ with composition.

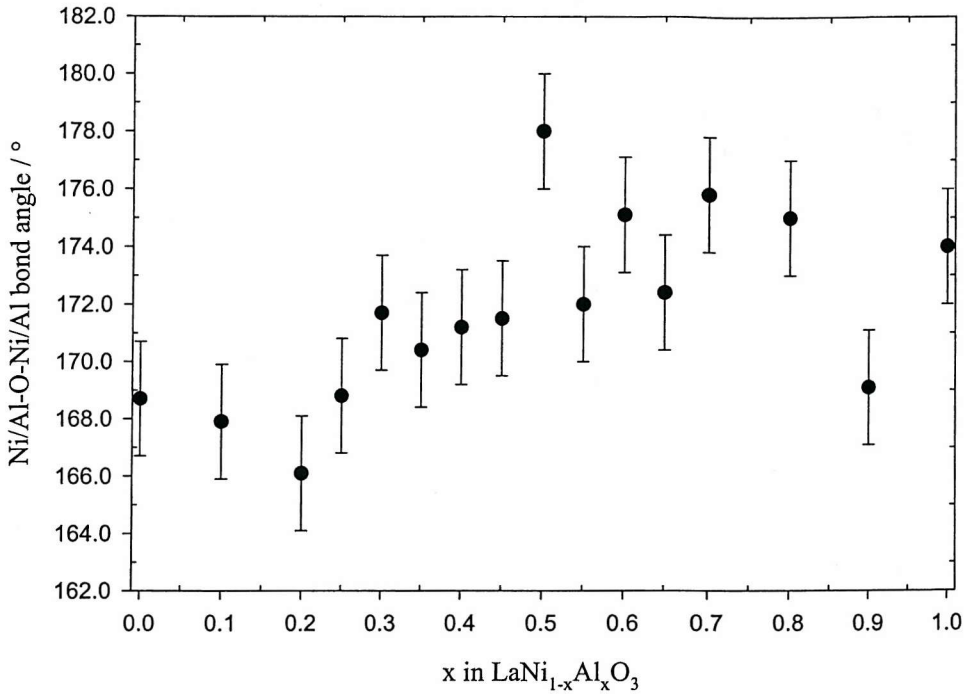

Figure 7.7. Variation of the B-O-B angle in $LaNi_{1-x}Al_xO_3$ with composition.

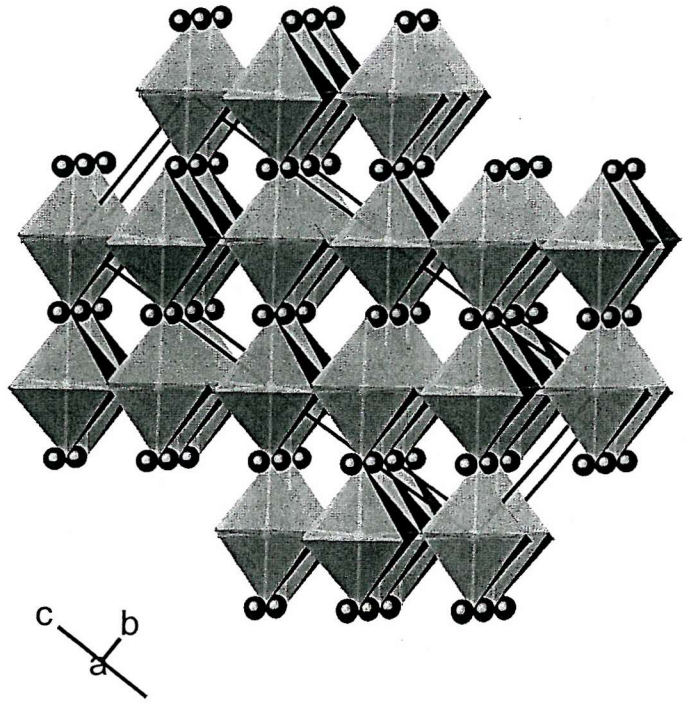

Figure 7.8. The crystal structure of $LaNi_{1-x}Al_xO_3$ as seen in Figure 7.2. The boundaries have been extended beyond the unit cell to show the linked polyhedra for greater clarity.

Another noticeable feature associated with this system is the changing oxygen environment of the La ions. There are three different La-O bonding distances in this structure, given in Table 7.2. As Al content increases the oxygen environment becomes more regular showing individual La-O distances gradually closer to the average. Using the distortion coefficient defined by Alonso *et al*[15], which is the sum of the square distance deviations for all the atoms of the co-ordination polyhedron,

$$\Delta_d = \sum (d-d_i)^2$$

a regular decrease of Δ_d for La polyhedra can be observed as Al dopant increases (see Table 7.2 and Figure 7.9).

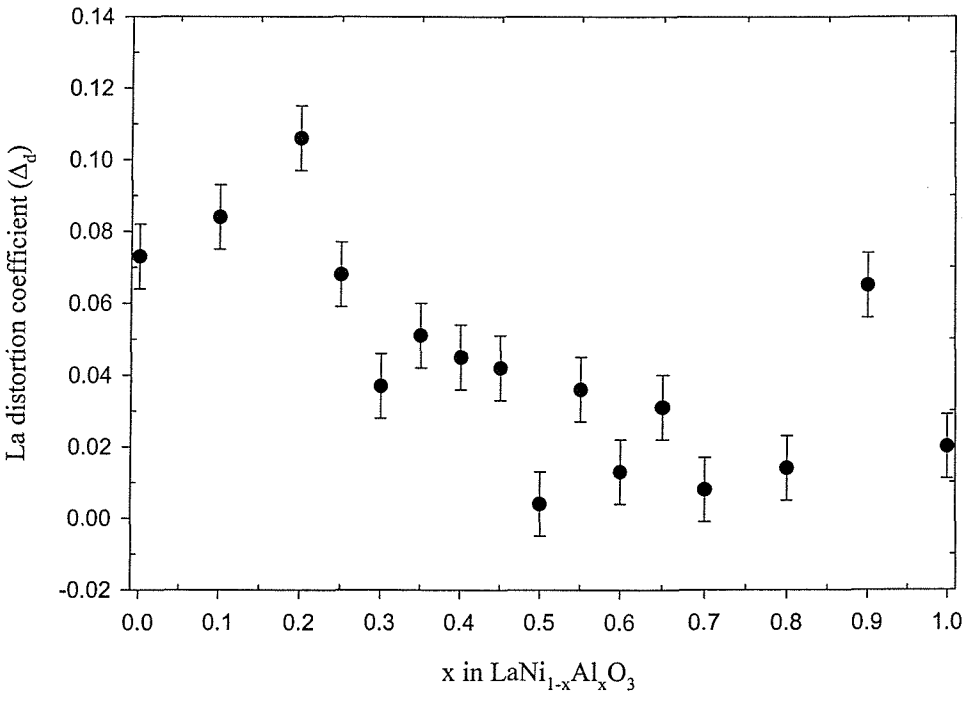

Figure 7.9. The distortion coefficient of La ions in $LaNi_{1-x}Al_xO_3$ as a function of composition.

7.4 Infra-red and Resistivity Measurements

The electronic properties of the $LaNi_{1-x}Al_xO_3$ system were investigated by collecting infra-red and resistivity measurements. In the infra-red spectrum, a metallic oxide will generally show a strong absorption across the whole region associated with the collective electronic states. An insulating oxide will absorb at discrete frequencies in the infra-red region associated with the M-O modes. In general, perovskite related oxides show two prominent bands in the region 1000-250 cm^{-1}, which are assigned to the internal modes of the BO_6 octahedra. The integrated area under the two bands is observed to increase in the order of increasing electrical resistivity, and in the event of a material passing through an insulator-metal phase transition, the two bands will no longer be observed. The changes of the relative intensity of these bands in $LaNi_{1-x}Al_xO_3$ were recorded to observe the relationship with the change of measured resistivity of the materials.

Room temperature infra-red data were collected on a Perkin-Elmer Spectrum One Fourier-Transform Infra-red Spectrometer (FT-IR) with CsI optics. Each composition (0.002 g) was intimately mixed with dry spectroscopic grade KBr (0.2 g) in a quantitative manner to allow an accurate comparison of spectra. The mixtures were pressed into discs of ~0.5 mm thickness under 8 tonnes/cm^2 of pressure. Spectra were recorded over a range of 4000-250 cm^{-1} with a resolution of 2 cm^{-1}.

Resistivity measurements for each composition at room temperature were carried out using the four-probe technique. Each sample was pressed into a pellet under ~10 tonnes/cm^2 and carefully cut to form a bar of rough dimensions 8 x 4 x 2 mm and uniform in size. Electrically conductive silver paint was used as the contact for the wires. The potential difference and the four terminal resistance was measured using a Fluke 8840A multimeter with a D.C. current source.

7.4.1 Results

Table 7.3. Combined infra-red integrated band intensities and resistivity measurements for $LaN_{1-x}Al_xO_3$ as a function of composition.

x	Combined integrated band intensity ($\nu_{B\text{-}O} + \delta_{B\text{-}O}$)	Resistivity (ρ) / Ωcm	log ρ
0.0	-	1.6×10^{-3} *	-2.795 *
0.10	13.2	0.028	-1.553
0.20	10.2	0.086	-1.066
0.25	17.3	0.490	-0.310
0.30	23.5	-	-
0.35	34.1	1.77	0.248
0.40	18.9	2.40	0.380
0.50	39.3	10.80	1.033
0.55	67.6	-	-
0.60	119.1	48.96	1.690
0.65	108.0	1421.0	3.153
0.70	147.8	4415.0	3.645
0.80	182.7	11093	4.045
0.90	224.4	-	-

* Value taken from Reference [18] due to meter scale parameters.

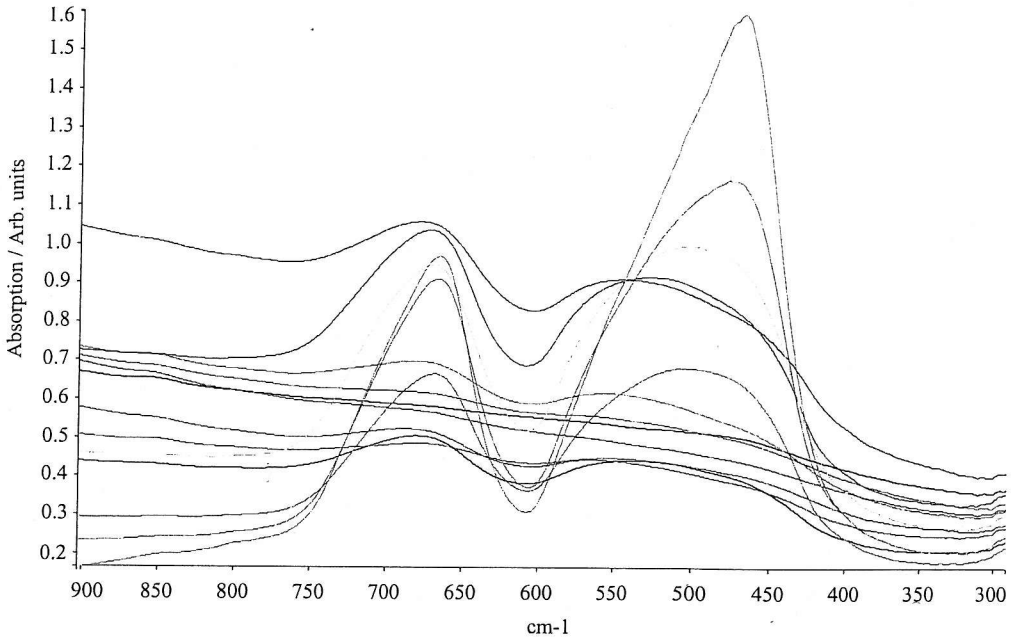

Figure 7.10. Compositional-dependent infra-red spectra of $LaNi_{1-x}Al_xO_3$ (See below for key).

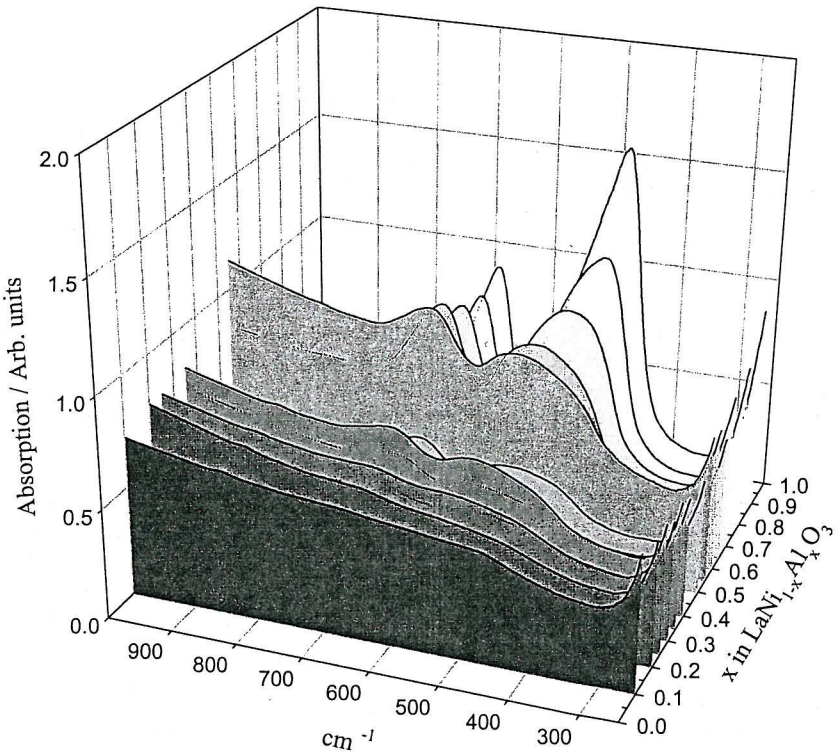

Figure 7.11. 3D plot of compositional-dependent infra-red spectra of $LaNi_{1-x}Al_xO_3$.

Representative compositional dependent infra-red spectra of $LaNi_{1-x}Al_xO_3$ are shown in Figure 7.10 and a 3D plot in 7.11 (only a section of the spectra are shown for greater clarity). The spectra, which were measured at room temperature comprises two discrete features at *ca.* 670 and 475 cm^{-1}. These can be assigned to the B-O stretch (ν_{B-O}) and B-O deformation (δ_{B-O}) of the BO_6 octahedra, respectively. The remainder of the spectrum, not pictured, shows no other distinguishing features. It can be seen that the band intensity of the two modes decrease, which is in line with decreasing Al content. The high nickel concentration materials show very little band intensity and on reaching $LaNi_{0.9}Al_{0.1}O_3$ the bands have virtually disappeared. This is expected behaviour since $LaNiO_3$ is metallic and will show a strong absorption across the whole infra-red region, whereas $LaAlO_3$ is an insulator at room temperature and should show intensity in this area. To show a good comparison of each spectrum the normalised integrated band intensity areas were calculated for each composition, which can be found in Table 7.3. A plot of the combined area for the two bands as a function of composition can be seen in Figure 7.12.

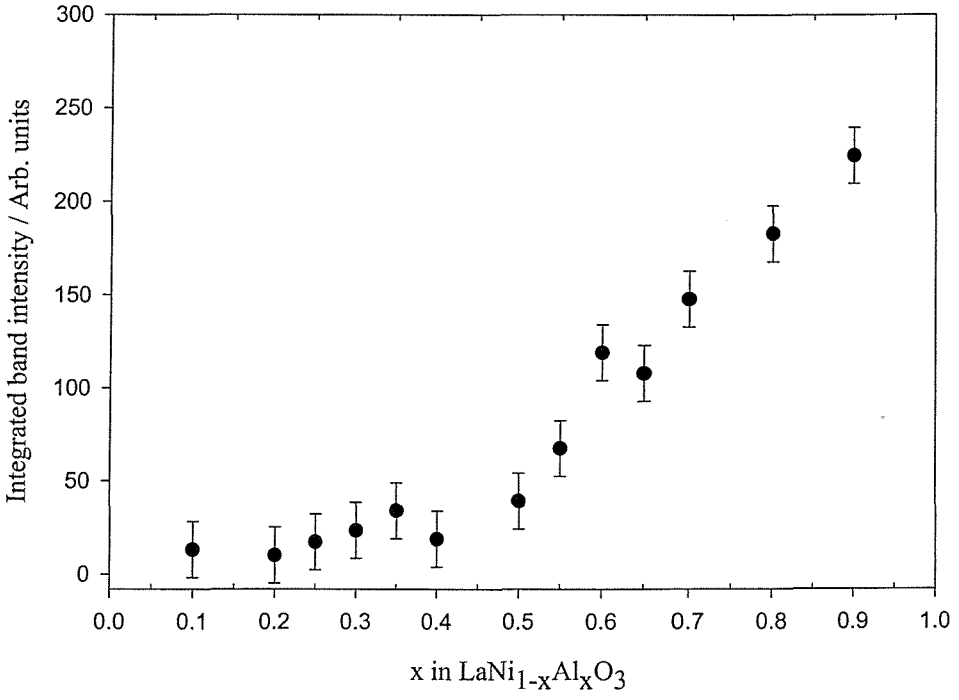

Figure 7.12. Compositional-dependent variation of the combined integrated band intensities of $LaNi_{1-x}Al_xO_3$.

The plot may be interpreted as two distinct gradients (within experimental error bars). The first gradient shows a gentle increase of integrated band intensity as aluminium is added to the system. At the 50 % level of aluminium concentration there is a sharp increase of band intensity producing the second much steeper gradient, which is constant to the end of the solid-solution. It is clear that there is a distinct change in the system at this point, which is certainly electronic in nature. To investigate this observation further we must turn to the resistivity measurement data. The resistivities of the samples measured can be found in Table 7.3 along with the logged values of each measurement. A plot of resistivity as a function of sample composition is shown in Figure 7.13 and a log resistivity plot in Figure 7.14.

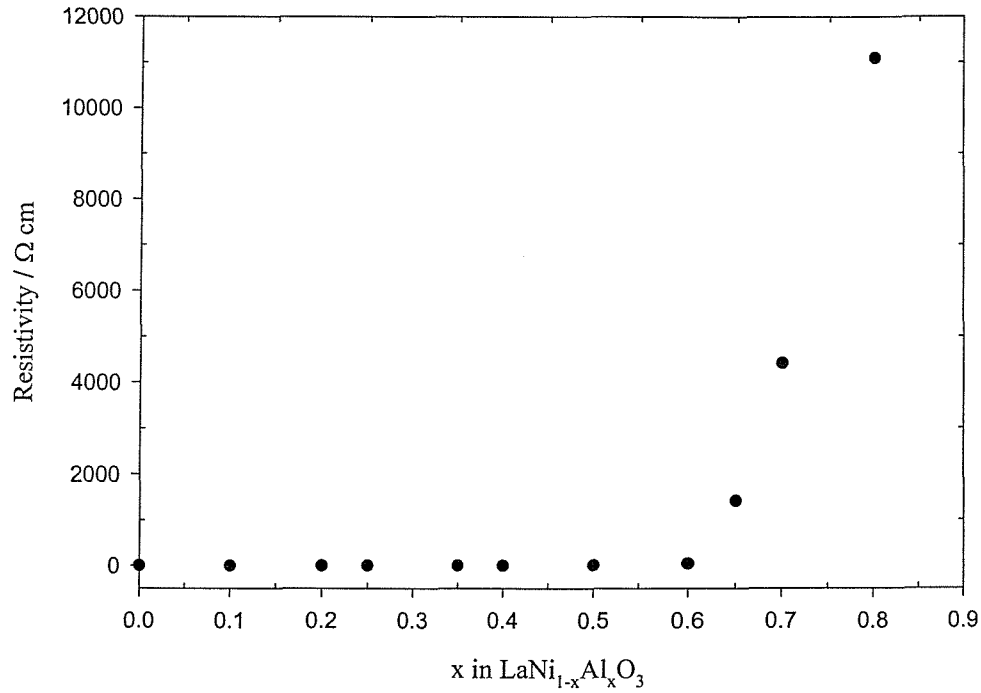

Figure 7.13. Resistivity as a function of composition for $LaNi_{1-x}Al_xO_3$.

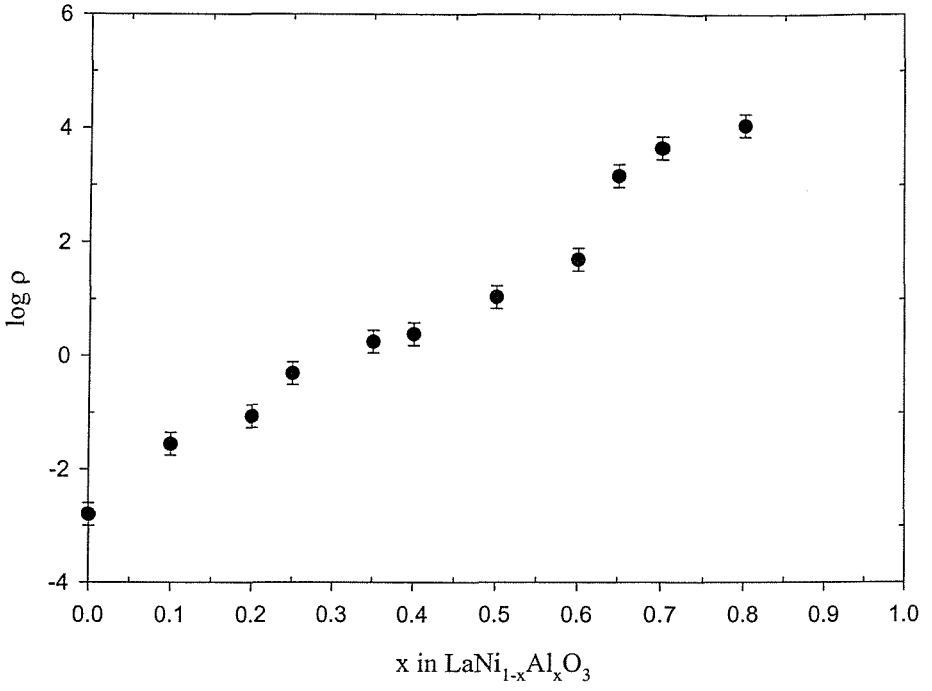

Figure 7.14. Log resistivity as a function of composition for $LaNi_{1-x}Al_xO_3$.

Looking at the resistivity plot in Figure 7.13 there seems to be little change in the resistance behaviour until 60 % of the nickel has been replaced by aluminium. At this point there is a large increase in resistivity, which spans several orders of magnitude over the remainder of the series. The value for $LaNi_{0.1}Al_{0.9}O_3$ was too large to be measured with the meter used for this study. For a clearer picture of the resistance behaviour the values were logged to reduce the scale. The log plot shows a linear increase in resistivity over the entire solid-solution with a marked increase at 60 % aluminium concentration.

7.4.2 Discussion

From the sets of infra-red spectra and resistivity measurements similar trends are immediately apparent. The integrated band intensity of the materials increases as the aluminium concentration increases, which is also what is observed for the resistivity. The band intensities show a sharp change in gradient at 50 % aluminium concentration, which is also reflected in the resistivity data whose sharp increase is a little higher at 60 %

aluminium concentration. A direct comparison to the two sets of data is easily made, by overlapping their respective plots on the same graph (see Figure 7.15).

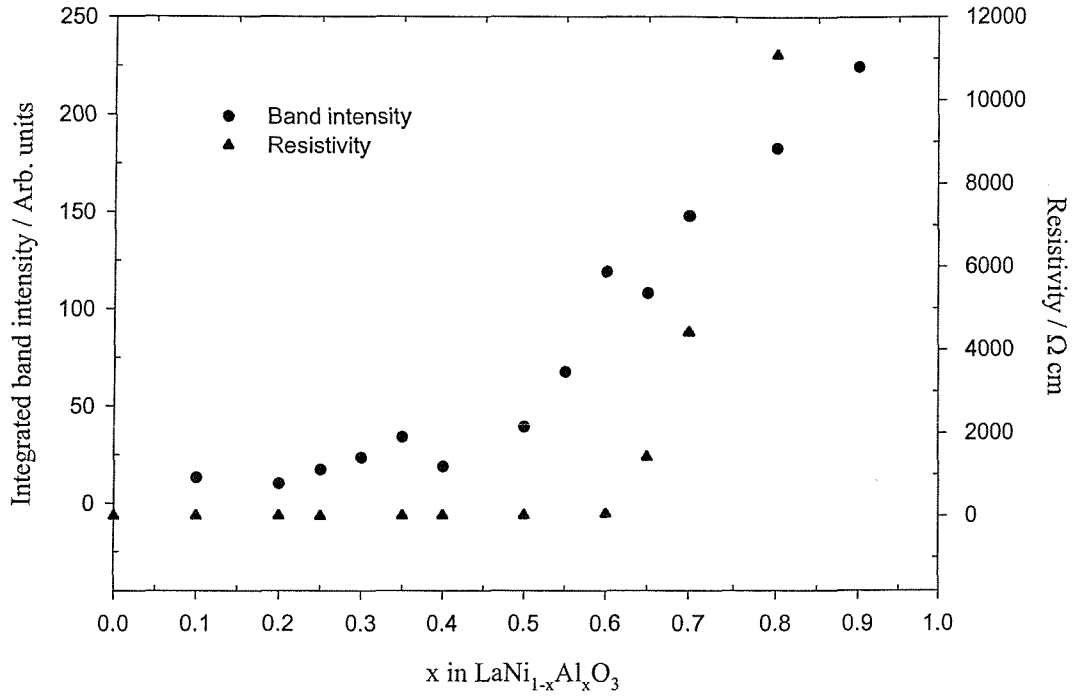

Figure 7.15. Resistivity and integrated band intensity of $LaNi_{1-x}Al_xO_3$ as a function of composition.

It is fair to conclude that a distinct electronic change is apparent in the $LaNi_{1-x}Al_xO_3$ system observed in both infra-red and resitivity results. The system is seen to progressively become more insulating as aluminium is added at the expense of nickel. However, the nature of the trend shows no conclusive evidence of a metal-insulator transition. Ganguly *et al* carried out a comprehensive study of mixed nickelate systems in terms of their physical properties[19]. They studied the systems $LaNi_{1-x}M_xO_3$ where M = Mn, Cr, Fe and Co) and saw M-I transitions for each system at varying concentrations dependent on the transition metal, M. When M = Mn or Cr the transition takes place at 5 % and 10 % dopant respectively accompanied by a sharp increase in log resistivity followed by a less marked linear increase for the rest of the compositions. When M = Fe or Co the transition takes place at 35 % dopant for both systems accompanied by a sharp exponential increase in log

resistivity after the transition. In this system we see a gradual increase in resistivity rather than an abrupt change (Figure 7.14) with the exception of the increase at x = 0.6. Therefore, with $LaNi_{1-x}Al_xO_3$ another type of change takes place, which may be explained by percolation theory[20,21].

Percolation theory deals with the effects of varying the richness of interconnections present in a random system. If we consider a 2D network represented by a large square lattice of interconnections representing bonds (Figure 7.16).

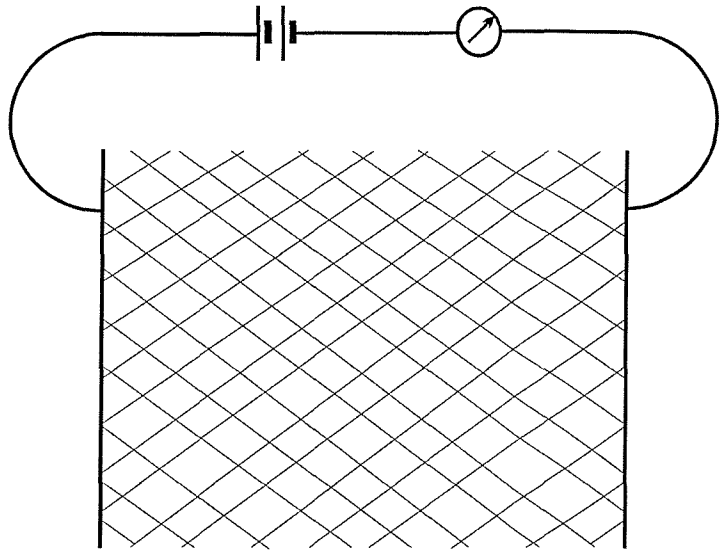

Figure 7.16. 2D square lattice interconnected network.

If the links in the net are cut at random, the fraction that need to be cut to electronically isolate the two boundary bars depends on where the net is cut since the linking resistors are not equivalent to each other. This remains true for all finite networks, however, if the size of the net goes to infinity, there will be a definite answer to the problem. For an ideal resistor net, there is a sharp transition for the resistance of the net as a function of the fraction of uncut links. If the fraction of uncut bonds is higher than the transition value, the net will be insulating, and below the value it will be conducting. This represents the basic idea of percolation, which is the existence of a sharp transition at which the long range connectivity of the system disappears. The value at which the transition takes place is known as the percolation threshold. The value at which the transition takes place is

calculated using probability. The conduction path can be either blocked by a cut bond or unblocked by an uncut bond. The relative concentration of unblocked bonds is x, and of the blocked bonds is 1-x. The distribution of blocked and unblocked bonds is fixed and remains constant in time. The probability of any given bond being unblocked is donated $P^b(x)$. The critical probability, $x_c(b)$, otherwise known as the percolation threshold is defined as the upper limit of the values of x for which $P^b(x) = 0$. Above the threshold the probability $P^b(x)$ increases continuously until $P^b(x) = 1$. So, if we refer to the above infinite 2D square lattice in Figure 7.16 the percolation threshold, $x_c(b)$, will be at 0.5. Each lattice type will have its own percolation threshold value, which generally decreases with complexity. For example, a honeycomb lattice has three routes that a conduction path can follow, compared to four routes in the square lattice, and its threshold is $x_c = 0.65$. This honeycomb lattice is depicted in Figure 7.17 below.

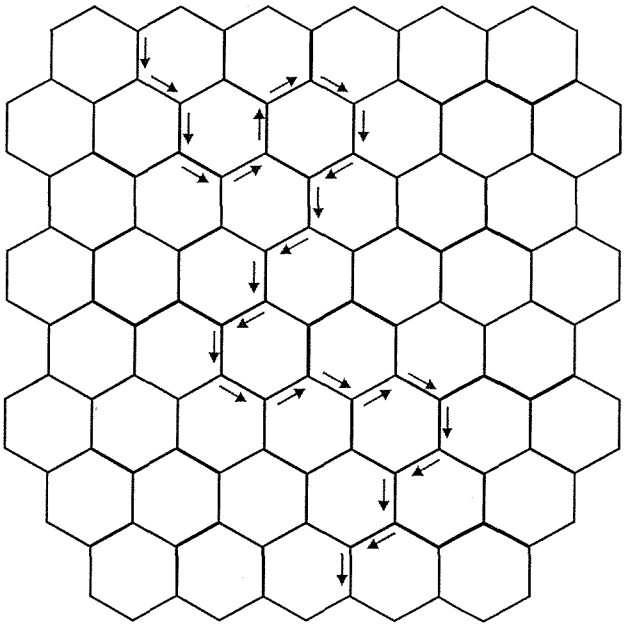

Figure 7.17. A section of a 2D honeycomb lattice. The arrows follow one of many different conduction paths possible.

The basis behind percolation theory has been discussed which brings us to the second problem – "the site problem". Here all the bonds are unblocked, and it is the sites that can be blocked or unblocked. Blocked sites will permit no flow of electrons in any direction. The fraction of unblocked sites is donated by x and $P^s(x)$ is the probability of a random site providing a conduction path to an infinite number of sites. As in the bond problem, there is

a percolation threshold $x_c(s)$, which is the upper bound of x values for which $P^s(x) = 0$. Usually, the bond and site problems are discussed in terms of cluster statistics, rather than conductance flow from site to site. This approach can be applied to the lattice concerning the $LaNi_{1-x}Al_xO_3$ system and its 3D lattice.

The perovskite unit cell is based on a *face centred cubic* lattice with rhombohedral and orthorhombic forms common distorted variations of the ideal form (see Chapter 1 for a more detailed explanation). The $LaNi_{1-x}Al_xO_3$ system possesses a rhombohedral structure for the entire solid-solution. The electronic transfer responsible for the conductivity in lanthanide nickelates is carried out through the overlapping Ni 3d and O 2p orbitals. Although the lanthanide ion has an effect on the different electronic properties exhibited by these nickelate systems, it plays no direct part in the actual conductance path of the materials. Therefore, it is for this reason that the La ions can be removed from the $LaNi_{1-x}Al_xO_3$ structure for the purpose of this discussion. On removing the La ions, we are now left with a *primitive cubic* lattice, which is depicted in Figure 7.18. It can be seen that on each transition metal site there are six possible initial directions the conductance path can take. The nickel and aluminium ions are arranged at random across the infinite 3D lattice. As soon as the aluminium ions are incorporated into the lattice, the conduction path will be blocked at these sites. The electrons will then have to follow a different direction for conduction to be present in the material. The probability of meeting an aluminium site will carry on increasing with increasing concentration, leading to the formation of clusters. Eventually, there will be a point where there is an infinite cluster of aluminium ions that block all conduction paths, leading to a large jump in the resistance. This will be the percolation threshold of the system. The values of the percolation threshold for commonly studied lattices are summarised in Table 7.4[20].

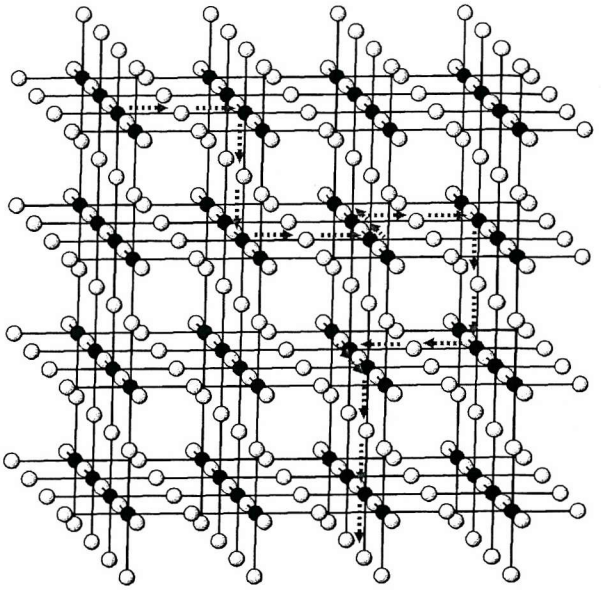

Figure 7.18. The perovskite lattice depicting the linked BO_6 octahedra with the 'A' cations removed for clarity. The black spheres are 'B' cations distributed at random across the structure, and the white spheres are oxygen ions. The arrows show the different paths that electronic conduction can follow.

Table 7.4. Percolation threshold x_c for various lattices. Exact values are shaded. All other values were obtained by numerical methods (taken from Ref. 20).

Lattice	$x_c(b)$	$x_c(s)$
Honeycomb	0.653	0.696
Square	0.500	0.590
Triangular	0.347	0.500
Diamond	0.389	0.431
Primitive cubic	0.251	0.315
Body centred cubic	0.178	0.248
Face centred cubic	0.122	0.200

Since x is the concentration of unblocked sites, the concentration of blocked sites is 1-x. From Table 7.4 we see the threshold for a *primitive cubic* lattice is 0.315, which is the critical concentration of unblocked sites; the concentration of x for nickel in $LaNi_{1-x}Al_xO_3$. Therefore, the concentration of blocked sites will be 1 - 0.315, giving a value of 0.685; the concentration of x for aluminium in $LaNi_{1-x}Al_xO_3$. This is the theoretical value of critical

concentration of aluminium at which conduction will cease for the $LaNi_{1-x}Al_xO_3$ system. The experimental value obtained from the resistivity data (Figures 7.13 and 7.14) was 0.6 which gives a good agreement, within experimental error, that the proposed mechanism of conduction is correct. It must be noted that the calculated values do not take into account the whole picture, which is more complex, and are merely used in this case as an indication. The transition value of x for aluminium from the infra-red data (Figure 7.12) was found to be a little lower at ~ 0.5, but this is the concentration at which the phonons start to be screened, which increases intensity thereon. Also, the infra-red technique probes only the surface of the material, unlike the resistivity measurements which are conducted across the bulk. In addition, percolation theory demands a totally random model, which might not be the case.

7.5 Conclusions

The $LaNi_{1-x}Al_xO_3$ system can be readily prepared at ambient pressure for all compositions using a citrate gel precursor technique. All compositions were found to be stoichiometric in oxygen content determined by TGA, and crystallise in a rhobohedral unit cell with space group R-3c. On addition of aluminium to the solid-solution, a linear decrease in cell volume was found across the series. On further examination of the structural refinement data, several other trends were apparent. Increasing aluminium concentration led to a gradual shift of the oxygen x co-ordinate which was reflected in a gradually decreasing Ni/Al-O bond length. A decrease in the Ni/Al-O-Ni/Al bond angle was also observed which progressively approached the ideal cubic perovskite angle of 180 ° at higher aluminium content. The oxygen environment of the La ions was found to become more regular with increasing aluminium concentration. Overall, the structure became increasingly less distorted as nickel was replaced by aluminium, which is explained by perovskite tolerance factor considerations.

Resistivity measurements showed the $LaNi_{1-x}Al_xO_3$ system to become more insulating across the series by several orders of magnitude. The increase in resistivity was gradual and linear until 60 % aluminium concentration, whereupon there was a sudden jump in resistivity. This was also reflected in the infra-red spectra results which showed a linear increase in integrated band intensity, with a steeper increase in the gradient at the 50 %

aluminium concentration mark. The jump in resistivity could be explained by applying percolation theory where the threshold of the $LaNi_{1-x}Al_xO_3$ system was at $x = 0.6$. This was found to be close to the calculated value of 0.685.

There was found to be no evidence of a structural change or anomaly at the threshold value, or at any other point in the solid-solution, although if there was it would be very unlikely to be detected by PXD.

In summary, a complete solid-solution between $LaNiO_3$ and $LaAlO_3$ has been prepared and the structures of each composition determined by PXD. Several structural trends were determined across the series. Resistivity measurements showed the materials to all behave like semiconductors with the exception of $LaNiO_3$, which is metallic. The $LaNi_{1-x}Al_xO_3$ system has been interpreted to have a conductance percolation threshold of $\sim x = 0.6$.

7.6 References

[1] J. L. Garcia-Munoz, Rodriguez-Carvajal, P. Lacorre and J. B. Torrance, *Phys. Rev. B* **46** 4414 (1992).

[2] J. García, D. Beltrán, F. Sapiña and M.J. Sanchis, *J. Alloys Compounds* **188** 170 (1992).

[3] X. Granados, J. Fontcuberta, X. Obradors, L. Mañosa and J. B. Torrance, *Phys. Rev. B* **48** 11666 (1993).

[4] J. Blasco, M. Castro and J. García, *J. Phys. Condens. Matter* **6** 5875 (1994).

[5] D. D. Sarma, N. Shanti and P. Mahadevan, *J. Phys. Condens. Matter* **6** 10467 (1994).

[6] N. Gayathri, A. K. Raychaudhuri, X. Q. Xu, J. L. Peng and R. L. Greene, *J. Phys. Condens. Matter* **10** 1323 (1998).

[7] I. Álvarez, M. L. Veiga and C. Pico, *J. Solid State Chem.* **136** 313 (1998).

[8] J. B. Goodenough and P. Raccah, *J. Appl. Phys.* **36** 1031 (1965).

[9] J. P. Kemp and P. A. Cox, *Solid State Commun.* **75** 731 (1990).

[10] R. D. Shannon, *Acta Cryst.* **A32** 751 (1976).

[11] S. Geller and V. B. Bala, *Acta Cryst.* **9** 1019 (1956).

[12] T. A. Vanderah, C. K. Lowe-Ma and D. R. Gagnon, *J. Am. Ceram. Soc.* **77** (12) 3125 (1994).

[13] A. K. Adak and P. Pramanik, *Mater. Lett.* **30** 269 (1997).

[14] H. Lehnert, H. Boysen, P. Dreier and Y. Yu, *Z. Kristallogr.* **215** 145 (2000).

[15] M. J. Martínez-Lope, M. T. Casais and J. A. Alonso, *Eur. J. Solid State Inorg. Chem.* **32** 521 (1995).

[16] A. C. Larson and R. B. Von Dreele, *Generalsied Structure and Analysis System,* MS-H805, Los Almos, NM 87545 (1990).

[17] V. M. Goldschmidt, *Skrifter Norske Videnskaps-Akad.* Oslo, I. Mat.-Naturv. Kl., No. 8 (1926).

[18] P. Ganguly and N. Y. Vasanthacharya, *J. Solid State Chem.* **61** 164 (1986).

[19] P. Ganguly, N. Y. Vasanthacharya and C. N. R. Rao, *J. Solid State Chem.* **54** 400 (1984).

[20] B. I. Shklovskii, A. L. Efros, *Electronic Properties of Doped Semiconductors,* Springer, New York (1989).

[21] S. Kirkpatrick, *Rev. Mod. Phys.* **45** 574 (1973).